



National Library  
of Canada

Bibliothèque nationale  
du Canada

Canadian Theses Service

Service des thèses canadiennes

Ottawa, Canada  
K1A 0N4

## NOTICE

The quality of this microform is heavily dependent upon the quality of the original thesis submitted for microfilming. Every effort has been made to ensure the highest quality of reproduction possible.

If pages are missing, contact the university which granted the degree.

Some pages may have indistinct print especially if the original pages were typed with a poor typewriter ribbon or if the university sent us an inferior photocopy.

Previously copyrighted materials (journal articles, published tests, etc.) are not filmed.

Reproduction in full or in part of this microform is governed by the Canadian Copyright Act, R.S.C. 1970, c. C-30.

## AVIS

La qualité de cette microforme dépend grandement de la qualité de la thèse soumise au microfilmage. Nous avons tout fait pour assurer une qualité supérieure de reproduction.

S'il manque des pages, veuillez communiquer avec l'université qui a conféré le grade.

La qualité d'impression de certaines pages peut laisser à désirer, surtout si les pages originales ont été dactylographiées à l'aide d'un ruban usé ou si l'université nous a fait parvenir une photocopie de qualité inférieure.

Les documents qui font déjà l'objet d'un droit d'auteur (articles de revue, tests publiés, etc.) ne sont pas microfilmés.

La reproduction, même partielle, de cette microforme est soumise à la Loi canadienne sur le droit d'auteur, SRC 1970, c. C-30.

THE DISSOLUTION OF  
NIOBIUM AND ZIRCONIUM  
IN LIQUID STEEL

by

PANAGIOTIS GEORGE SISMANIS

A Thesis submitted to the Faculty of Graduate Studies and  
Research in partial fulfilment of the requirements for the  
degree of Doctor of Philosophy in Metallurgy

Department of Mining and Metallurgical Engineering

McGill University

© April 1987

Permission has been granted to the National Library of Canada to microfilm this thesis and to lend or sell copies of the film.

The author (copyright owner) has reserved other publication rights, and neither the thesis nor extensive extracts from it may be printed or otherwise reproduced without his/her written permission.

L'autorisation a été accordée à la Bibliothèque nationale du Canada de microfilmer cette thèse et de prêter ou de vendre des exemplaires du film.

L'auteur (titulaire du droit d'auteur) se réserve les autres droits de publication; ni la thèse ni de longs extraits de celle-ci ne doivent être imprimés ou autrement reproduits sans son autorisation écrite.

ISBN 0-315-44438-X

7

To Maria

"And as for certain truth,  
no man has seen it, nor will  
there ever be a man who  
knows about the gods and  
about all things I  
mention. For if he succeeds  
to the full in saying what is  
completely true, he himself  
is unaware of it; and  
Opinion is fixed by fate upon  
all things."

Xenophanes of Colophon  
(5th Century B. C.)

i

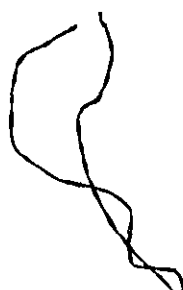
ABSTRACT

The dissolution rates of niobium and zirconium cylinders in liquid steel have been measured in a 'dynamic way', with the help of a data acquisition and process control facility. Two distinct periods were identified; the steel shell period and the free dissolution period.

Lower bath superheats allowed a reaction to take place at the steel shell/niobium interface while higher superheats didn't; the intermetallic compounds  $\text{Fe}_2\text{Nb}$  and  $\text{Fe}_2\text{Nb}_3$  were identified as the reaction products. Niobium dissolved relatively slowly in liquid steel and its dissolution speed was increased under dynamic conditions (i.e., inductively stirred baths).

In the case of zirconium, an exothermic reaction occurred at the steel shell/zirconium interface and the intermetallics  $\text{Fe}_2\text{Zr}$  and  $\text{FeZr}_2$  were identified as the reaction products. This reaction was triggered at 1220 K by the formation of a liquid Fe-Zr (76 at% Zr) eutectic. For the experimental conditions under which this study was performed, the hydrodynamic conditions of the steel baths did not seem to influence the dissolution rates of zirconium.

A simplified mathematical model was used in order to simulate the coupled heat and mass transfer phenomena which take place during the two periods.

  
RESUME

Les vitesses de dissolution de barres de niobium et de zirconium dans de l'acier liquide ont été mesurées dynamiquement à l'aide d'un système permettant l'acquisition des données et le contrôle du procédé. Deux étapes distinctes sont identifiables: une de dissolution de la peau d'acier suivie par la dissolution libre.

De basses températures de surfusion du bain ont permis de mettre en évidence une réaction à l'interface acier/niobium. Ce phénomène n'est pas observé pour des températures de surfusion plus élevées. La réaction observée à basses températures forme les composés intermétalliques  $Fe_2Nb$  et  $Fe_2Nb_3$ . Le niobium se dissout à vitesse relativement lente dans l'acier liquide mais elle augmente en régime dynamique (agitation du bain par induction).

Dans le cas du zirconium une réaction exothermique est observée à l'interface acier/zirconium et l'on a identifié les composés intermétalliques  $Fe_2Zr$  et  $FeZr_2$  comme produits de la réaction. Cette réaction commence à 1220 K par la formation d'un liquide eutectique Fe-Zr (76% atom. Zr). Pour les conditions expérimentales de cette étude l'agitation du bain d'acier ne semble pas influencer les vitesses de dissolution de zirconium.

Un modèle mathématique simplifié est proposé afin de simuler les phénomènes couplés de transport de chaleur et de masse ayant lieu durant les deux étapes.



## TABLE OF CONTENTS

	Page
ABSTRACT.....	i
RESUME.....	ii
LIST OF FIGURES.....	iii
LIST OF TABLES.....	xvi
CHAPTER 1 INTRODUCTION.....	1
1.1 PRELIMINARY REMARKS.....	1
1.2 ALLOY ADDITIONS IN STEELMAKING.....	2
1.3 NIOBIUM AS AN ALLOYING ELEMENT IN STEEL.....	3
1.4 ZIRCONIUM AS AN ALLOYING ELEMENT IN STEEL.....	4
CHAPTER 2 PREVIOUS WORK.....	7
2.1 GENERAL CONSIDERATIONS.....	7
2.2 DISSOLUTION IN LIQUID IRON ALLOYS.....	8
2.3 PRESENT WORK.....	32
CHAPTER 3 PHYSICO-CHEMICAL AND THERMODYNAMIC DATA FOR Nb, Zr, AND Fe-Nb, Fe-Zr ALLOYS.....	34
3.1 DATA FOR NIOBIUM.....	34
3.2 DATA FOR ZIRCONIUM.....	34
3.3 THERMOPHYSICAL AND TRANSPORT PROPERTIES OF LIQUID IRON.....	35
3.3.1 Phase Diagram.....	35
3.3.2 Density.....	35
3.3.3 Viscosity.....	37
3.3.4 Thermal Conductivity.....	37
3.3.5 Specific Heat and Latent Heat of Fusion..	38
3.3.6 Diffusivity.....	38
3.4 A THERMODYNAMIC ASSESSMENT OF THE IRON-NIOBIUM SYSTEM.....	39
3.4.1 Phases and Structures.....	39
3.4.2 Solid (Fe-Nb) Alloys.....	41
3.4.3 Liquid (Fe-Nb) Alloys.....	41

	Page
3.5 A THERMODYNAMIC ASSESSMENT OF THE IRON-ZIRCONIUM SYSTEM.....	44
3.5.1 Phases and Structures.....	44
3.5.2 Solid (Fe-Zr) Alloys.....	47
3.5.3 Liquid (Fe-Zr) Alloys.....	48
CHAPTER 4 EXPERIMENTAL PROCEDURE.....	55
4.1 INTRODUCTION.....	55
4.2 CYLINDER IMMERSION EXPERIMENTS.....	55
4.2.1 Materials.....	57
4.2.2 Adjusting the Steel Bath Chemistry.....	60
4.2.3 Immersing the Bath Thermocouple.....	61
4.2.4 Weight Sensor.....	62
4.2.5 Microprocessor Based Data Acquisition System.....	68
4.2.6 Procedure for Cylinder Immersion Tests....	68
4.2.7 Induction Heating of Composite Samples....	70
4.2.8 Electron Probe X-Ray Microanalysis.....	70
CHAPTER 5 RESULTS AND DISCUSSION ON THE Nb DISSOLUTION IN LIQUID STEEL.....	73
5.1 INTRODUCTION.....	73
5.2 REACTION AT THE STEEL SHELL AND Nb INTERFACE.....	74
5.3 INTERPRETATION OF DATA FROM THE DISSOLUTION EXPERIMENTS.....	82
5.4 CONSISTENCY AND ACCURACY OF THE METHOD.....	88
5.5 APPLICATION OF A MATHEMATICAL MODEL.....	89
5.5.1 Introduction.....	89
5.5.2 General Equations of the Model.....	91
5.5.3 Steel Shell Period.....	100
5.5.4 Free Dissolution Period.....	105
5.6 EFFECT ON THE DISSOLVED OXYGEN AND NITROGEN IN THE MELT.....	115
5.7 DISCUSSION.....	116
CHAPTER 6 RESULTS AND DISCUSSION ON THE Zr DISSOLUTION IN LIQUID STEEL.....	130
6.1 INTRODUCTION.....	130
6.2 REACTION AT THE STEEL SHELL AND Zr INTERFACE.....	131

	Page
6.3 INTERPRETATION OF DATA FROM THE DISSOLUTION EXPERIMENTS.....	142
6.4 APPLICATION OF THE MATHEMATICAL MODEL.....	148
6.4.1 Steel Shell Period.....	148
6.4.2 Free Dissolution Period.....	155
6.5 EFFECT OF THE DISSOLVED OXYGEN AND NITROGEN IN THE MELT.....	163
6.6 THE DISSOLUTION OF THE Fe-Zr (~80% Zr) FERRO-ALLOY IN LIQUID STEEL.....	166
6.7 DISCUSSION.....	172
 CHAPTER 7 THE DISSOLUTION OF NIOBIUM ALLOYS IN LIQUID STEEL.....	 188
7.1 INTRODUCTION.....	188
7.2 EXPERIMENTAL WORK.....	188
7.3 RESULTS AND DISCUSSION.....	190
7.4 THE EFFECT OF OXYGEN ON THE RECOVERY AND DISSOLUTION OF THE Fe-Nb ALLOYS IN LIQUID STEEL.....	194
7.5 THE DISSOLUTION OF Nb-Ni ALLOYS IN LIQUID STEEL.....	204
 CHAPTER 8 CONCLUSIONS.....	 211
 CHAPTER 9 FUTURE WORK.....	 214
 CHAPTER 10 CLAIM TO ORIGINALITY.....	 215
 ACKNOWLEDGEMENTS.....	 217
 APPENDIX I TYPICAL RESULTS FROM THE Nb IMMERSION TESTS.....	 219
 APPENDIX II TYPICAL RESULTS FROM THE Zr IMMERSION TESTS.....	 234
 APPENDIX III ESTIMATION OF EXOTHERMIC HEATS OF MIXING AND Zr MASS TRANSFER COEFFICIENTS DURING STEEL SHELL PERIOD.....	 253
 APPENDIX IV DEOXIDATION WITH NIOBIUM.....	 256
 REFERENCES.....	 259

LIST OF FIGURES

	Page
Figure 2.1 Schematic representation of the thermo-physical phenomena which take place when a solid addition is immersed in liquid steel.....	11
Figure 3.1 The iron-carbon phase diagram.....	36
Figure 3.2 The iron-niobium phase diagram.....	40
Figure 3.3 Partial and Integral Heats of mixing of the liquid iron-niobium alloys.....	43
Figure 3.4 The iron-zirconium phase diagram.....	45
Figure 3.5 Partial and Integral Heats of mixing of the liquid iron-zirconium alloys.....	52
Figure 3.6 Predicted Fe-Zr phase diagram L = LIQUID, A = Fe, B = Zr, C = Fe <sub>2</sub> Zr, and D = FeZr <sub>2</sub> ....	54
Figure 4.1 The induction furnace with its controls.....	56
Figure 4.2 A steel-bath thermocouple.....	63
Figure 4.3A Schematic representation of the induction furnace, the weight sensor, the bath thermocouple, and the immersed cylindrical specimen with one thermocouple along its axis.....	66
Figure 4.3B Schematic representation of the induction furnace, the weight sensor, the bath thermocouple, and the immersed cylindrical specimen with two thermocouples.....	67
Figure 4.4 The DAPC facility.....	69
Figure 4.5 Schematic cross-section of a composite sample (All dimensions are in millimeters).....	71
Figure 5.1 Cross-section of a niobium cylindrical specimen (1.905 cm in diameter) encased by the solidified steel shell. This sample had been immersed in liquid steel at 1600°C (1873 K) for 8 seconds.....	75

	Page	
Figure 5.2	Cross-section of a niobium cylindrical specimen (2.235 cm in diameter) encased by the solidified steel shell. This sample had been immersed in liquid steel at 1570°C (1843 K) for 15 seconds.....	77
Figure 5.3	Temperature versus time curve for an inductively heated iron-niobium composite sample.....	78
Figure 5.4	Temperature versus time curve for an inductively heated iron piece.....	79
Figure 5.5	A typical sample including a part of the iron-niobium interface during the steel shell period, used for Electron Probe X-Ray Microanalysis.....	81
Figure 5.6	Schematic representation of the forces applied to the load cell when a cylinder is immersed in liquid steel.....	83
Figure 5.7	Results from a typical niobium dissolution experiment in liquid steel. The cylinder diameter was 2.54 cm and its length was 18 cm. 1) Measured steel bath temperature; 2) Registered net downward force; 3) Measured and predicted (4) centerline temperature.....	86
Figure 5.8	Schematic representation of an addition with the solidified steel shell and the liquid steel; the various interfaces and the coordinate system used in the mathematical model are also illustrated.....	93
Figure 5.9	Schematic representation of an addition reacting exothermically during the steel shell period; the various interfaces and the coordinate system used in the mathematical model are also illustrated.....	95
Figure 5.10	Cross-section of a niobium cylindrical specimen (2.24 cm in diameter) encased by the solidified steel shell. This sample had been immersed in liquid steel at 1600°C (1873 K) for 8 seconds.....	101

- Figure 5.11 Predicted steel shell periods for niobium cylinders of various diameters.  
1) Time after immersion in which the reaction begins during the steel shell period;  
2) Steel shell period for a large value of generated heat flux;  
3) Steel shell period without any heat generation..... 103
- Figure 5.12 Predicted results on the possibility of the reaction's occurrence during the steel shell period with respect to steel bath superheat, cylinder diameter, and stirring conditions of the melt.  
1) No induction stirring (power off);  
2) Induction stirring (power on)..... 104
- Figure 5.13 Experimental and predicted results from a niobium experiment in liquid steel (see Figure 5.7). The cylinder diameter was 2.54 cm and its length was 18 cm.  
1) Predicted cylinder radius;  
2) Measured and predicted centerline temperature;  
3) Predicted temperature at the niobium/steel interface;  
4) Measured steel bath temperature..... 112
- Figure 5.14 Predicted heat fluxes during the free dissolution period.  
1) The inwards directed heat flux;  
2) The outwards directed heat flux;  
3) The generated (total) heat flux..... 114
- Figure 5.15 Arrhenius-type plot of the experimental mass transfer coefficients.  
Mass transfer coefficients deduced from tests which were performed under:  
1) Static conditions (power off);  
2) Dynamic conditions (power on)..... 123
- Figure 5.16 Niobium cylindrical specimens after immersion in liquid steel..... 125
- Figure 5.17 Niobium cylindrical specimens after immersion in liquid steel..... 126

- Figure 5.18 Predicted total dissolution times versus diameter for different steel bath temperatures and stirring conditions:  
 Static conditions (power off):  
 1) Liquid steel at 1590°C (1863 K);  
 2) Liquid steel at 1615°C (1888 K);  
 3) Liquid steel at 1640°C (1913 K).  
 Dynamic conditions (power on):  
 4) Liquid steel at 1610°C (1883 K)..... 128
- Figure 6.1 Cross-section of a zirconium cylinder (2.54 cm in diameter) after immersion in liquid steel. The arrows mark the original interface..... 132
- Figure 6.2A Temperature versus time for an inductively heated iron-zirconium composite sample.... 134
- Figure 6.2B Temperature versus time for an inductively heated iron-zirconium composite sample.... 135
- Figure 6.3A Cross-section of a zirconium cylinder (2.54 cm in diameter) after immersion in liquid steel at 1593°C (1866 K) for 4 seconds. The arrows mark the original interface..... 137
- Figure 6.3B Cross-section of a zirconium cylinder (2.54 cm in diameter) after immersion in liquid steel at 1593°C (1866 K) for 6 seconds. The arrows mark the original interface..... 138
- Figure 6.4A & B Typical samples including parts of the iron-zirconium interface during the steel shell period, used for Electron Probe X-Ray Microanalysis..... 140
- Figure 6.5 Results from a typical zirconium dissolution experiment in liquid steel. The cylinder diameter was 3.81 cm and its length was 20.5 cm.  
 1) Measured steel bath temperature;  
 2) Registered net downward force;  
 3) Measured and predicted temperature at a distance 1.4 cm apart from the center.  
 4) Measured and predicted centerline temperature..... 143

- Figure 6.6 Results from a typical zirconium dissolution experiment in liquid steel. The cylinder diameter was 3.81 cm and its length was 20.5 cm.
- 1) Measured steel bath temperature;
  - 2) Registered net downward force;
  - 3) Measured and predicted temperature at a distance 1.4 cm apart from the center;
  - 4) Measured and predicted centerline temperature..... 147
- Figure 6.7 Measured and predicted temperatures in a 2.54-cm-diameter zirconium cylinder..... 150
- Figure 6.8 A & B Two zirconium cylinders (2.54 cm in diameter) after immersion in liquid steel at 1593°C (1866 K) for 4 seconds (A), and 6 seconds (B)..... 153
- Figure 6.9 Experimental and predicted results for the zirconium cylinders shown in Fig. 6.8A and B.
- 1) Predicted radius;
  - 2) Initial radius;
  - 3) Measured and predicted extent of the reaction at the steel shell;
  - 4) Measured and predicted extent of the reaction at the zirconium..... 154
- Figure 6.10 Experimental and predicted results from a zirconium experiment in liquid steel (see Figure 6.5). The cylinder diameter was 3.81 cm and its length was 20.5 cm.
- 1) Predicted cylinder radius;
  - 2) Measured and predicted centerline temperature;
  - 3) Predicted temperature at the zirconium/steel interface;
  - 4) Measured steel bath temperature..... 158
- Figure 6.11 Experimental and predicted results from a zirconium experiment in liquid steel (see Figure 6.6). The cylinder diameter was 3.81 cm and its length was 20.5 cm.
- 1) Predicted cylinder radius;
  - 2) Measured and predicted centerline temperature;
  - 3) Predicted temperature at the zirconium/steel interface;
  - 4) Measured steel bath temperature..... 159

	Page	
Figure 6.12	Predicted heat fluxes during the free dissolution period. 1) The inwards directed heat flux; 2) The outwards directed heat flux; 3) The generated (total) heat flux.....	162
Figure 6.13	Results from a typical dissolution experiment of a (80% grade) ferrozirconium lump in liquid steel at 1635°C (1908 K). 1) Measured steel bath temperature; 2) Registered net downward force.....	167
Figure 6.14	Predicted total melting times versus lump diameter (considered as a sphere) for various conditions: Static conditions (power off): 1) Liquid steel at 1610°C (1883 K). Dynamic conditions (power on): 2) Liquid steel at 1620°C (1893 K); 3) Liquid steel at 1635°C (1908 K).....	171
Figure 6.15	Arrhenius-type plot of the experimental mass transfer coefficients. Mass transfer coefficients deduced from tests which were performed under: (O) Static conditions (power off); (Δ) Dynamic conditions (power on).....	179
Figure 6.16	Predicted total dissolution times versus diameter under various temperatures: 1) Liquid steel at 1590°C (1863 K); 2) Liquid steel at 1615°C (1888 K); 3) Liquid steel at 1640°C (1913 K).....	183
Figure 6.17	Predictions for the effect of exothermicity on the steel bath superheat. 1) Without any induction stirring; 2) With induction stirring.....	186
Figure 7.1	Results from a typical dissolution experiment of a high-purity ferroniobium lump in liquid steel under static conditions. 1) Measured steel bath temperature; 2) Registered net downward force.....	191
Figure 7.2	Results from a typical dissolution experiment of a high-purity ferroniobium lump in liquid steel under dynamic conditions. 1) Measured steel bath temperature; 2) Registered net downward force.....	192

Figure 7.3 Predictions for the total dissolution times of high-purity ferroniobium lumps, considered as spheres, as a function of lump diameter and experimental conditions:  
 Static conditions (power off):  
 1) Liquid steel at 1610°C (1883 K);  
 2) Liquid steel at 1630°C (1903 K).  
 Dynamic conditions (power on):  
 1) Liquid steel at 1620°C (1893 K);  
 2) Liquid steel at 1630°C (1903 K)..... 193

Figure 7.4 Schematic cross-section of the induction furnace with ferroalloy lump, weight sensor, CELOX oxygen-probe system, and the intelligent satellite microperipheral µMAC-5000.... 197

Figure 7.5 Typical experimental result obtained from measuring dissolution of standard ferro-niobium in liquid steel. The active oxygen of liquid steel for this case is shown in Figure 7.6..... 199

Figure 7.6 Typical experimental results obtained by the CELOX oxygen-probe system. Just prior to measuring the dissolution rate of the standard ferroniobium lump (Figure 7.5), curve 1 shows the measured temperature, and curve 2 depicts the recorded active oxygen in liquid steel in ppm..... 200

Figure 7.7 Niobium recovery from standard ferroniobium lumps as a function of active oxygen in liquid steel. Curve 1 shows the regression line..... 202

Figure 7.8 Dissolution speed of standard grade ferro-niobium lumps as a function of active oxygen in liquid steel..... 203

Figure 7.9 A typical experimental result from the melting of a niobium-nickel lump in liquid steel.  
 1) Measured steel bath temperature;  
 2) Registered net downward force..... 206

Figure 7.10 Predictions for total melting times of spherical niobium-nickel lumps in liquid steel under static conditions:  
 1) Liquid steel at 1600°C (1873 K);  
 2) Liquid steel at 1615°C (1888 K);  
 3) Liquid steel at 1630°C (1903 K)..... 209

Figure 7.11 A typical sequence of events occurring during a typical melting test of a niobium-nickel alloy in liquid steel..... 210

Figure I-1 Results from a typical niobium dissolution experiment (Run no. 7, Table 5.2) in liquid steel. The cylinder diameter was 2.54 cm and its length was 18 cm.

- 1) Measured steel bath temperature;
- 2) Registered net downward force;
- 3) Measured and predicted (4) centerline temperature.....220

Figure I-2 Results from a typical niobium dissolution experiment (Run no. 6, Table 5.2) in liquid steel. The cylinder diameter was 2.54 cm and its length was 18 cm.

- 1) Measured steel bath temperature;
- 2) Registered net downward force;
- 3) Measured and predicted (4) centerline temperature.....221

Figure I-3 Results from a typical niobium dissolution experiment (Run no. 2, Table 5.2) in liquid steel. The cylinder diameter was 2.54 cm and its length was 18 cm.

- 1) Measured steel bath temperature;
- 2) Registered net downward force;
- 3) Measured and predicted (4) centerline temperature..... 222

Figure I-4 Results from a typical niobium dissolution experiment (Run no. 14, Table 5.2) in liquid steel. The cylinder diameter was 3.81 cm and its length was 12.4 cm.

- 1) Measured steel bath temperature;
- 2) Registered net downward force;
- 3) Measured and predicted temperature 1.4 cm apart from the cylinder axis;
- 4) Measured and predicted centerline temperature..... 223

Figure I-5 Results from a typical niobium dissolution experiment (Run no. 1, Table 5.2) in liquid steel. The cylinder diameter was 2.54 cm and its length was 18 cm.

- 1) Measured steel bath temperature;
- 2) Registered net downward force;
- 3) Measured and predicted (4) centerline temperature..... 224

Figure I-6 Results from a typical niobium dissolution experiment (Run no. 8, Table 5.2) in liquid steel. The cylinder diameter was 1.905 cm and its length was 18 cm.

- 1) Measured steel bath temperature;
- 2) Registered net downward force..... 225

- Figure I-7 Results from a typical niobium dissolution experiment (Run no. 11, Table 5.2) in liquid steel. The cylinder diameter was 1.905 cm and its length was 18 cm.  
1) Measured steel bath temperature;  
2) Registered net downward force..... 226
- Figure I-8 Results from a typical niobium dissolution experiment (Run no. 18, Table 5.2) in liquid steel. The cylinder diameter was 1.905 cm and its length was 18 cm.  
1) Measured steel bath temperature;  
2) Registered net downward force..... 227
- Figure I-9 Results from a typical niobium dissolution experiment (Run no. 13, Table 5.2) in liquid steel. The cylinder diameter was 1.905 cm and its length was 18 cm.  
1) Measured steel bath temperature;  
2) Registered net downward force..... 228
- Figure I-10 Results from a typical niobium dissolution experiment (Run no. 15, Table 5.2) in liquid steel. The cylinder diameter was 1.905 cm and its length was 18 cm.  
1) Measured steel bath temperature;  
2) Registered net downward force..... 229
- Figure I-11 Results from a typical niobium dissolution experiment (Run no. 9, Table 5.2) in liquid steel. The cylinder diameter was 1.905 cm and its length was 18 cm.  
1) Measured steel bath temperature;  
2) Registered net downward force..... 230
- Figure I-12 Results from a typical niobium dissolution experiment (Run no. 16, Table 5.2) in liquid steel. The cylinder diameter was 1.905 cm and its length was 18 cm.  
1) Measured steel bath temperature;  
2) Registered net downward force..... 231
- Figure I-13 Results from a typical niobium dissolution experiment (Run no. 10, Table 5.2) in liquid steel. The cylinder diameter was 1.905 cm and its length was 18 cm.  
1) Measured steel bath temperature;  
2) Registered net downward force..... 232

- Figure I-14 Results from a typical niobium dissolution experiment (Run no. 12, Table 5.2) in liquid steel. The cylinder diameter was 1.905 cm and its length was 18 cm.  
 1) Measured steel bath temperature;  
 2) Registered net downward force..... 233
- Figure II-1 Results from a typical zirconium dissolution experiment (Run no. 2, Table 6.4) in liquid steel. The cylinder diameter was 2.54 cm and its length was 18 cm.  
 1) Measured steel bath temperature;  
 2) Registered net downward force;  
 3) Measured and predicted centerline temperature..... 235
- Figure II-2 Results from a typical zirconium dissolution experiment (Run no. 6, Table 6.4) in liquid steel. The cylinder diameter was 2.54 cm and its length was 18 cm.  
 1) Measured steel bath temperature;  
 2) Registered net downward force;  
 3) Measured and predicted centerline temperature..... 236
- Figure II-3 Results from a typical zirconium dissolution experiment (Run no. 12, Table 6.4) in liquid steel. The cylinder diameter was 2.54 cm and its length was 18 cm.  
 1) Measured steel bath temperature;  
 2) Registered net downward force;  
 3) Measured and predicted centerline temperature..... 237
- Figure II-4 Results from a typical zirconium dissolution experiment (Run no. 7, Table 6.4) in liquid steel. The cylinder diameter was 2.54 cm and its length was 18 cm.  
 1) Measured steel bath temperature;  
 2) Registered net downward force;  
 3) Measured and predicted centerline temperature..... 238
- Figure II-5 Results from a typical zirconium dissolution experiment (Run no. 11, Table 6.4) in liquid steel. The cylinder diameter was 2.54 cm and its length was 18 cm.  
 1) Measured steel bath temperature;  
 2) Registered net downward force;  
 3) Measured and predicted centerline temperature..... 239

Figure II-6 Results from a typical zirconium dissolution experiment (Run no. 8, Table 6.4) in liquid steel. The cylinder diameter was 2.54 cm and its length was 18 cm.  
 1) Measured steel bath temperature;  
 2) Registered net downward force;  
 3) Measured and predicted centerline temperature..... 240

Figure II-7 Results from a typical zirconium dissolution experiment (Run no. 4, Table 6.4) in liquid steel. The cylinder diameter was 2.54 cm and its length was 18 cm.  
 1) Measured steel bath temperature;  
 2) Registered net downward force;  
 3) Measured and predicted centerline temperature..... 241

Figure II-8 Results from a typical zirconium dissolution experiment (Run no. 9, Table 6.4) in liquid steel. The cylinder diameter was 2.54 cm and its length was 18 cm.  
 1) Measured steel bath temperature;  
 2) Registered net downward force;  
 3) Measured and predicted centerline temperature..... 242

Figure II-9 Results from a typical zirconium dissolution experiment (Run no. 5, Table 6.4) in liquid steel. The cylinder diameter was 1.905 cm and its length was 18 cm.  
 1) Measured steel bath temperature;  
 2) Registered net downward force..... 243

Figure II-10 Results from a typical zirconium dissolution experiment (Run no. 1, Table 6.4) in liquid steel. The cylinder diameter was 1.905 cm and its length was 18 cm.  
 1) Measured steel bath temperature;  
 2) Registered net downward force..... 244

Figure II-11 Results from a typical zirconium dissolution experiment (Run no. 3, Table 6.4) in liquid steel. The cylinder diameter was 1.905 cm and its length was 18 cm.  
 1) Measured steel bath temperature;  
 2) Registered net downward force..... 245

- Figure II-12 Results from a typical zirconium dissolution experiment (Run no. 18, Table 6.5) in liquid steel. The cylinder diameter was 2.54 cm and its length was 18 cm.
- 1) Measured steel bath temperature;
  - 2) Registered net downward force;
  - 3) Measured and predicted centerline temperature..... 246
- Figure II-13 Results from a typical zirconium dissolution experiment (Run no. 21, Table 6.5) in liquid steel. The cylinder diameter was 2.54 cm and its length was 18 cm.
- 1) Measured steel bath temperature;
  - 2) Registered net downward force;
  - 3) Measured and predicted centerline temperature..... 247
- Figure II-14 Results from a typical zirconium dissolution experiment (Run no. 19, Table 6.5) in liquid steel. The cylinder diameter was 2.54 cm and its length was 18 cm.
- 1) Measured steel bath temperature;
  - 2) Registered net downward force;
  - 3) Measured and predicted centerline temperature..... 248
- Figure II-15 Results from a typical zirconium dissolution experiment (Run no. 13, Table 6.5) in liquid steel. The cylinder diameter was 1.905 cm and its length was 18 cm.
- 1) Measured steel bath temperature;
  - 2) Registered net downward force..... 249
- Figure II-16 Results from a typical zirconium dissolution experiment (Run no. 16, Table 6.5) in liquid steel. The cylinder diameter was 1.905 cm and its length was 18 cm.
- 1) Measured steel bath temperature;
  - 2) Registered net downward force..... 250
- Figure II-17 Results from a typical zirconium dissolution experiment (Run no. 17, Table 6.5) in liquid steel. The cylinder diameter was 1.905 cm and its length was 18 cm.
- 1) Measured steel bath temperature;
  - 2) Registered net downward force..... 251

Figure II-18 Results from a typical zirconium dissolution experiment (Run no. 15, Table 6.5) in liquid steel. The cylinder diameter was 1.905 cm and its length was 18 cm.

- 1) Measured steel bath temperature;
- 2) Registered net downward force..... 252

LIST OF TABLES

	Page
Table 2.1 Additions with Melting Range Lower than the Liquid Steel Melting Point.....	9
Table 2.2 Additions with Melting Range Higher than the Liquid Steel Melting Point.....	10
Table 2.3 Dissolution Experiments in Liquid Iron Alloys.....	15
Table 2.4 Dissolution Experiments in Pure Liquid Iron or Low Carbon Liquid Iron Alloys.....	20
Table 3.1 Integral Heats of Formation of Solid Fe-Nb Alloys.....	42
Table 3.2 Integral Heats of Fromation of Solid Fe-Zr Alloys.....	49
Table 4.1 Chemical analysis of Niobium and Zirconium cylinders in ppm.....	58
Table 4.2 Thermal and Physical Properties of Niobium, Zirconium, and Armco-Iron.....	59
Table 4.3 Typical values of the Coefficients A and B (Eqn. 4.1), obtained by calibration tests....	65
Table 5.1 Mass Transfer Coefficients during niobium free dissolution under static conditions.....	119
Table 5.2 Experimentally measured (-dr/dt) and deduced mass transfer coefficient ( $K_{Nb}$ ) during niobium free dissolution under static (Runs 1-13), and dynamic (Runs 14-18) conditions.....	121
Table 6.1 Experimentally measured rates of the 80% grade ferrozirconium.....	170
Table 6.2 Estimated Heat and Mass Fluxes during the Steel shell and Free dissolution periods.....	173
Table 6.3 Mass transfer coefficients of zirconium in the beginning of the free dissolution.....	175
Table 6.4 Experimentally measured (-dr/dt) and mean mass transfer coefficients during zirconium free dissolution under static conditions.....	177

	Page
Table 6.5 Experimentally measured $(-dr/dt)$ and mean mass transfer coefficients during zirconium free dissolution under dynamic conditions....	178
Table 7.1 Chemical Compositions of ferroalloys tested..	189
Table 7.2 Solution Rates of Nb-Ni lumps in liquid steel under Static Conditions.....	207

THE DISSOLUTION OF  
NIOBIUM AND ZIRCONIUM  
IN LIQUID STEEL

## CHAPTER 1

### 1. INTRODUCTION

#### 1.1 PRELIMINARY REMARKS

In recent years, the process of steel alloy development has greatly benefited from the large amount of research carried out in that area. This research has led to a much improved appreciation of the relationship between micro-structure and mechanical properties, so that new alloy steels can now be developed on the basis of reasonably well understood metallurgical phenomena from the physical metallurgy viewpoint. However, at the refining stage of the alloy steelmaking route, a lot of research still has to be carried out particularly on the solution rates and mechanisms of solid additives (i.e., ferroalloys) in the raw liquid steel. Especially in recent years, the tight chemical specifications which the market demands from the steelmakers have as a result the introduction of more careful ferroalloy addition practices which should reflect repeatable and consistently high ferroalloy recoveries, and hence more economic savings and profit. The development of these practices is directly related to the accumulated knowledge on the subject. Therefore, a thorough understanding of the solution mechanisms and their kinetics is of paramount importance from both the academic and industrial points of view.

## 1.2 ALLOY ADDITIONS IN STEELMAKING.

The steel is termed alloyed, if the content of alloying elements in it, is greater than in common carbon steel. For instance, a steel is related to the category of alloy steels, if it contains more than 0.6% Si or more than 0.8% Mn, while common carbon steel usually contains 0.17 - 0.37% Si and not more than 0.7% Mn. Various alloying elements are employed in steelmaking, whose presence imparts special mechanical and other properties to the steel.

These may be either metals (i.e., Mn, Ni, Co, Ti, Nb, V) or non-metals (i.e., C, S, P, N, B). Their solubility in iron may be very diverse, some elements (Pb, Ag, Bi) being practically insoluble.

Introducing 'small additions' of elements or their compounds (in amounts not more than 0.1%) into the melt, microalloying of the steel is done, with the aim of improving appreciably the mechanical and service properties of the final steel.

The effects provided by microalloying are deeper deoxidation, desulphurization and degassing of steel; changes in the shape and properties of nonmetallic inclusions and their distribution in microvolumes of the metal; changes in the composition and state of grain boundaries; refinement of metal grains and control of their growth upon heating.

Microalloying can also affect the critical points,

recrystallization temperature and hardenability of steel; this often happens when some metallic additions, such as Ti, V, Nb, Zr, Ta, etc., are introduced in the liquid steel.

In general, there are many reasons for the introduction of alloying elements into liquid steel.

Some of the most important ones, are to<sup>1</sup> :

- (1) Improve strength at ordinary temperatures;
- (2) Improve mechanical properties at either high or low temperatures;
- (3) Increase hardenability;
- (4) Improve toughness at any minimum hardness of strength;
- (5) Increase corrosion resistance;
- (6) Increase wear resistance;
- (7) Improve magnetic properties.

In this work, the study of the dissolution of niobium and zirconium in liquid steel, has been undertaken. Some of the most important applications of niobium and zirconium, in the steel industry, are presented below.

### 1.3 NIOBIUM AS AN ALLOYING ELEMENT IN STEEL

The two principal uses of niobium in steels are, as a grain refiner and, for the formation of an extremely hard and stable carbide<sup>1</sup>. The two uses are metallurgically related.

As a grain refiner, niobium is very important in those HSLA steels which are controlled rolled; many current

controlled rolling schedules depend on the precipitation of NbC (N) during hot working<sup>1</sup>. Understandably, this application accounts for the major tonnage consumption of niobium, and still promises to be its area of maximum growth potential. As a carbide former, niobium has seen use for many years in the 'stabilization' of austenitic 18/8 stainless steels against sensitization-induced intergranular corrosion. It is also a constituent of abrasion-resistant steels, steels for elevated temperature service, and numerous superalloys.

Steels microalloyed with niobium, show considerable promise in the production of high strength reinforcing bars. Niobium provides additional strengthening, beyond that resulting from carbon and manganese. Because only about one-half the amount of niobium (0.012% Nb = 0.025% V) is needed<sup>1</sup> to produce the same strength increase brought about by vanadium additions, niobium steels can have economic advantages for the steelmaker.

#### 1.4 ZIRCONIUM AS AN ALLOYING ELEMENT IN STEEL

Zirconium is highly reactive and forms stable compounds with oxygen, sulfur, nitrogen and carbon. Its affinity for the first three of these elements accounts for its principal use in steelmaking<sup>1</sup>:

The control of nonmetallic (sulfide and oxysulfide) inclusions and the fixation of nitrogen, primarily in boron steels. Zirconium will also inhibit grain growth and prevent

strain aging, although its use for either of these functions is quite limited.

Although zirconium is reasonably plentiful, elaborate extractive metallurgical processes make the pure metal very expensive. Fortunately, these operations are not required for the zirconium addition agents used in steelmaking. Nonetheless, its relatively high price and the availability of cheaper replacements, has restricted its general acceptance as an alloying agent in steels.

With its strong ability to fix sulfur, zirconium can be used as a partial replacement for manganese to prevent hot shortness, during rolling/forging processes<sup>1</sup>. The fixation of sulfur has a beneficial effect on transverse ductility and impact properties as well. Levels of zirconium between 0.03 and 0.30% are known to prevent the formation of the detrimental grain boundary film sulfides.

The hardenability factor for zirconium probably lies between those for vanadium and titanium. However, for practical and economic reasons, zirconium is not used for the sake of promoting deep hardening.

The presence of zirconium compounds does, however, reduce grain coarsening, permitting the use of higher hardening or carburizing temperature. Zirconium produces only slight changes in the mechanical properties of quenched and tempered steels, though these changes are generally beneficial. It produces a more uniform distortion during

heat treatment than, for example, vanadium. Zirconium improves ductility and impact strength, raises the yield/tensile ratio, improves weldability and eliminates porosity.

In high alloy steels, zirconium increases hardness but decreases ductility. Several quenched and tempered HSLA steels, contain 0.10 - 0.15% Zr, mainly for sulfide shape control.

CHAPTER 2

2. PREVIOUS WORK

2.1 GENERAL CONSIDERATIONS

The solution of a solid in a liquid represents a classical example of a heterogeneous process. Although most such processes involve a rather complex set of individual reaction steps, there are certain elementary aspects which are common to a wide range of reactions.

The transfer of the material of a substance from a solid to a liquid state, can be characterized as melting or as dissolution.

The difference between melting and dissolution is, that dissolution occurs when the solid material comes in contact with the liquid at temperatures below the melting point of the solid. The dissolution process can be divided in two basic consecutive steps. The first is the surface reaction where the solid goes through a phase change to the liquid. In the case of metallic additions, the phase change is actually the result of the rupture of the metallic bond at the interface, for which a large amount of energy is required. The second step is the transport of the resulting solute atoms from the interface into the bulk liquid by diffusion through a boundary layer. Either step could be rate-controlling in the dissolution process.

Additions in liquid steel can be classified into two categories. The first are those with a melting range lower than that of liquid steel. Table 2.1 gives a list of such additions. The second category of additions are those with melting ranges higher than that of liquid steel. Examples of some of these additions are listed in Table 2.2.

Figure 2.1 shows, in schematic form, the relevant thermophysical phenomena which take place when a solid addition is immersed in a bath of molten steel.

The first four routes refer to low melting range additions while the fifth one depicts the case of dissolution of high melting point additions.

Routes 1, 2, 3 and 5 are analyzed in a work by Guthrie<sup>2</sup>, while route 4 is presented in great detail by Argyropoulos and Guthrie in references 3, 4. The microexothermic route (Route 6) has been introduced in a recent work<sup>5</sup> by Argyropoulos.

## 2.2 DISSOLUTION IN LIQUID IRON ALLOYS

Extensive studies on the kinetics of dissolution of solid materials in liquid iron-carbon melts have been conducted over the past thirty years.

The great majority of these experiments were done in either high carbon iron alloy melts or carbon saturated iron alloy melts.

Table 2.1

Additions with Melting Range  
Lower than the Liquid Steel Melting Point

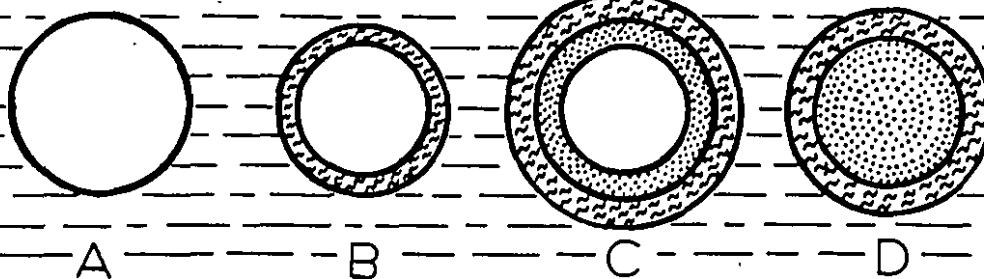
<u>Addition</u>	<u>Melting Range or Melting Point</u> <sup>1</sup>	
50% Ferrosilicon	1210 - 1227°C	(1483 - 1500 K)
75% Ferrosilicon	1204 - 1316°C	(1474 - 1589 K)
Standard Ferromanganese	1071 - 1266°C	(1344 - 1539 K)
Low Carbon Silicomanganese	1215 - 1260°C	(1488 - 1533 K)
Charge Chrome 50-55% Cr	1404 - 1482°C	(1677 - 1755 K)
Aluminum	660°C	(933 K)

Table 2.2

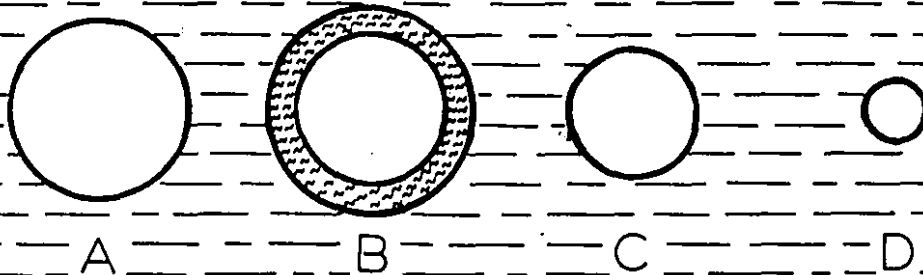
Additions with Melting Range  
Higher than the Liquid Steel Melting Point

<u>Addition</u>	<u>Melting Range</u> <u>Melting Temperature</u> <sup>1</sup>
Niobium	2467°C (2740 K)
Zirconium	1852°C (2125 K)
Vanadium	1902°C (2175 K)
Titanium	1670°C (1943 K)
Molybdenum	2617°C (2890 K)
Tantalum	3014°C (3287 K)
Tungsten	3407°C (3680 K)
FeMo (62% Mo)	1540 - 1800°C (1813 - 2073 K)
FeW (74% W)	1640 - 2700°C (1913 - 2973 K)
FeNb (60% Nb)	1600 - 1650°C (1873 - 1923 K)
FeV (80% V)	1670 - 1890°C (1943 - 2163 K)

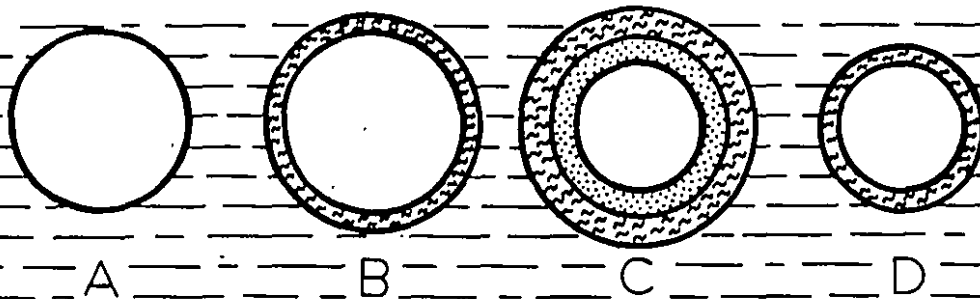
Route 1



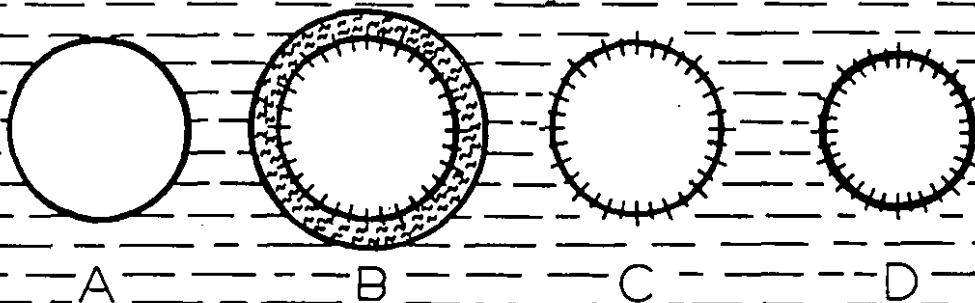
Route 2



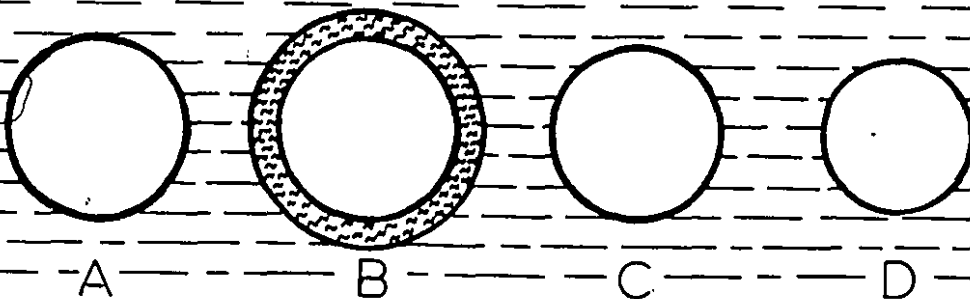
Route 3



Route 4



Route 5



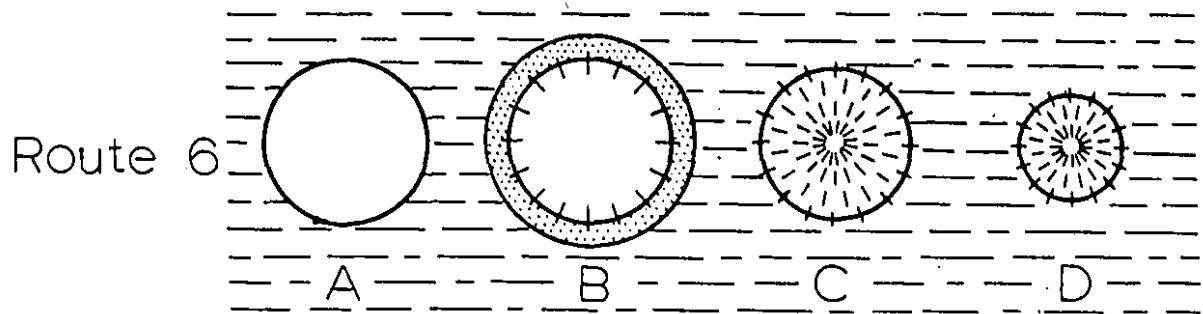


Figure 2.1

Additions with melting range below the melting point of liquid steel follow one of the routes 1, 2, 3. Additions which exhibit exothermic reaction with liquid steel follow route 4. Route 5 refers to high melting range additions. Route 6 refers to microexothermic alloying additions in liquid steel.

Route 1

The introduction of FeMn, SiMn, Al in steel melts with low bath superheats for example, can cause internal melting (1C) of the addition which in some cases (the melting) is completed (1D) before the remelting of the enclosing shell.

Route 2

In this case, internal melting of the addition may start but it is not completed as the encasing shell melts back (2C). Alloys with large diameters and low thermal conductivities immersed in liquid steel with high bath superheats (80-100 K) can exhibit this behaviour.

Route 3

Once the addition is re-exposed (3C), another shell (or series of shells) of solidified steel (3D) may be formed.

Route 4

An exothermic reaction starts at (4B) and steel shell melts back very fast; typical examples are Si, Fe-75% Si.

Route 5

Typical examples are Fe-V, Fe-Mo, Fe-W.

Route 6

It is also referred as the Microexothermic route. The addition (generally a powder compact) is surrounded by a steel shell (6B). The duration of the steel shell is very short due to the low thermal conductivity of the ferroalloy compact. However, a reaction starts at the compact steel shell interface. This reaction proceeds very quickly into the interior of the ferroalloy compact (i.e., 6C and 6D) where the addition melts.

Far fewer experiments have been conducted in low carbon and relative pure iron alloy melts.

Table 2.3 lists metallic systems of solids dissolved in iron based melts for which experimental data have been reported. These experiments have been classified according to experimental mode and geometry. The experimental mode can be classified into two subgroups; static and dynamic.

In the static method, the solid specimens were held motionless in liquid, and natural convection, influenced the dissolution rate.

In the dynamic method, specimens were rotated so that forced convection affected their rate of dissolution. For most of the reported experiments, cylindrical or disk shaped specimens were used.

However, there are two exceptions:

1) Biletskii and Shumikhin<sup>15</sup> studied the dissolution of spherical graphite particles in cast iron melts;

2) Niwa et al.<sup>23</sup> also used an alumina crucible to study the reaction of the alumina with carbon dissolved in molten iron. The crucibles used were either alumina or graphite, apart from a few exceptions, where magnesia crucibles were used.

The dissolution in liquid iron alloys was reported to be a diffusion rate controlled process under most conditions. An exception is the one reported by Karchin and Grigoryan<sup>11</sup> who observed that the dissolution rate of pyrographite in an

Table 2.3

## Dissolution Experiments in Liquid Iron Alloys

Liquid	Solid	Specimen	Mode	Reference
Fe-C	Graphite	Cylinder	Static	6
Fe-C	Graphite	Cylinder	Static	7
Fe-C	Graphite	Cylinder	Static and Rotating	8
Fe-C	Graphite	Cylinder	Rotating	9
Fe-Mn	Graphite		Static	10
Fe-C	Graphite		Rotating	11
Pig Iron	Graphite	Disk	Static	12
Fe-C	Graphite	Disk	Rotating	13
Fe-Ni	Graphite	Disk	Rotating	13
Fe-P	Graphite	Disk	Rotating	13
Fe-Si	Graphite		Rotating	13
Fe-C	C			14
Cast Iron	Graphite	Spherical		15
Fe-C	Graphite			16
Fe-C	Si-C			16
Fe-C	C			17
Fe-C	Co	Disk	Rotating	18
Fe-C	Cr	Disk	Rotating	18
Fe-C	Mo	Disk	Rotating	18
Fe-C	Ni	Disk	Rotating	18
Fe-C	Si	Disk	Rotating	18
Fe-C	Ti	Disk	Rotating	18
Fe-C	W	Disk	Rotating	18

...cont.

Table 2.3 Continued

Liquid	Solid	Specimen	Mode	Reference
Fe-C <sub>sat</sub>	Cr	Disk	Rotating	19
Fe-C <sub>sat</sub>	CrC	Disk	Rotating	19
Fe-C <sub>sat</sub>	Fe	Disk	Rotating	19
Fe-C <sub>sat</sub>	Mo	Disk	Rotating	19
Fe-C <sub>sat</sub>	W	Disk	Rotating	19
Fe-C <sub>sat</sub>	WC	Disk	Rotating	19
Gray Iron	SiC	Cylinder	Rotating	20
Pig Iron	C-Steel	Cylinder	Rotating and Static	21
Fe-C <sub>sat</sub>	Fe	Cylinder	Rotating	22
Fe-C <sub>sat</sub>	Al <sub>2</sub> O <sub>3</sub>	Crucible	Static	23
Fe-C	C-Steel	Cylinder	Static	24
Fe-C	C-Steel	Cylinder	Rotating and Static	25
Fe-C	Cu-Mg		Static	26
Fe-C	C-Steel	Cylinder	Static and Rotating	27
Fe-C-S	Ce		Static	28
Fe-C-Si	Ce		Static	28
FeO-Fe <sub>2</sub> O <sub>3</sub>	Fe	Cylinder	Rotating	29
Fe-C	Mg-Alloy		Static	30
Fe-C <sub>sat</sub>	Al <sub>2</sub> O <sub>3</sub>	Cylinder	Static and Rotating	31
Fe-C	Fe			32
Fe-N <sub>sat</sub>	BN	Disk	Static	33
Fe-B	BN	Disk	Static	33
Fe-C <sub>sat</sub>	CaC <sub>2</sub>	Cylinder	Rotating	34

...cont.

Table 2.3 continued

Liquid	Solid	Specimen	Mode	Reference
Pig Iron	C-Steel	Cylinder	Static	35
Pig Iron	C-Steel	Cylinder	Static	36
Fe-C	Fe	Cylinder	Static and Rotating	37
Fe-C <sub>sat</sub>	Mo	Cylinder	Rotating	38
Fe-S	Fe		Rotating	39
Fe-Cu	Fe	Cylinder	Rotating	40
Fe-C	Nb			41
Fe-C <sub>euctect</sub>	Mo	Cylinder	Static	42
Cast Iron	Si	Disk	Rotating	43
Cast Iron	Ti	Disk	Rotating	43
Cast Iron	Cr	Disk	Rotating	43
Cast Iron	Co	Disk	Rotating	43
Cast Iron	Ni	Disk	Rotating	43
Cast Iron	Mo	Disk	Rotating	43
Cast Iron	W	Disk <sup>0</sup>	Rotating	43
Fe-C <sub>sat</sub>	Fe	Cylinder	Static and Rotating	44
Fe-C	Fe	Cylinder	Static and Rotating	45
Fe-C-Si-P	Fe-C-Si	Lumps	Static	46
Fe-C-Si-P	Fe-C-Si-S	Lumps	Static	46
Fe-C	Fe-V	Fine lumps	Static	47
Fe-C	Fe-Cr	Fine lumps & Cylinders	Static	47
Fe-C	Fe-Ti	Fine lumps	Static	47

...cont.

Table 2.3 continued

Liquid	Solid	Specimen	Mode	Reference
Fe-C	Fe-Mn	Fine lumps	Static	47
Fe-C	Fe-Cr-C	Cylinder	Static and Rotating	48
Fe-C	C(graphite)	Cylinder	Rotating	49
Cast Iron	C(graphite)	Lumps	Static	50
Fe-Fe <sub>2</sub> O <sub>3</sub>	Fe	Pellets	Static	51

iron-carbon melt was anisotropic with respect to different crystallographic faces at high rotational speeds. They found that the solution interface reaction of graphite became the controlling step at high stirring rates.

Various additions relevant to steelmaking practices studied for dissolution kinetics in low carbon iron-based melts are listed in Table 2.4.

In all cases and immediately following immersion a solid steel shell solidifies around the addition.

The precise manner under which the steel shell behaves (i.e. freezing or melting) is very important for low melting point additives. However, its importance substantially lessens in the case of high melting point additions. In the first case, the dominant factor in the thermophysical phenomena is heat transfer, while in the latter, mass transfer becomes more important. For the dissolution of 50% ferro-silicon in liquid steel, a 'double heat effect' is applied to the steel shell such that the dissolution reaction becomes self-accelerating<sup>3,4</sup>.

Krupman and Yavoiskii<sup>42</sup> investigated the dissolution of molybdenum in Armco Iron. They distinguish two periods in the dissolution process. The first corresponded to the 'thermal' period where a solid shell freezes around the molybdenum. The second was the 'diffusion' period which began after the temperature had equalized between the bulk liquid steel and the molybdenum specimen. They proposed the following

Table 2.4

Dissolution Experiments in Pure Liquid (Iron or  
Low Carbon Liquid Iron Alloys

Dissolving Solid.	Specimen	Experimental Mode	Reference
Fe-Mn	Cylinder and Sphere	Static	2
Si-Mn	Cylinder and Sphere	Static	2
Fe-Si (50%)	Cylinder	Static	3
Fe-Si (50%)	Cylinder	Static	4
Mo	Cylinder	Static and vibrating	42
Ti	Disk	Rotating	43
Cr	Disk	Rotating	43
Nb	Disk	Rotating	43
Mo	Disk	Rotating	43
W	Disk	Rotating	43
FeMo (62% Mo)	Disk	Rotating	43
FeW (74% W)	Disk	Rotating	43
FeNb (60% Nb)	Disk	Rotating	43
C (graphite)	Lumps	Static	46
Si	Lumps	Static	46
Cr	Lumps	Static	46
Mo	Lumps	Static	46
Mo	Cylinder	Static and Rotating	52
W	Cylinder	Static and Rotating	52
Fe-Mn	Cylinder	Static	53
Cr-Mn	Cylinder	Static	53
Fe-Cr	Cylinder	Static	53

...cont.

Table 2.4 continued

Dissolving Solid	Specimen	Experimental Mode	Reference
Fe-Mn	Lumps with Isotopes	Static	54
Si-Mn	Lumps with Isotopes	Static	54
TiN		Rotating	55
Ferro-alloys			56
Fe-Mn	Cylinder	Static	57
Si-Mn	Cylinder	Static	57
Fe-Si	Cylinder	Static	57
Al	Sphere	Static	58
Al	Sphere	Rotating	59
V	Cylinder	Static	60
Ti	Cylinder	Static	60,61,62
Ferro-alloys	Lumps	Static	63
Mo	Slab	Static	64
Fe	Sponge Pellets	Static	65
C (graphite)	Cylinder	Rotating	66
C	Disk	Rotating	67
Cr	Cylinder	Rotating	68
Fe-Cr	Cylinder	Rotating	68
Fe-Cr	Lumps	Static	69
Ferro-alloys	Lumps	Static	70
Ferro-alloys	Powder Compacts	Static	71

relationship for the dependence of mass transfer coefficients on temperature:

$$\log K = - \frac{14800}{T} + 4.87, \quad (2.1)$$

K : cm/sec

T : K

Based on their data, an activation energy for the solution of molybdenum in liquid iron was calculated and shown to be at 273 kJ/mole (65.1 kcal/mol). They explained this surprisingly high value of activation energy on the basis of liquid phase diffusion. However, more recent work by Ershov et al.<sup>72</sup> and Ono et al.<sup>73</sup> has shown that the activation energy for the diffusion of molybdenum in liquid iron is only in the order of 59 kJ/mol (14.5 kcal/mol). Consequently, their explanation based on a liquid phase diffusion controlled process must be regarded with some doubt.

Shantarin and Shurygin<sup>43</sup> studied the dissolution rates of Ti, Cr, Mo, W and FeNb, FeMo, FeW in molten pure iron. They used a disk of metal rotating in liquid iron. They found that the dissolution rates in pure iron increase in the order of Mo-W-Cr-Ti and among the ferro-alloys (FeNb, 60% Nb) - (FeMo, 62% Mo) - (FeW, 74% W). They did not provide any explanation and the precise mechanisms were neither considered nor identified. Based on their results, they calculated diffusion coefficients which were found to be in agreement with the recent work of Ershov et al.<sup>72</sup>

Bungardt et al.<sup>52</sup> studied the dissolution of molybdenum and tungsten in liquid steel under conditions of free and forced convection, respectively.

In the case of forced convection, they used rotation of their cylinders as well as flow of argon gas through the iron bath at a rate of 3.8 cm<sup>3</sup>/sec. They found that the dissolution rate of molybdenum was higher than that of tungsten at 1863 K (1590°C), and that the mass transfer coefficients were about the same. At temperatures below 1910 K (1637°C) the reaction of tungsten with liquid iron resulted in the intermetallic combination Fe<sub>7</sub>W<sub>6</sub> whose structure permitted no conclusion of any preferred diffusibility of the constituent elements.

Teziyan<sup>54</sup> studied the dissolution kinetics of ferroalloys in steel ladles. He labelled the alloys with radioisotopes, immersed them in liquid steel for specific times and measured the loss in weight of the alloy and the radioactivity of metal samples from the ladle.

The experiments were carried out in both quiescent and intensively stirred liquid steel baths. Data on the kinetics and mechanisms of dissolution of ferromanganese and silicomanganese were processed statistically. Regression equations were formulated for the time of dissolution as a function of lump size and metal temperature in relatively quiescent metal baths.

They obtained:

$$T_p = 100 + 27.75 x_1 - 17.25 x_2 + 2 x_1^2 + 2 x_2^2 - 5.25 x_1 x_2 \quad (2.2)$$

$$T_p = 63 + 2.5 x_1 - 12.5 x_2 + 2.7 x_1^2 + 1.4 x_2^2 - 2.5 x_1 x_2 \quad (2.3)$$

where:

$T_p$  : duration of solution (sec)

$x_1$  : parameter characterizing the diameter of the sample  $d$ (mm)  $x_1 = (d-50)/10$

$x_2$  : parameter characterizing the temperature of the metal  $t^{\circ}\text{C}$   $x_2 = (t-50)/15$ .

Equation (2.2) gives the solution time for ferromanganese while equation (2.3) gives the solution time for silico-manganese. Terziyan claimed that these equations were determined with a sufficient degree of accuracy for predicting solution times of ferro-alloy lumps, measuring from 40 to 180 mm in diameter at bath temperatures ranging between 1560 and 1650 $^{\circ}\text{C}$  (1833 to 1923 K).

Later, Gourtsoyannis et al.<sup>58</sup> developed a mathematical model predicting the melting history of aluminum spheres immersed suddenly into liquid steel. Their model predicted the formation of a solid shell of steel which rapidly froze around the aluminum sphere during the first seconds of immersion. The model also demonstrated how partial melting of the object can begin while still encased within the steel shell.

It was shown that the enclosed object would continue to melt at a rate which depended on

- (a) the rate of evolution of latent heat as the steel shell solidifies, and

(b) the rate of convective heat transfer from the bath to the outer surface of the steel shell.

Argyropoulos<sup>57</sup> conducted a series of experiments to study the melting characteristics of ferromanganese and silicomanganese cylinders in molten steel baths. In his work, a heat transfer model simulating the thermal events which occur when ferromanganese and silicomanganese cylinders are immersed in molten baths, was developed. The experimental results were found to be in substantial agreement with model predictions. The steel bath cooling rate and superheat were shown to be significant factors on solution kinetics of these alloys, while steel bath viscosity had no significant effect.

The modification of dissolution kinetics by the high exothermic heat of dissolution to molten steel was also studied by Argyropoulos and Guthrie<sup>3,4</sup>. In this work, the kinetics of dissolution of solid cylinders of 50 wt% ferrosilicon in liquid steel was studied. It was shown that the customary frozen shell of steel was formed around the ferrosilicon cylinder following its initial immersion. Premature internal melting of the cylinder then began as a result of liquid eutectic of Fe<sub>2</sub>Si composition forming at the inner steel shell/ferrosilicon boundary. This phenomenon was shown to trigger exothermic dissolution and erosion of the steel shell at the inner surface. The outer boundary of the steel shell melted back concurrently as a result of

convective heat transfer from the steel bath. The net result of exothermic dissolution phenomena is that considerably shortened shell dissolution times can be observed in comparison to more conventional ferro-alloy/steel systems.

Povolotskii et al.<sup>74</sup> investigated the diffusion of deoxidants such as Al, Si, Mn in molten iron using the capillary method. The diffusion coefficients,  $D_m$ , and energies of activation,  $E$ , for diffusion of the deoxidants in iron containing various amounts of carbon were determined.

They found that in the case of separate diffusion in a melt containing oxygen, the higher the deoxidizing capacity of the element, the greater was the activation energy of diffusion. Thus, with diffusion in an iron containing 0.003 - 0.010% oxygen, the energy of activation of aluminum, silicon and manganese is 145.7 kJ (34.7 kcal), 121.2 kJ (29 kcal), 101.2 kJ (24.1 kcal), per mole of the diffusing element.

Mucciardi<sup>59</sup> studied light alloy addition techniques in steelmaking. Aluminum wires of 6.4 to 15.9 mm in diameter were fed into steel melts while their 'apparent' weights were monitored. It was found that the maximum depth of penetration of an aluminum wire fed into molten steel can be expressed in the dimensional equation:

$$\text{Depth (m)} = \frac{145.5 \text{ Diameter (m)}^{0.86} \text{ Velocity (m/s)}^{0.52}}{\text{Superheat (K)}^{0.34}} \quad (2.47)$$

Argyropoulos studied the kinetics of dissolution of vanadium<sup>60</sup> and titanium<sup>61,62</sup> in liquid steel. For both cases,

two periods were distinguished: the steel shell period and the free dissolution period. During the steel shell period with pure vanadium and ferrovanadium alloys, no reaction was observed between the steel shell and vanadium. For low grade ferrovanadium alloys, the dissolution proceeds via a heat transfer mechanism. On the other hand, for high grades, ferrovanadium mass transfer mechanisms dominate. He proposed the following relation for the mass transfer coefficient  $K$  (cm/sec) with respect to the absolute temperature  $T$  (K), for the case of the dissolution of the pure vanadium in liquid steel:

$$\log K = - \frac{15707.7}{T} + 6.082 \quad (2.5)$$

The value of the activation energy, that he derived for the forementioned case, is 300.6 kJ/mol (71.5 kcal/mol).

In the case of titanium, it was shown that the customary frozen shell of steel encases the cylinder following its initial immersion. Premature internal dissolution then begins as a result of liquid eutectic of  $\text{Fe}_{0.3}\text{Ti}_{0.7}$  composition forming at the inner steel shell boundary. It was pointed out<sup>60,61</sup>, that this phenomenon triggered an exothermic dissolution and erosion of the inner surface of the steel shell. The net result was to shorten considerably shell melting times. In the second, or free dissolution period it was found that the surface temperature of the exposed titanium, cylinder rose above the bath temperature as a result of continued exothermic dissolution phenomena. This caused the dissolution process to become self-accelerating.

A simplified mathematical model of the process has been developed to describe the complex coupled heat and mass transfer phenomena involved<sup>60,62</sup>. He correlated his experimental results with an Arrhenius type of equation and he deduced the following relationship between the mass transfer coefficient  $K$ (cm/sec) and the absolute temperature  $T$ (K):

$$\log K = - \frac{15481.54}{T} + 7.2846 \quad (2.6)$$

According to those data, the apparent activation energy for the solution of titanium in liquid steel was found to be 296.3 kJ/mol (or 70.5 kcal/mol). He attributed this relatively large value of activation energy to two reasons. First, the average steel bath temperature during the free dissolution period did not represent the temperature of the dissolving interface which was higher. Second, the exothermic reaction altered the fluid flow patterns in the vicinity of the dissolving interface and made the effective boundary layer thinner, thereby increasing the sensitivity of experimental mass transfer coefficients to changes in temperature.

Argyropoulos also, in a more recent study<sup>63</sup>, measured in a 'dynamic way' the dissolution characteristics of ferroalloys used in the steel industry.

With the 'dynamic way' it is meant, that a microprocessor based system was used for data collection. The same method had been used for his work on titanium and vanadium<sup>60,61</sup>. The ferroalloy samples, he used, were the same as the ones utilized in the steel industry.

He worked with different grades of ferrosilicon, ferrovanadium and ferroniobium. He concluded, that for the aforementioned ferroalloys, silicon and the different grades of ferrosilicon exhibit the highest solution rates. For the ferrosilicon alloys, the dissolution rate increases as the silicon content increases. Finally, he pointed out, that the high purity grade ferroniobium dissolves faster in liquid steel than the standard purity grade one. He attributed this result to the lower exothermicity exhibited by the standard ferroniobium, due to the presence of the impurities of Si and Al (totally 6%).

Using the rotating disk method Han et al.<sup>67</sup>, performed dissolution studies in order to measure the diffusion coefficient of carbon in liquid steel. Ericsson et al.<sup>66</sup>, studied the influence of sulphur on the rate of carbon dissolution in liquid iron, by rotating graphite cylinders in Fe-C-S melts with different sulphur content. They found that sulphur decreases the rate of carbon dissolution in liquid iron and to a minor extent they attributed this behaviour to the decrease of carbon solubility when sulphur is added.

There is some work done on the rate of dissolution of solid iron in iron-carbon melts (Table 2.3). Recently, Mori et al.<sup>44</sup>, studied the rates of dissolution of stationary or rotating cylindrical iron specimens containing various amounts of oxygen into a molten carbon-saturated liquid iron alloy with evolution of CO. In the case of stationary dissolution,

the evolution of CO was found to have a marked effect on the dissolution rate. The highest dissolution rate which was observed at 1400°C (1673 K) for iron containing 0.96% oxygen was 590 times as large as the lowest rate observed at 1200°C (1473 K) for aluminum-killed iron. In the case of rotational dissolution of iron specimens containing oxygen, at lower number of revolutions per minute (rpm), the rate was controlled mainly by the extent of CO evolution, while at higher rpm, the effect of rotation became predominant.

Seaton et al.<sup>65</sup>, investigated the rate of dissolution of pre-reduced iron in molten steel. The dissolution of sponge iron pellets was accompanied by a continuous gas evolution which was due mainly to the reduction of iron oxides remaining in the pellets by the carbon within the system. They found that the rate of heat transfer from the bath to the pellet increased with increasing gas evolution and the melting process was simulated by a mathematical model by assuming heat transfer control.

Benda<sup>47</sup> investigated the dissolution of selected ferroalloys of vanadium, chromium, titanium and manganese. Ferroalloy test samples were chopped up fine (50-100 g) and dropped into the melt. After expiration of a fixed time period they were removed from the bath and their initial and final weights were compared. For the case of ferrochrome, cylindrical samples with a height to diameter ratio of  $h : d = 1$ , were used as well. By monitoring the change of the carbon content

of the metal bath, the influence of carbon content in ferrochrome on the dissolution kinetics, was studied. He noticed that a steel-shell is formed around the ferroalloy upon immersion which gradually melts back exposing the sample directly to the liquid metal. He pointed out that the melting point of the ferroalloys plays an important role in their dissolution; the higher the melting point of a ferroalloy the more time it takes to dissolve. Some of his important findings were that FeV (36% V) dissolved faster than FeV (82% V), FeTi (68% Ti) dissolved faster than FeTi (26% Ti and 35% Ti) and that FeCr with 6.2% C dissolved faster than FeCr with 0.11% C.

In another work, Shumikhin et al.<sup>46</sup> studied some thermodynamic and kinetic parameters of dissolution of graphite, silicon, chrome and molybdenum in iron at 1700°C and Fe-C-Si, Fe-C-Si-S, Fe-C-Si-P melts at 1600°C. They measured the heats of dissolution with the use of a high-temperature vacuum isothermal calorimeter. They pointed out that the dissolution of carbon, silicon, chrome and molybdenum can be affected on with diverse elements. The presence of silicon within the Fe-C melt, for example, resulted in increase of an endothermal effect of carbon dissolution; conversely, when the melt contained carbon then silicon dissolved with less heat liberation. Also, the presence of silicon and carbon in the melt decreases the endothermic heat effect of chrome dissolution. Moreover, they described that sulphur

and phosphorus lessen, essentially, the thermal effect of chrome and molybdenum dissolution in iron-based melts.

The knowledge and appreciation of the endothermic or exothermic phenomena which are involved in a dissolution process in liquid steel are of paramount importance. The understanding of two different aspects of exothermicity, the Microexothermicity and the Macroexothermicity<sup>5</sup>, has resulted in the production of a new family of ferroalloys, the micro-exothermic ferroalloys which have exhibited faster dissolution rates and better and more consistent recoveries than the conventional ones.

One typical example of such a ferroalloy is the micro-exothermic ferroniobium<sup>71</sup>, which is currently used in the steel industry.

### 2.3 PRESENT WORK

In the present study, the dissolution of niobium and zirconium cylinders has been examined in a 'dynamic way'. A microprocessor-based data acquisition and process control facility (DAPC) was employed in order to record the bath and cylinder temperatures, and to monitor the change of the apparent weight of the dissolving specimens. Two distinct periods were identified: the steel shell period and the free dissolution period. Experimental results and predictions based on a simplified mathematical model were obtained, which will be discussed in the next sections. The dissolution of

some ferroniobium and ferrozirconium alloys has been studied in a similar manner, and predictions for their dissolution times have been deduced. Finally, the effect of active oxygen in liquid steel on the solution rate and niobium recovery for lumps of standard ferroniobium has been investigated as well.

CHAPTER 33. PHYSICO-CHEMICAL AND THERMODYNAMIC DATA FOR Nb, Zr  
AND Fe-Nb, Fe-Zr ALLOYS3.1 DATA FOR NIOBIUM

Niobium (also called columbium) metal has the atomic number 41 in the periodic classification of the elements, and is in the same group with vanadium and tantalum. It has an atomic weight 92.9064<sup>75</sup> and its density at 20°C is 8600 kg/m<sup>3</sup> (8.6 g/cm<sup>3</sup>)<sup>75</sup>.

Niobium crystallizes in the body-centered cubic system and there is no transformation recorded till its melting point at 2740 K (2467°C)<sup>76</sup>. The latent heat of fusion for niobium is 26.4 kJ/mol (6302 cal/g-atom)<sup>76</sup> and its boiling point is 5013 K (4740°C)<sup>1</sup>.

3.2 DATA FOR ZIRCONIUM

Zirconium metal has the atomic number 40 in the periodic classification of the elements, and is in the same group with titanium and hafnium. It has an atomic weight 91.22<sup>75</sup> and its density at 20°C is 6490 kg/m<sup>3</sup> (6.49 g/cm<sup>3</sup>)<sup>75</sup>.

$\alpha$ -Zr has an hexagonal closed packed structure<sup>76</sup>; at high temperatures it transforms to  $\beta$ -Zr, which has a body centered cubic structure<sup>76</sup>. The transformation temperature is recorded to be at 1136 K (863°C) and the latent heat of transformation from the  $\alpha$  to the  $\beta$  phase, is 3.94 kJ/mol (941 cal/g-atom), as it is recommended by Hultgren et al.<sup>76</sup>.

The melting point of the pure zirconium is 2125 K (1852°C) and its latent heat of fusion is 16.9 kJ/mol (4038 cal/g-atom)<sup>76</sup>. Its boiling point is high, namely at 5023 K (4750°C)<sup>1</sup>.

### 3.3 THERMOPHYSICAL AND TRANSPORT PROPERTIES OF LIQUID IRON

#### 3.3.1 Phase Diagram

The Fe-C phase diagram shown in Fig. 3.1 is the one recorded in the Thermochemistry for steelmaking, Vol. II, by Elliott et al.<sup>78</sup>. The melting point of pure iron is reported to be 1809 K (1536°C). Iron liquidus values at different temperatures ranging between 1809 K (1536°C) and 1773 K (1500°C) tabulated by Elliott et al.<sup>78</sup> were used to obtain the following expression for the melting point of the liquid steel:

$$T_{mp} \text{ (K)} = 1809.1 - 29.55 W_c - 85.7 W_c^2 \quad (3.1)$$

where  $W_c$  = the carbon weight percent.

#### 3.3.1 Density

The density of pure iron at various temperatures is reported in many sources including: Thermochemistry for steelmaking, Vol. II, by Elliott et al.<sup>78</sup>, Lucas<sup>79</sup>, Lange<sup>80</sup> and in the Metals Reference Handbook by Smithells<sup>75</sup>.

Smithells gives the density of the liquid iron at  $T_0 = 1809 \text{ K (1536°C)}$  as  $D_0 = 7015 \text{ kg m}^{-3}$  (7.015 gr cm<sup>-3</sup>).

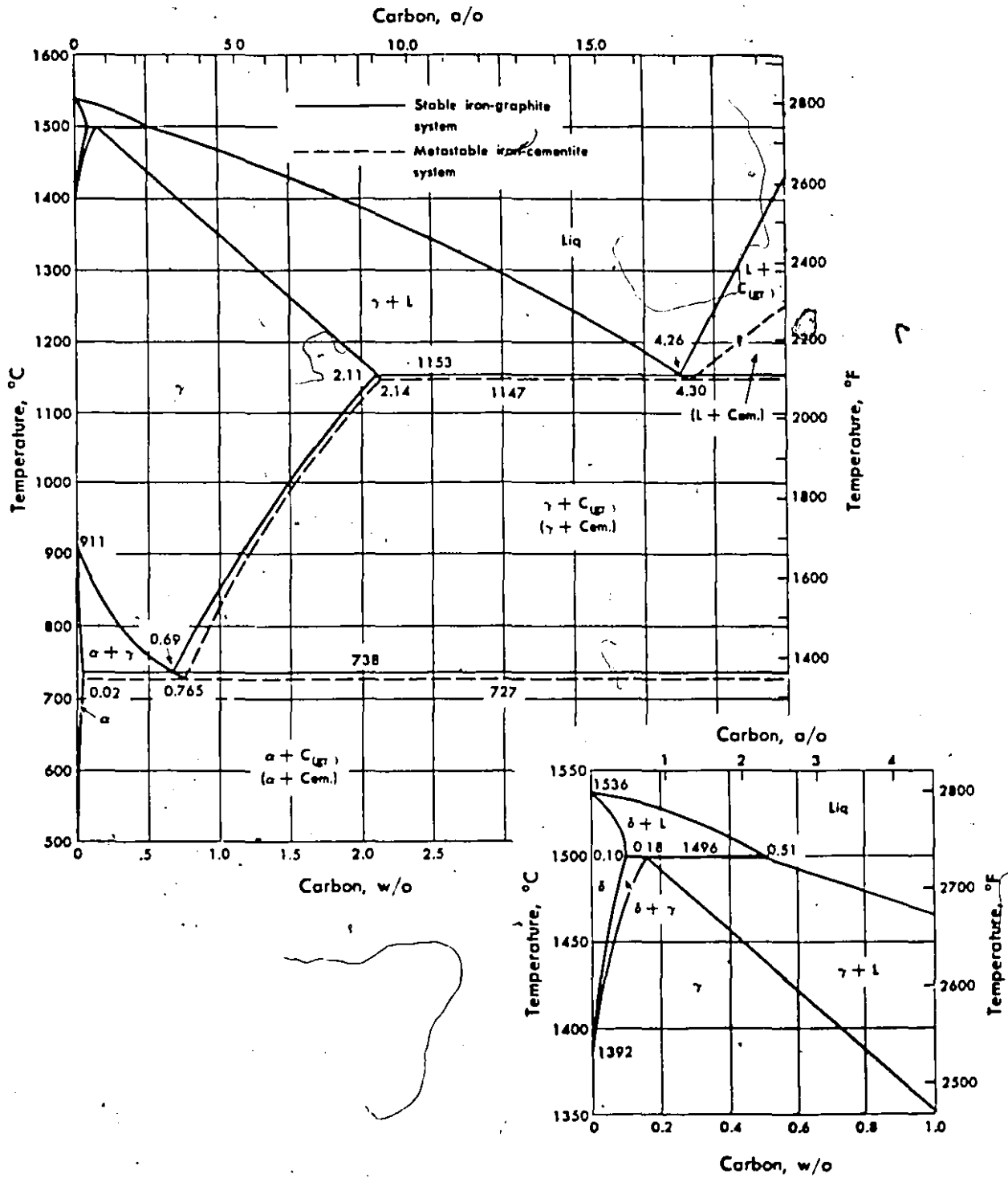


Figure 3.1 The iron-carbon phase diagram

At higher temperatures, the density of the liquid iron is given by the following equation<sup>75</sup>:

$$D = D_0 + (T - T_0) (dD/dT) \quad (3.2)$$

where  $D_0$  is the density of the liquid iron at the melting point  $T_0$  and  $dD/dt = -0.883 \text{ kg/m}^3\text{K}$ . These values have been adopted in the present work.

### 3.3.3 Viscosity

Turkdogan<sup>81</sup> has presented data for the viscosity of the liquid iron at its melting point. The value quoted is 4.95 mPa·sec (4.95 cP) with  $E$  equal to 41.58 kJ.

The variation in viscosity with temperature for liquid iron is given by Smithells<sup>75</sup>.

$$n = n_0 \exp \left( \frac{E}{RT} \right) \quad (3.3)$$

where  $n_0$  : 0.3699 mPa·sec

$E$  : 41.4 kJ/mol

$R$  : gas constant 8.3144 J/mol K

### 3.3.4 Thermal Conductivity

The variation of the thermal conductivity of the iron with temperature is given by Turkdogan<sup>81</sup>. At the melting point of pure iron, it is quoted as  $30 \text{ W m}^{-1} \text{ K}^{-1}$

( $0.071 \text{ cal cm}^{-1} \text{ sec}^{-1} \text{ } ^\circ\text{C}^{-1}$ ), at 1873 K ( $1600^\circ\text{C}$ )  $35 \text{ W m}^{-1} \text{ K}^{-1}$  ( $0.083 \text{ cal cm}^{-1} \text{ sec}^{-1} \text{ } ^\circ\text{C}^{-1}$ ).

### 3.3.5 Specific Heat and Latent Heat of Fusion

Data for the specific heat of iron have been summarized by Elliot et al.<sup>78</sup>. Lange<sup>80</sup> also reviewed experimental data for the specific heat of pure iron. The tabulated values of specific heat were used to obtain an average over a range of temperature. Smithells<sup>75</sup>, suggests the value 795 J/kg K for the specific heat of the liquid iron at its melting point.

The latent heat of fusion was chosen to be 15 kJ/g-atom<sup>75</sup>, a value reported to range between 13.4 and 15.5 kJ/g-atom.

### 3.3.6 Diffusivity

Ershov et al.<sup>72</sup>, studied the diffusion of various alloying elements in liquid iron over the temperature range 1823 K to 1973 K (1550 to 1700°C).

They used electron microprobe analysis for the determination of the concentration profiles. An exponential form  $D_m = D_0 \exp(-Q/RT)$  was deployed to determine the temperature dependence of the diffusivity.

For the diffusion coefficient of Nb in liquid iron the following values were derived:

$$\begin{aligned} D_0 &= 25.5 \cdot 10^{-8} \text{ m}^2/\text{sec} \\ Q &= 63.6 \text{ kJ/mol} \end{aligned} \quad (3.4)$$

Hence, the diffusion coefficient of Nb in liquid steel at 1873 K (1600°C) was calculated to be  $4.3 \cdot 10^{-9} \text{ m}^2/\text{sec}$ .

For the diffusion coefficient of Zr in liquid iron the following values were derived:

$$D_0 = 22.5 \cdot 10^{-8} \text{ m}^2/\text{sec}$$

$$Q = 51.9 \text{ kJ/mol} \quad (3.5)$$

Therefore, the diffusion coefficient of Zr in liquid steel at 1873 K (1600°C) was calculated to be  $8.0 \cdot 10^{-9} \text{ m}^2/\text{sec}$ .

### 3.4 A THERMODYNAMIC ASSESSMENT OF THE IRON-NIOBIUM SYSTEM

#### 3.4.1 Phases and Structures

The phase diagram shown in Figure 3.2 represents the results of several investigators and it was taken from the reference No. 86. The melting point of Nb, 2,477°C (2750 K), is a secondary reference point (IPTS-68).

The Fe-Nb system displays four intermetallic phases,  $\text{Fe}_2\text{Nb}$ ,  $\text{Fe}_{21}\text{Nb}_{19}$  or  $\text{Fe}_7\text{Nb}_6$ ,  $\text{Fe}_2\text{Nb}_3$  and  $\text{Fe}_x\text{Nb}_y$  (ca. 11 at.% Fe) and three eutectic reactions. The mutual solid solubility of the two metals is relatively small. The  $\text{Fe}_2\text{Nb}$  phase is a Laves phase (MgZn<sub>2</sub> type), is Pauli-paramagnetic and melts congruently. Values for the melting point vary from 1630°C (1903 K) to 1655°C (1928 K).

The  $\text{Fe}_{21}\text{Nb}_{19}$  phase was claimed to have the tetragonal  $D8_b$  structure isotypic with CrFe. It is stable above 600°C (873 K) although this superstructure could not be verified by some investigators<sup>86</sup>. It is believed that it is not a  $\sigma$ -phase but of the  $W_6\text{Fe}_7$  type denoted as  $\mu$ -phase. It may be pointed out that the structures of  $\sigma$  and  $\mu$  are closely related. The notation should thus be  $\text{Fe}_7\text{Nb}_6$  rather than  $\text{Fe}_{21}\text{Nb}_{19}$ .

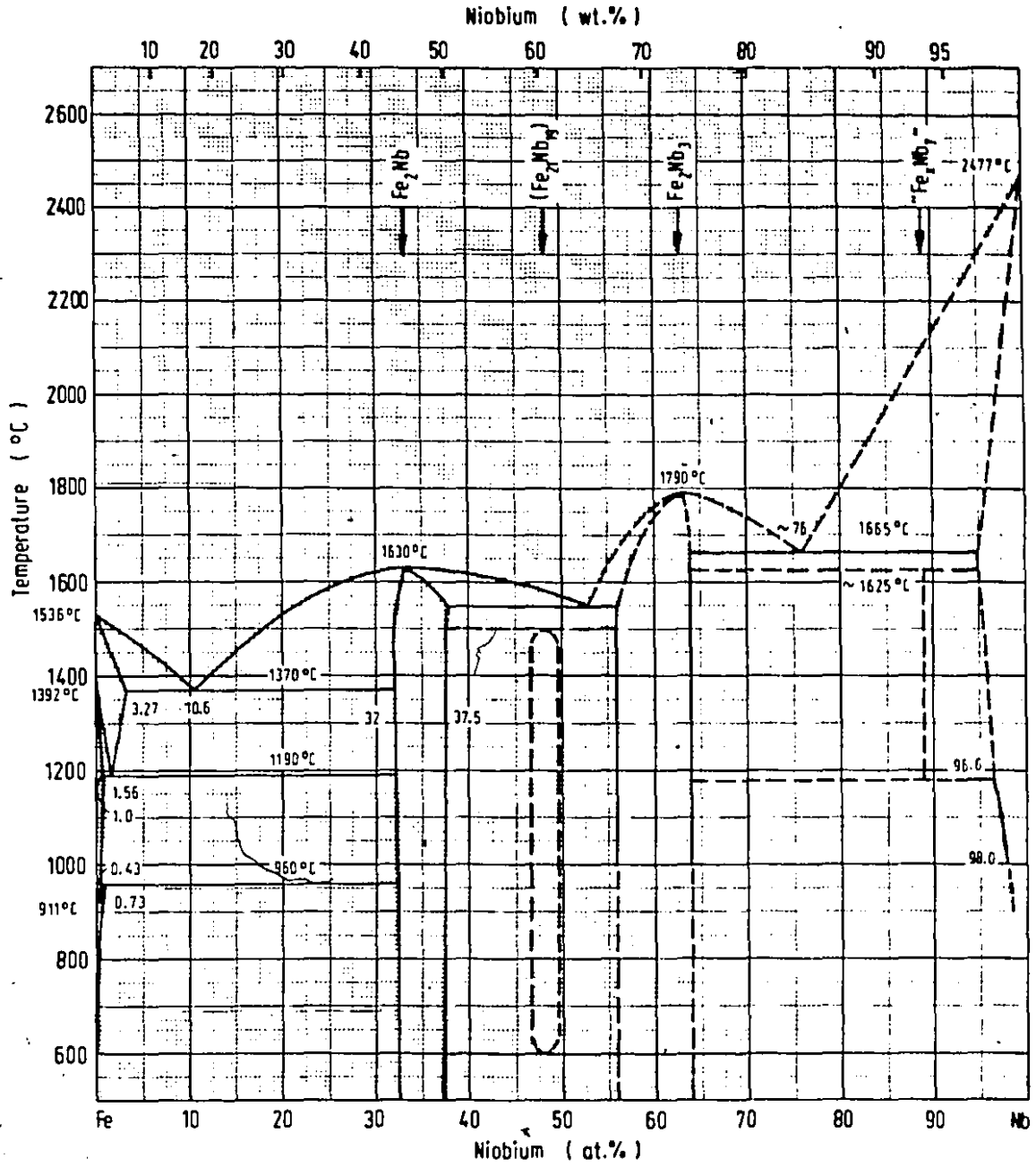


Figure 3.2 The iron-niobium phase diagram

The  $\text{Fe}_2\text{Nb}_3$  phase was found to possess the  $\text{Ti}_2\text{Ni}$ -type structure<sup>86</sup> and it melts congruently between  $1790^\circ\text{C}$  (2063 K) and  $1800^\circ\text{C}$  (2073 K). Some investigators<sup>86</sup> could not establish evidence for its existence.

The proposed phase diagram includes a Nb-rich phase at about 89 at.% Nb existing possibly between  $1180^\circ\text{C}$  (1453 K) and  $1625^\circ\text{C}$  (1898 K). The structure has not been determined and the compound has not been verified up till now.

#### 3.4.2 Solid (Fe-Nb) Alloys

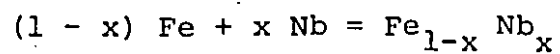
Experimental determination of the integral heat of formation for the intermetallic  $\text{Fe}_2\text{Nb}$  compound has been carried out by Barbi<sup>87</sup> and Rezukhina et al.<sup>88</sup>. Both researchers used galvanic cells to succeed in their investigations. Their results are presented in Table 3.1 together with predicted values for the heat of formation of various Fe-Nb intermetallics, (which are ordered compounds and may or may not exist), given by Miedema<sup>89</sup>.

#### 3.4.3 Liquid (Fe-Nb) Alloys

Iguchi et al.<sup>90</sup> have measured the heats of mixing of the Fe-Cr, Fe-Mo, Fe-W, Fe-V, Fe-Nb and Fe-Ta liquid alloys, with the use of a calorimeter. For the case of the Fe-Nb system they noted that the mixing was exothermic. They measured the heats of mixing for up to 25 at.% Nb. Their results have been correlated by the present author with the

Table 3.1

Integral Heats of Formation of Solid Fe-Nb Alloys



$x_{\text{Nb}}$	T(K)	$\Delta H$ , kJ/mol atoms	Reference
0.166	298	-11	89
0.250	298	-17	89
0.333	298	-21	89
0.333	1200	-23.7	87
0.333	298	-20.5	88
0.500	298	-23	89
0.667	298	-18	89
0.750	298	-14	89
0.833	298	-9	89

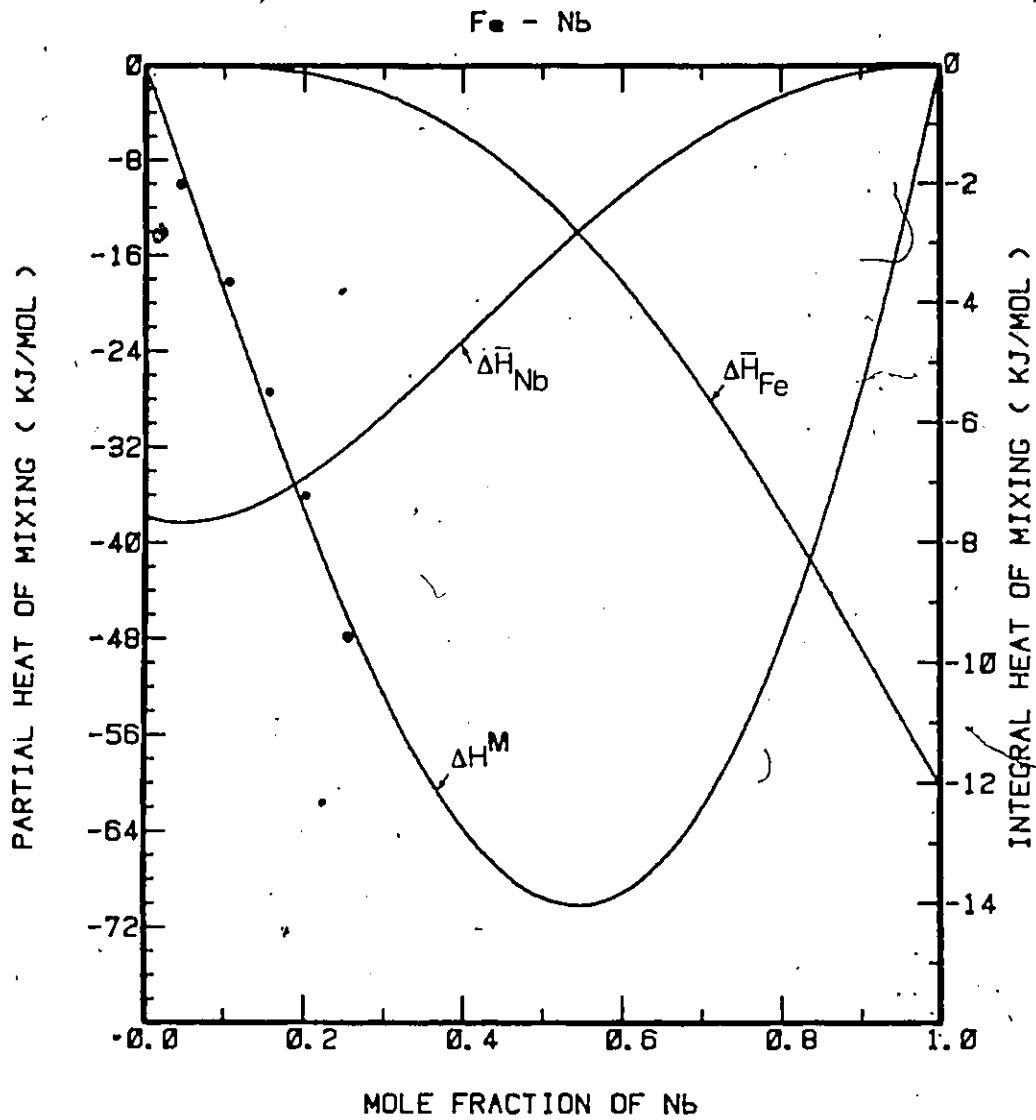


Figure 3.3 Partial and Integral Heats of mixing of the liquid iron-niobium alloys

use of the F\*A\*C\*T system<sup>91</sup>. For this purpose it was assumed that the iron-niobium system forms sub-regular solutions in the liquid state.

The following equations were derived in kJ/mol atoms:

Integral heat of mixing:

$$\Delta H^M = X_{Fe} X_{Nb} (-37.756 - 48.869 X_{Nb} + 26.351 X_{Nb}^2) \quad (3.6)$$

Partial heat of mixing:

$$\Delta \bar{H}_{Nb} = X_{Fe}^2 (-37.756 - 97.738 X_{Nb} + 79.053 X_{Nb}^2) \quad (3.7)$$

The partial molar heat of mixing of Nb at infinite dilution in liquid iron is:

$$\Delta \bar{H}_{Nb}^0 = -37.756 \quad (\text{kJ/mol atoms}) \quad (3.8)$$

At 1873 K (1600°C), the activity coefficient of Nb at infinite dilution in liquid iron was estimated to be:

$$\gamma_{Nb}^0 = 0.09 \quad (3.9)$$

In Figure 3.3, the  $\Delta H^M$ ,  $\Delta \bar{H}_{Nb}$  and  $\Delta \bar{H}_{Fe}$  curves are presented as a function of the atomic fraction of Nb, at 1873 K.

### 3.5 A THERMODYNAMIC ASSESSMENT OF THE IRON-ZIRCONIUM SYSTEM

#### 3.5.1 Phases and Structures

Numerous investigators have published data on the Fe-Zr system. Still, the phase relationships in the Zr-rich region require more experimental work. The Fe-Zr phase diagram shown in Figure 3.4 has been taken from Reference 86.

The Fe-Zr system displays four, probably five intermediate phases, namely<sup>86</sup>:  $Fe_3Zr$ , fcc, isotypic with  $Mn_{23}Th_6$ ;  $Fe_2Zr$ ,

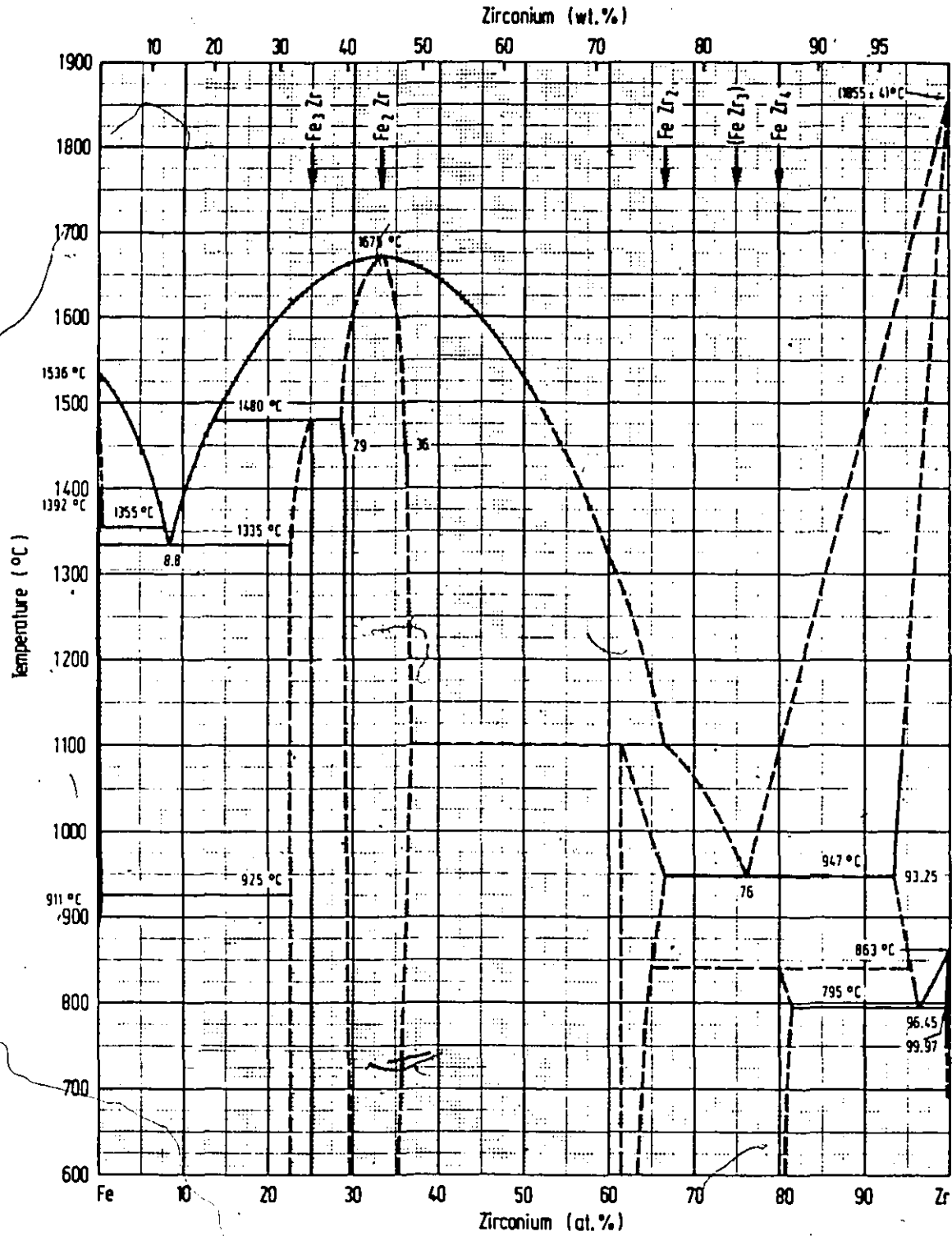


Figure 3.4 The iron-zirconium phase diagram

fcc  $\text{MgCu}_2$ -type Laves phase;  $\text{FeZr}_2$ , bc tetragonal  $\text{Al}_2\text{Cu}$ -type;  $\text{FeZr}_3$ ; orthorhombic crystal system<sup>92</sup> isomorphous<sup>93</sup> with  $\text{Re}_3\text{B}$ ;  $\text{FeZr}_4$ , whose structure has not been determined yet<sup>86</sup>. In a recent study<sup>93</sup> only the phases  $\text{Fe}_2\text{Zr}$ ,  $\text{FeZr}_2$  and  $\text{FeZr}_3$  could only be identified. They assumed that contamination by oxygen can give rise to the formation of a compound which has the same diffraction peaks with the  $\text{FeZr}_4$  phase. The most stable compounds were found to be  $\text{Fe}_2\text{Zr}$  and  $\text{FeZr}_3$ . They considered that the  $\text{FeZr}_2$  is a high temperature phase. The melting point of Zr,  $1855^\circ\text{C}$  (2128 K), is a secondary reference point (IPTS-68 revised 1975). The phase  $\text{Fe}_3\text{Zr}$  is formed peritectically<sup>86</sup> at  $1480^\circ\text{C}$  (1753 K), shows a range of homogeneity of about 3 at.% Zr and is ferromagnetic below  $275^\circ\text{C}$  (548 K). The phase  $\text{Fe}_2\text{Zr}$  exhibits an appreciable range of homogeneity extending from 29-36 at.% Zr at  $1450^\circ\text{C}$  (1723 K). Information relating to the melting temperature<sup>86</sup> varies somewhat from  $1645^\circ\text{C}$  (1918 K) to  $1675^\circ\text{C}$  (1948 K). This phase is ferromagnetic<sup>86</sup> with a Curie temperature decreasing from  $475 - 310^\circ\text{C}$  (748 - 583 K) with increasing Zr content (29 - 36 at.% Zr). Presence of small amounts of oxygen apparently converts the bc tetragonal structure of  $\text{FeZr}_2$  to the complex fcc structure<sup>86</sup>, isotypic with  $\text{NiTi}_2$ . In the Zr-rich region the liquidus has not been determined yet<sup>86</sup>. In a recent study<sup>94</sup> the crystallization of melt-spun Fe-Zr metallic glasses was investigated. They found that unlike Cu-Zr and Ni-Zr, the immediate crystallization products

could not be understood in terms of the equilibrium crystalline phase diagram. They described that all crystallization products were metastable or unstable phases. They found that in the composition range  $\text{Fe}_{25}\text{Zr}_{75}$  to  $\text{Fe}_{33}\text{Zr}_{67}$ , something like 'explosive crystallization' occurred. They pointed out that the present phase diagram should be modified to include a eutectic at 37.5 at.% Fe (62.5 at.% Zr, Zr-rich region). They claimed that this would produce a maximum in the phase diagram at  $\text{FeZr}_2$ , fact which would establish this phase as a more stable one, than it is presently considered.

### 3.5.2 Solid (Fe-Zr) Alloys

Schneider et al.<sup>95</sup> determined activities of the components of the  $\text{Fe}_2\text{Zr}$  phase from solubilities in liquid Mg, at 1023 K. The solubility of the component of the alloy, divided by the solubility of the pure component equals the activity, since the solubilities are so small that the assumption of Henry's law is valid. From these activities and their temperature coefficients, the integral quantities can be calculated. However, no details and none of the original data are given in the paper<sup>77,95</sup>.

Recently, Gachon et al.<sup>96</sup> measured the enthalpy of the formation of the  $\text{Fe}_2\text{Zr}$  phase by direct reaction calorimetry at high temperatures. They performed some checks to ensure that the stoichiometry and the structure of the phase was obtained. The above mentioned experimental results are given

in Table 3.2 together with predicted values for the heats of formation of various Fe-Zr intermetallics, (which are ordered compounds and may or may not exist), given by Miedema<sup>89</sup>.

### 3.5.3 Liquid (Fe-Zr) Alloys

After extensive literature survey the author found out only one published work on the heat of mixing of liquid Fe-Zr alloys. Stomakhin et al.<sup>97,99</sup> used a vacuum resistance furnace to investigate the enthalpies of formation of dilute solutions based on iron, cobalt and nickel. In their paper they gave only one value however, the partial molar heat of mixing of Zr at infinite dilution in liquid steel:

-80.3 kJ/mol atoms. They worked in the region of very dilute solutions (max 0.1 at.% Zr) but they didn't describe any experimental conditions or methodology they followed to deduce this value. In a private communication, Iguchi<sup>98</sup> informed the author that he had tried to measure the heats of mixing of liquid Fe-Zr alloys, but he failed as he could not prevent oxidation of the phases before mixing.

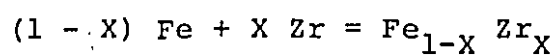
Adopting Hardy's model<sup>100</sup> on sub-regular solutions and using the Facility for the Analysis of Chemical Thermodynamics (F\*A\*C\*T System)<sup>91</sup> the following equation was derived for the integral heat of mixing of liquid Fe-Zr alloys (in kJ/mol atoms):

$$\Delta H^M = X_{Fe} X_{Zr} (-82.634 - 14.644 X_{Zr}) \quad (3.10)$$

This formula was found to be good enough to reproduce the

Table 3.2

Integral Heats of Formation of Solid Fe-Zr Alloys



$X_{\text{Zr}}$	T(K)	$\Delta H$ , kJ/mol atoms	Reference
0.166	298	-19	89
0.250	298	-28	89
0.333	298	-34	89
0.333	1023	-24.7 ( $\pm 3.5$ )	95
0.333	1760	-29.7 ( $\pm 1.7$ )	96
0.500	298	-37	89
0.667	298	-27	89
0.750	298	-20	89
0.833	298	-13	89

Fe-Zr phase diagram with the aid of the F\*A\*C\*T System. For the partial molar heats of mixing the following equations were deduced (in kJ/mol atoms):

$$\Delta\bar{H}_{\text{Fe}} = X_{\text{Zr}}^2 (-97.278 - 29.288 X_{\text{Fe}}) \quad (3.11)$$

$$\Delta\bar{H}_{\text{Zr}} = X_{\text{Fe}}^2 (-82.634 - 29.288 X_{\text{Zr}}) \quad (3.12)$$

So, the partial molar heat of mixing of Zr at infinite dilution in liquid iron was found to be -82.634 kJ/mol atoms, a value very close to the one given by Stomakhin et al.<sup>97,99</sup>

It would be interesting to estimate the activity coefficient of Zr at infinite dilution in liquid iron,  $\gamma_{\text{Zr}}^0$ , at 1873 K. Lupis and Elliott proposed a model<sup>101</sup> to describe the quasi-regular solutions with the following relationship:

$$\bar{G}_i^E = \Delta\bar{H}_i \left(1 - \frac{T}{\tau}\right) \quad (3.13)$$

and

$$\Delta\bar{H}_i = \tau \bar{S}_i^E \quad (3.14)$$

where  $\bar{G}_i^E$ ,  $\bar{S}_i^E$  are the excess partial molar free enthalpy and the excess partial molar entropy respectively, of the solute element  $i$ ;  $\Delta\bar{H}_i$  is the partial molar heat of mixing of the element  $i$ ;  $T$  is the absolute temperature in Kelvin;  $\tau$  is a parameter formally representing the temperature at which the solution can be considered ideal ( $\bar{G}_i^E = 0$ ).

Lupis and Elliott<sup>101</sup> showed that the correlation between  $\bar{S}_i^E$  and  $\Delta\bar{H}_i$  for 90 liquid and solid solutions based on a series of solvents (Au, Cd, Zn, Ag, Bi, Cu, Hg, etc.) at temperatures from 293 K to 1426 K is satisfied when

$$\tau = 3000 (\pm 1000) \text{ K} \quad (3.15)$$

Ostrovskiy et al.<sup>99</sup>, performed calculations using this model for systems based on iron and nickel. They used available experimental data. They proposed that Hardy's model on sub-regular solutions gives more accurate results, as far as the modelling of the integral heat of mixing ( $\Delta H^M$ ) was concerned. They pointed out that the value 7150 K for the parameter  $\tau$  resulted in an excellent fit of data based on the iron and nickel systems:

$$\bar{G}_i^E = \Delta \bar{H}_i \left( 1 - \frac{T}{7150} \right) \quad (3.16)$$

Applying this formula for the system Fe-Zr one has:

$$\bar{G}_{Zr}^E = X_{Fe}^2 (-82.634 - 29.288 X_{Zr}) \left( 1 - \frac{T}{7150} \right) \quad (3.17)$$

and at infinite dilution ( $\lim X_{Zr} = 0$  and  $\lim X_{Fe} = 1$ ):

$$\bar{G}_{Zr}^{0E} = -82.634 \left( 1 - \frac{T}{7150} \right) \quad (3.18)$$

But, as the equation (3.19) is generally true<sup>102</sup>

$$\bar{G}_{Zr}^{0E} = R T \ln \gamma_{Zr}^0 \quad (3.19)$$

The following functional relationship between  $\gamma_{Zr}^0$  and T is derived:

$$\log \gamma_{Zr}^0 = 0.604 - \frac{4317}{T} \quad (3.20)$$

So, the following values of  $\gamma_{Zr}^0$  are obtained at three different temperatures:

(°C)	T(K)	$\gamma_{Zr}^0$
1550	1823	0.017
1600	1873	0.020
1650	1923	0.023

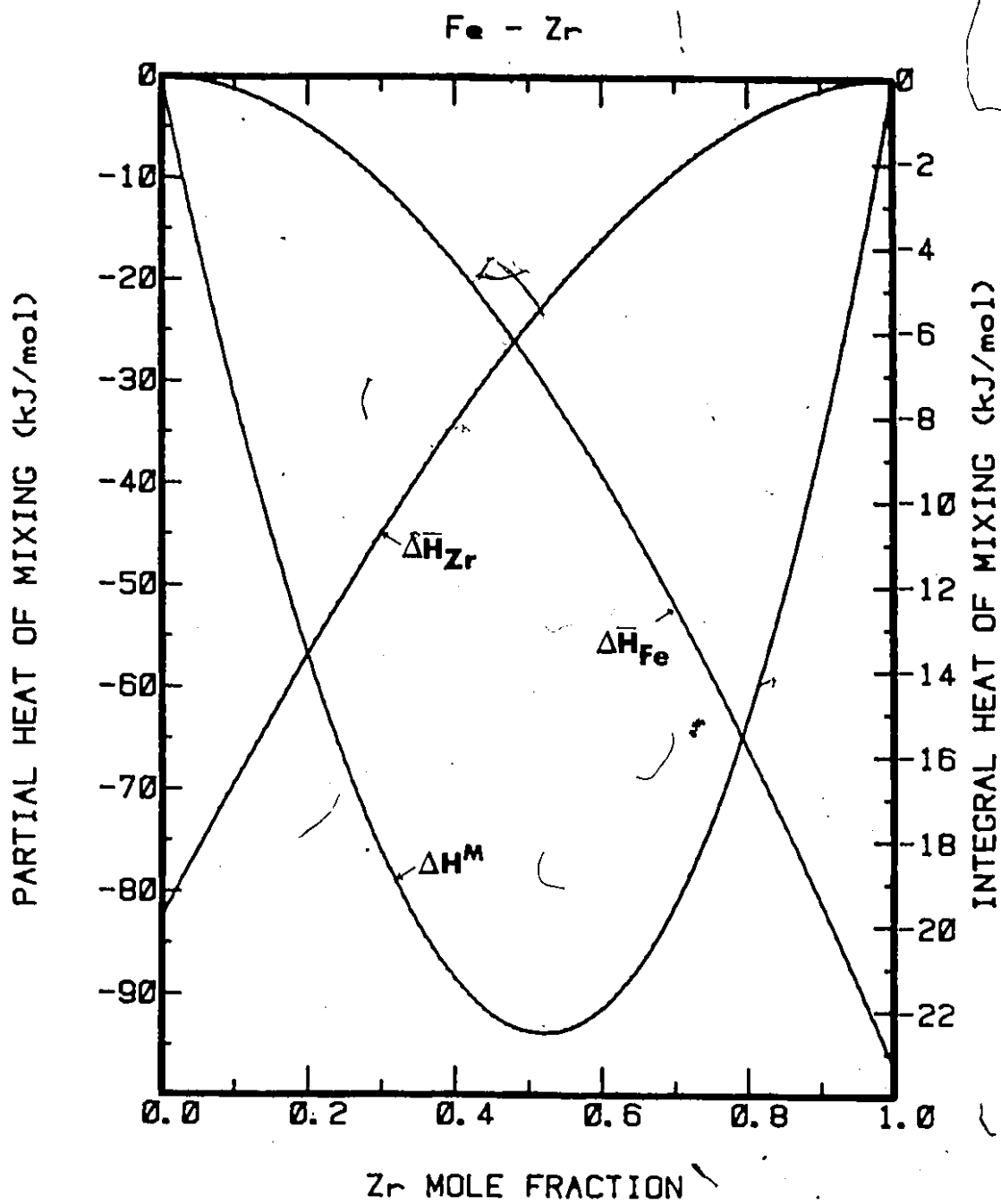


Figure 3.5 Partial and Integral Heats of mixing of the liquid iron-zirconium alloys

It is worth noticing that the  $\gamma_{Zr}^0$  increases as the temperature increases, which is well expected for exothermic mixing. For the calculations above, pure molten zirconium has been selected as its standard state. Figure 3.5 shows the heats of mixing of liquid Fe-Zr alloys in graphical form. In order to test the validity of these results (i.e., the presented relationships for the heat of mixing of liquid Fe-Zr alloys), the Fe-Zr phase diagram was predicted based upon them and the F\*A\*C\*T System. Figure 3.6 presents the predicted Fe-Zr phase diagram. The computations were performed for the liquid (i.e., the determination of the liquidus curve), and the intermetallics  $Fe_2Zr$  and  $FeZr_2$ , which were considered as stoichiometric compounds. As there is no available data concerning the free enthalpies of the various solid phases, no calculations were performed for these phases and, because of this, there are no solid solutions present in the predicted phase diagram. Nevertheless, there is generally a very good agreement between the experimental (Figure 3.4) and predicted (Figure 3.6) liquidus curves.



## CHAPTER 4

### 4. EXPERIMENTAL PROCEDURE

#### 4.1 INTRODUCTION

In this chapter materials and experimental procedures used, are presented in detail. For most of the experimental work, the data collection has been carried out using the Data Acquisition and Process Control Facility (DAPC), while part of it (i.e., Section 7.4) has been succeeded with the help of the Intelligent Measurement Facility (INMEFA). Some description of the DAPC is given below but for more details about the INMEFA, the reader is referred to reference No. 83.

#### 4.2 CYLINDER IMMERSION EXPERIMENTS

The cylinder immersion tests were carried out using a BRADLEY meltmaster furnace, which is capable of containing and melting the steel. It was a 400 Volts, 100 kW, 130 kVA, 3 kHz unit. The inductotherm coils had 9 turns in a length of 35.6 cm, with an internal coil diameter of 33.0 cm. The alumina crucible, (90%  $Al_2O_3$ , 10%  $SiO_2$  supplied by Engineered Ceramics), had an internal diameter of 19.7 cm and a height of 35.6 cm. The molten charge normally filled the crucible to within 2.5 cm from the top. All of the heats were made by induction remelting an initial charge of ARMCO iron in an alumina crucible. Figure 4.1 shows the induction furnace with its controls.

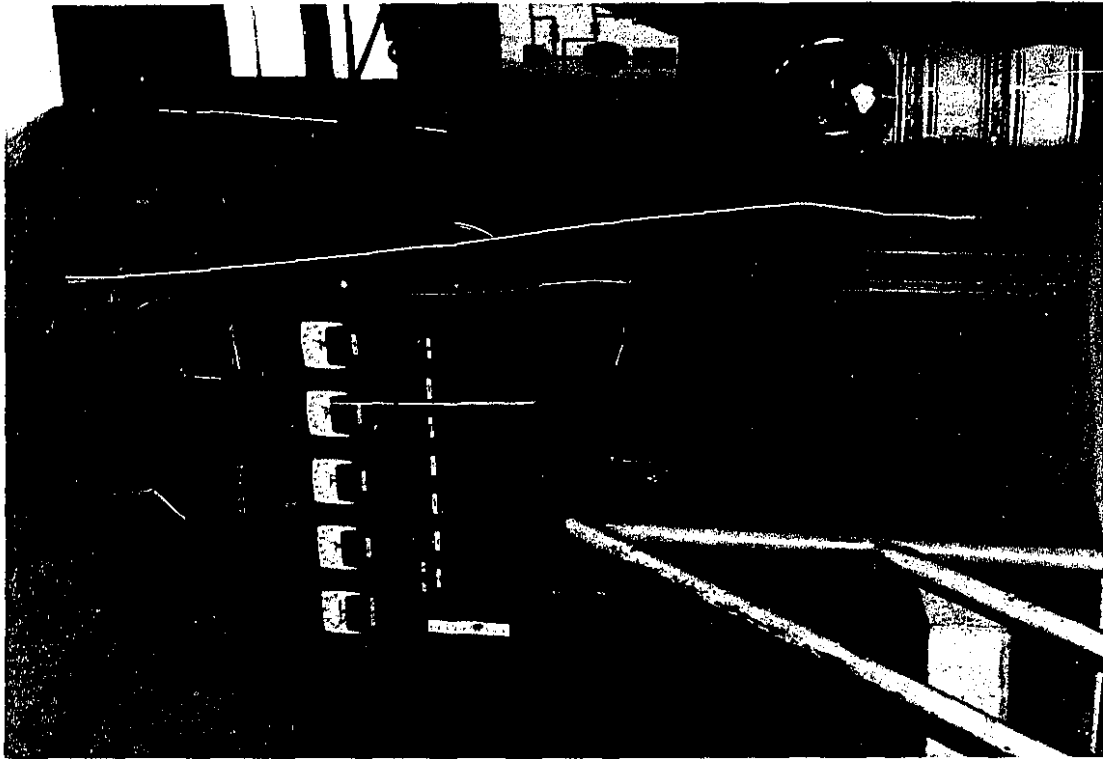


THE QUALITY OF THIS MICROFICHE IS HEAVILY DEPENDENT UPON THE QUALITY OF THE THESIS SUBMITTED FOR MICROFILMING.

UNFORTUNATELY THE COLOURED ILLUSTRATIONS OF THIS THESIS CAN ONLY YIELD DIFFERENT TONES OF GREY.

LA QUALITE DE CETTE MICROFICHE DEPEND GRANDEMENT DE LA QUALITE DE LA THESE SOUMISE AU MICROFILMAGE.

MALHEUREUSEMENT, LES DIFFERENTES ILLUSTRATIONS EN COULEURS DE CETTE THESE NE PEUVENT DONNER QUE DES TEINTES DE GRIS.



The induction furnace with its controls.

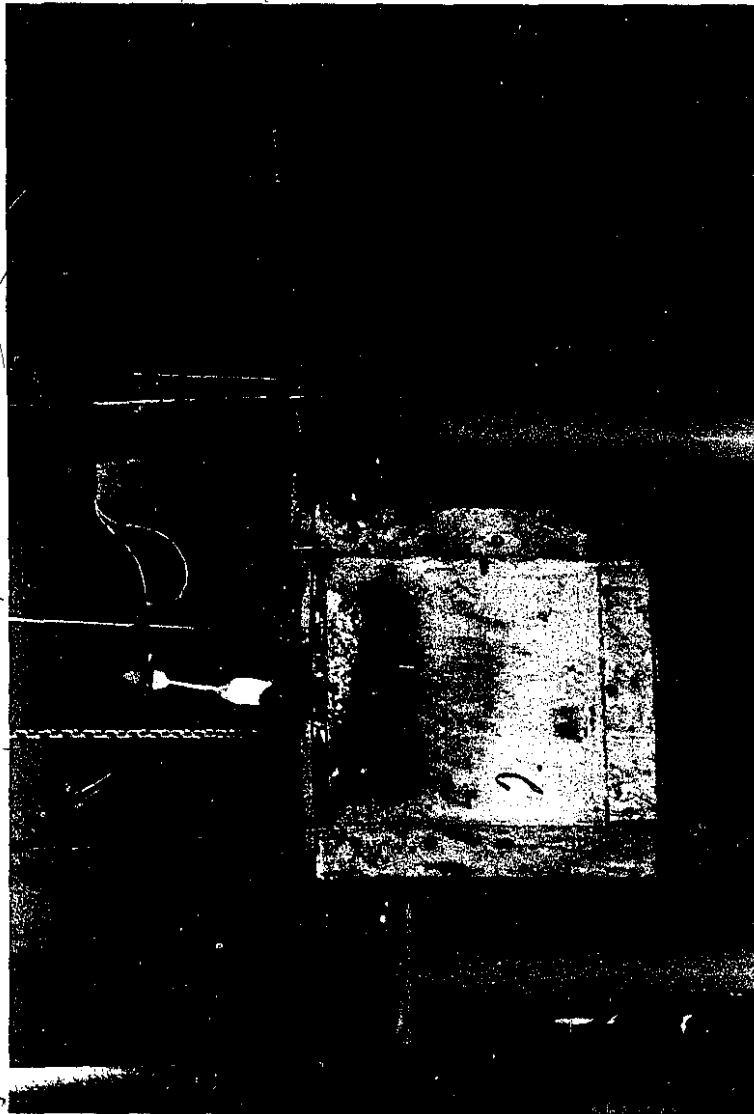


Figure 4.1

#### 4.2.1 Materials

The niobium cylinders used, were purchased from KBI, a division of CABOT Corporation, Reading, Pennsylvania, U.S.A.. The zirconium cylinders used, were purchased from TELEDYNE, WAH CHANG ALBANY, Albany, Oregon, U.S.A..

In Table 4.1, the chemical composition of the niobium and zirconium cylinders used, is presented. The maximum concentration of the impurities is given in ppm, and all other metallic residuals that may exist, are expected to be 40 ppm maximum each.

The properties of the niobium and zirconium cylinders, estimated from similar properties of the pure metals, along with their sources, are presented in Table 4.2. High purity iron melts were made by melting ARMCO iron having a nominal composition of 0.02% - 0.03% carbon, 0.05% manganese, 0.007% phosphorus, 0.01% - 0.018% sulphur, 0.001% silicon and iron the balance.

For both the niobium and zirconium cylinders, the necessary thermocouple inserts were made by drilling out 0.31 cm diameter holes. The tips of these holes in the cylindrical body were located at a distance about 10 cm from the top. In order to reduce the bottom effects to the cylinder, a steel cap was placed very firmly on the bottom of the cylinders. This cap was thicker at the corners where the melting is generally faster.

Table 4.1

Chemical Analysis in ppm

Element	Cylinder	
	Niobium	Zirconium
Oxygen	250	820
Nitrogen	100	40
Carbon	100	110
Hydrogen	10	20
Silicon	50	50
Tantalum	2000	--
Hafnium	100	100
Tungsten	500	50
Chromium	40	100
Titanium	100	31
Aluminum	40	53
Iron	100	690
Copper	40	52
Nickel	50	35
Molybdenum	50	25
Niobium	balance	--
Zirconium	100	balance

Table 4.2

Thermal and Physical Properties of  
Niobium, Zirconium and Armco Iron

Property		Niobium	Zirconium	Armco Iron
S O L I D	Density (kg/m <sup>3</sup> )	8600 <sup>75</sup> (298 K)	6490 <sup>75</sup> (298 K)	7506 <sup>84</sup> (1500 K)
	Heat Capacity (J/kg K)	268 <sup>75</sup> (298 K)	289 <sup>75</sup> (298 K)	698 <sup>84</sup> (1500 K)
	Thermal Conductivity (W/m K)	54.1 <sup>75</sup> (298 K)	22.6 <sup>75</sup> (298 K)	32.1 <sup>84</sup> (1500 K)
Melting Point (K)		2740 <sup>76</sup>	2125 <sup>76</sup>	1793 (est)
Phase Transformation (K)		--	1136 <sup>76</sup>	--
Latent Heat of Transformation (J/kg)		--	2465.5 <sup>76</sup>	--
L I Q U I D	Density (kg/m <sup>3</sup> )	7830 <sup>75</sup> (2740 K)	5800 <sup>75</sup> (2125 K)	6960 <sup>84</sup> (1870 K)
	Heat Capacity (J/kg K)	--	--	822 <sup>84</sup> (1870 K)
	Thermal Conductivity (W/m K)	--	--	41.2 <sup>84</sup> (1870 K)
	Viscosity (Pa·sec)	--	8.0 10 <sup>-3</sup> <sup>75</sup> (2125 K)	5.1 10 <sup>-3</sup> <sup>84</sup> (1870 K)
	Volumetric Coefficient of Expansion (K <sup>-1</sup> )	--	--	1.4 10 <sup>-4</sup> <sup>84</sup> (1870 K)
	Prandtl Number	--	--	0.12
Latent Heat of Fusion (kJ/kg)		283.8 <sup>76</sup>	185.2 <sup>76</sup>	268.5 <sup>82</sup>

#### 4.2.2 Adjusting the Steel Bath Chemistry

Sixty-five kg heats of Armco iron were melted down. The bath temperature was brought up to 1600°C (1873 K) and thereafter maintained within  $\pm 20$  K. For this measurement, Leeds and Northrup Dip-Tip thermocouples were used, which were type R (platinum/platinum-13% rhodium). The EMF measurements were taken with a Fluke 8600A digital voltmeter. At this stage the oxygen content of the bath was generally found<sup>83</sup> to be around 1200  $\pm$  50 ppm.

A 150 g FeSi (75 wt% in Si) addition, followed for deoxidation purposes. The lumps were stirred in the melt for about 30 seconds. Following this, 300 g of aluminum rods 1.905 cm in diameter were immersed. Immediately after, less than 40 g of lime were dispersed in the surface of the melt. At this point the accumulated slag was quite fluid and skimmed off easily.

As the author's experience with the experimental procedure had grown during the years of this research, he found out that an excellent free surface of liquid steel can be achieved if the slag is skimmed off after having turned the power to the induction furnace off, for about 40 seconds. This is a relatively good time interval in which the deoxidation products can rise easily to the surface without being entrained back into the melt, as it would have happened in an agitated melt.

With a probe supplied by Electro-Nite Co. and with the

help of the INMEFA<sup>83</sup> data acquisition facility, the active oxygen content of the steel was found to be in the range of 5 to 10 ppm. In order to keep the niobium and zirconium contents of the steel bath to a minimum, only a limited number of niobium and zirconium cylinders were immersed in each heat. In any case, the total content of the impurities of the steel bath, never exceeded the 3.0 wt% mark. In the end of every experimental work, it was found that the steel was highly 'killed'. Actually, the final active oxygen content, of the steel bath, was found to be close to 1 ppm for most of the cases.

#### 4.2.3 Immersing the Bath Thermocouple

Once the bath chemistry had been correctly adjusted, the next step involved the immersion of a bath thermocouple.

A continuous monitoring of the bath temperature is critical to the success of these dipping tests, since melting times are normally inversely proportional to superheat temperatures ( $T_{\text{bath}} - T_{\text{M.P. Fe}}$ ). For typical steel plant conditions, this only amounts to at most 100 K, so for a  $\pm 5\%$  error, instantaneous bath temperature must be known to be within  $\pm 5$  K maximum.

The thermocouple system chosen was a type R (Platinum/Platinum-13% rhodium). The thermocouple wires had been appropriately placed in a 99.8% alumina double-bore insulator tube (McDaniel) with O.D. 2.38 mm. The whole system was

contained in a 99.8% alumina sheath 5 mm I.D., 7 mm O.D., 46 cm long with one end closed.

In order to prevent slag erosion (of alumina tube) at the melt surface, a cement 'collar' 9 cm long and about 3.2 cm in diameter was bound around it over the appropriate distance.

Another cement collar of the same diameter and a length of 2.5 cm was placed 6.5 cm from the open end of the alumina sheath. This latter collar allowed better attachment of the alumina tube to the support stand. Figure 4.2 shows a bath thermocouple.

The whole thermocouple assembly was lowered to within 5 cm of the bath surface for about ten minutes, and it was connected with a Fluke 8600A digital voltmeter. It was then lowered to just above the melt surface for about ten minutes. When the temperature was at  $1000^{\circ}\text{C}$  (1273 K), the tip was immersed to a depth of 6 cm. The maximum life achieved for a thermocouple immersed in this way was three hours at temperatures ranging between  $1550^{\circ}\text{C}$  and  $1650^{\circ}\text{C}$  (1823 K to 1923 K).

The platinum wires of bath and cylinder thermocouples were long and were connected with cold junction compensators, type CJ-R, supplied by Omega Engineering Inc., Stamford, CT., U.S.A..

#### 4.2.4 Weight Sensor

In this work, advantage was taken of a piece of equipment which has been constructed<sup>58</sup> at McGill University. Using

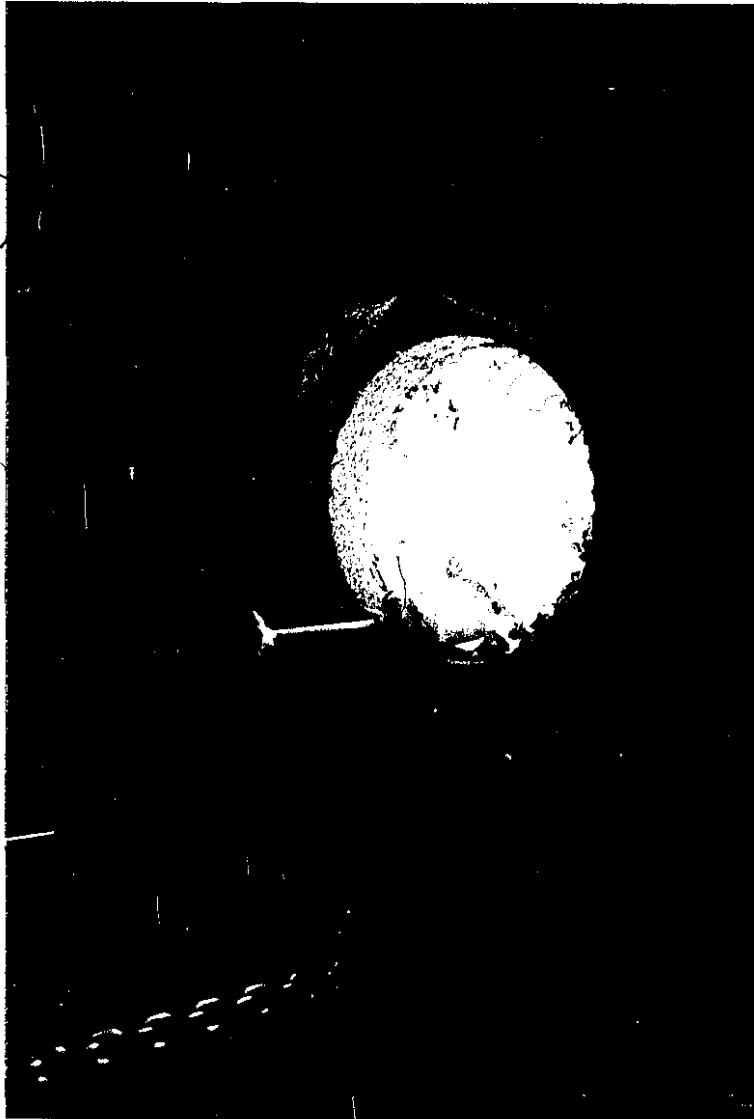
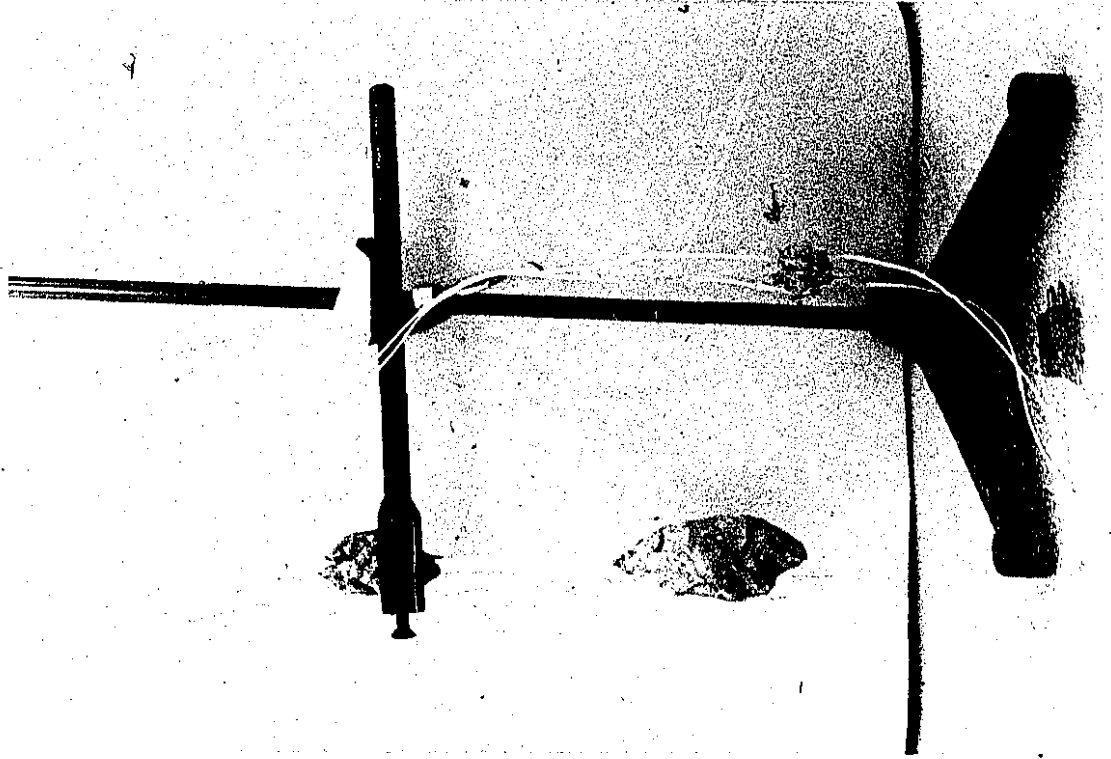


Figure 4.2 A steel-bath thermocouple.

this equipment, the apparent weight of the addition in the steel bath was monitored.

In essence, the equipment provides a feeding mechanism driven by an 1/3 HP variable speed DC motor, plus a weight sensor (load cell) capable of measuring both tensile and compressive loads.

The load cell was calibrated by suspending known weights from it and by subsequently measuring the output signal for the input excitation voltage of 12.43 DC. The excitation voltage was supplied by a special DC solid state electronic equipment (MODEL 2B35J) purchased from the ANALOG DEVICES, U.S.A., and assembled in the laboratory for this reason. Three LEBOW-type load cells of maximum capacities 22.3 N (5 lbs), 44.6 N (10 lbs) and 111.4 N (25 lbs) were used.

The following linear calibration curve was found to relate very well the net downward force with the analog (output) signal from the load cell (correlation coefficient 1.000):

$$\text{Net Downward Force (N)} = A \text{ (mV)} + B \quad (4.1)$$

Table 4.3 shows typical values of the two coefficients (A,B) which were obtained from the calibration tests together with the resolution for each load-cell type. Figures 4.3 A and 4.3 B give a schematic representation of the induction furnace with the bath thermocouple, the weight sensor, and the immersed specimen.

Table 4.3

Typical values of the coefficients  
A and B (Eqn. 4.1), obtained by  
calibration tests.

Load Cell of Max. Capacity (N)	A	B	Resolution (mN)
22.3	-0.5458	-7.5516	± 5
44.6	1.8043	-2.0601	±11
111.4	3.6813	16.9945	±22

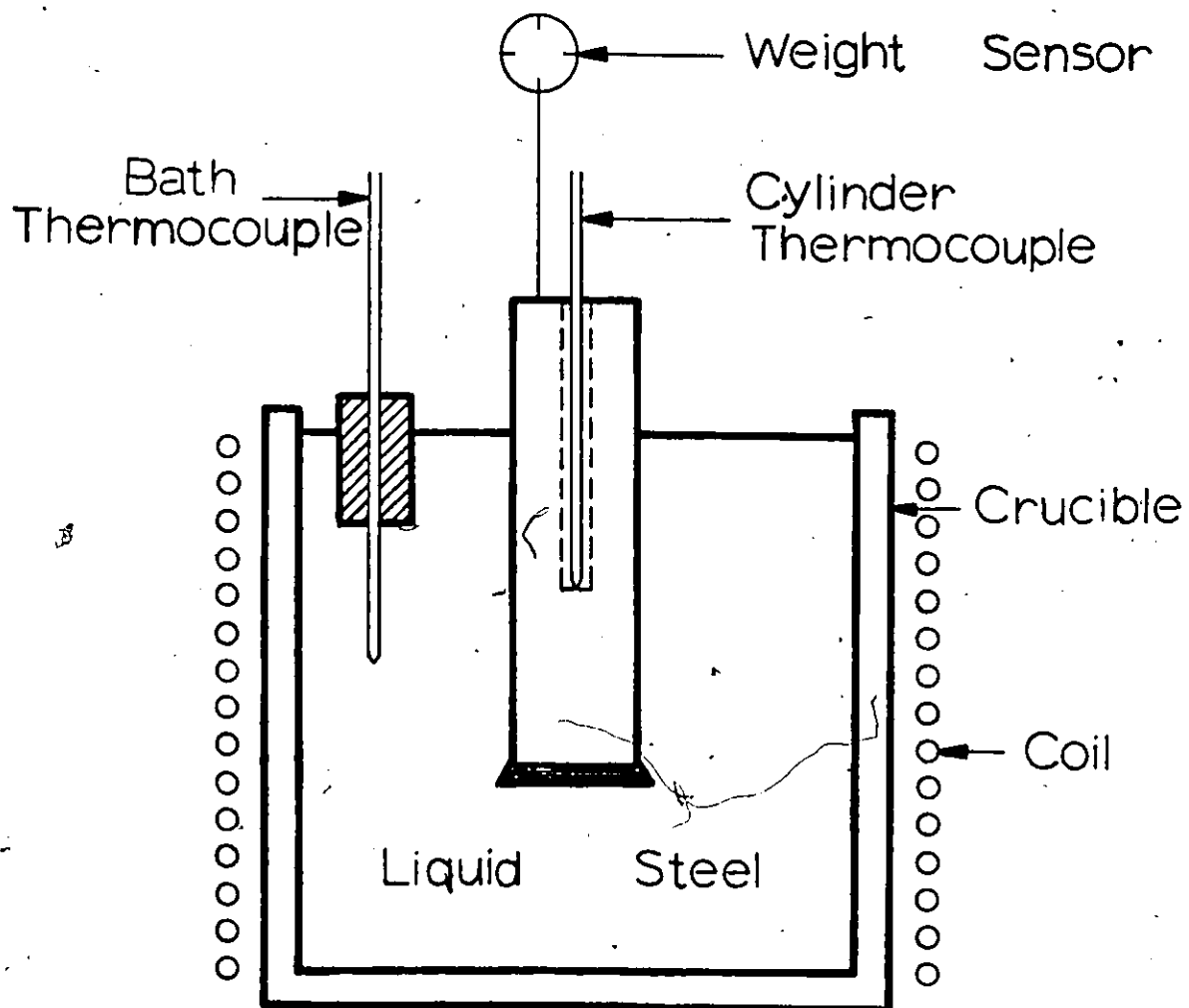


Figure 4.3A Schematic representation of the induction furnace, the weight sensor, the bath thermocouple, and the immersed cylindrical specimen with one thermocouple along its axis.

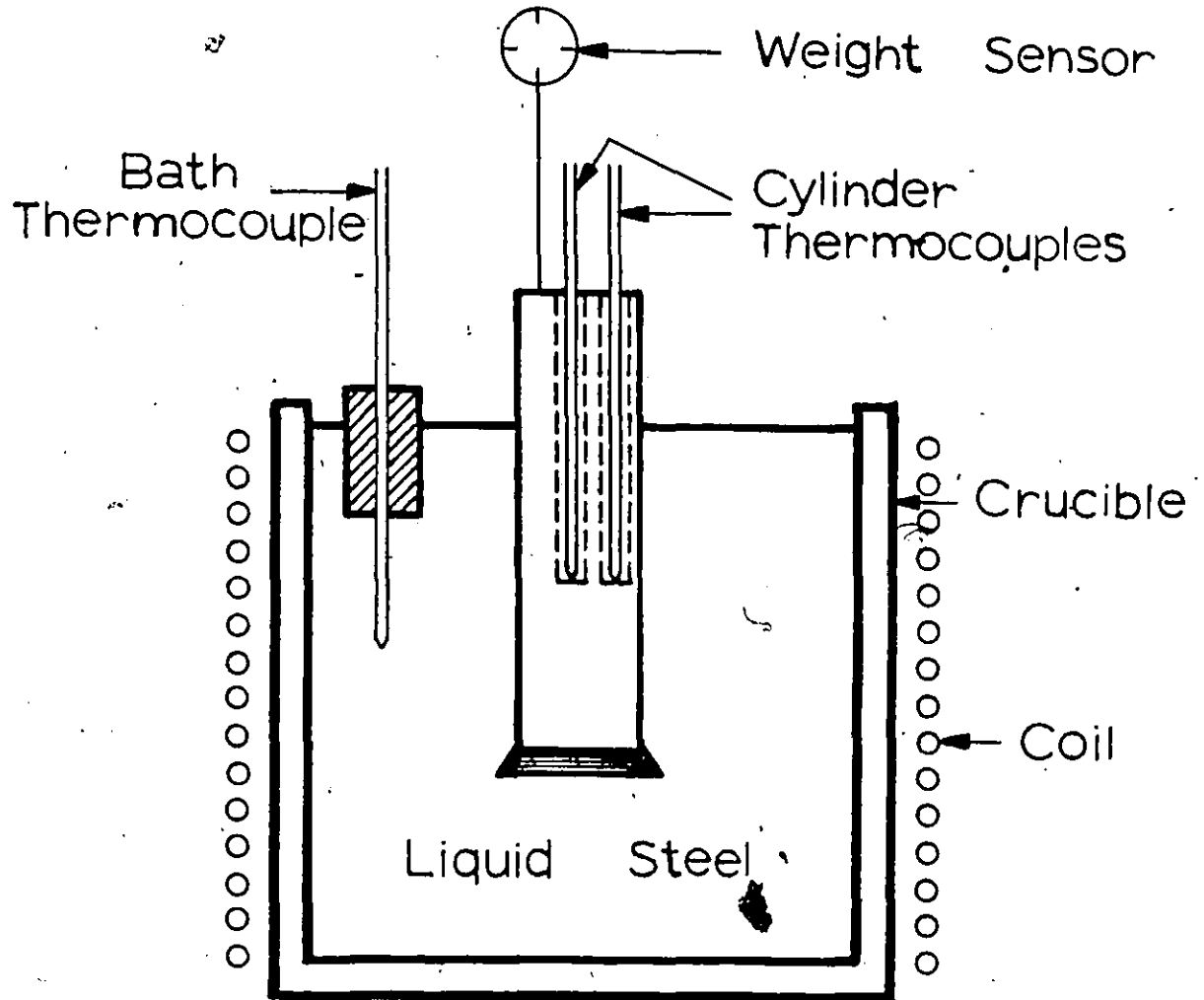


Figure 4.3B Schematic representation of the induction furnace, the weight sensor, the bath thermocouple, and the immersed cylindrical specimen with two thermocouples.

#### 4.2.5 Microprocessor Based Data Acquisition System

The monitoring of analog signals from the transducers (i.e., thermocouples and load cell) was carried out with the Data Acquisition and Process Control (DAPC) facility, which has been especially designed and constructed for this kind of study. Figure 4.4 shows a schematic layout of the DAPC facility. Full details of this system, as well as hardware and software aspects are given in the reference 85.

#### 4.2.6 Procedure for Cylinder Immersion Tests

Once the steel bath chemistry had been correctly adjusted and the bath thermocouple had been immersed into the steel bath, the temperature of the melt was brought up to 5-10 K above the specified temperature. The power to the induction furnace was then reduced and the bath thermocouple output was registered with the help of a FLUKE 8600A Digital Voltmeter. At the same time, the apparatus which carried the load cell was then brought to the top of the steel bath, and scanning of the specified channels started a few seconds prior to immersion. When the message 'Data Acquisition Finished' appeared on the terminal the remaining portion of the cylinder was withdrawn from the steel bath and removed from the load cell. Depending on the selected number of channels, the data collection rate was for most of the cases, 4 measurements per second per channel.

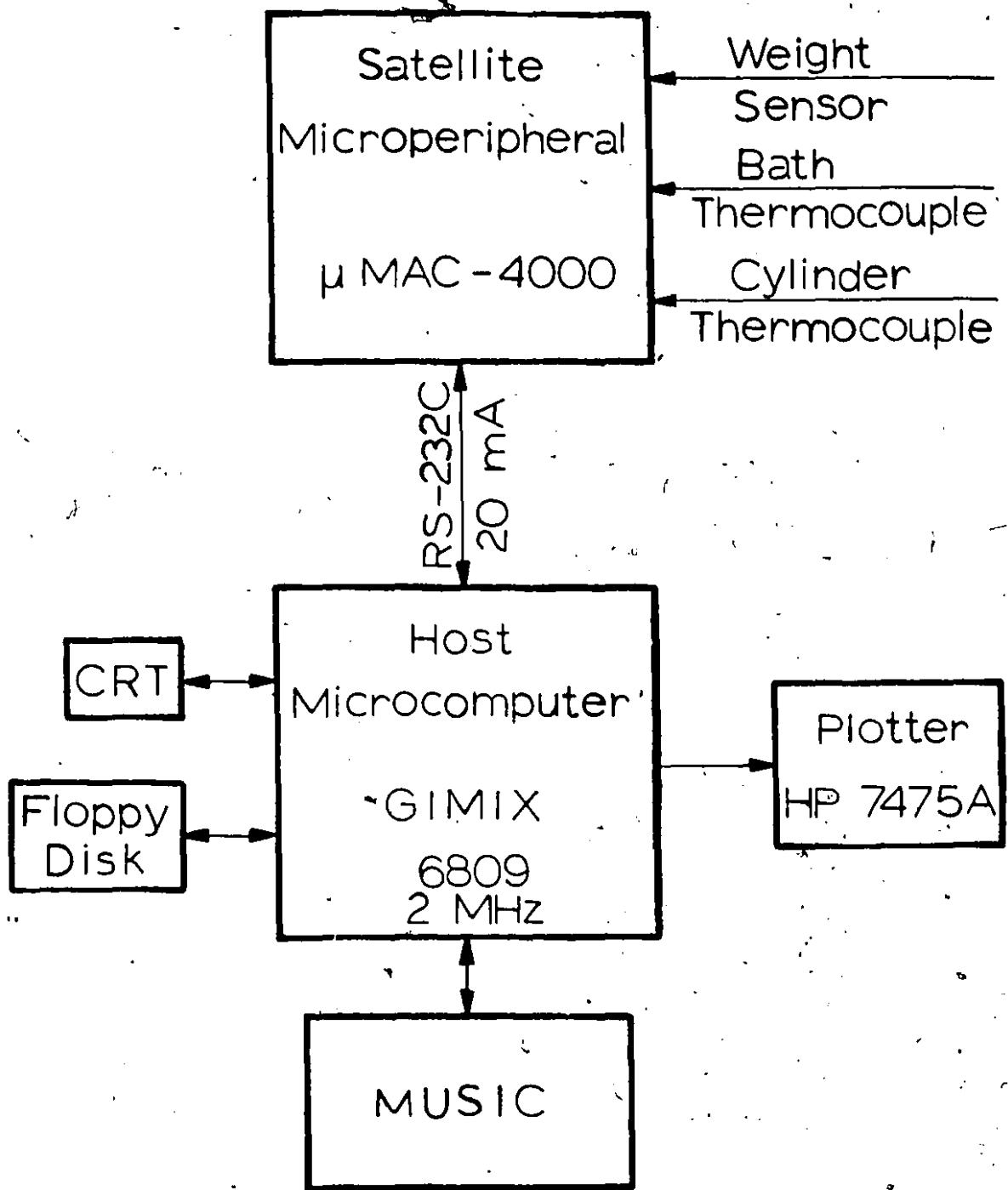


Figure 4.4 The DAPC Facility

#### 4.2.7 Induction Heating of Composite Samples

In order to find out when and how the exothermic reaction between steel and zirconium (or niobium) started, small composite cylindrical samples were machined and pressed tightly together, and they were heated in an induction coil. Figure 4.5 shows a schematic cross-section of a composite sample parallel to the cylinder axis. Similar composite specimens were also made of pure niobium and mild steel. The mild steel had a nominal composition of 0.025% C, 0.05 % Mn, 0.007% P, 0.018% S, 0.001% Si, balance iron. As the coefficient of expansion<sup>75</sup> (in the range of 273 to 373 K) for iron is 1.68 and 2.05 times larger than the ones for niobium and zirconium, respectively, it was indispensable to encase the steel part, especially for the zirconium situation, in order to assure a good contact and therefore, to produce a permanent steel/zirconium interface. A small hole with a diameter of 3.2 mm was then drilled through the iron up to the interface. The composite sample was placed in the induction coil and through it, thermocouple wires were passed until the hot junction met the interface. The specimen was then heated up inductively, and the temperature-time history of the interface was recorded with the DAPC facility.

#### 4.2.8 Electron Probe X-Ray Microanalysis

For the quantitative analysis of the reaction zones during the steel shell periods of niobium and zirconium

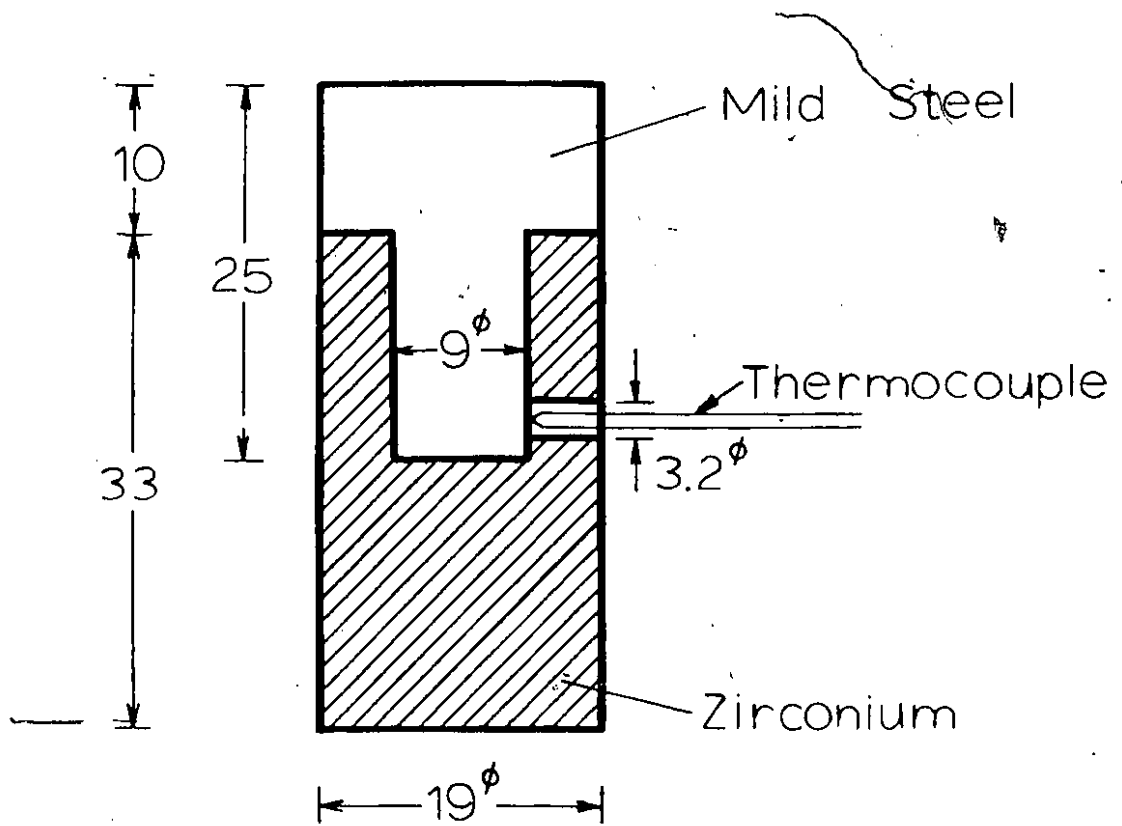


Figure 4.5 Schematic cross-section of a composite sample. (All dimensions are in millimeters).

cylinders in liquid steel, a Camebax electron microprobe (Model MB1) made by Cameca Instruments, France, was used. It was a wavelength dispersive system consisting of four spectrometers. A microprocessor-based system provided the means of communication between the microprobe itself and the user. The estimated analysis time was approximately 100 seconds per analysis point, generally as much as its spectrum accumulation time.

For the quantitative analysis of iron and niobium, the standards used were made from pure iron and niobium metals. For the quantitative analysis of zirconium, the standard used was a zirconium compound called zircon ( $ZrSiO_4$ ), with a chemical composition of 49.8% Zr, 15.3% Si, and 34.9 % O. A typical value for the sensitivity of this instrument is about 100 ppm.

CHAPTER 55. RESULTS AND DISCUSSION ON THE Nb DISSOLUTION IN LIQUID  
STEEL5.1 INTRODUCTION

In this chapter, the experimental results obtained from the dissolution of niobium cylinders immersed in liquid steel, are discussed. Two set of immersion tests were carried out. The first set involved simple dipping experiments in which niobium cylinders were immersed in liquid steel for different time periods. They were then withdrawn and the steel shell thicknesses were measured. An investigation was performed in order to examine any possible reaction between the niobium and the steel, during the steel shell period. The total number of niobium cylinders used for this set of tests was seven. The cylinder diameters ranged from 1.905 cm to 2.54 cm.

The second set of immersion tests involved the dipping of niobium cylinders together with simultaneous monitoring of cylinder and steel bath temperatures, and apparent weight during the dissolution. Twenty-one cylinders were used for this set. The cylinder diameters were ranged from 1.905 cm to 3.81 cm. For the cylinders with a 2.54-cm-diameter only the centerline temperature was measured while for the cylinder with a 3.81 cm diameter (it was only one), temperatures at two locations were measured: one at the centerline, the other at a position close to the edge of the cylinder. In this chapter, a typical experimental result is analysed

together with model predictions. Two periods are identified which are analysed in detail. In Appendix I, typical results for the second set of immersion tests are presented in graphical form.

## 5.2 REACTION AT THE STEEL SHELL AND Nb INTERFACE

Figure 5.1 shows a cross-section of a niobium sample which is encased by the solidified steel shell. This sample comes from a niobium cylinder with 1.905 cm in diameter immersed in liquid steel at  $1600^{\circ}\text{C}$  (1873 K) for 8 seconds. Simple inspection reveals that no reaction has taken place between the niobium cylinder and the shell. Also, if any reaction has actually happened in a microscopic scale, this has not proceeded in any appreciable macroscopic extent.

A question arised whether a reaction can really happen during the steel shell period. Referring to the Fe-Nb phase diagram (Figure 3.2), one should expect some reaction to occur between the outer surface of the niobium cylinder and the inner surface of the steel shell, as there are some intermetallic compounds which are formed in the Fe-Nb system. It was considered that heat transfer might be the cause that the reaction didn't occur. If the starting point (i.e., temperature) for the reaction were high enough, then immersing the niobium cylinder at  $1600^{\circ}\text{C}$  (1873 K) would make its solidified shell to melt back before the reaction temperature would have been reached. For this reason, a search for the

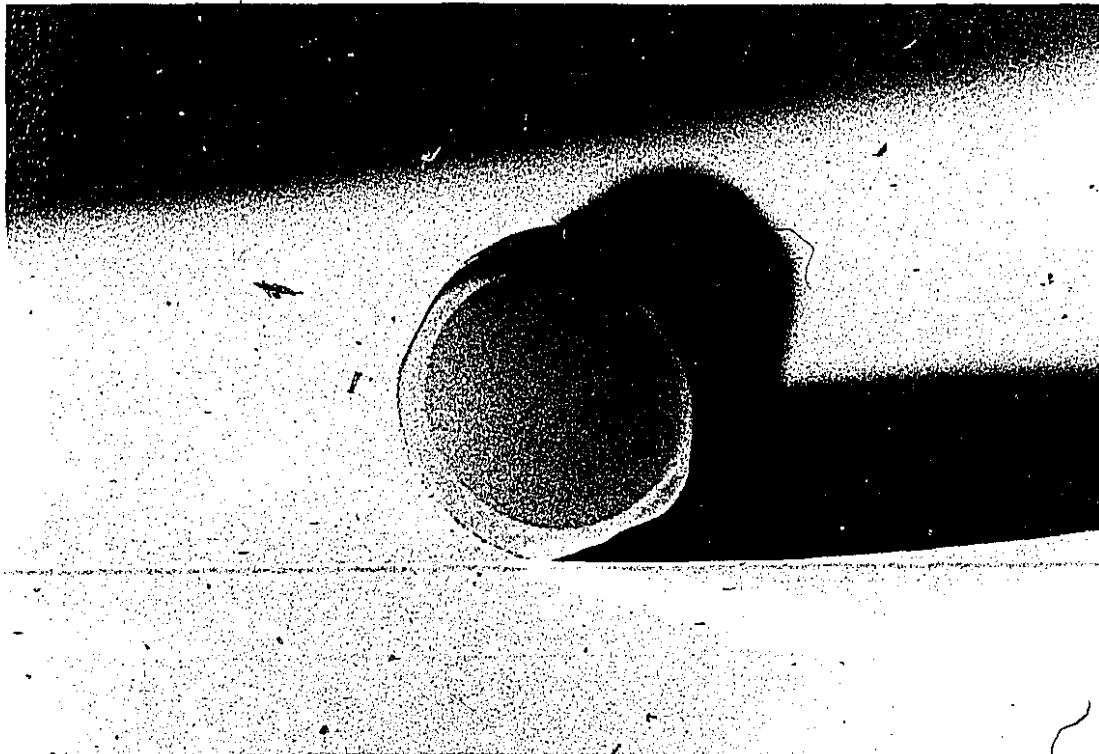


Figure 5.1 Cross-section of a niobium cylindrical specimen (1.905 cm in diameter) encased by the solidified steel shell. This sample had been immersed in liquid steel at 1600°C (1873) for 8 seconds.

reaction was undertaken at lower bath temperatures, that is, at lower bath superheats where more time is required for the shell to melt back. In Figure 5.2, a cross-section of a niobium cylinder (2.235 cm in diameter) together with the solidified shell is shown. Simple inspection reveals that a reaction has occurred, indeed. This cylinder had been immersed in liquid steel at  $1570^{\circ}\text{C}$  (1843 K), for 15 seconds; with the use of a mathematical model (see Section 5.5) it was predicted that the reaction might start at the 11th second after immersion while the steel shell period would end 23 seconds after immersion. From the Fe-Nb phase diagram (Figure 3.2), one can notice that there is a liquid eutectic that forms at  $1370^{\circ}\text{C}$  (1643 K) at about 10.6 at. % Nb. This value ( $1370^{\circ}\text{C}$ ) was considered as the reaction temperature in the model used, and this is a relatively large value to be reached within the steel shell period. The assumption about the reaction temperature was validated from some extra experimental work, as well. As described in Section 4.2.7, composite samples of niobium and low carbon steel were heated in an air induction furnace. In Figure 5.3, a typical experimental result from this set of tests, is depicted. One can notice that after the 84th second the temperature at the niobium/iron interface of the composite sample has a tendency to increase more in an abrupt manner, and after the range of  $1350^{\circ}\text{C}$  -  $1400^{\circ}\text{C}$  (1623 K - 1673 K) the temperature measurements become erratic, while the power input is kept

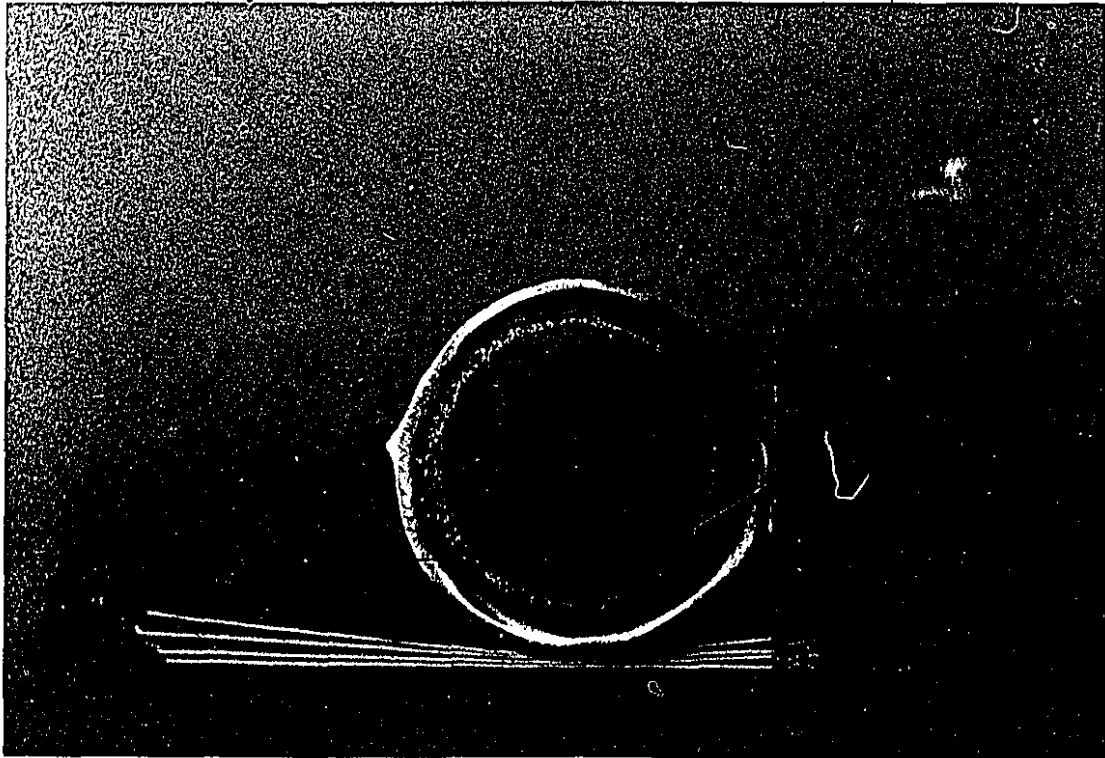


Figure 5.2 Cross-section of a niobium cylindrical specimen (2.235 cm in diameter) encased by the solidified steel shell. This sample had been immersed in liquid steel at 1570°C (1843 K) for 15 seconds.

## Fe-Nb comp. sample (35 kW)

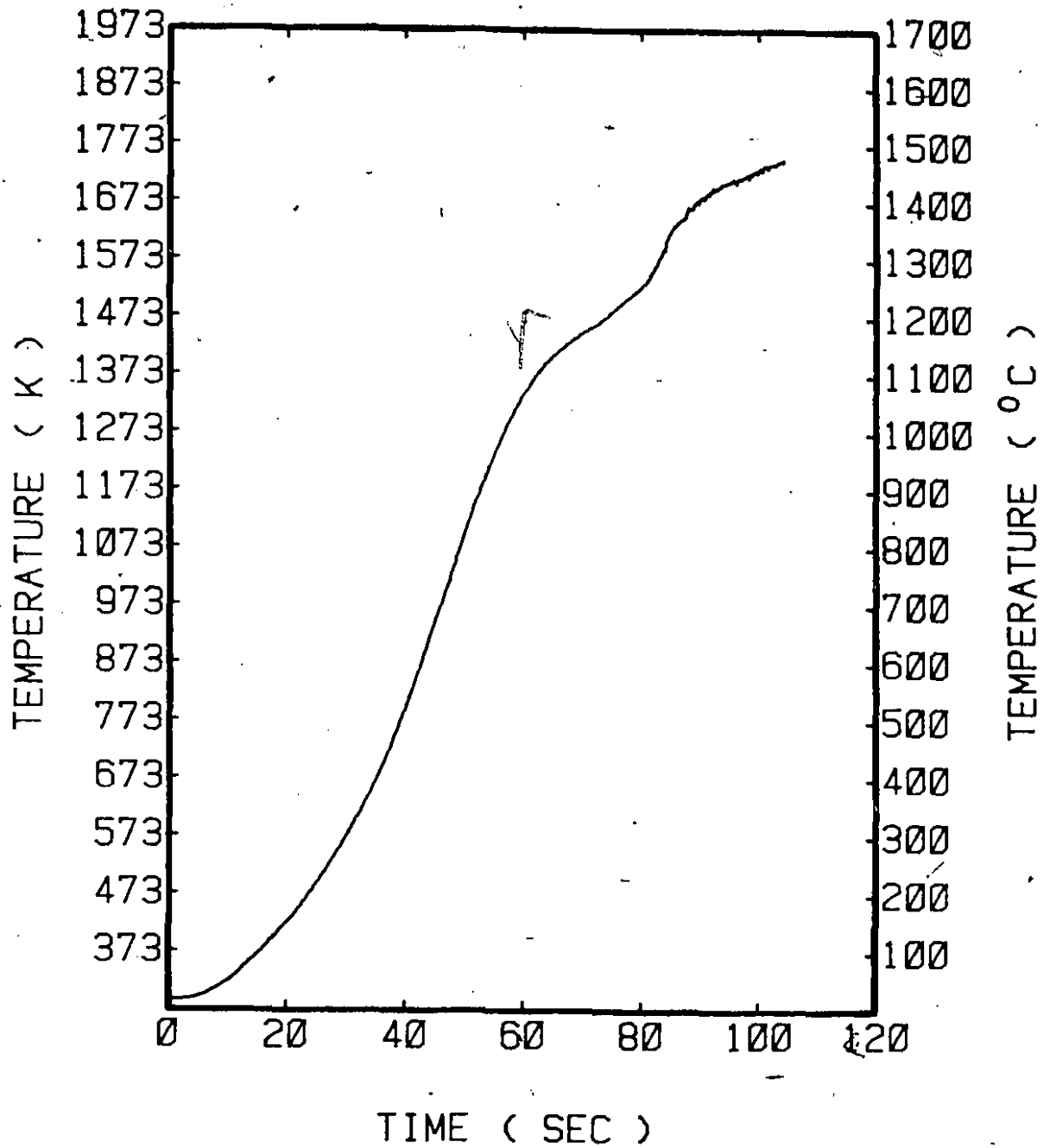


Figure 5.3 Temperature versus time curve for an inductively heated iron-niobium composite sample.

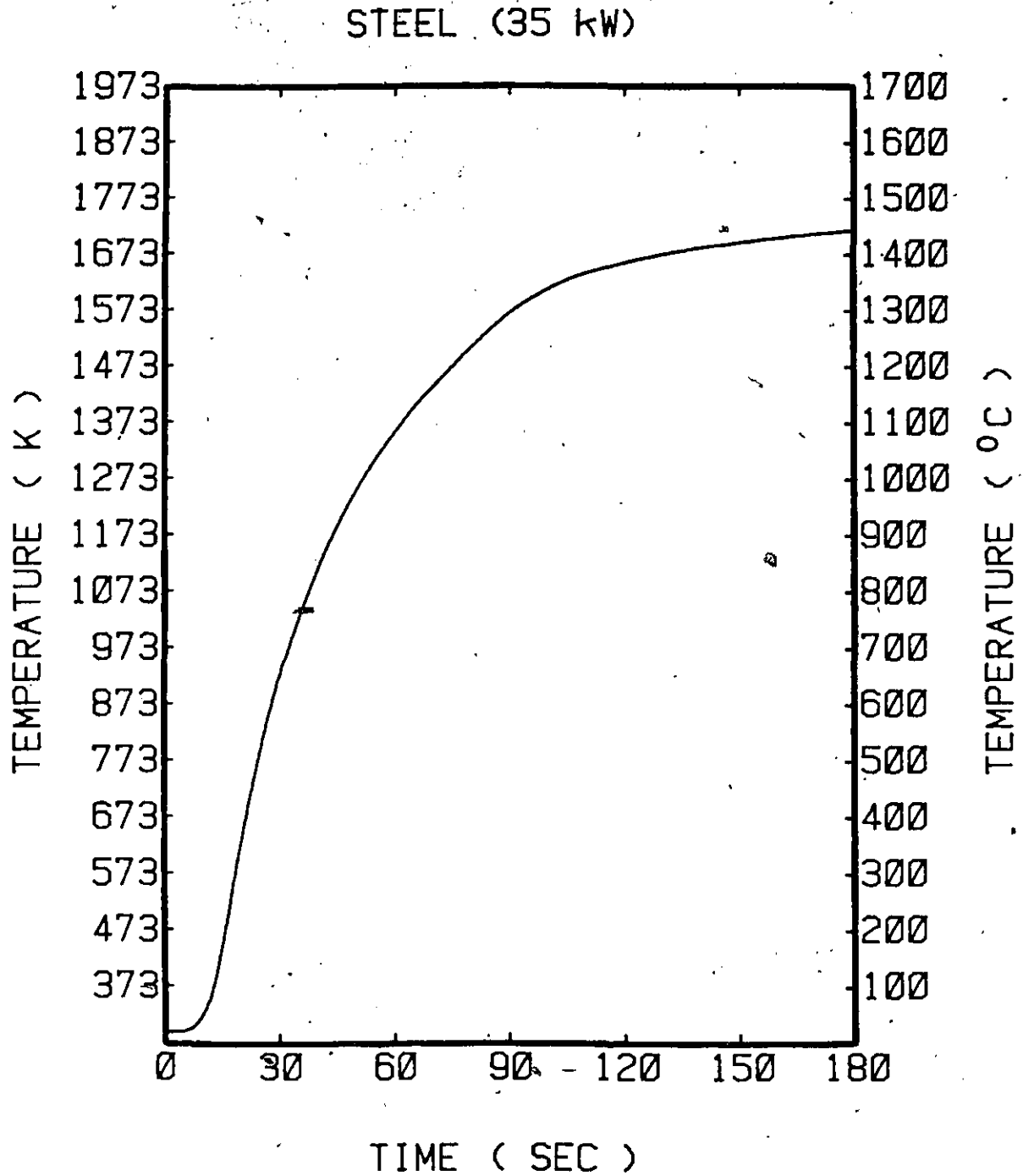


Figure 5.4 Temperature versus time curve for an inductively heated iron piece.

constant at 35 kW. This means that there is a "chemical attack" on the tip of the thermocouple because of the reaction. The Figure 5.4 is presented here for comparison. It is a typical experimental result from the heating of a low carbon steel sample, having the same dimensions with the composite samples and being heated with the same power input (35 kW) in the same induction coil. It is obvious that after the 80th second the temperature of the sample does not increase appreciably and it approaches an almost constant value (around 1430°C or 1703 K).

As described in Section 4.2.8, Electron Probe X-Ray Microanalysis of some samples, taken from niobium cylinders immersed at low bath superheats, was performed. A typical sample used for this kind of analysis is presented in Figure 5.5. Basically, only two Fe-Nb intermetallic compounds were identified: The  $Fe_2Nb$  (or  $Fe_{0.667}Nb_{0.333}$ ) and the  $Fe_2Nb_3$  (or  $Fe_{0.4}Nb_{0.6}$ ). An error analysis was performed on the data obtained from the microprobe analysis and the following error margins were deduced for the identification of the intermetallics: For the  $Fe_2Nb$  or  $Fe_{0.667}Nb_{0.333}$  the experimental errors for the determination of the iron and niobium mole fractions were found to be 0.002 and 0.001, respectively; for the  $Fe_2Nb_3$  or  $Fe_{0.4}Nb_{0.6}$  the experimental errors for the determination of the iron and niobium mole fractions were found to be almost the same, 0.012. In the reaction zone, the average composition was

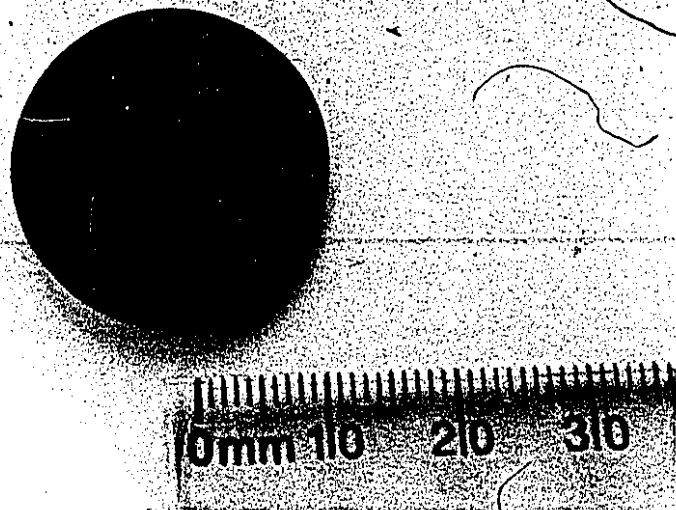
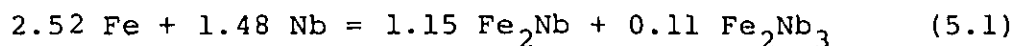


Figure 5.5 A typical sample including a part of the iron-niobium interface during the steel shell period, used for Electron Probe X-Ray Microanalysis.

found to be 37% niobium-mole-fraction (i.e., corresponding to 49.4 wt% Nb), and 63% iron-mole-fraction (i.e., corresponding to 50.6 wt% Fe). The following (overall) reaction can be considered that takes place:



In the reaction products, the presence of the  $\text{Fe}_2\text{Nb}$  intermetallic compound dominates. In reality, the composition of the reaction products is 84.6 wt%  $\text{Fe}_2\text{Nb}$  and 15.4 wt%  $\text{Fe}_2\text{Nb}_3$ . In section 5.5.2, more about the reaction and predictions for the steel shell period will be given.

### 5.3 INTERPRETATION OF DATA FROM THE DISSOLUTION EXPERIMENTS

With the help of the data acquisition facility (DAPC) presented in Chapter 4, the weight sensor (load cell) registers a decrease in the net downward force. The rate at which the force changes then allows the rate of dissolution to be monitored. Figure 5.6 shows schematically the forces which act on the load cell when a cylinder is immersed in liquid steel. Mathematically this can be expressed as follows:

$$F_{\text{NDF}} = F_{\text{G}} - F_{\text{B}} \quad (5.2)$$

where

- $F_{\text{NDF}}$  : Net downward force. This is the force which the load cell registers;
- $F_{\text{G}}$  : Gravitational force;
- $F_{\text{B}}$  : Buoyancy force.

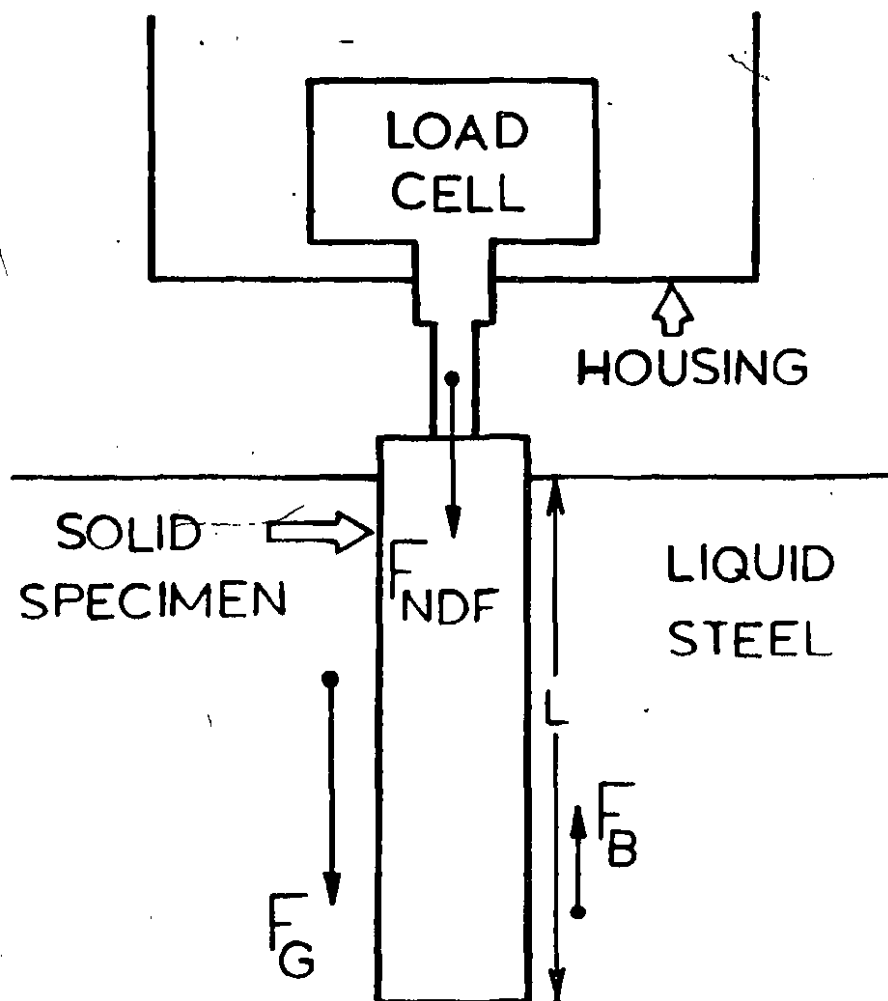


Figure 5.6 Schematic representation of the forces applied to the load cell when a cylinder is immersed in liquid steel.

The gravitational force  $F_G$  can be expressed by the following equation:

$$F_G = V_{\text{out}} \rho_{\text{Nb,s}} g + V_{\text{imm}} \rho_{\text{Nb,s}} g \quad (5.3)$$

where

$V_{\text{out}}$  : The volume of the portion of the cylinder which is outside of the liquid steel during the dissolution (in  $\text{m}^3$ );

$V_{\text{imm}}$  : The volume of the rest portion of the cylinder which is inside the liquid steel during the dissolution (in  $\text{m}^3$ );

$\rho_{\text{Nb,s}}$  : The density of the niobium cylinder (in  $\text{kg}/\text{m}^3$ );

$g$  : The gravitational constant,  $9.81 \text{ m}/\text{s}^2$ .

The term  $F_B$  describes the buoyancy force. According to the principle of Archimedes, any object wholly or partially immersed in a fluid is buoyed up by a force equal to the weight of the displaced fluid. This can be written in mathematical form as:

$$F_B = V_{\text{imm}} \rho_{\text{Fe,l}} g \quad (5.4)$$

where  $\rho_{\text{Fe,l}}$  : The density of the liquid steel.

Combining the equations (5.2), (5.3) and (5.4):

$$F_{\text{NDF}} = V_{\text{out}} \rho_{\text{Nb,s}} g + V_{\text{imm}} \rho_{\text{Nb,s}} g - V_{\text{imm}} \rho_{\text{Fe,l}} g \quad (5.5)$$

Differentiating the equation (5.5) with respect to time and assuming that the difference  $(\rho_{\text{Nb,s}} - \rho_{\text{Fe,l}})$  is constant (i.e., independent of time) one has:

$$\frac{dF_{NDF}}{dt} = \frac{dv_{imm}}{dt} (\rho_{Nb,s} - \rho_{Fe,l}) g \quad (5.6)$$

Figure 5.7 depicts some typical results from the niobium dissolution experiments. The diameter of the cylinder was 2.54 cm and its length was 18 cm. The thermocouple which had been placed along the centerline of the cylinder was 8 cm away from the cylinder's bottom.

Curve 1 of Figure 5.7 shows the temperature of the liquid steel as registered by the DAPC facility. The data acquisition system started monitoring the dissolution parameters a few seconds prior to immersion of the niobium cylinder into liquid steel. Curve 2 of the same figure, presents the force (i.e., the net downward force) registered by the load cell during the dissolution experiment. During the period AB the load cell registers only the gravitational forces; vibrations are usually recorded as the cylinder is lowered towards the surface of the melt. When the leading edge of the niobium cylinder touches the surface of the steel bath, the force which the load cell monitors starts decreasing. This is due to the increase in the buoyancy forces and is represented in line 2 by the segment BC. The subsequent segment CD in line 2 depicts the steel shell period during which a shell of solid steel freezes around the cylinder. The force registered by the load cell remains almost constant during this period. This can be attributed to the fact that the expansion of the niobium cylinder and the freezing of

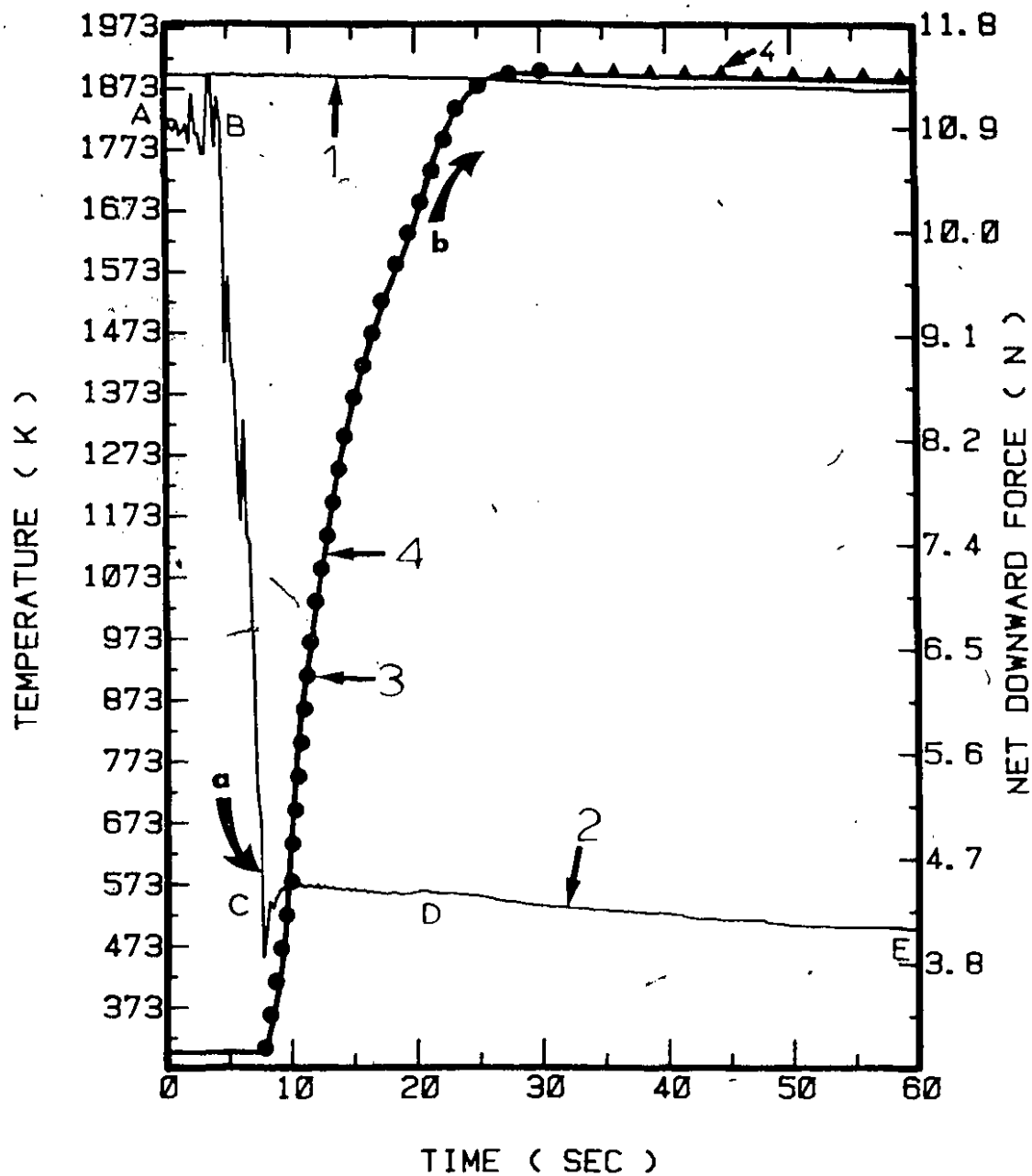


Figure 5.7 Results from a typical niobium dissolution experiment in liquid steel. The cylinder diameter was 2.54 cm and its length was 18 cm.  
 1) Measured steel bath temperature;  
 2) Registered net downward force;  
 3) Measured and predicted (4) centerline temperature.

the steel shell tend to compensate each other so that only minor effects appear on the overall force balance, provided they occur simultaneously.

The segment DE of curve 2 shows the free dissolution period where there is no frozen steel shell around the niobium cylinder. During this period the volume of the niobium cylinder decreases due to the dissolution and consequently, the buoyancy forces also decrease (Eqn. 5.4). The net result is that the force which the load cell registers decreases during this period. Here it should be noted that the segment DE of curve 2 does not show the total free dissolution period of the niobium cylinder in liquid steel. Niobium dissolves slowly in liquid steel, and hence, it would take more time than the one corresponding to the time period of the segment DE to assimilate completely in the liquid steel.

Curve 3 shows experimental and predicted temperatures along the centerline of the niobium cylinder. The solid lines represent predictions while the points show the measured temperatures. Time zero for the cylinder's temperature is taken to be the time corresponding to point C, that is, when the immersion period has just been completed.

Referring to Figure 5.7, the centerline temperature (curve 3) increases rapidly just after the immersion. Niobium does not suffer any solid-state phase transformation, and it also has a relatively high thermal conductivity with a value more than two times larger the thermal conductivity of zirconium (Table 4.2).

The dissolution of niobium in liquid steel involves two, distinct periods. The first is 'the steel shell period' and the second is 'the free dissolution period'. Referring to Figure 5.7, the time coordinate of the curve arrow tips (a, b) show where each one of the above periods start. The steel shell period lies between a and b while the free dissolution period starts at b. In the next sections of this chapter, these periods are analysed in more detail.

#### 5.4 CONSISTENCY AND ACCURACY OF THE METHOD

The validity of the results registered by the weight sensor were checked for each cylinder immersion test. Thus, the immersion length for each cylinder could be found by measuring the length before and after its immersion. From the immersion length, the volume of the immersed part of the cylinder was determined. With the aid of the equation (5.5), the expected net downward force was calculated. Referring to Figure 5.7, the difference of the values of the net downward force at points B and C of curve 2 was within 5% of that calculated. The initial and final mass of the cylinder was also measured with a precision balance. The difference of the net downward force at points D and E is the difference of the apparent weight of the cylinder during this part (segment DE) of the free dissolution. This apparent weight is directly related with the real mass of the cylinder which has been dissolved and in this way, this value of the dissolved

mass was checked against the measured weight loss of the cylinder. These two values should not differ more than 5%. An experimental run was rejected if it failed one of these tests. Accordingly, about 16% of the experimental runs were rejected. The most important reason for this was slag freezing onto the cylinder near the surface of the melt.

The accuracy of the method depends upon the difference between the steel bath density and the density of the individual element tested. The larger this difference, the higher the accuracy of the displaced weight measurements. In this respect the accuracy of estimation of the volumetric change of the addition during the dissolution can be found using equation (5.6), and the accuracy (resolution) of the weight sensor. In the case of the niobium cylinders for example, the volumetric change could be estimated within an accuracy of  $\pm 1.7 \text{ cm}^3$ , while for the zirconium cylinders, the accuracy of the volumetric change was within  $\pm 3.2 \text{ cm}^3$ .

## 5.5 APPLICATION OF A MATHEMATICAL MODEL

### 5.5.1 Introduction

In order to facilitate the analysis of the phenomena that take place during the steel shell and the free dissolution periods of niobium and zirconium in liquid steel, it was considered advantageous to use an existing mathematical model, which has been developed<sup>59,60</sup> to predict heat and mass

transfer events which occur when a high melting point additive is held motionless below the surface of a steel bath. The additive is chosen to be of a cylindrical shape since heat transfer phenomena can be described relatively easily in cylindrical geometry and there are experimental values of heat transfer coefficients for similar cases in steel baths. This model is a one-dimensional (radial) model, because of the fact that temperatures within the main body of the cylinder are affected mainly by heat entering in the radial direction from the bath, ignoring any heat transfer by conduction up through the bottom surface. The explicit finite difference method was employed to solve the set of unsteady state differential equations of heat transfer and accompanying boundary conditions and equations. In the following section the general equations of the model in rigorous mathematical form will be presented. Discretization equations for the numerical solution of the model will not be presented here; the interested reader is referred to the references 59, 60 and 61 for more details about this. It is important to note though, that a computer program based on this model and written in FORTRAN computing language, was compiled with a FORTRAN-H compiler and executed on an AMDAHL computer. Then the same program was compiled with an Absoft FORTRAN-77 Compiler (Version 2.1) and executed on an EXORmacs (MPU-68000) MOTOROLA designed pseudo-32-bit microprocessor. Once the performance of the program had been checked to the last

detail in both systems, executions of the program were performed by the EXORMacs entirely thereafter. Computational results were obtained for both metals (i.e., niobium and zirconium) and will be presented in the present and the following chapters.

### 5.5.2 General Equations of the Model

The heat conduction equation expressed in cylindrical coordinates has the form<sup>103</sup>:

$$\frac{1}{r} \frac{\partial}{\partial r} \left( kr \frac{\partial T}{\partial r} \right) + \frac{1}{r^2} \frac{\partial}{\partial \phi} \left( k \frac{\partial T}{\partial \phi} \right) + \frac{\partial}{\partial z} \left( k \frac{\partial T}{\partial z} \right) + \dot{q} = \rho c_p \frac{\partial T}{\partial t} \quad (5.7)$$

where  $T$  : the temperature at a specific location inside the cylinder;

$k$  : thermal conductivity;

$\rho$  : density;

$c_p$  : heat capacity;

$\dot{q}$  : heat generation per unit volume per unit time inside the cylinder;

$r$  : radial distance;

$z$  : axial distance;

$\phi$  : angle.

In the absence of heat conduction in the axial direction, then  $\partial T / \partial z = 0$ . If in addition, the heat flow is symmetrical with respect to the angular component, (i.e., conditions at  $r$  and  $z$ , uniform and independent of  $\phi$ ), then the above equation reduces to:

$$\frac{1}{r} \frac{\partial}{\partial r} \left( kr \frac{\partial T}{\partial r} \right) + \dot{q} = \rho c_p \frac{\partial T}{\partial t} \quad (5.8)$$

Finally, without any heat generation ( $\dot{q} = 0$ ), this general equation simplifies to that for transient radial conduction of heat in a cylinder:

$$\rho c_p \frac{\partial T}{\partial t} = \frac{1}{r} \frac{\partial}{\partial r} \left( kr \frac{\partial T}{\partial r} \right) \quad (5.9)$$

Equation (5.9) is solved to determine the temperature distribution inside the solid additive and the solidified steel shell. Figure 5.8 presents a typical set of events taking place during the steel shell period for a cylindrical additive immersed in liquid steel. The diagram represents a schematic cross-section perpendicular to the cylinder's axis. One can use the equation (5.9) to write appropriate expressions for transient heat conduction in the solid additive and the steel shell:

Solid additive:  $0 \leq r \leq r_1$  ,  $0 \leq t \leq t_{\text{total}}$

$$\rho_s c_{p_s} \frac{\partial T}{\partial t} = \frac{1}{r} \frac{\partial}{\partial r} \left( k_s r \frac{\partial T}{\partial r} \right) \quad (5.10)$$

Solid steel shell:  $r_1 \leq r \leq r_2$  ,  $0 \leq t \leq t_{\text{total}}$

$$\rho_{\text{Fe}} c_{p_{\text{Fe}}} \frac{\partial T}{\partial t} = \frac{1}{r} \frac{\partial}{\partial r} \left( k_{\text{Fe}} r \frac{\partial T}{\partial r} \right) \quad (5.11)$$

Generally for zirconium and for low bath superheats in the case of niobium, when the steel shell/additive interface exceeds a certain threshold temperature, an exothermic reaction is initiated. This phenomenon has been approximated

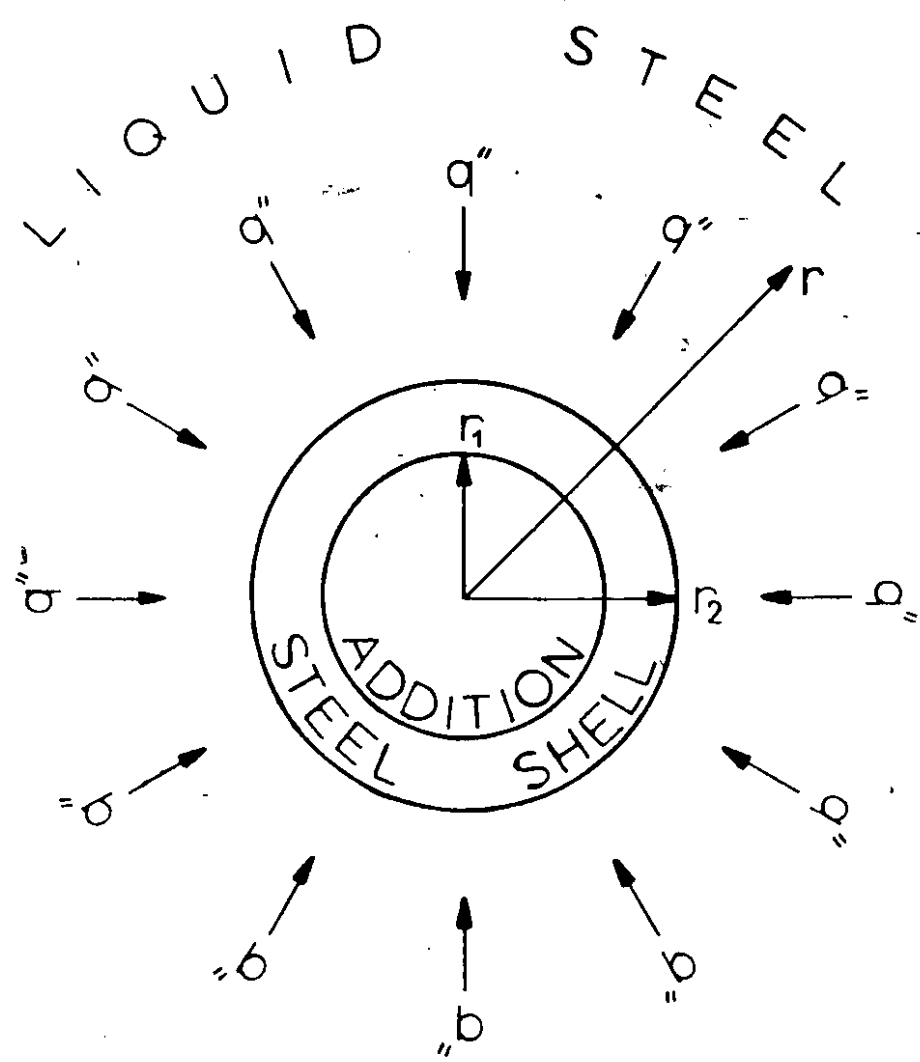


Figure 5.8 Schematic representation of an addition with the solidified steel shell and the liquid steel; the various interfaces and the coordinate system used in the mathematical model are also illustrated.

(in its simplest form) with a constant heat generation term at the inner steel shell interface, together with associated erosion of the steel shell. This erosion is caused by a constant flux of dissolved additive (i.e., zirconium), supplied through dissolution of its core. Figure 5.9 presents these phenomena in schematic form.

#### A) Initial Conditions

Prior to immersion, the temperature of the cylinder can be taken to be uniform at  $T_0$ . Expressing the above condition mathematically, (I.C.1) for  $t = 0$  and  $0 \leq r \leq r_1$

$$T = T_0 \quad (5.12)$$

Similarly, bulk temperatures within the steel bath can be taken to be constant prior to immersion: (I.C.2)  $t = 0$  and  $r > r_1$ ,

$$T = T_B \quad (5.13)$$

#### B) Boundary Conditions

In writing boundary conditions, these have been listed in a systematic way starting at the cylinder's center and time zero, and proceeding radially outward towards the liquid steel bath. Although the problem has been expressed in terms of five boundary conditions, those applying at the inside steel-shell boundary change once exothermic reaction begins. The boundary conditions are:

$$\begin{aligned} \text{(B.C.1)} \quad & 0 \leq t \leq t_{\text{total}}, \quad r = 0 \\ & \frac{\partial T}{\partial r} = 0 \end{aligned} \quad (5.14)$$

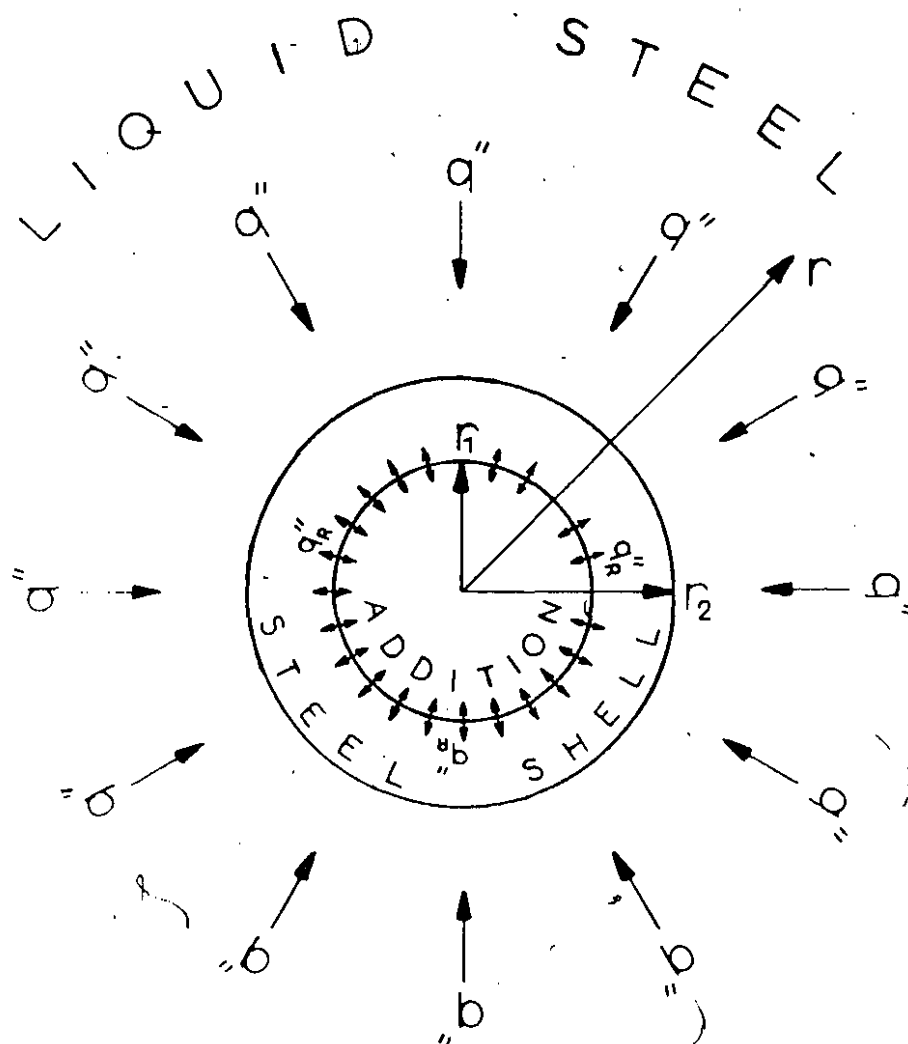


Figure 5.9 Schematic representation of an addition reacting exothermically during the steel shell period; the various interfaces and the coordinate system used in the mathematical model are also illustrated.

$$(B.C.2A) \quad 0 \leq t \leq t_R, \quad r = r_1$$

$$q'' = k_{Fe} \frac{\partial T}{\partial r} = k_s \frac{\partial T}{\partial r}$$

$$\text{and } q'' = \frac{T_{Fe}^* - T_s^*}{R_T} \quad (5.15)$$

where  $T_{Fe}^*$  and  $T_s^*$  represent the interfacial temperature of the iron and solid additive interfaces in imperfect thermal contact.

$$(B.C.2B) \quad t_R < t < t_{total}, \quad r = r_1$$

$$-k_{Fe} \frac{\partial T}{\partial r} + N_s'' \Delta H_R = -k_s \frac{\partial T}{\partial r} \quad (5.16)$$

where  $R_T = 0$ , and  $N_s'' = K_s (C_s - C_{s/Fe})$

The boundary condition (B.C.2B) suggests that when the exothermic reaction starts, the difference between heat fluxes into and out of the interface or reaction zone must be balanced by the heat flux generated by the exothermic reaction. Furthermore, when the reaction starts the contact resistance disappears (i.e.,  $R_T = 0$ ), and it is assumed that the reaction zone remains at the original iron/additive interface.

$$(B.C.3) \quad 0 \leq t \leq t_{total}, \quad r = r_2$$

$$T = T_{M.P.Fe} \quad (5.17)$$

Equation (5.17) means that the temperature at the interface between the steel shell and the liquid steel, is in fact,

the melting point of the steel bath.

$$(B.C.4) \quad 0 < t < t_{\text{total}}, \quad r = r_2$$

$$\left( k_{\text{Fe}} \frac{\partial T}{\partial r} \right)_{\text{Fe, shell}} = \rho_{\text{Fe}} \lambda_{\text{Fe}} \frac{\partial r}{\partial t} + h ( T_{\text{BATH}} - T_{\text{M.P. Fe}} ) \quad (5.18)$$

where  $\lambda_{\text{Fe}}$  is the latent heat of fusion of the melt.

Equation (5.18) represents a heat balance for the moving steel solidification front at the steel shell/liquid steel interface.

The heat transfer coefficient ( $h$ ) from the bath to the enclosing steel shell surface, has been deduced from the following dimensionless correlation:

$$\text{Nu}_{\text{I}} = C \text{Ra}_{\text{I}}^{1/3} \quad (5.19)$$

where  $\text{Nu}_{\text{I}}$  : the Nusselt number;

$\text{Ra}_{\text{I}}$  : the Rayleigh number;

$\text{I}$  : the cylinder length

and  $C$  is a constant depending on the experimental conditions.

Actually,  $C = 0.23$  when there is some induction stirring to the melt (i.e., the power to the induction furnace is kept on during the test), and  $C = 0.17$  when the induction furnace is turned off during the test. The validity of the equation (5.19) has been verified from another independent study<sup>104,105</sup>, in which cylindrical specimens were immersed in steel baths similar (in quantity) to those used for the present study.

$$(B.C.5) \quad 0 < t < t_{\text{total}}, \quad r \rightarrow \infty$$

$$T = T_{\text{BATH}} \quad (5.20)$$

The last boundary condition demonstrates that the temperature of the steel bath far from the steel shell can be regarded as being constant.

To model the free dissolution period of niobium and zirconium in liquid steel, an effective heat transfer coefficient ( $h_{\text{eff}}$ ) was introduced. This was done so, in order to take into account the convective heat transfer between the dissolving cylindrical additive and the steel bath. The heat flux that leaves the cylinder and goes into the melt during the free dissolution period, is called the 'outward flux', and is given by the formula:

$$q_{\text{out}}'' = h_{\text{eff}} (T_{\text{I}} - T_{\text{B}}) \quad (5.21)$$

where  $T_{\text{I}}$  - the temperature of the cylindrical additive at its dissolving front;

$T_{\text{B}}$  - the temperature of the bath.

It is obvious, that  $q_{\text{out}}''$  can be positive or negative depending on the sign of the difference ( $T_{\text{I}} - T_{\text{B}}$ ).

The inward flux  $q_{\text{in}}''$ , that is the flux that enters the cylindrical additive at its dissolving front, is given by the following equation:

$$q_{\text{in}}'' = k \left( \frac{\partial T}{\partial r} \right)_{\text{I}} \quad (5.22)$$

where  $k$  = the thermal conductivity of the additive; the derivative of the temperature with respect to the radial distance ( $\partial T / \partial r$ ), is taken at the interface (I).

A simple energy balance at the dissolving front demonstrates that the sum of the inward and outward fluxes is

equal to the generated heat per unit surface per unit time due to the exothermic dissolution:

$$k \left( \frac{\partial T}{\partial r} \right)_I + h_{\text{eff}} (T_I - T_B) = N_j'' \Delta \bar{H}_j^0 \quad (5.23)$$

where  $N_j''$  = the molar flux of the dissolving element  $j$ ;

$\Delta \bar{H}_j^0$  = the partial molar heat of mixing at infinite dilution of  $j$ .

The molar flux  $N_j''$  of the dissolving element  $j$  can also be written as:

$$N_j'' = \frac{\rho}{M} \frac{dr}{dt} \quad (5.24)$$

where  $\rho$  = the density of  $j$ ;

$M$  = the molecular weight of  $j$ ;

$\frac{dr}{dt}$  = the reduction of the cylindrical additive's radius per time, or simply the dissolution speed.

One can group some constant parameters together:

$$Q_V = \frac{\rho}{M} \Delta \bar{H}_j^0 \quad (5.25)$$

where  $Q_V$  is the generated heat per unit volume.

So, the equation (5.23) now becomes:

$$k \left( \frac{\partial T}{\partial r} \right)_I + h_{\text{eff}} (T_I - T_B) = Q_V \frac{dr}{dt} \quad (5.26)$$

The above formula (5.26) has been used to model heat transfer events during the free dissolution of niobium and zirconium in liquid steel. In the following sections, the estimation of the effective heat transfer coefficient ( $h_{\text{eff}}$ )

will be described, and results based on this equation will be presented as well.

### 5.5.3 Steel Shell Period

In the section 5.2, the subject about the reaction at the niobium/steel shell interface had been discussed. It was pointed out, that a reaction does happen once there is enough time for the starting temperature of the reaction to be reached, before the shell melts back. As the reaction temperature for this case is relatively high  $1370^{\circ}\text{C}$  ( $1643\text{ K}$ ), the reaction does not practically happen or, it does just a few seconds before the end of the steel shell period. In Figure 5.10 one can notice that the reaction has not actually taken place yet. This is a cross-section from a niobium cylinder 2.24 cm in diameter, which had been immersed for 8 seconds in a steel melt at  $1600^{\circ}\text{C}$  ( $1873\text{ K}$ ). The model predicted that the reaction should start 10 seconds after immersion and that the steel shell period should last 13.5 seconds. Similar predictions were made for niobium cylinders with diameters in the range of 1 cm to 5 cm. Stagnant steel baths were assumed (i.e., the power to the induction furnace was turned off during the hypothetical test) at  $1600^{\circ}\text{C}$  ( $1873\text{ K}$ ), and with a melt cooling-rate  $0.25\text{ K/sec}$ . These results are shown in Figure 5.11. Line 1 represents the time for the reaction to start for a specific diameter cylinder. Two shell periods are presented. Curve 2 gives the steel shell

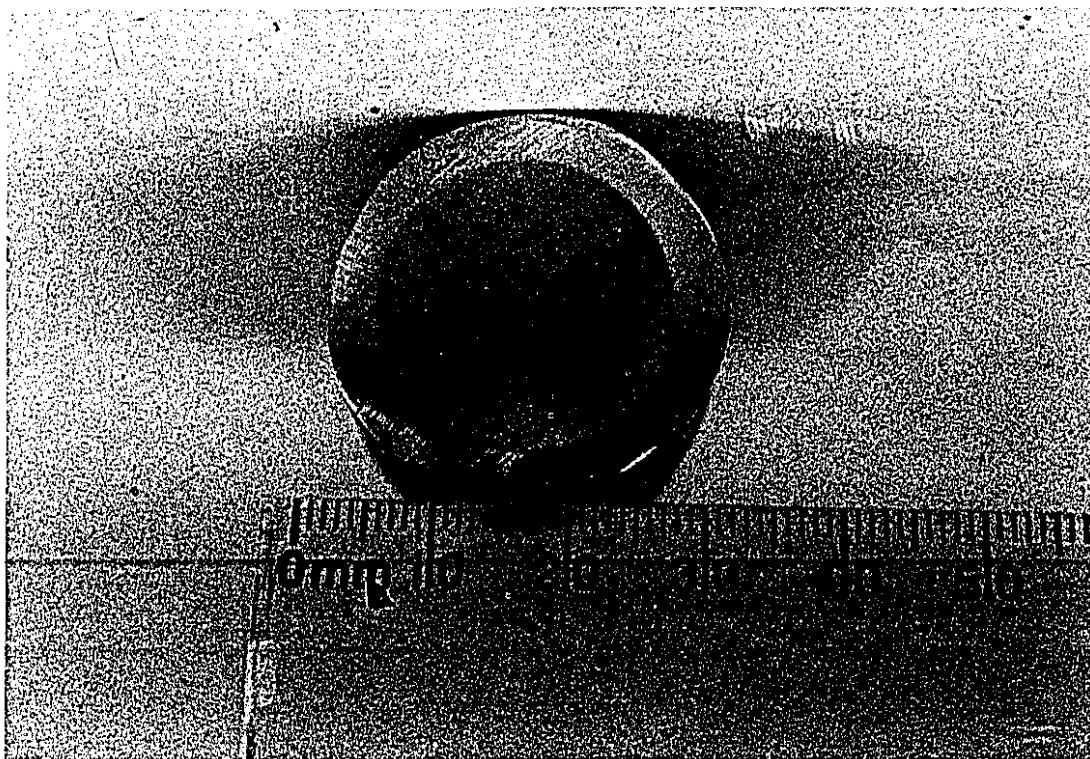


Figure 5.10 Cross-section of a niobium cylindrical specimen (2.24 cm in diameter) encased by the solidified steel shell. This sample had been immersed in liquid steel at  $1600^{\circ}\text{C}$  (1873 K) for 8 seconds.

period for a specific diameter niobium-cylinder in which the generated heat flux due to the exothermic reaction (equation 5.1) has a relatively large value  $360.2 \text{ kW/m}^2$  ( $8.61 \text{ cal/cm}^2/\text{sec}$ ). This is considered to be a large value, as it is of the same order of magnitude with the heat fluxes estimated for the steel shell period of zirconium cylinders in liquid steel (see Chapter 6). Curve 3 gives the steel shell period for the extreme case in which the generated heat flux is zero. One may question why those two values for the steel shell period of a specific diameter cylinder happen to be so close. This can be explained on the basis that the reaction takes place in the last stages of the steel shell period and hence, the heat transfer by convection from the fluid to the cylinder becomes more important than any other generated heat due to the exothermic reaction. Furthermore, this makes the precise determination of the generated heat flux due to the reaction in the steel shell period impossible. On the other hand, most of the experimental work has been carried out with niobium cylinders of maximum diameter 2.54 cm, and as it is depicted in the Figure 5.11, at smaller diameters the two shell periods become almost identical.

Before closing the discussion about the steel shell period of niobium cylinders in steel melts, one last thing should be pointed out. In Figure 5.12, predictions are given on the possibility of the reaction's occurrence. Curve 1 shows predictions for liquid steel without induction stirring

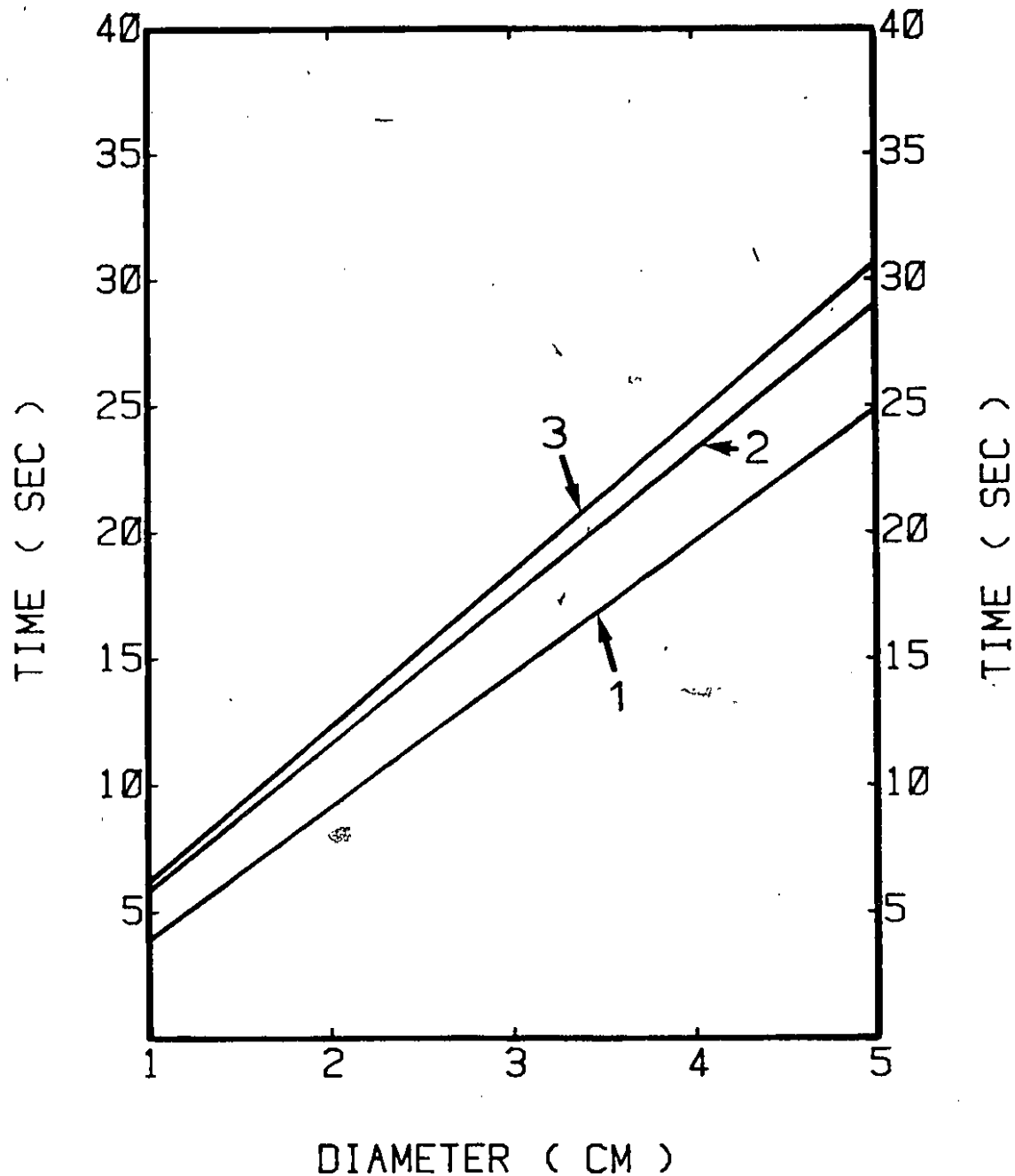


Figure 5.11 Predicted steel shell periods for niobium cylinders of various diameters.

- 1) Time after immersion in which the reaction begins during the steel shell period;
- 2) Steel shell period for a large value of generated heat flux;
- 3) Steel shell period without any heat generation.

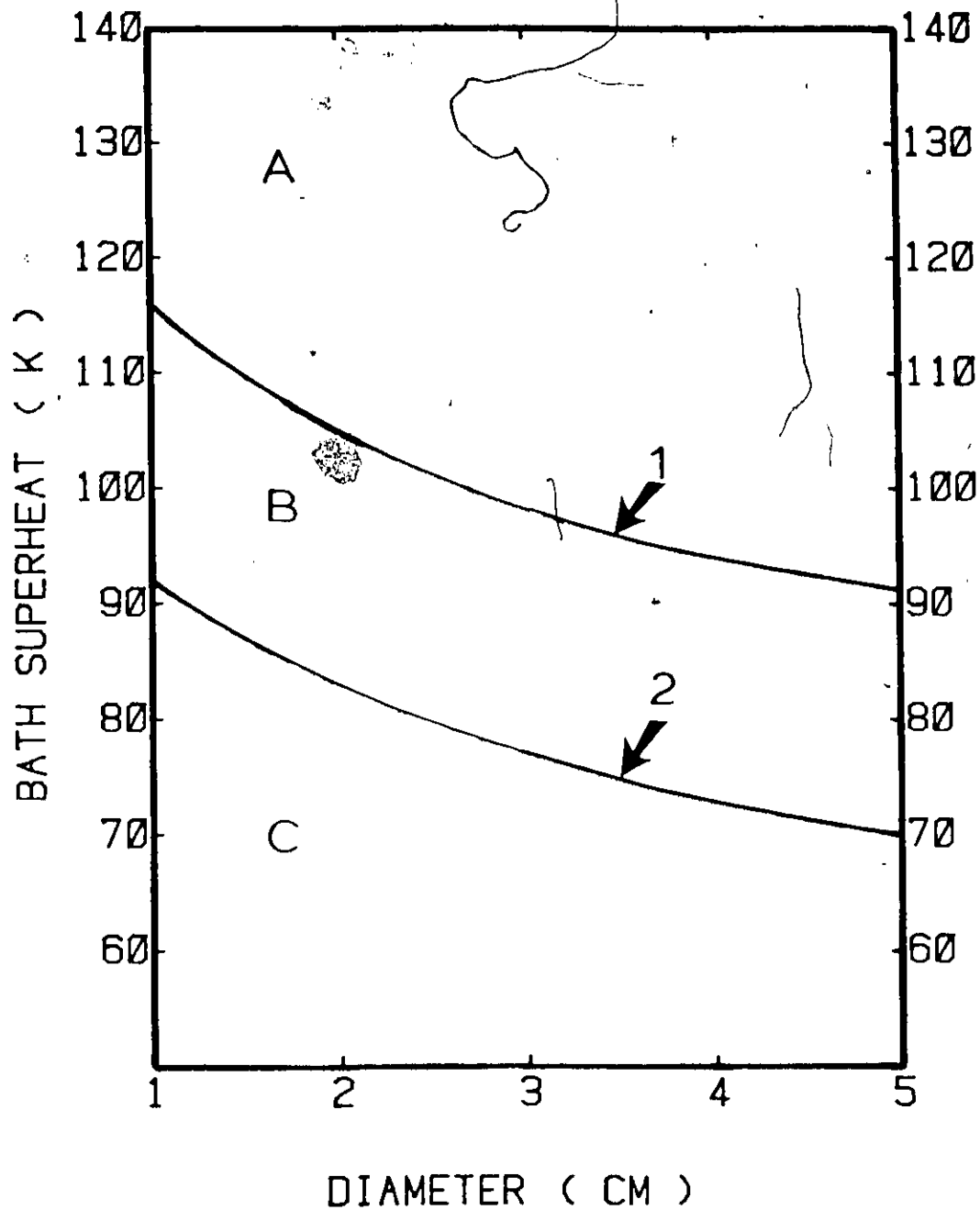


Figure 5.12 Predicted results on the possibility of the reaction's occurrence during the steel shell period with respect to steel bath superheat, cylinder diameter, and stirring conditions of the melt.  
1) No induction stirring (power off);  
2) Induction stirring (power on).

(i.e., power off) and cooling rate 0.25 K/sec, while Curve 2 shows predictions for liquid steel with induction stirring (i.e., power on) and cooling rate 0.05 K/sec. Three regions can be identified: In region A no reaction can practically happen during the steel shell period. The bath superheats are high enough so that the convective heat-transfer events are so predominant, that the steel shell melts back before the reaction temperature is reached at the niobium/steel shell interface. In region B no reaction can in reality take place for inductively stirred melts but, the reaction will happen for quiescent baths. Finally, in region C the steel bath superheats are low enough, so that relatively long steel shell periods are expected to happen and hence, the reaction will occur irrespective of the convective heat transfer characteristics of the steel melts.

#### 5.5.4 Free Dissolution Period

Referring to Figure 5.6, the volume of the immersed portion of the niobium cylinder can be expressed as:

$$V_{\text{imm}} = \pi r^2 L \quad (5.27)$$

where  $r$  : the cylinder radius;

$L$  : the immersed cylinder length.

From equation (5.6) using (5.27) one has:

$$\frac{dF_{\text{NDF}}}{dt} = \frac{d(\pi r^2 L)}{dt} (\rho_{\text{Nb},s} - \rho_{\text{Fe},l}) g \quad (5.28)$$

Assuming that the dissolution takes place in the radial direction only, the cylinder length (L) can be considered as constant, independent of time. This assumption is valid in view of the special precautions which were taken to that effect (see Section 4.2.1). Consequently, equation (5.28) can be written as:

$$\frac{dF_{NDF}}{dt} = \pi L \frac{d(r^2)}{dt} (\rho_{Nb,s} - \rho_{Fe,l}) g$$

or

$$\frac{dF_{NDF}}{dt} = 2\pi L r \frac{dr}{dt} (\rho_{Nb,s} - \rho_{Fe,l}) g \quad (5.29)$$

Equation (5.29) shows how the radial velocity of the dissolving interface varies in relation to the rate at which the net downward force changes, as registered by the load cell.

During the free dissolution period, heat is generated in the vicinity of the dissolving niobium interface; this results from the intermixing of liquid iron with niobium. Mathematically, this has been described by equation (5.26). An effective heat transfer coefficient ( $h_{eff}$ ) has been introduced in order to estimate the heat transfer between the cylinder and the melt (i.e., the outward heat flux,  $q_{out}''$ ). Actually, there is no information available on heat transfer characteristics for problems of this nature or in other words, there is not any correlation in the literature, from which a value for the heat transfer coefficient ( $h_{eff}$ ) could be obtained. However, there is a way that an

approximation can be made. First of all, niobium dissolves slowly in liquid steel and therefore, the rate of change of the cylinder radius ( $dr/dt$ ) which is small, can be considered as a constant at least for the initial stages of the free dissolution. Second, the dissolution rate of niobium in liquid steel is influenced by the fluid flow characteristics of the melt. Higher dissolution rates have been measured with induction stirring than without it (see Section 5.7). Third, at the time the steel shell period terminates and the free dissolution period starts, there cannot be any instantaneous change of the heat transfer coefficient. When a niobium cylinder dissolves in a steel melt without induction stirring, then the dissolution proceeds in an environment where natural convection prevails. There will be some degree of turbulence during the dissolution and as of that, the Nusselt number ( $Nu_D$ ) based on the diameter of the cylinder will be proportional to the Rayleigh number ( $Ra_D$ ) raised to the power of  $1/3$ . A correlation of this type suggests that the effective heat transfer coefficient will be independent of the diameter ( $D$ ) of the dissolving cylindrical specimen. But as it was mentioned previously, the heat transfer coefficient at the beginning of the free dissolution must be equal to the heat transfer coefficient ( $h_0$ ) estimated at the end of the steel shell period using the correlation (5.19) and  $C = 0.17$  (i.e., power off). So, for the free dissolution of a niobium cylinder under conditions of natural convection

in a quiescent (i.e., no inductively stirred) steel bath, the following formula can be used:

$$h_{\text{eff}} = h_0 \quad (5.30)$$

When the dissolution of niobium (or the dissolution of zirconium in general; see next Chapter) takes place in an inductively stirred melt, the equation (5.30) is not valid any more. This is so, because it seems more reasonable that conditions of forced than free convection prevail. For the cylinder in cross-flow, where the flow of a fluid is normal to the axis of the cylinder, the following empirical correlation<sup>103</sup> is important from the standpoint of engineering calculations for heat transfer in forced convection environments:

$$\text{Nu}_D = C_1 \text{Re}_D^m \text{Pr}^{1/3} \quad (5.31)$$

where  $\text{Nu}_D$  ( $= hD/k$ ), the Nusselt number;

$\text{Re}_D$  ( $= U_c D/\nu$ ): the Reynolds number;

Pr: The Prandtl number of the fluid.

$C_1, m$  are constants.

For a specific fluid and for a certain temperature range the Pr number is almost constant and hence, the equation (5.31) can be written as:

$$\text{Nu}_D = C_2 \text{Re}_D^m \quad (5.32)$$

Recently, Churchill and Bernstein<sup>106</sup> have proposed a single comprehensive equation which covers the entire range of  $\text{Re}_D$  for which data are available, as well as a wide range of Pr.

The equation is recommended for all  $Re_D Pr > 0.2$  and has the form:

$$Nu_D = 0.3 + \frac{0.62 Re_D^{1/2} Pr^{1/3}}{[1 + (0.4/Pr)^{2/3}]^{1/4}} \left[ 1 + \left( \frac{Re_D}{282000} \right)^{5/8} \right]^{4/5} \quad (5.33)$$

For liquid steel where  $Pr \approx 0.12$  the equation (5.33) can be used when  $Re_D > (0.2/0.12) = 1.7$ . But for a 2.54 cm diameter cylinder, and a steel melt of a  $7.6 \cdot 10^{-7} \text{ m}^2/\text{sec}$  kinematic viscosity, it takes only a minimum cross-flow velocity of the order of 0.05 mm/sec for this constraint to be satisfied. Minimal natural convection driven forces can develop velocities of this order in liquid steel, although the velocity of the liquid steel in the vicinity of the dissolving cylinder should be of the order of a few centimeters per second. In any case, equation (5.33) can be applied to liquid steel, and the present author used this correlation to deduce a relationship of the form (5.32), for engineering calculations in liquid steel ( $Pr \approx 0.12$ ) only:

$$Nu_D = 0.22 Re_D^{0.52} \quad (5.34)$$

The above correlation gives the same  $Nu_D$  numbers as the equation (5.33) for liquid steel for Reynolds numbers in the range 300 to 15000; least-squares fitting was employed for the determination of its coefficients and the correlation coefficient was found to be 0.999. What is of great importance in equation (5.34), is the power to which the Reynolds number is raised/or in other words, the functional relationship of the  $Nu_D$  number with the  $Re_D$  number. One has

$$Nu_D \propto Re_D^{0.52}$$

or

$$\frac{h_{eff} D}{k} \propto \left( \frac{U_c D}{\nu} \right)^{0.52} \quad (5.35)$$

It is clear from equation (5.35) that the heat transfer coefficient ( $h_{eff}$ ) is related to the cross-flow velocity ( $U_c$ ). During the free dissolution however, the density difference between the dissolving metal and the liquid steel generates motion of the fluid along the cylinder axis and not across it, leaving the cross-flow velocity ( $U_c$ ) almost constant. Therefore, from equation (5.35) one can derive that:

$$h_{eff} \propto D^{-0.48} \quad (5.36)$$

Equation (5.36) clearly states that the effective heat transfer coefficient increases as the free dissolution proceeds. This is a reasonable result since during the free dissolution period mass transfer phenomena appear, and become equally important with the heat transfer ones, so that, the overall convective heat transfer increases due to the cumulative effect of two events. Recalling the fact that the heat transfer coefficient ( $h_0$ ) at the end of the steel shell period should be the same with the heat transfer coefficient at the beginning of the free dissolution period, one finally has:

$$h_{eff} = h_0 \left( \frac{D_0}{D} \right)^{0.48} \quad (5.37)$$

Equation (5.37) can also be used to describe the heat transfer events at the initial stages of the free dissolution

of niobium cylinders, even when natural convection prevails, since the rate of change of the cylinder radius per unit time is small, so that  $D \approx D_0$ , and hence  $h_{\text{eff}} \approx h_0$ , which is in agreement with the equation (5.30).

In Figure 5.13, theoretical predictions based on the model are presented. Curve 1 shows the radius of the cylinder by time, for the experiment presented in Figure 5.7. Two regions are identified: The steel shell period (region A) and the free dissolution period (region B). In region A, the radius of the cylinder is larger than the initial one due to the presence of the shell. In region B, the radius of the cylinder has been estimated from a deduced value of the rate of radius change by time (Equation 5.29), from the segment DE of Curve 2 (Figure 5.7). It is observed that the rate of niobium dissolution in liquid steel is actually small. Curve 2 shows the temperature at the centerline of the cylinder. This temperature increases fast and it finally exceeds that of the steel bath (Curve 4). The same can be observed for Curve 3, which is the temperature of the moving front. During the steel shell period, it represents the temperature at the niobium/solidified shell interface, while in the free dissolution period, it is the temperature of the dissolving front. This temperature finally exceeds the melt temperature, as it is expected, due to the exothermic dissolution. It is worth noticing that the two temperatures (Curve 2 and 3), finally become almost the same. This can

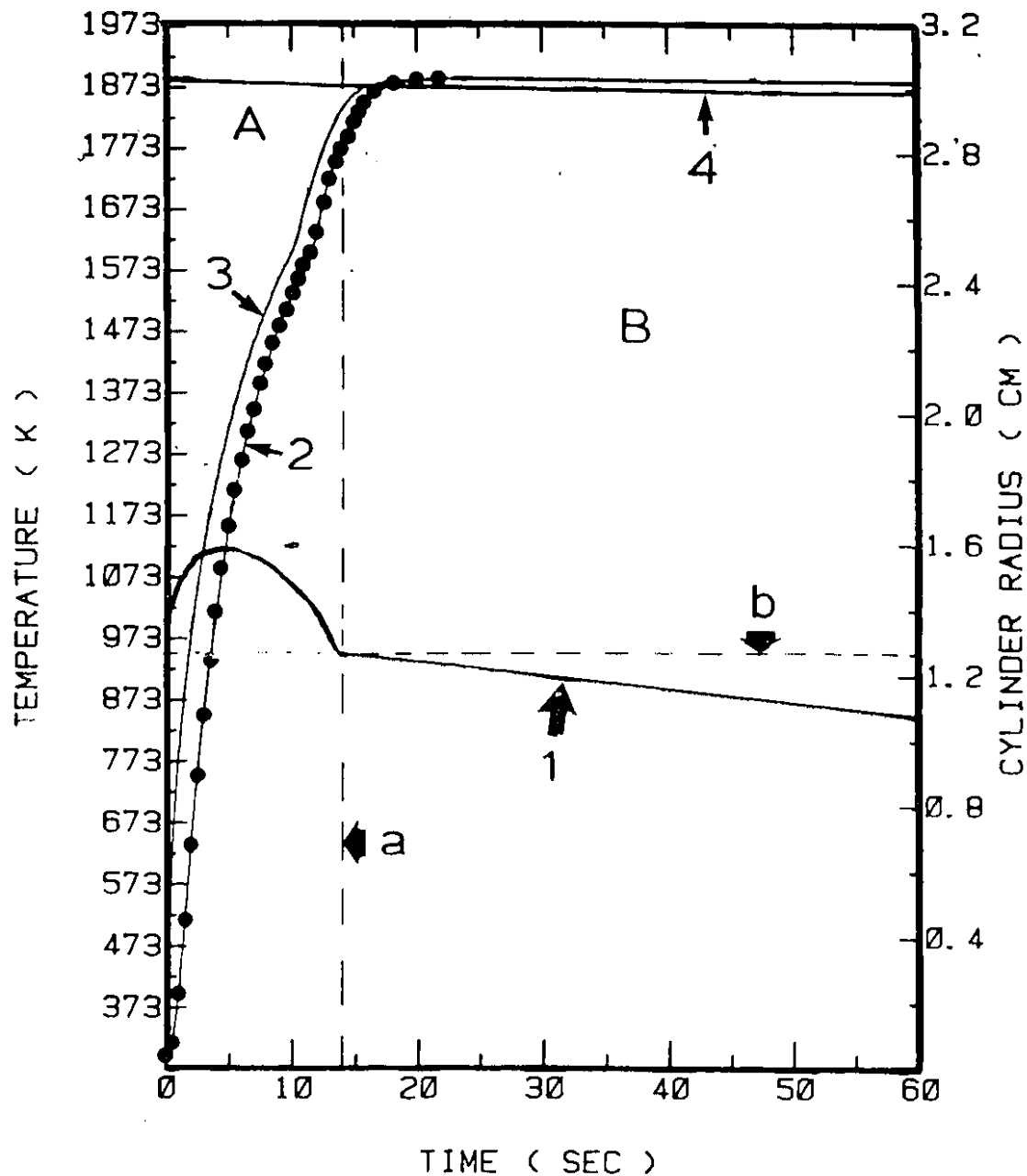


Figure 5.13 Experimental and predicted results from a niobium experiment in liquid steel (see Figure 5.7). The cylinder diameter was 2.54 cm and its length was 18 cm.

- 1) Predicted cylinder radius;
- 2) Measured and predicted centerline temperature;
- 3) Predicted temperature at the niobium/steel interface;
- 4) Measured steel bath temperature.

be explained on the fact that the dissolution speed of niobium in liquid steel is small, and as of that, the generated heat due to the exothermic dissolution is small as well. On the other hand, the thermal conductivity of niobium is large (almost two times the thermal conductivity of zirconium at high temperatures) therefore, the temperature distribution inside the cylinder becomes almost flat or in mathematical terms:

$$k \frac{\partial T}{\partial r} \approx 0 \quad (5.38)$$

From equation (5.26) one then has (because of eqn. 5.38):

$$h_{\text{eff}} (T_I - T_B) \approx Q_v \frac{dr}{dt}$$

or

$$T_I - T_B \approx \frac{Q_v}{h_{\text{eff}}} \frac{dr}{dt} \quad (5.39)$$

For the dissolution of niobium, the right-hand-side part of the equation (5.39) is almost constant. So this formula suggests that the temperature of the dissolving front of a niobium cylinder in liquid steel exceeds the temperature of the melt by a constant value, at least for the initial stages of the free dissolution.

In Figure 5.14, the estimated heat fluxes during the free dissolution of niobium in liquid steel, are presented. Curve 1 represents the inward flux ( $q_{\text{in}}''$ ) while Curve 2 demonstrates the outward flux ( $q_{\text{out}}''$ ). These are computational results as well. It is observed that the inward flux ( $q_{\text{in}}''$ ) decreases appreciably by time to an almost zero value. On

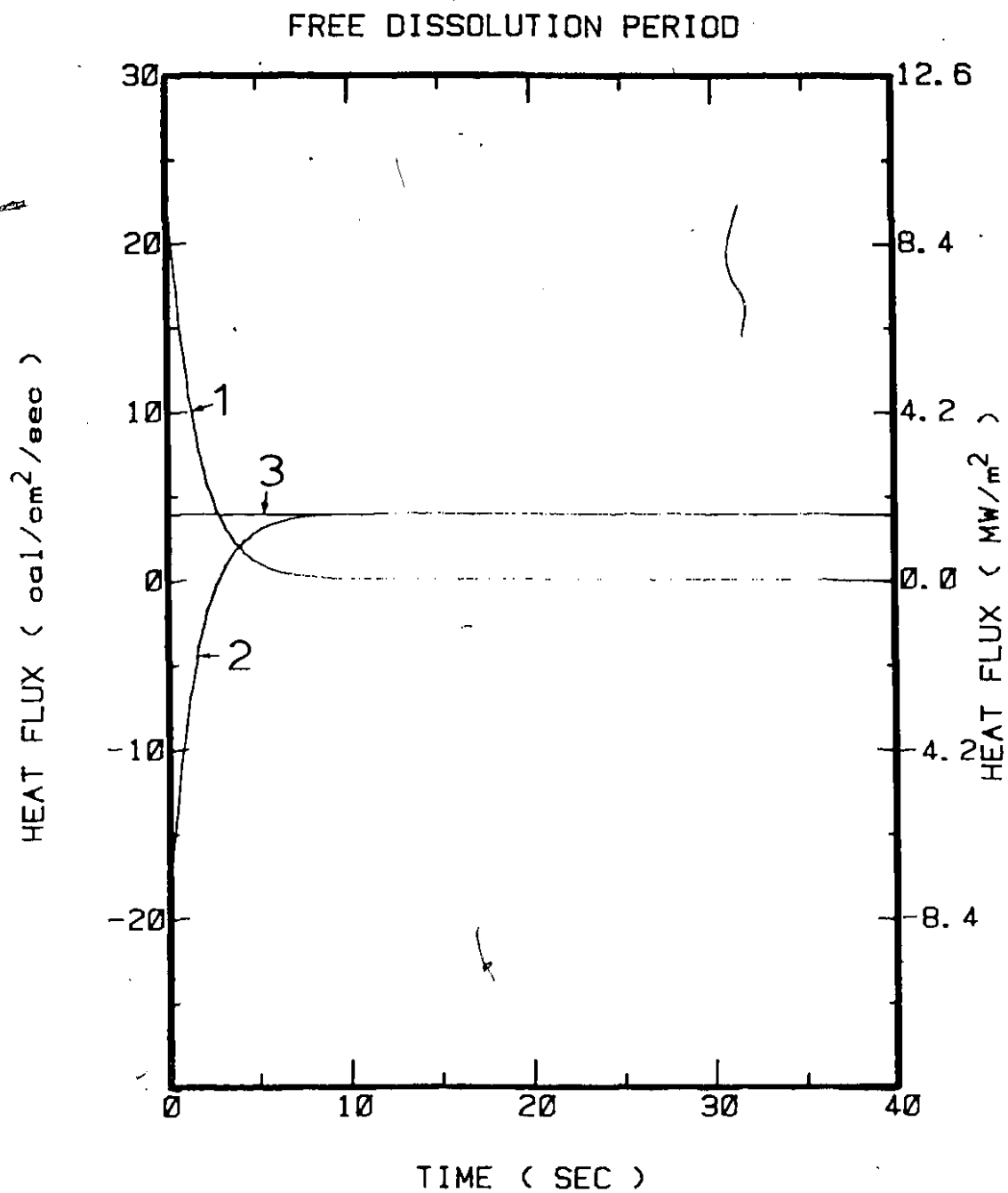


Figure 5.14 Predicted heat fluxes during the free dissolution period.

- 1) The inwards directed heat flux;
- 2) The outwards directed heat flux;
- 3) The generated (total) heat flux.

the other hand, the outward flux ( $q''_{out}$ ) increases appreciably by time, until it attains an almost constant value. Their algebraic sum is the total (generated) heat flux ( $q''_{tot}$ ), presented by Curve 3. This is constant during the free dissolution period of niobium in liquid steel, at least for its initial stage.

#### 5.6 EFFECT OF THE DISSOLVED OXYGEN AND NITROGEN IN THE MELT

With the way the steel bath chemistry was adjusted (Section 4.2.2) the active oxygen level in the melt was less than 10 ppm. The dissolved nitrogen in the melt was determined to be less than 50 ppm (0.005 wt% N). Evans and Pehlke<sup>107</sup> have found that 11.41 wt% Nb can be at equilibrium with 0.209 wt% N at 1600°C (1873 K) in liquid steel without any nitride formation. So, no reaction between the dissolved nitrogen and the dissolving niobium, at this low level of nitrogen, should be expected. In their book, Bodsworth and Bell<sup>108</sup>, suggest that two niobium oxides can form, depending on the niobium concentration in the melt. Niobium forms the spinel  $FeO \cdot Nb_2O_5$ , at low residual concentrations, while the oxide  $NbO_2$  is the product at higher concentrations. Thermodynamic calculations reveal (Appendix IV) that 250 ppm of dissolved oxygen can be at equilibrium with 1.25 wt% Nb in liquid steel, without any further oxide formation. Therefore, at these low levels of oxygen in the steel baths under which the tests were carried out, no interference from the dissolved

oxygen should take place during the dissolution and inter-mixing of niobium with liquid steel.

### 5.7 DISCUSSION

As indicated in previous sections, free dissolution commences once the steel shell period ends. In general, it is expected the free dissolution of niobium cylinders to be controlled by mass transport of dissolved niobium, through a niobium-rich boundary layer adjacent to the cylinder, out into the liquid steel bath. Thus, continuity at the dissolving interface dictates that:

Net moles of niobium lost from cylinder per unit time  
 = Net moles of niobium diffusing into steel bath per  
 unit time, i.e.,

$$-\frac{d}{dt} (\pi r^2 L \rho_{\text{Nb}} / M_{\text{Nb}}) = K_{\text{Nb}} 2\pi r L (C_{\text{Nb}}^{*L} - C_{\text{Nb}}^B) \quad (5.40)$$

where  $r$  : cylinder radius;

$L$  : immersed cylinder length;

$\rho_{\text{Nb}}$  : niobium density;

$M_{\text{Nb}}$  : niobium molecular weight;

$C_{\text{Nb}}^{*L}$  : liquidus concentration of niobium at the  
 temperature of steel bath;

$C_{\text{Nb}}^B$  : bulk concentration of niobium in the steel;

$K_{\text{Nb}}$  : experimental mass transfer coefficient.

Since  $L$ ,  $\rho_{\text{Nb}}$ , and  $M_{\text{Nb}}$  are independent of time and  $C_{\text{Nb}}^B$  is equal to zero, equation (5.40) reduces to:

$$-\frac{dr}{dt} = \frac{K_{Nb} C_{Nb}^{*L}}{\rho_{Nb} / M_{Nb}} \quad (5.41)$$

Based on this expression, an experimental mass transfer coefficient can be estimated.

A general form of the nondimensional correlation for mass transfer with natural convection<sup>111</sup> is expressed in the following relationship from an analogy to heat transfer:

$$Sh = a (Gr_m Sc)^m \quad (5.42)$$

where  $Sh$ ,  $Gr_m$ , and  $Sc$  are Sherwood number, Grashof number, and Schmidt number, respectively, and  $a, m$  are constants. These are some of the characteristic numbers for mass transfer, and more details about them can be found in references 112 and 113. For the study of dissolution of the iron-carbon system under static conditions, Pehlke et al.<sup>37</sup> have demonstrated a quite reasonable approximation with the best fit of the data yielding the equation:

$$Sh = 0.149 (Gr_m Sc)^{0.294} \quad (5.43)$$

Minowa et al.<sup>27</sup> have reported that the relationship could be expressed by the following representation:

$$Sh = 0.11 (Gr_m Sc)^{1/3} \quad (5.44)$$

Furthermore, for other metals<sup>114</sup> (Cu-Pb, Zn-Hg, Sn-Hg, Steel-Zn), the experimental results were treated as follows:

$$Sh = 0.124 (Gr_m Sc)^{1/3} \quad (5.45)$$

Ravoo et al.<sup>115</sup> suggested the following correlation for turbulent free-convection mass transfer around vertical

cylinders and flat plates:

$$Sh = 0.13 (Gr_m Sc)^{1/3} \quad (5.46)$$

On the basis of the results of the present study, in which the product  $(Gr_m Sc)$  is above  $10^{10}$ , and a turbulent boundary layer is formed in the neighbourhood of the solid additive, it is possible to use equation (5.46) to estimate mass transfer coefficients ( $K_m$ ) as follows:

$$K_m = D_m \frac{Sh_L}{L} \quad (5.47)$$

where  $L$  : the immersion length;

$Sh_L$  : the Sherwood number based on the characteristic length  $L$ ;

$D_m$  : the diffusion coefficient of the dissolving metal (i.e., niobium) in liquid steel.

It is worth noting that the equations (5.46) and (5.47) were used very recently by Ishida<sup>116</sup> to predict mass transfer coefficients and compare them with experimental ones, for a dissolution study of solid nickel in liquid tin under static conditions. In Table 5.1, a comparison is demonstrated between experimental and theoretically predicted (eqns. 5.46 and 5.47) mass transfer coefficients during the free dissolution period of niobium in liquid steel, and at different bath temperatures. It can easily be observed that these values are within an order of magnitude close, but the experimental mass transfer coefficients are 1.2 to 1.6 times the predicted ones for the specific temperature range. This can be justified by two reasons: First, niobium dissolves

Table 5.1

Mass Transfer Coefficients during  
niobium free dissolution under  
Static Conditions.

Temperature	Experimental Mass Transfer Coefficient (cm/sec)	Predicted Mass Transfer Coefficient from eqn. (5.46) (cm/sec)
1603 <sup>o</sup> C (1876 K)	0.0055	0.00436
1612 <sup>o</sup> C (1885 K)	0.0059	0.00444
1624 <sup>o</sup> C (1897 K)	0.0065	0.00454
1632 <sup>o</sup> C (1905 K)	0.0071	0.00460
1642 <sup>o</sup> C (1915 K)	0.0074	0.00469
1664 <sup>o</sup> C (1937 K)	0.0077	0.00488

with an exothermic fashion in liquid steel and therefore, larger mass transfer coefficients than the ones predicted by eqn. (5.46) are expected, since the correlation (5.46) is used to describe mass transfer events under natural convection, in the turbulent flow regime, and in the absence of any endothermic or exothermic phenomena. Second, as niobium dissolves slowly in steel and exhibits small values of generated heat due to the exothermic dissolution, the experimental and predicted mass transfer coefficients should be relatively close, and they are indeed! However, the experimental mass transfer coefficients have a greater dependence on temperature than the predicted ones. This may be due to the development of a larger degree of turbulence in the vicinity of the niobium interface, than in the one which is associated with the correlation (5.46).

Values of the dissolution speed (i.e.,  $-dr/dt$ ) of niobium cylinders at various steel bath temperatures, during the initial stages of the free dissolution, were estimated for the 18 different runs and are presented in Table 5.2. Most of these values have been deduced from tests which were carried out under static conditions (Runs 1-13), that is, the power to the induction furnace was turned off (i.e., power off) during the test. Using equation (5.41), mass transfer coefficients were also computed. In order to derive an Arrhenius type of relationship between the deduced mass transfer coefficient under static conditions ( $K_{Nb}^{OFF}$ ) and the absolute temperature ( $T$ ), a regression analysis was performed:

Table 5.2

Experimentally measured  $(-dr/dt)$  and deduced mass transfer coefficients ( $K_{Nb}$ ) during niobium free dissolution under static (Runs 1-13), and dynamic (Runs 14-18) conditions.

Run no.	Temperature		$(-dr/dt) 10^3$ (cm/sec)	$K_{Nb} 10^3$ (cm/sec)
	(°C)	(K)		
1	1603	1876	4.52	5.55
2	1625	1898	5.24	6.44
3	1596	1869	4.49	5.52
4	1606	1879	4.61	5.66
5	1612	1885	4.80	5.90
6	1627	1900	5.40	6.64
7	1632	1905	5.75	7.07
8	1605	1878	4.51	5.54
9	1642	1915	6.09	7.48
10	1646	1919	6.16	7.57
11	1656	1929	5.88	7.22
12	1664	1937	6.27	7.70
13	1624	1897	4.83	6.47
-----				
14	1600	1873	6.02	7.39
15	1613	1886	7.12	8.75
16	1605	1878	6.27	7.71
17	1615	1888	6.98	8.58
18	1630	1903	8.12	9.97

$$\log K_{Nb}^{OFF} = A - \frac{B}{T} \quad (5.48)$$

where  $A = 2.5416 \pm 0.419$

$$B = 8982.4 \pm 795.8$$

with a correlation coefficient 0.959 at 11 degrees of freedom and a standard error of estimate 0.016. The apparent activation energy was estimated to be 41.1 ( $\pm 3.6$ ) kcal/mol or in SI units, 172 ( $\pm 15$ ) kJ/mol. The correlation (5.48) is presented in Figure 5.15 as line 1 along with the experimental values. In the same graph, line 2 correlates mass transfer coefficients as a function of the steel bath temperatures, from a few tests which were carried out under dynamic conditions, that is, the power to the induction furnace was kept on during each test. The straight line 2 (Figure 5.15) was drawn according to the following Arrhenius-type equation, which was the result of a regression analysis based on the experimental results derived under dynamic conditions:

$$\log K_{Nb}^{ON} = A' - \frac{B'}{T} \quad (5.49)$$

where  $A' = 6.24 \pm 0.76$

$$B' = 15674 \pm 1438$$

with a correlation coefficient 0.988 at 3 degrees of freedom and a standard error of estimate 0.021. The apparent activation energy in this case was estimated to be 71.7 ( $\pm 3.3$ ) kcal/mol or, in SI units, 300.0 ( $\pm 13.8$ ) kJ/mol. It is obvious that these values of mass transfer coefficients are 30 to 70 percent larger than the ones presented for static conditions. Therefore, the induction stirring, or in other

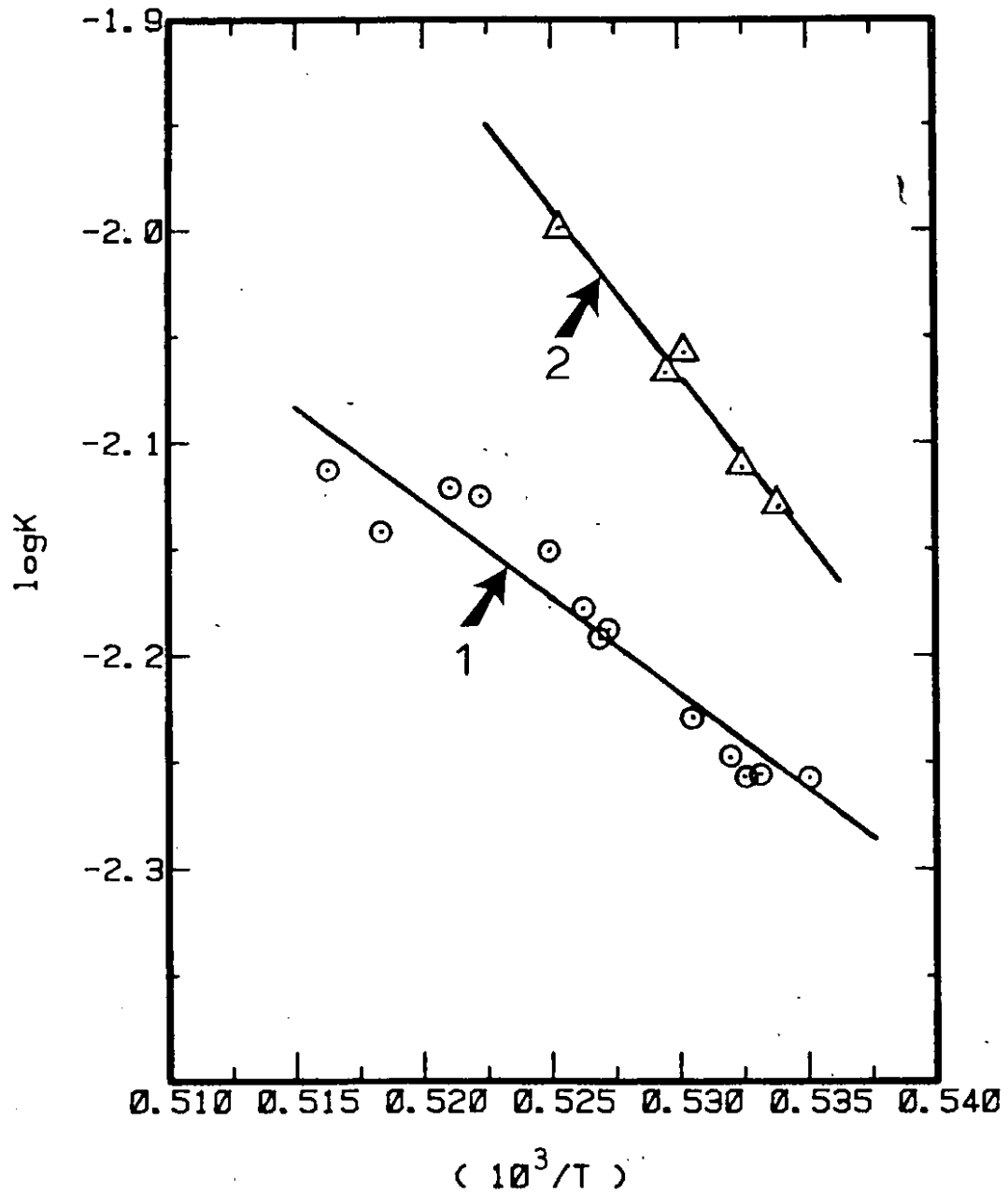


Figure 5.15 Arrhenius-type plot of the experimental mass transfer coefficients.

Mass transfer coefficients deduced from tests which were performed under:  
 1) Static conditions (power off);  
 2) Dynamic conditions (power on).

words, the fluid flow characteristics in the vicinity of the cylinder, have a great effect on the dissolution rate of niobium in liquid steel, and hence, for the experimental conditions under which the tests were carried out, it seems that diffusion through a liquid phase mass-transfer boundary layer was the rate-controlling step.

It should be pointed out once more, that the presented values for the mass transfer coefficients are valid for the early stages of niobium dissolution in liquid steel. At the later stages of niobium dissolution where the mass transfer phenomena take place at smaller radii, or equivalently, at higher curvatures, the dissolution speed and the mass transfer coefficients might be larger. Figures 5.16 and 5.17 show some niobium cylindrical specimens immersed in steel baths at different temperatures, and for various times. One can notice the formation of a 'frustum' on the upper part of the cylinder close to the liquid's free surface. If a niobium cylinder is kept immersed in a steel bath for prolonged times, then the dissolution proceeds faster in the region around the 'frustum', and finally, the cylinder is cut there and settles on the bottom of the crucible. For this reason it is impossible to collect data relevant to the free dissolution period of niobium in liquid steel until its completion.

Nevertheless, assuming that the values for the dissolution speed ( $-dr/dt$ ) presented in Table 5.2, remain approximately

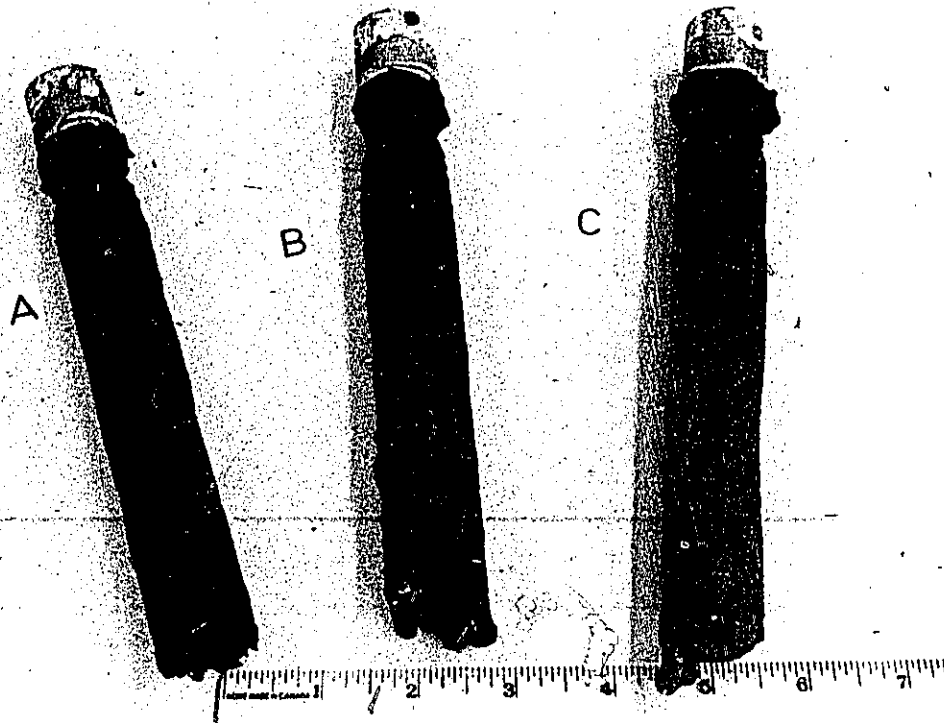


Figure 5.16 Niobium cylindrical specimens after immersion in liquid steel.

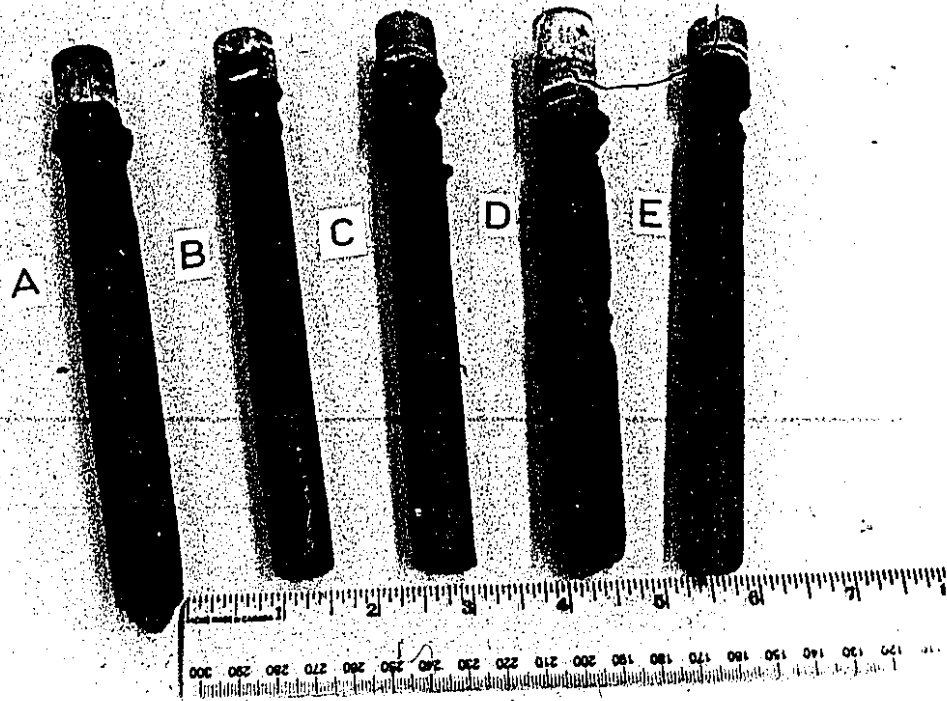


Figure 5.17 Niobium cylindrical specimens after immersion in liquid steel.

constant during the free dissolution period, one can correlate the average value of the dissolution speed at a specific bath temperature, as follows:

$$-\left[\frac{dr}{dt}\right]_{\text{avg}}^{\text{OFF}} = (0.03042 T - 52.486) \cdot 10^{-3} \quad (5.50)$$

where  $-\left[\frac{dr}{dt}\right]_{\text{avg}}^{\text{OFF}}$  = average dissolution speed (cm/sec) under static conditions;  
 $T$  = average steel bath temperature in Kelvin.

The correlation coefficient was found to be 0.947 at 11 degrees of freedom and a standard error of estimated equal to  $0.23 \cdot 10^{-3}$ . In this way, for a given set of experimental conditions, the mathematical model can be used to predict the steel shell period, while the equation (5.50) can be used to predict the free dissolution period. The sum of those two periods represents the total dissolution time. Some results are presented in Figure 5.18.

Similarly, the rate of radius change by time under dynamic conditions was correlated as a function of the bath temperature, and the following statistically significant equation was obtained:

$$-\left[\frac{dr}{dt}\right]_{\text{avg}}^{\text{ON}} = (0.07118 T - 127.316) \cdot 10^{-3} \quad (5.51)$$

where  $-\left[\frac{dr}{dt}\right]_{\text{avg}}^{\text{ON}}$  = average dissolution speed (cm/sec) under dynamic conditions;  
 $T$  = average steel bath temperature in Kelvin.

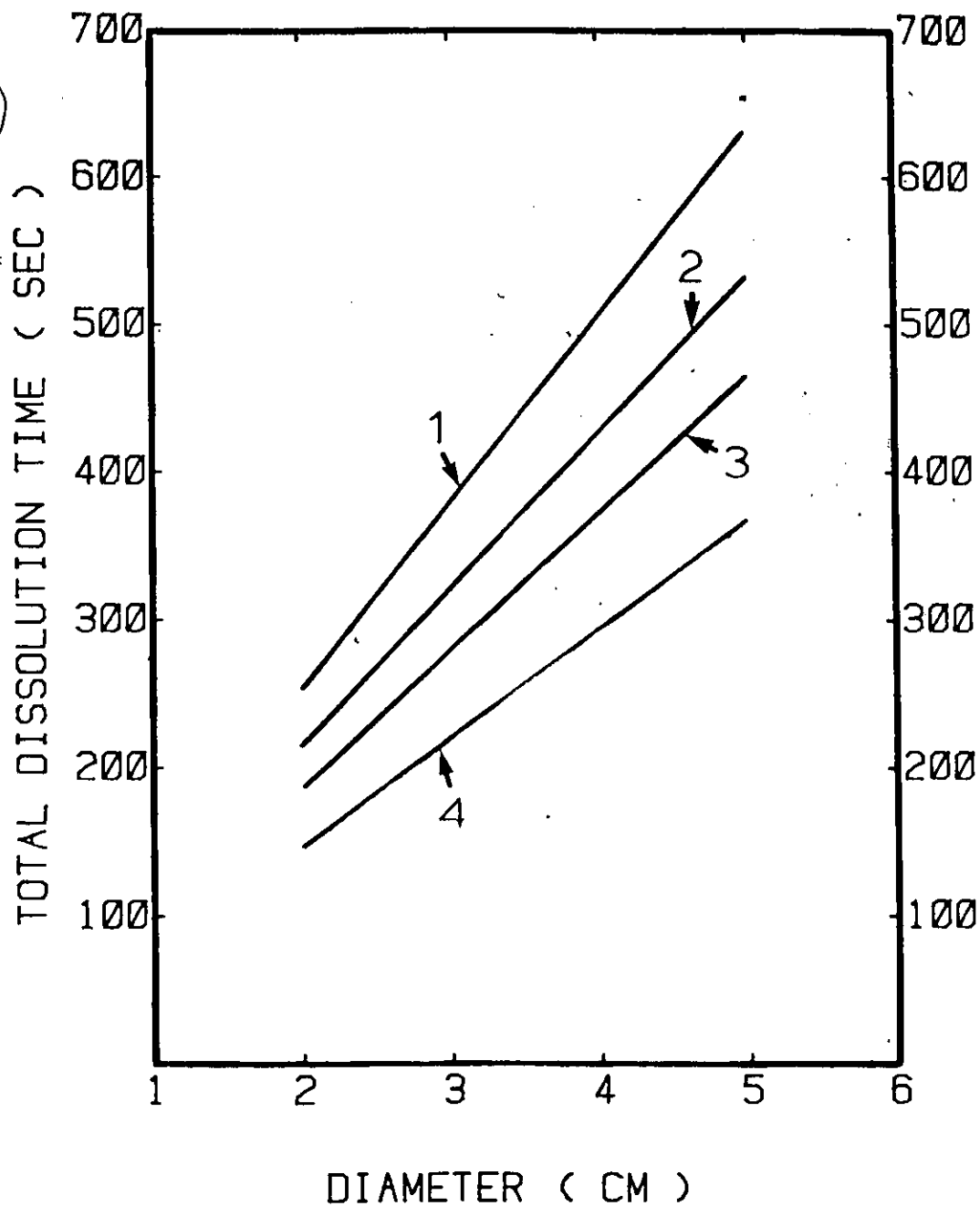


Figure 5.18 Predicted total dissolution times versus diameter for different steel bath temperatures and stirring conditions:

- Static conditions (power off):
- 1) Liquid steel at 1590°C (1863 K);
  - 2) Liquid steel at 1615°C (1888 K);
  - 3) Liquid steel at 1640°C (1913 K).
- Dynamic conditions (power on):
- 4) Liquid steel at 1610°C (1883 K).

The correlation coefficient was found to be 0.99, at 3 degrees of freedom, and a standard error of estimate equal to  $0.134 \cdot 10^{-3}$ . In fact, line 4 (Figure 5.18) has been drawn according to eqn. (5.51) and the values of the steel shell periods predicted by the model.

CHAPTER 66. RESULTS AND DISCUSSION ON THE Zr DISSOLUTION IN  
LIQUID STEEL6.1 INTRODUCTION

In this chapter, the experimental results obtained from the dissolution of zirconium cylinders immersed in liquid steel, are discussed. Three sets of immersion tests were carried out. The first set involved simple dipping experiments in which zirconium cylinders were immersed for different time periods. Except for measuring the steel shell thicknesses, the most important target of this set of tests was to measure the extent of the reaction zone, and identify the possible intermetallic compounds which were formed during the steel shell period. The total number of zirconium cylinders used for this set of experiments was five. The cylinder diameters ranged from 1.905 cm to 2.54 cm. In the second and third set of tests zirconium cylinders were immersed in steel baths and their dissolution was studied in a 'dynamic' way, that is, the cylinder and steel bath temperatures as well as the apparent weight of the dissolving sample were monitored during the dissolution process. The second set of tests is characterized by the dissolution of zirconium cylinders in liquid steel under static conditions (i.e., the power to the induction furnace was shut off during the test; power off), while in the third set, zirconium cylinders were immersed in

inductively stirred steel baths (i.e., power on). Twenty-seven cylinders were used for these two sets. Their diameters were in the range of 1.905 cm to 3.81 cm. For the cylinders with a 2.54 cm diameter only the centerline temperature was measured, while for the cylinders with a 3.81 cm diameter (there were three cylinders of them), temperatures at two locations were measured: one at the centerline, the other at a position close to the edge of the cylinder.

In this chapter, a typical experimental result is analyzed together with model predictions. Two periods are identified, which are analysed in detail. In Appendix II, typical results for the last two sets of immersion tests are presented in graphical form.

## 6.2 REACTION AT THE STEEL SHELL AND Zr INTERFACE

Zirconium is well-known as a reactive metal. The Fe-Zr phase diagram (Figure 3.4) shows several intermetallic compounds which can be formed as reaction products between iron and zirconium. For this reason, from the beginning of this study, there was a suspicion that an exothermic reaction between iron and zirconium should take place during the steel shell period. Preliminary work showed that a reaction started between zirconium and the encasing steel shell during the initial stages of immersion. Figure 6.1 shows a picture of the reaction occurring at the steel shell/zirconium interface.

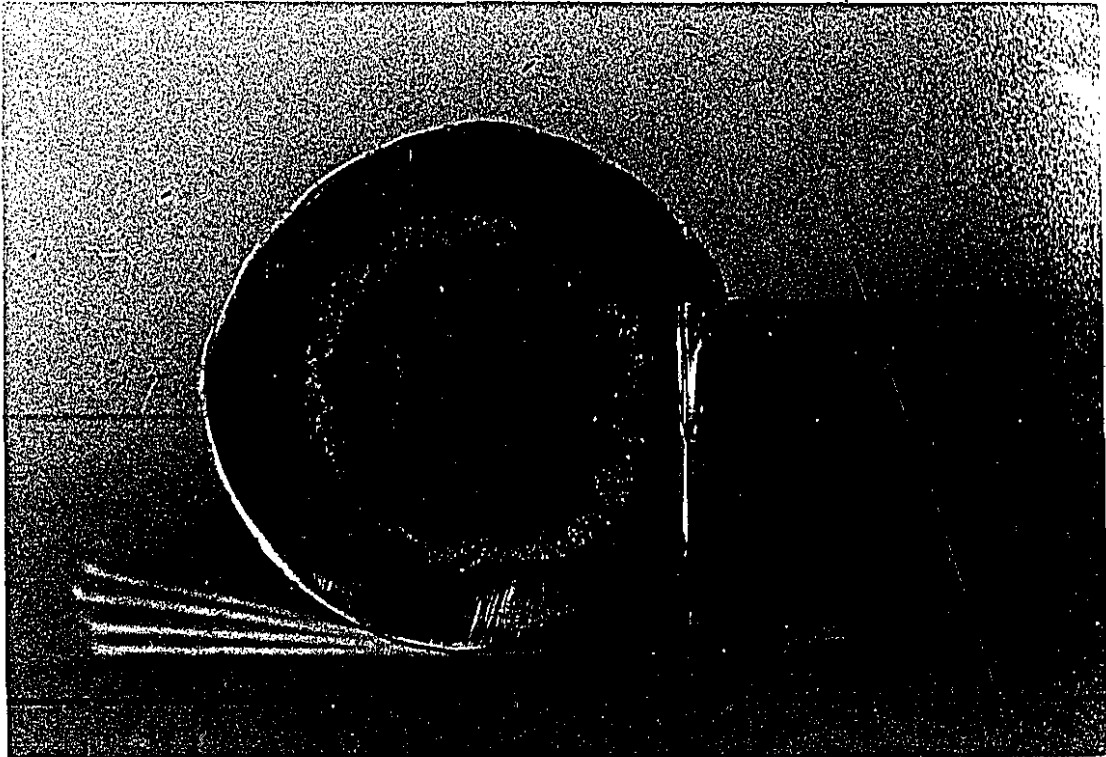


Figure 6.1 Cross-section of a zirconium cylinder (2.54 cm in diameter) after immersion in liquid steel. The arrows mark the original interface.

Composite samples of iron and zirconium were inductively heated. The preparation of these samples is described in Chapter 4. A typical experimental result from this set of tests is given in Figure 6.2A. The Curve shows the temperature at the iron/zirconium interface. This temperature increases fast and at around  $1000^{\circ}\text{C}$  ( $1273\text{ K}$ ) the thermocouple is destroyed as its tip is chemically "attacked" by a liquid formed as a reaction product. The reaction releases so much heat that not only the iron but the zirconium (with a melting point of  $1852^{\circ}\text{C}$  or  $2125\text{ K}$ ) around the interface melts, as well! From this experimental curve (Figure 6.2A), it seems that the exothermic reaction had started around  $1023\text{ K}$ , a value corresponding to the inflexion point A. Another experimental result of this kind is presented in Figure 6.2B. In this case, the temperature around the iron-zirconium interface increases rapidly, and at about  $1300\text{ K}$  the temperature recordings become erratic, because the tip of the thermocouple comes in touch with the liquid reaction product, and as a result, it is completely destroyed after a few seconds. Probably, the reaction had started earlier but the thermocouple registered this event some time later, when the temperature was about  $1300\text{ K}$ . From these two extreme experimental cases, it seems that the starting temperature for the exothermic reaction lies somewhere between  $1023\text{ K}$  and  $1300\text{ K}$ . Zirconium is a very reactive metal, and as of this, intermetallic formation with iron can be initiated even at temperatures

## Fe-Zr comp. sample (35 kW)

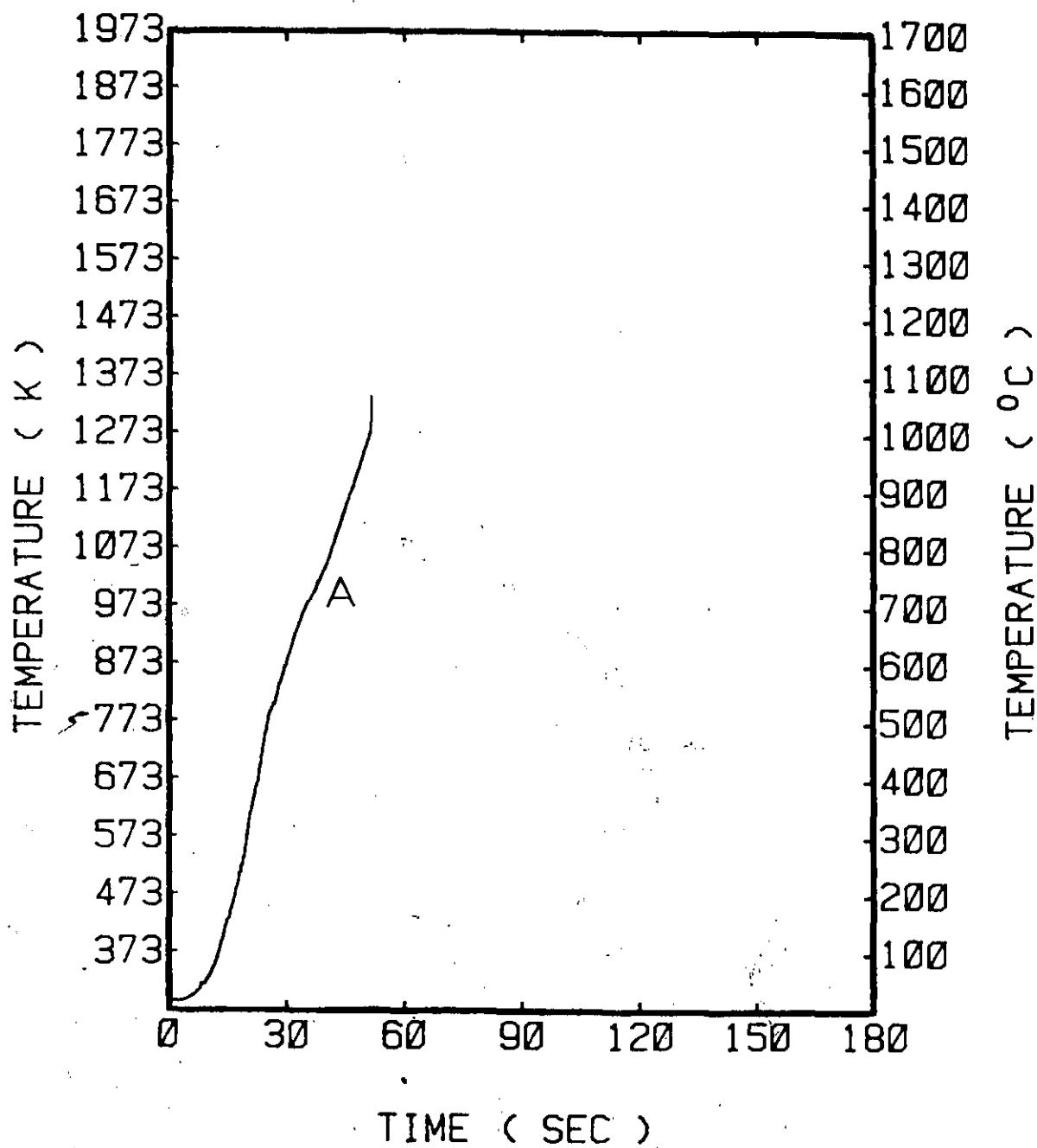


Figure 6.2A Temperature versus time for an inductively heated iron-zirconium composite sample.

## Fe-Zr comp. sample (35 kW)

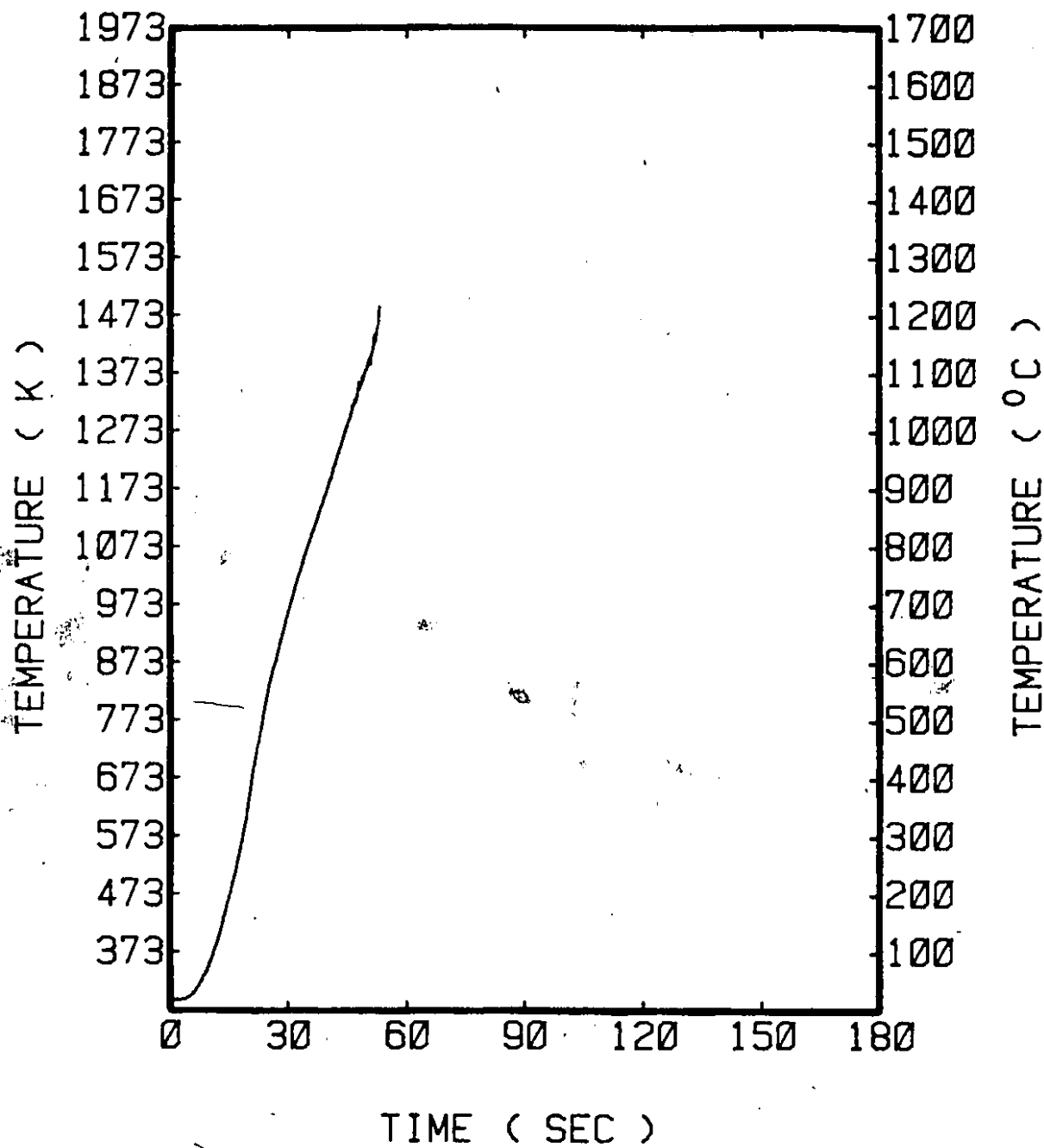


Figure 6.2B Temperature versus time for an inductively heated iron-zirconium composite sample.

as low as 1000 K. This however, is greatly depended upon the physicochemical condition of the interface. For example, the existence of an oxide at the interface can considerably disturb or prevent the reaction process. Regardless, the formation of the liquid product is what really matters, especially in the modelling of the steel shell period of zirconium in liquid steel. From the Fe-Zr phase diagram (Figure 3.4), one can observe that a liquid eutectic can be formed at 1220 K (947°C); this value was selected as the starting reaction temperature. This temperature is in fact between the experimentally determined values, and it is also associated with the formation of a liquid (eutectic) product. The eutectic liquid provides the necessary trigger for the exothermic reaction to proceed even faster. Some material was extracted from the interface after the test, it was ground to a powder form, and then it was examined with the X-Ray diffraction method. The intermetallic compound  $\text{FeZr}_2$  was the only identified compound, but the material was found to be somewhat amorphous; probably the liquid product was not perfectly crystallized.

Figures 6.3A and 6.3B show the cross-section of two zirconium cylinders (2.54 cm in diameter), which had been immersed in quiescent steel baths at 1593°C (1866 K). The cylinder in Figure 6.3A was kept in the melt for 4 seconds, while the cylinder in Figure 6.3B was kept in the melt for 6 seconds. One can notice that the reaction has proceeded

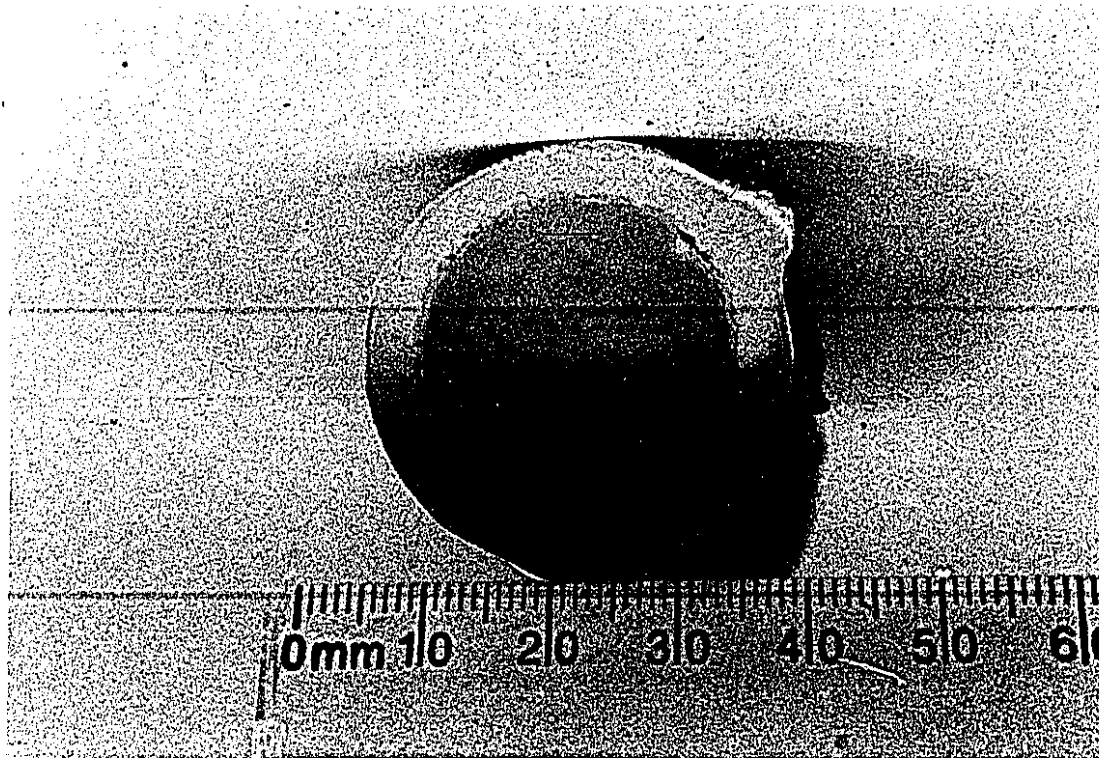


Figure 6.3A Cross-section of a zirconium cylinder (2.54 cm in diameter) after immersion in liquid steel at  $1593^{\circ}\text{C}$  (1866 K) for 4 seconds. The arrows mark the original interface.

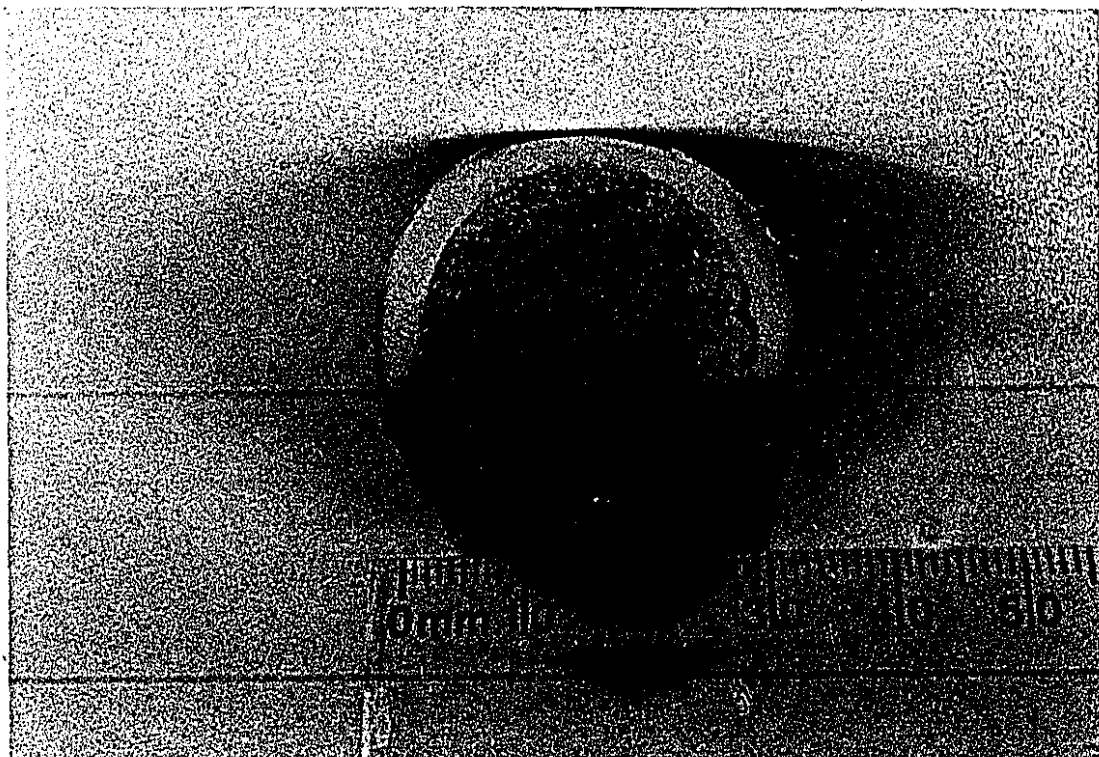
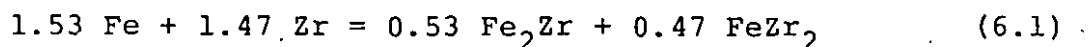


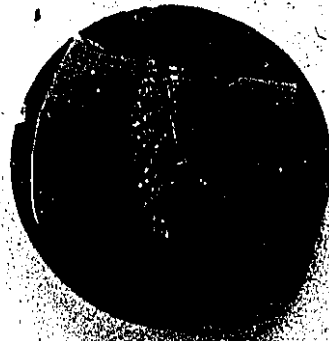
Figure 6.3B Cross-section of a zirconium cylinder (2.54 cm in diameter) after immersion in liquid steel at 1593°C (1866 K) for 6 seconds. The arrows mark the original interface.

more in the second case (Figure 6.3B) than in the first (Figure 6.3A). The model predicted that the reaction should start 2.8 seconds after immersion, with a total steel shell period of 14 seconds.

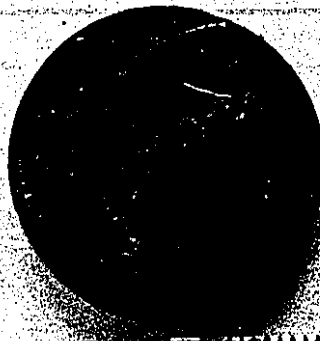
In Figures 6.4A and 6.4B two typical samples, used for Electron Probe X-Ray Microanalysis, are presented. Detailed investigations in the reaction zone revealed that the formation of only two intermetallic compounds took place: the high melting point intermetallic compound  $\text{Fe}_2\text{Zr}$  (or  $\text{Fe}_{0.667}\text{Zr}_{0.333}$ ), and the low melting point one  $\text{FeZr}_2$  (or  $\text{Fe}_{0.333}\text{Zr}_{0.667}$ ). An error analysis was performed on the data obtained from the microprobe analysis, and the following error margins were deduced for the identification of the intermetallics: For both of them the experimental errors for the determination of the iron and zirconium mole fractions were found to be 0.001 and 0.002, respectively. For example, the  $\text{Fe}_{0.333}\text{Zr}_{0.667}$  was identified as a compound  $\text{Fe}_x\text{Zr}_y$  with  $x = 0.333 \pm 0.001$  and  $y = 0.667 \pm 0.002$ . In the reaction zone, the average composition was found to be 49% zirconium-mole-fraction (i.e., corresponding to 61 wt% Zr), and 51% iron-mole-fraction (i.e., corresponding to 39 wt% Fe). In general, the following (overall) reaction is proposed to occur during the steel shell period of zirconium in liquid steel:



The reaction between iron and zirconium happened almost at equimolar concentrations. The intermetallic compound  $\text{FeZr}_2$



A



B



Figure 6.4 A &amp; B

Typical samples including parts of the iron-zirconium interface during the steel shell period, used for Electron Probe X-Ray Microanalysis.

had also been verified with the help of the X-Ray diffraction method, as a product at the reaction zone of the inductively heated composite samples. As it was previously mentioned, this intermetallic has a low melting point (around  $1100^{\circ}\text{C}$  or  $1373\text{ K}$ ) and therefore, it melts congruently a short time after the exothermic reaction has been initiated. It seems that the following steps take place at the steel shell/zirconium interface in relation with the reaction:

- The reaction starts at the eutectic temperature ( $947^{\circ}\text{C}$  or  $1220\text{ K}$ ), and some liquid eutectic forms to accelerate the reaction kinetics.

- Intermetallic compound formation follows and two intermetallic compounds have been identified: the high melting point  $\text{Fe}_2\text{Zr}$ , and the low melting point  $\text{FeZr}_2$ .

- The reaction is exothermic and liquid  $\text{FeZr}_2$  forms, which provides an additional effect for the erosion of the inner surface of the steel shell. When liquid forms, any gap between the inner surface of the solidified steel shell and the outer surface of the zirconium cylinder is filled with liquid, and hence, any contact resistance vanishes. In this way more convective heat is supplied to the cylinder by the melt, some more heat is generated from the exothermic reaction (6.1), and therefore, liquid products form so that the steel shell period dramatically decreases. For example, for the case presented in Figure 6.3 and described above, the model predicted a steel shell period of 18.0 seconds in the absence of any exothermic reaction. More details about

the zirconium's steel shell period in liquid steel will be described in later sections of this chapter. In Appendix III, estimations for the heat of mixing due to reaction (6.1), and mass transfer coefficients during the steel shell period are given.

### 6.3 INTERPRETATION OF DATA FROM THE DISSOLUTION EXPERIMENTS

Figure 6.5 depicts some typical results from the zirconium dissolution experiments. The diameter of the cylinder was 3.81 cm and its length was 20.5 cm. One thermocouple had been placed along the cylinder axis, while a second thermocouple was 1.4 cm apart from the center. Curve 1 of Figure 6.5 shows the bath temperature as registered by the DAPC facility. The data acquisition system started monitoring the dissolution parameters a few seconds prior to immersion of the zirconium cylinder into liquid steel. Curve 2 of the same figure presents the force (i.e., the net downward force) registered by the load cell during the dissolution experiment. During the period AB the load cell registers only the gravitational forces; vibrations are usually recorded as the cylinder is lowered towards the surface of the melt. When the leading edge of the zirconium cylinder touches the surface of the steel bath, the force which the load cell registers starts decreasing. This is due to the increase in the buoyancy forces and is represented in line 2 by the segment BC. The subsequent segment CD in line 2 depicts the steel shell period during which a shell of solid steel

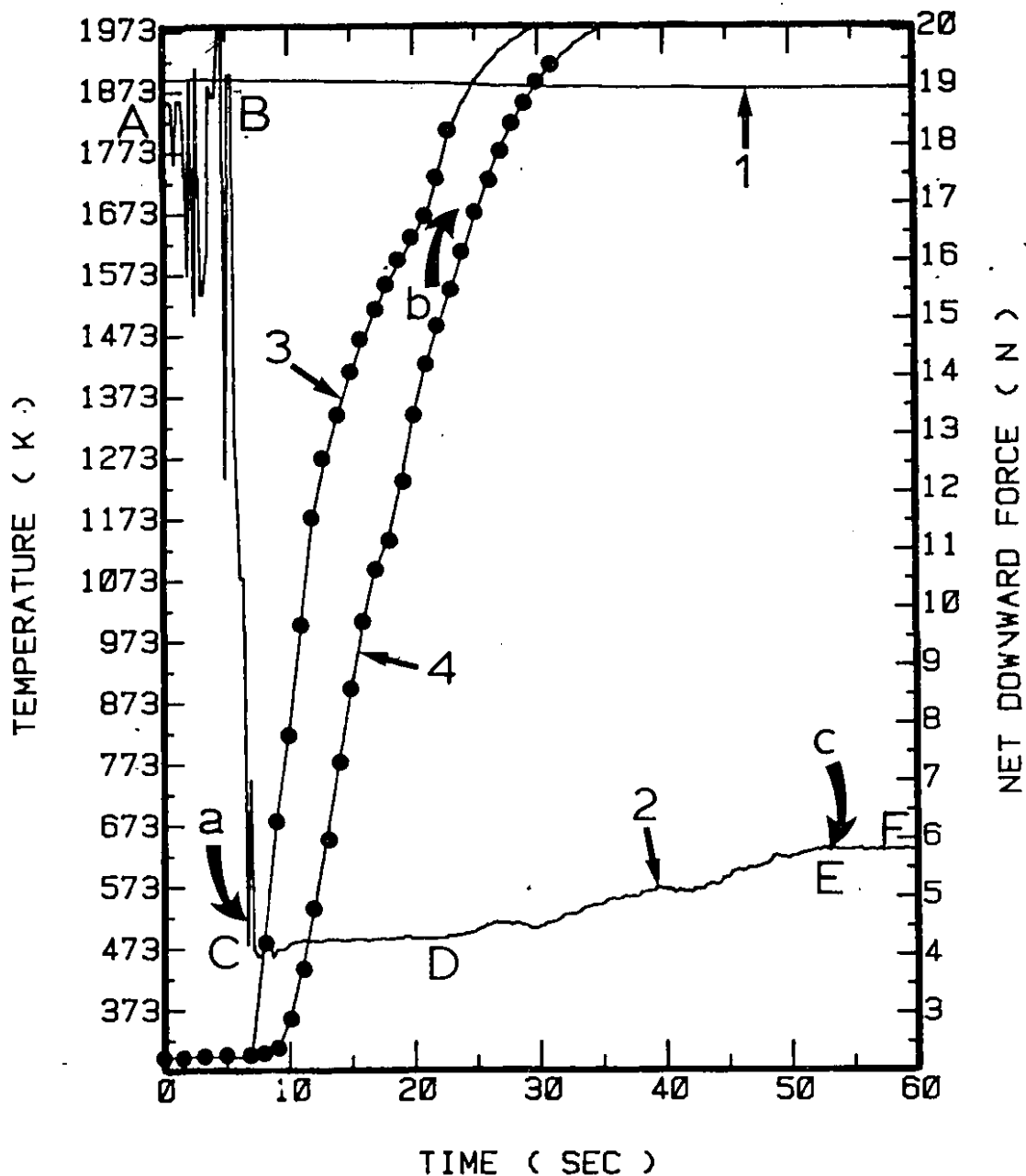


Figure 6.5 Results from a typical zirconium dissolution experiment in liquid steel. The cylinder diameter was 3.81 cm and its length was 20.5 cm.

- 1) Measured steel bath temperature;
- 2) Registered net downward force;
- 3) Measured and predicted temperature at a distance 1.4 cm apart from the center;
- 4) Measured and predicted centerline temperature.

freezes around the cylinder. The force registered by the load cell remains almost constant during this period. This can be attributed to the fact that the expansion of the zirconium cylinder and the freezing of the steel shell tend to compensate each other so that only minor effects appear on the overall force balance, provided they occur simultaneously.

The segment DE of Curve 2, shows the free dissolution period where there is no frozen steel shell period around the zirconium cylinder. During this period, the volume of the zirconium cylinder decreases due to dissolution and consequently, the buoyancy forces also decrease. Equation (5.6) can be written for the zirconium case as follows:

$$\frac{dF_{NDF}}{dt} = \frac{dv_{imm}}{dt} (\rho_{Zr,s} - \rho_{Fe,l}) g \quad (6.2)$$

where now, the density of niobium ( $\rho_{Nb,s}$ ) has been substituted by the zirconium density ( $\rho_{Zr,s}$ ). The density of zirconium at elevated temperatures is smaller than the density of liquid steel so, the density difference ( $\rho_{Zr,s} - \rho_{Fe,l}$ ) is less than zero; the rate of the change of the volume of the dissolving zirconium cylinder is also a negative number. Therefore, the rate of the change of the net downward force increases during the free dissolution (segment DE). At the point E the immersed portion of the zirconium cylinder has been dissolved completely in the melt. The point E signifies the end of the free dissolution, therefore not any interesting phenomena are recorded during the period from E to F.

Curves 3 and 4 of the Figure 6.5, show predicted and experimental temperatures in the interior of the zirconium cylinder. The solid lines represent predictions, while the points show the measured temperatures. Curve 4 depicts the temperature at the cylinder's axis while Curve 3 shows the temperature at a distance 1.4 cm apart. Time zero for the cylinder's temperatures is taken the time corresponding to point C, where the cylinder has just been completely immersed in the steel bath.

Referring to Figure 6.5, the centerline temperature (Curve 4) increases rapidly up to the 17th second of immersion. A reduction in the rate of the temperature rise then follows up to the 19th second. The cause for this slowed ascent can be explained in terms of the endothermic transformation of  $\alpha$ -Zr to  $\beta$ -Zr. This occurs at a temperature of  $863^{\circ}\text{C}$  (1136 K). As demonstrated, there is a good agreement between experimental and predicted temperatures. Unfortunately, the two thermocouples were destroyed before the completion of the test. Specifically, the thermocouple which was placed close to the edge of the cylinder (i.e., 1.4 cm from the center) was destroyed around the end of the steel shell period. It is important to note however, that there is a change in the slope of the temperature at this point (Curve 3), fact which reveals the exothermic behaviour of the mixing of iron and zirconium in the reaction zone during the steel shell period. The thermocouple which was placed along the centerline of the cylinder lasted somewhat longer, until the initial

stages of the free dissolution. However, the most important aspect of the experimental values of the temperature distribution inside the zirconium cylinder is that they seem to increase so much, that finally they become greater than the temperature of the liquid steel. In fact, computational work suggests that the temperature of the cylinder approaches the melting point of zirconium, during the final stages of the free dissolution. In a later section, this topic will be discussed in a more detailed manner. Another event should be pointed out: in Figure 6.5 the bath temperature (Curve 1) initially drops with a certain rate due to the immersion of the relatively "cool" zirconium cylinder and the turning off of the induction furnace during the test. As the dissolution of the zirconium cylinder proceeds however, the temperature of the melt remains almost constant. This fact means that the heat losses from the melt are balanced by the heat liberated during the mixing of the dissolving zirconium and the liquid steel. Curve 1 of Figure 6.6 illustrates that the temperature of the melt increases towards the final stages of the free dissolution. This can be attributed to the fact, that this test was performed with induction heating (i.e., power on), and as of that, the exothermic heat released, exceeded the heat losses from the melt to the environment, and therefore, the bath temperature increased. The immersed zirconium cylinder had the same dimensions with the one mentioned previously, and depicted by the Figure 6.5.

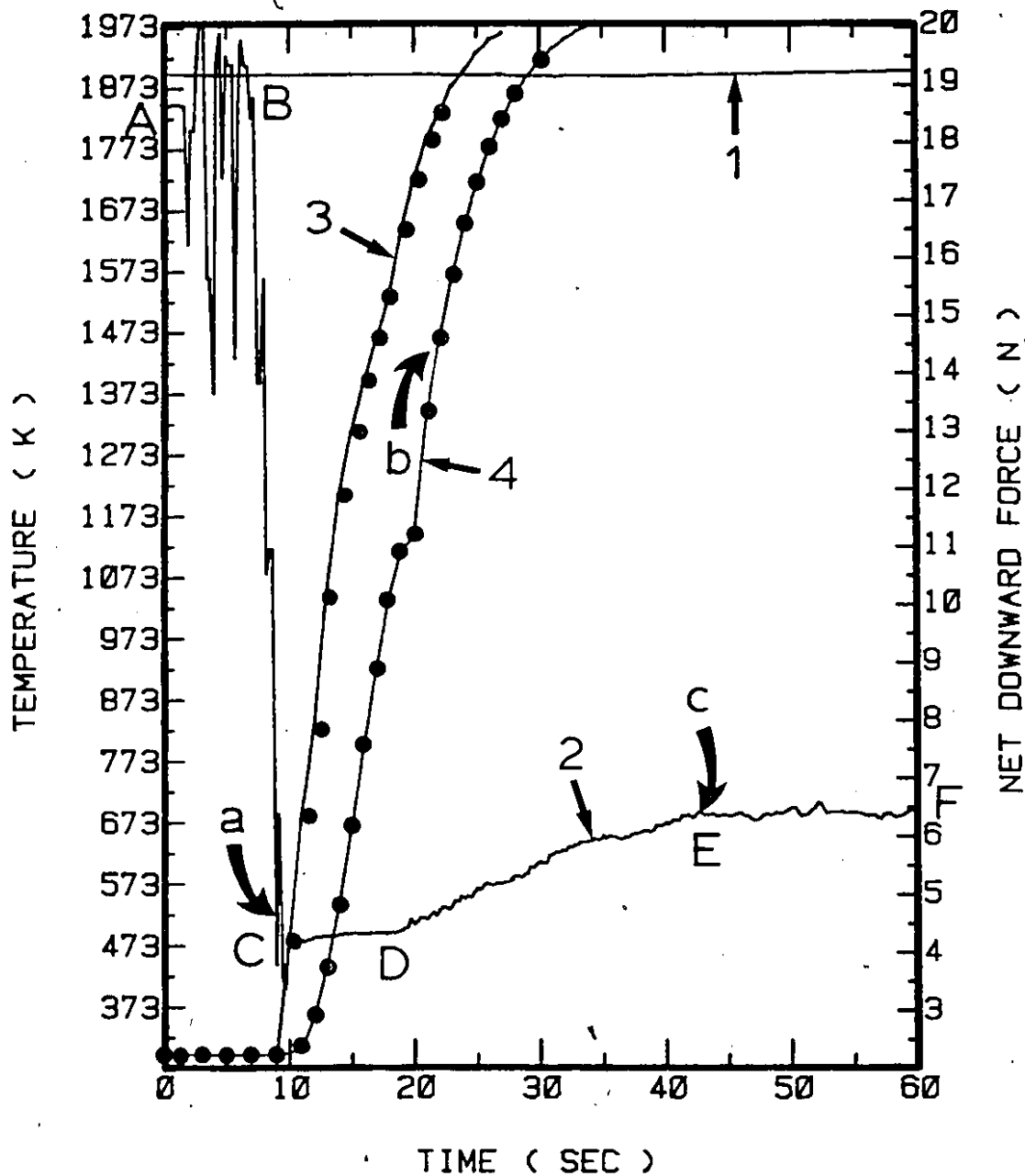


Figure 6.6 Results from a typical zirconium dissolution experiment in liquid steel. The cylinder diameter was 3.81 cm and its length was 20.5 cm.

- 1) Measured steel bath temperature;
- 2) Registered net downward force;
- 3) Measured and predicted temperature at a distance 1.4 cm apart from the center;
- 4) Measured and predicted centerline temperature.

As in the case of niobium, the dissolution of zirconium in liquid steel involves two distinct periods. The steel shell period and the free dissolution period. Referring to Figure 6.5, the time coordinate of the curved arrow tips (a,b) show where each one of the above periods start. The steel shell period lies between a and b while the free dissolution period starts at b and ends at c. In the next sections of this chapter, these periods are analyzed in more detail.

#### 6.4 APPLICATION OF THE MATHEMATICAL MODEL

In this section, some predictions will be presented based on the semi-empirical heat and mass transfer model which has been described mathematically in the Section 5.5. The predictions concern the estimation of the internal heat generation during the steel shell period, and the inwards directed heat flux during the free dissolution period.

##### 6.4.1 Steel Shell Period

In order to estimate the heat generation due to the reaction in the steel shell period, it was decided that the phenomenon of the exothermic heat release should best be reported as an interfacial heat flux,  $q_s''$  (Eqn. 5.16, B.C.2B):

$$q_s'' = N_s'' \Delta H_R \quad (6.3)$$

where,  $N_s''$  is the corresponding molar flux of zirconium to the inner steel shell interface;

$\Delta H_R$  is the heat released/mole of zirconium.

The same formalism had been followed by Argyropoulos and Guthrie<sup>60</sup> for the modelling of the steel shell period of titanium in liquid steel. The exothermic reaction between dissolved zirconium and the steel shell was expected to take place in a thin mass transfer boundary layer adjacent to the internal part of the shell. In the computational procedure, an empirically determined heat generation term ( $\dot{q}_s$ ) was applied to the volume element adjacent to the initial shell at  $r_1$  (Figure 5.9). The following formula relates the interfacial heat flux  $q_s''$  with the heat generation term  $\dot{q}_s$ :

$$\delta\dot{Q} = \dot{q}_s \delta V = q_s'' \delta A \quad (6.4)$$

where  $\delta A$  and  $\delta V$  represent elemental areas and volumes in the numerical scheme, and  $\delta\dot{Q}$  is the rate of heat release within the elemental volume adjacent to the steel shell.

Figure 6.7 shows experimental temperature-time data (points) for a 2.54 cm diameter cylinder placed in a bath of 1603°C (1876 K) without induction heating (power off). These may be compared with the continuous curve 1, predicted for conditions of zero heat generation. The arrow a denotes the time at which the encasing steel shell is predicted to have entirely melted back to expose solid zirconium. Curve 2 denotes experimental results and model predictions, considering the rate of internal heat generation equal to 9 cal/cm<sup>2</sup>/sec (0.376 MW/m<sup>2</sup>). Arrow b shows the time at which the steel shell period is predicted to end, and marks the start of the

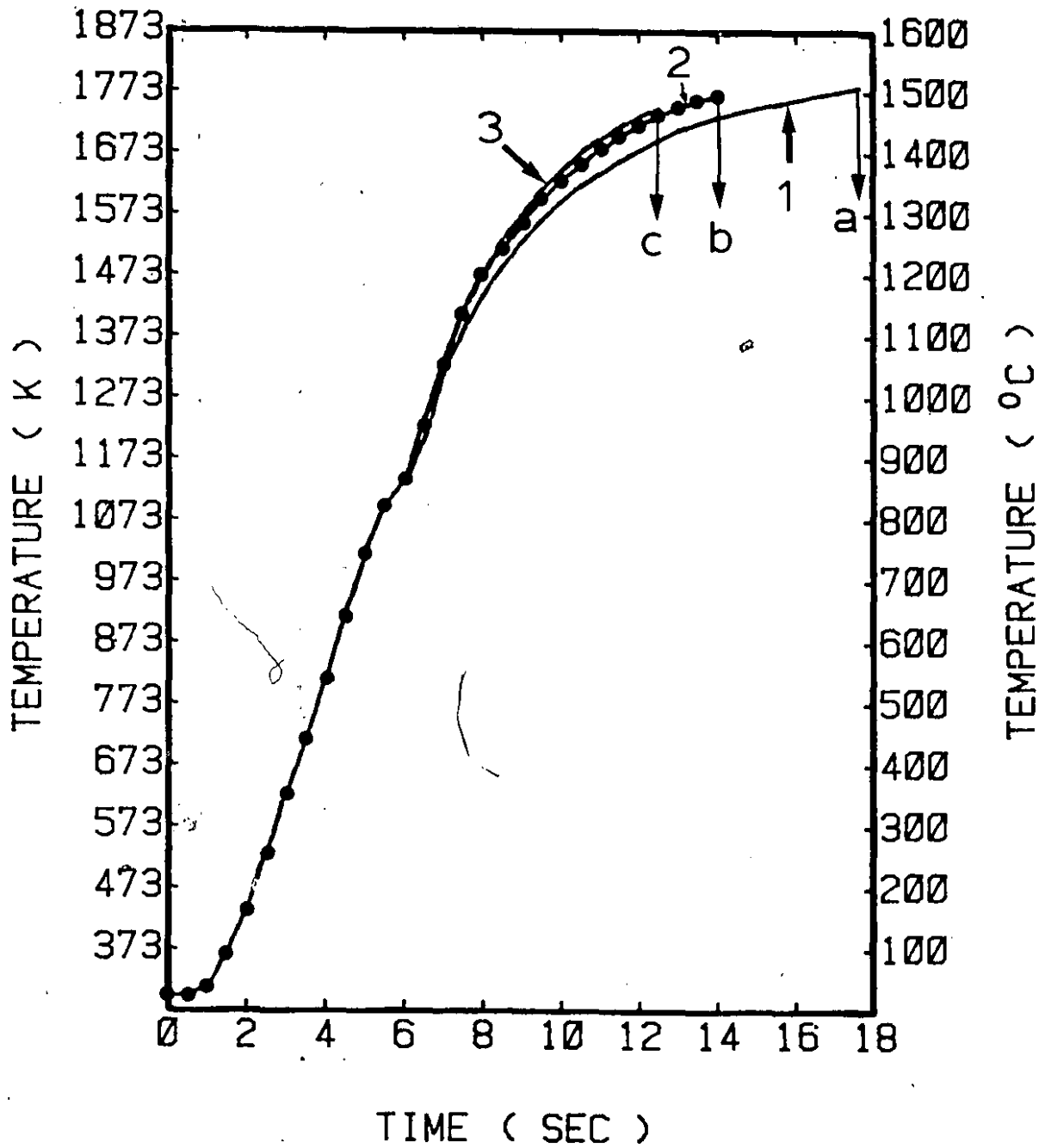
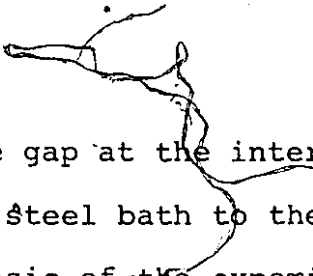


Figure 6.7 Measured and predicted temperatures in a 2.54-cm-diameter zirconium cylinder.

free dissolution period. Curve 3 presents model predictions considering the rate of the internal heat generation equal to  $10 \text{ cal/cm}^2/\text{sec}$  ( $0.418 \text{ MW/m}^2$ ). Again, the arrow points out the end of the steel shell period. The results of ten cylinders were analyzed in the same way. The rate of heat generation thus deduced, varied from  $8.6 \text{ cal/cm}^2/\text{sec}$  ( $0.36 \text{ MW/m}^2$ ) to  $12.9 \text{ cal/cm}^2/\text{sec}$  ( $0.54 \text{ MW/m}^2$ ). From these values, an effective mass transfer coefficient for zirconium could be obtained. The procedures used for this kind of estimations are described in Appendix III. In this manner, the estimated mass transfer coefficient for zirconium in the steel shell period ranged from  $0.046 \text{ cm/sec}$  to  $0.069 \text{ cm/sec}$ . Similarly, the estimated mass transfer coefficient for iron in the steel shell period ranged from  $0.013 \text{ cm/sec}$  to  $0.019 \text{ cm/sec}$ . It should be noted that the heat generation term is introduced in the computational scheme, only when the interface of zirconium/steel shell has reached the starting temperature of the reaction, which was selected to be  $947^\circ\text{C}$  ( $1220 \text{ K}$ ). For the computations involved in the steel shell period, the interfacial thermal resistance was chosen to be  $8 \text{ cm}^2\text{sec}^\circ\text{C/cal}$  ( $.1912 \text{ m}^2\text{K/kW}$ ). This value is not an arbitrarily selected constant, but a value which was estimated on the basis of previous work on this subject<sup>105,117</sup>. Once the reaction temperature is reached however, the interfacial thermal resistance becomes zero (Eqn. 5.16, B.C.2B). This is so, because liquid eutectic is expected to form which



fills the gap at the interface. The convective heat flux from the steel bath to the zirconium cylinder was determined on the basis of the experimental dimensionless correlation given by equation (5.19).

Figures 6.8A and 6.8B show two zirconium cylinders 2.54 cm in diameter, which were immersed in liquid steel at 1593°C (1866 K) for 4 seconds (Figure 6.8A), and for 6 seconds (Figure 6.8B). Cross-sections of these two cylinders have already been presented (see the Figures 6.3A and 6.3B). One can notice how much the reaction has proceeded for the second cylinder (i.e., the one immersed for 6 seconds). Immersion of another zirconium cylinder at the same bath temperature for longer periods was not attempted, as it was expected that the steel shell might break and slip off during withdrawal. For those two cylinders the shell thicknesses and the reaction zones were measured. Experimental and predicted results are shown in Figure 6.9. Line 1 shows how the outer radius of the cylinder changed with time. Line 2 depicts the initial radius of the cylinder. The dashed lines 3 and 4 present the predicted extent of the internal exothermic dissolution reaction, and give the location of the steel shell and the zirconium interfaces, respectively. Predictions from the model reveal that the reaction was expected to start 2.8 seconds after immersion. Based on the stoichiometry of the reaction (Eqn. 6.1) and the measured thicknesses of the reaction zones, the extent of

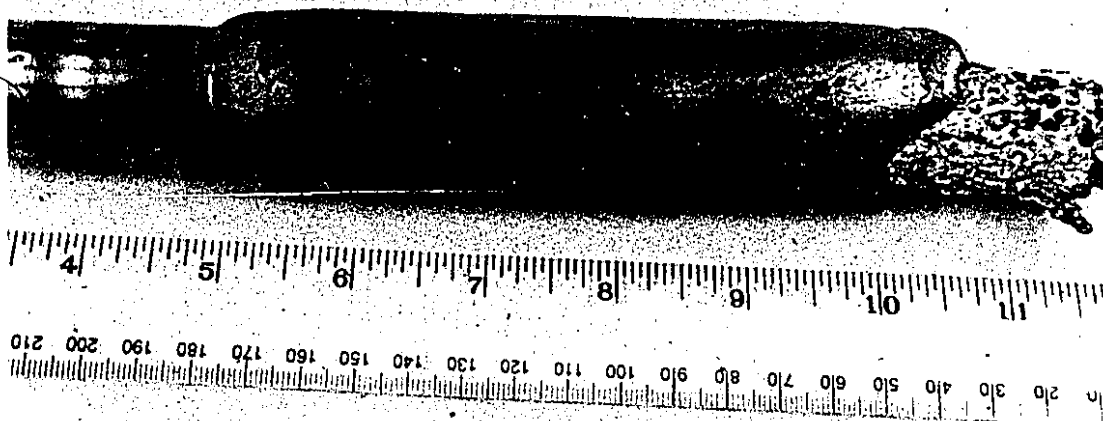
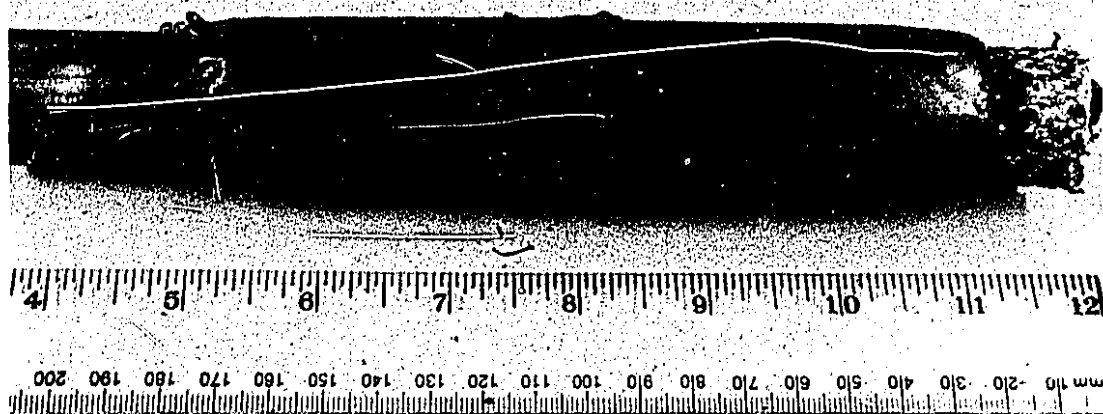


Figure 6.8 A & B Two zirconium cylinders (2.54 cm in diameter) after immersion in liquid steel at  $1593^{\circ}\text{C}$  (1866 K) for 4 seconds (A), and 6 seconds (B).

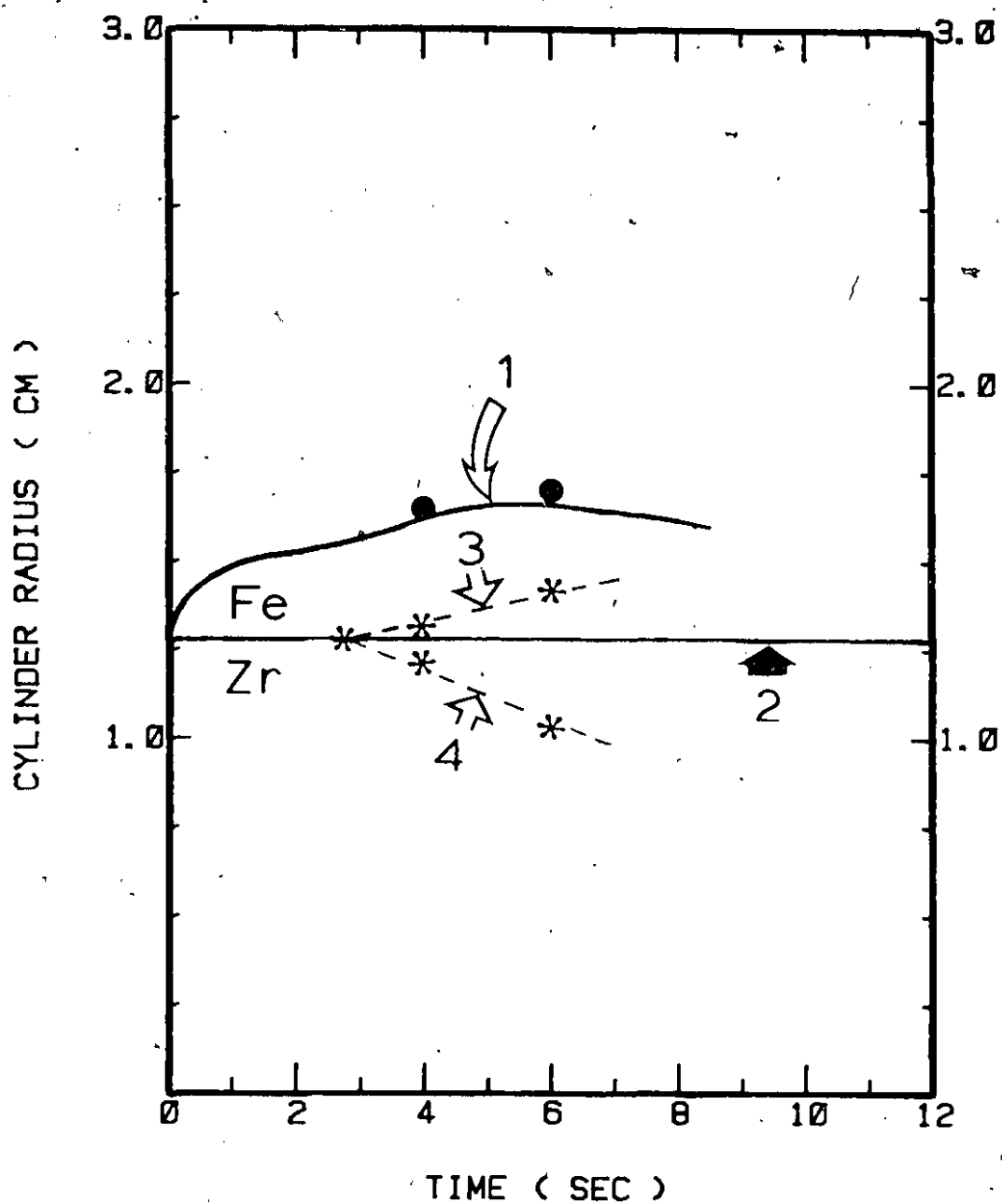


Figure 6.9 Experimental and predicted results for the zirconium cylinders shown in Fig. 6.8A and B.

- 1) Predicted radius;
- 2) Initial radius;
- 3) Measured and predicted extent of the reaction at the steel shell;
- 4) Measured and predicted extent of the reaction at the zirconium.

the erosion of the steel shell and the zirconium cylinder was determined. It seems that the extent of the erosion of the zirconium cylinder was larger than the one of the steel shell, fact which is in agreement with the deduced larger values for the mass transfer coefficient of zirconium with respect to iron (Appendix III). The good agreement between the experimental and the predicted results reveals that the determination of the heat generation during the steel shell period, although semi-empirical, gives consistent results.

#### 6.4.2 Free Dissolution Period

In the previous section, a way to compute the radius of a zirconium cylinder immersed in liquid steel during the steel shell period was described. In this section, the radius of a zirconium cylinder during the free dissolution period will be estimated. One could solve this problem directly from the experimental results with the application of equation (5.29), in this case for zirconium. However, another method was employed here, which may imply a more fundamental insight in the free dissolution of zirconium in liquid steel. Referring to Figure 6.5 and 6.6 (and the Figures in Appendix II), it can be noticed that in the free dissolution period of zirconium in liquid steel (segment DE), the rate of change of the net downward force is almost constant, or in other words, the net downward force is approximately a linear

function of time. One might wonder why that could be so, but a least-squares fitting of the experimental results, for the segment DE (illustrated in Figures 6.5 and 6.6), resulted in a first degree polynomial with a correlation coefficient around 0.988. This is of great importance, as it can be used in the estimation of the rate of change of the radius of the cylinder. Mathematically, this can be described as follows: From equation (6.2) one has

$$\frac{dF_{NDF}}{dt} = \frac{dV_{imm}}{dt} (\rho_{Zr,S} - \rho_{Fe,l}) q = \text{Constant}$$

or

$$\frac{dV_{imm}}{dt} = \text{Constant}$$

or

$$\frac{d}{dt} (\pi r^2 L_{imm}) = \text{Constant}$$

or assuming only radial dissolution  $2\pi r L_{imm} \frac{dr}{dt} = \text{Constant}$

and finally:

$$-\frac{dr}{dt} = \frac{C_1}{r} \quad (6.3)$$

Equation (6.3) is a very important one as it introduces the aspect of "acceleration" in the dissolution process. In fact it explicitly declares that the dissolution speed increases during the free dissolution period of zirconium in liquid steel. In this manner, it becomes very large during the final stages of the free dissolution where  $r \rightarrow 0$ . This equation was introduced in the model in order to compute the radius of the cylinder during the free dissolution period.

The effective heat transfer coefficient given by equation (5.37) was used to estimate the convective heat transfer between the dissolving cylinder and the bath. Using also the general equations of the model (described in Section 5.5.2), the temperature distribution inside the zirconium cylinder was computed. Figures 6.10 and 6.11 present these estimations for the experimental cases presented in Figures 6.5 and 6.6, respectively. Line a divides the diagram in two regions: A, the steel shell period and B, the free dissolution period. Line b shows the initial radius of the cylinder. Curve 1 depicts the radius of the zirconium cylinder. In region A, it is the shell that makes the radius larger than the initial one. In region B, the radius decreases and the acceleration phenomena become more pronounced, during the final stages of the free dissolution. Curve 2 is the centerline temperature of the cylinder, while Curve 3 is the temperature of the cylinder half nodal-point distance from the steel shell/zirconium interface (region A), or the liquid steel/zirconium interface (region B). It is quite interesting, that both temperatures approach the melting point of zirconium during the final stages of the free dissolution. This is due to the exothermic manner by which the dissolution proceeds. As it has been described in Section 3.5.3 the partial molar heat of mixing of Zr at infinite dilution in liquid iron is  $-82.634$  kJ/mol atoms or  $-19.75$  kcal/gr-atom. This is a relatively high value (i.e., in absolute value), and the

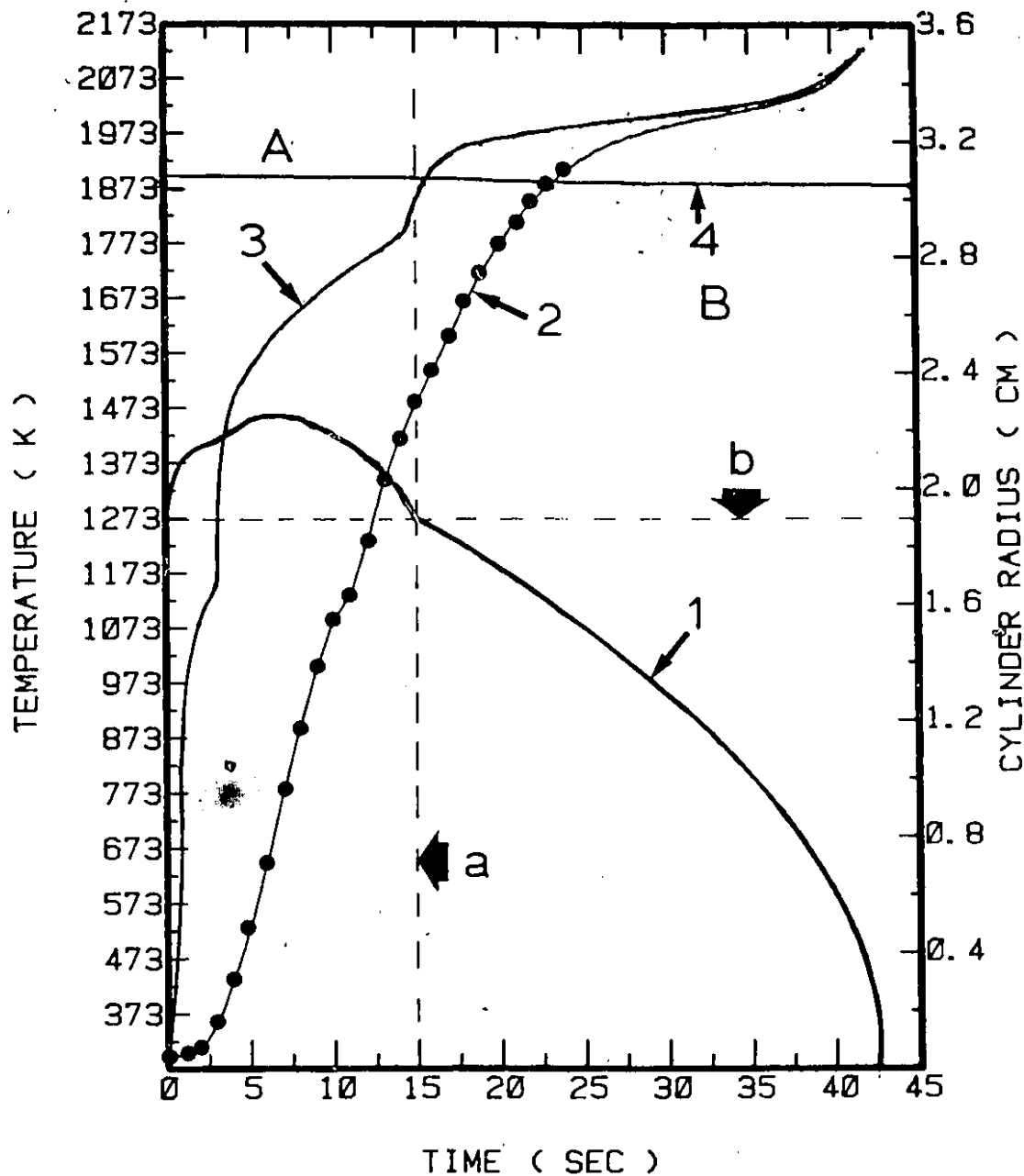


Figure 6.10 Experimental and predicted results from a zirconium experiment in liquid steel (see Fig. 6.5). The cylinder diameter was 3.81 cm and its length was 20.5 cm.

- 1) Predicted cylinder radius;
- 2) Measured and predicted centerline temperature;
- 3) Predicted temperature at the zirconium/steel interface;
- 4) Measured steel bath temperature.

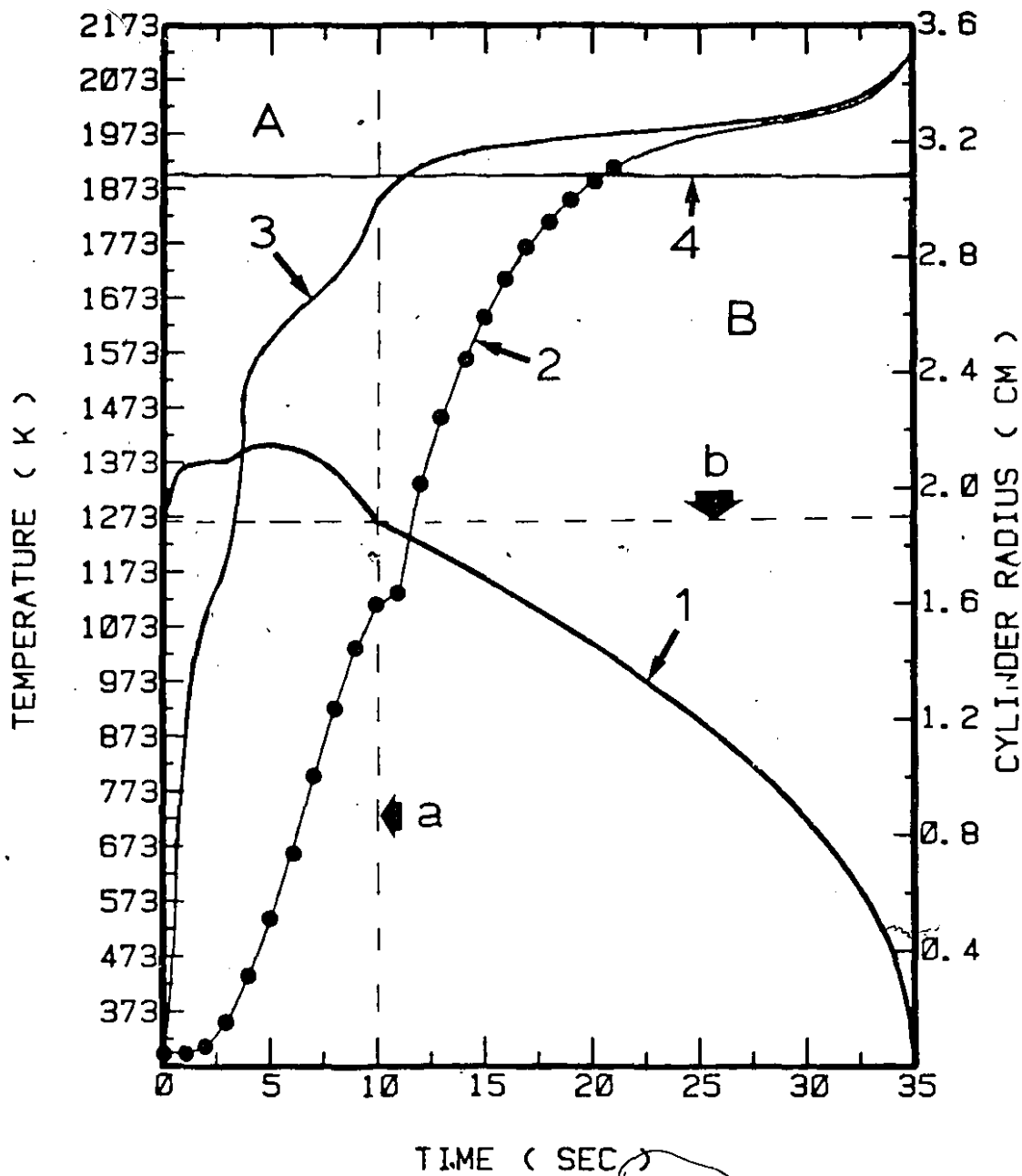


Figure 6.11 Experimental and predicted results from a zirconium experiment in liquid steel (see Fig. 6.6). The cylinder diameter was 3.81 cm and its length was 20.5 cm.

- 1) Predicted cylinder radius;
- 2) Measured and predicted centerline temperature;
- 3) Predicted temperature at the zirconium/steel interface;
- 4) Measured steel bath temperature.

important aspect is that this is the heat liberated per gr-atom of dissolved Zr in a relatively large mass (~65 kg) of liquid steel. As discussed in Section 5.52, the total heat flux generated during the free dissolution period is:

$$q_{\text{tot}}'' = N_{\text{Zr}}'' \Delta \bar{H}_{\text{Zr}}^0 \quad (6.4)$$

where  $\Delta \bar{H}_{\text{Zr}}^0 = -82.634 \text{ kJ/mol}$  and

$N_{\text{Zr}}''$  = the molar flux of the dissolving zirconium.

From equation (5.24) and (6.3), it is obvious that the molar flux increases during the free dissolution; the same is true for the  $q_{\text{tot}}''$ . As described by equation (5.23), the sum of the inwards directed heat flux  $q_{\text{in}}''$  (i.e., towards the dissolving zirconium interface), and the outwards directed heat flux  $q_{\text{out}}''$  is equal to the generated (total) heat flux:

$$q_{\text{tot}}'' = q_{\text{in}}'' + q_{\text{out}}'' \quad (6.5)$$

The total heat flux  $q_{\text{tot}}''$  can be estimated from equation (6.4) while the heat flux  $q_{\text{out}}''$  can be deduced from equation (5.21). Their difference is the inwards directed heat flux  $q_{\text{in}}''$ . Its estimation is critical to the computation of the temperature distribution inside the dissolving cylinder. One should expect that the value of the  $q_{\text{in}}''$  should be larger in the beginning of the free dissolution, just after the shell has melted back, and when the cylindrical specimen is relatively cooler in comparison with the melt. The direct exposure of the zirconium cylinder to the melt, and its exothermic

dissolution heat it up rapidly, and it starts getting hotter than the liquid steel. At the same time, the steel bath acts as a liquid metal heat-exchanger to the dissolving sample. The melt absorbs most of the exothermically generated heat, and therefore, the  $q_{in}''$  decreases. Although the inwards directed heat flux drops to a relatively small value, it is enough to heat the cylinder up to its melting point.

Figure 6.12 presents these details in graphical form. The computations have been carried out for the experimental case presented in Figure 6.5. Curve 1 depicts the inwards directed heat flux  $q_{in}''$ . Curve 2 shows the outwards directed heat flux  $q_{out}''$ , and Curve 3 illustrates the generated (total) heat flux  $q_{tot}''$ . It is interesting to observe, that the inwards directed heat flux ( $q_{in}''$ ) decreases in an almost exponential manner, while most of the generated heat goes to the melt at the final seconds of the free dissolution. This verifies the idea that the  $q_{in}''$  should decrease, obtaining the value zero at least in the last second of the free dissolution, where the last portion of the generated heat should be absorbed by the melt.

Concluding this section, it should be pointed out that an average value for the  $q_{in}''$  can be determined, during the free dissolution period. For example, with numerical integration the average value of the inwards directed heat flux (Curve 1 of Figure 6.12) was found to be  $6.2 \text{ cal/cm}^2/\text{sec}$  ( $0.26 \text{ MW/m}^2$ ). Similar analysis was performed for twelve

## FREE DISSOLUTION

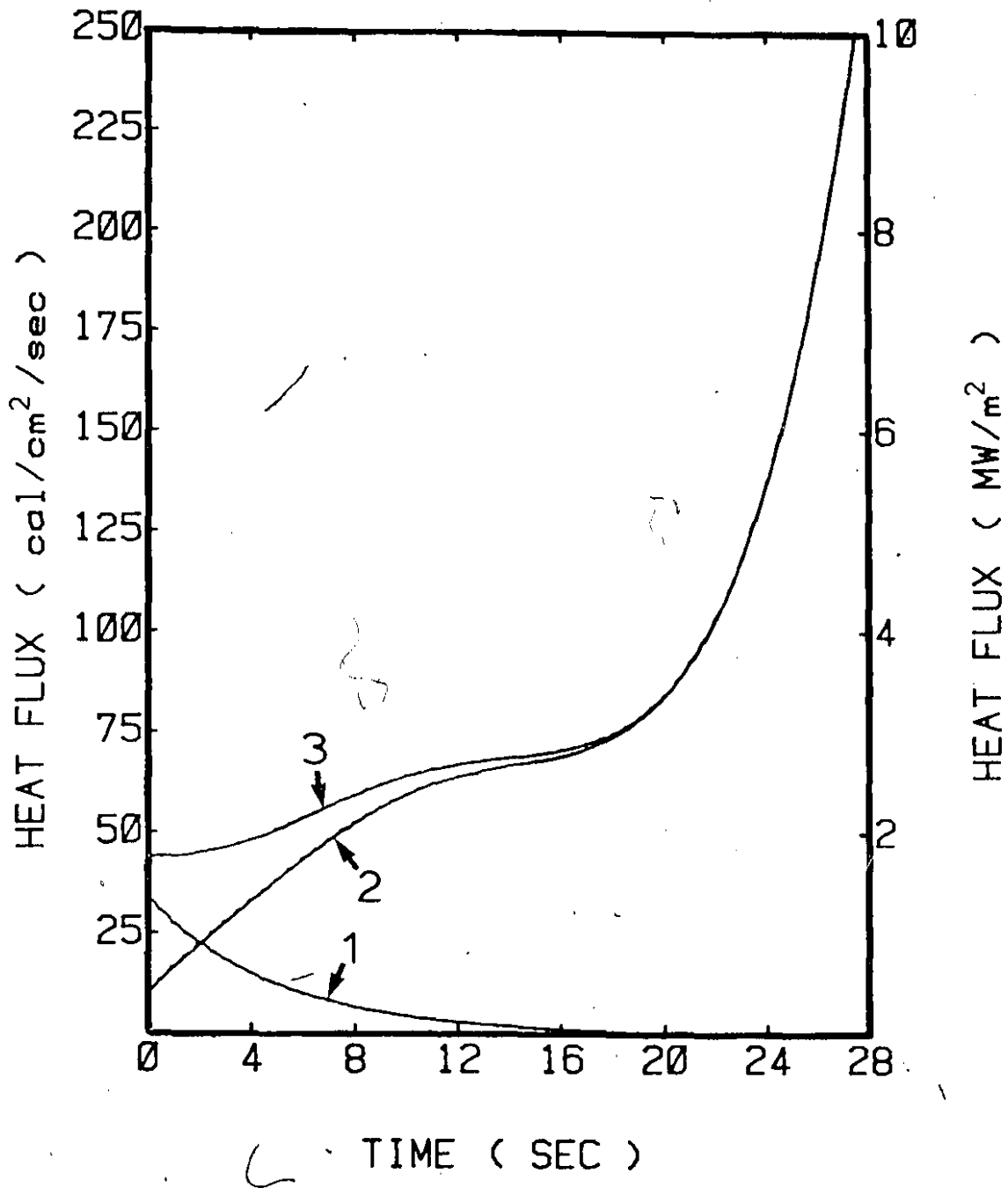


Figure 6.12 Predicted heat fluxes during the free dissolution period.

- 1) The inwards directed heat flux;
- 2) The outwards directed heat flux;
- 3) The generated (total) heat flux.

experimental cases and, the average value of the inwards directed flux  $q_{in}''$ , during the free dissolution period, was found to be:

$$(q_{in}'')_{avg} = 8.65 \pm 2.45 \text{ cal/cm}^2/\text{sec}$$

or

$$(q_{in}'')_{avg} = 0.36 \pm 0.10 \text{ MW/m}^2$$

It is quite interesting to note, that this value is very close to the one reported by Argyropoulos and Guthrie<sup>60</sup>, for the inwards directed heat flux during the free dissolution of titanium in liquid steel:  $8.25 \pm 1.75 \text{ cal/cm}^2/\text{sec}$  or  $0.345 \pm 0.073 \text{ MW/m}^2$ . In their model, they had assumed that the inwards directed heat flux was constant during the free dissolution period. Although in the present study, the inwards directed heat flux was not kept constant during the free dissolution period, it is quite intriguing to note that in average values, the two models give predictions which agree very well with each other.

#### 6.5 EFFECT OF THE DISSOLVED OXYGEN AND NITROGEN IN THE MELT

Evans and Pehlke<sup>107</sup> have measured experimentally the solubility of nitrogen in liquid binary alloys of iron with zirconium at  $1600^\circ\text{C}$  (1873 K). Some of their results are summarized below:

[% Zr]	[% N]	$K' = \frac{[\% \text{ Zr}]}{[\% \text{ N}]}$
0.253	0.0425	0.01076
0.322	0.0432	0.01391
0.409	0.0225	0.00921
0.558	0.0185	0.01032

It's worth noting, that from these results it seems that up to 185 ppm of nitrogen can co-exist with 0.558 wt% Zr in liquid iron, without any zirconium nitride precipitating to an appreciable extent. The solubility products  $K'$  were statistically treated by the present author, and the following value was determined for  $K'$ :

$$K' = 0.011 \pm 0.002 \quad (6.6)$$

Assuming this value to be constant at 1600°C (1873 K), it is estimated that with 50 ppm N in the melt the corresponding equilibrium concentration of zirconium is around (0.011/0.005) or 2.2 wt% Zr. This concentration of zirconium in the 65 kg steel bath would correspond to the immersion of three zirconium cylinders (2.54 cm in diameter), although after each test, most of the dissolved zirconium was skimmed off the melt together with the formed slag; it is repeated here, that zirconium has a smaller density than liquid steel. Experimentally, it was measured that the nitrogen in the melt was around 50 ppm. Therefore, the dissolution of zirconium was not influenced by the dissolved nitrogen in liquid steel, for the experimental conditions, under which the tests were carried out.

Zirconium is known as a powerful deoxidant in liquid steel. Theoretical calculations reveal that it can react with dissolved oxygen at concentrations as low as 1 ppm. The deoxidation practice which was followed in these tests (Section 4.2.2) reduced the active oxygen content to

concentrations around 10 ppm (maximum). So, at least for thermodynamic reasons, the dissolved oxygen can react with the dissolving zirconium cylinder. A simplified analysis will follow in order to confirm that this has a negligible effect on the dissolution: With a dissolved oxygen concentration of 10 ppm (max), the total oxygen content in the liquid steel is  $10 \cdot 10^{-6} \cdot 65000 \text{ g} = 0.65 \text{ g O} = 0.04 \text{ mol O}$ . Assuming that this oxygen reacts completely with the dissolving zirconium to form  $\text{ZrO}_2$ , it will require  $(0.04/2) = 0.02 \text{ mol}$  of Zr. Now even for the immersion of the smallest in diameter zirconium cylinder used in these experiments (1.905 cm in diameter), a mass of 220 g of zirconium will generally be dissolved. Then the percentage loss of zirconium due to the reaction with oxygen will be  $0.02 (91.22/220) 100\% = 0.8\%$ , or equivalently 99.2% of the dissolving zirconium cylinder will react exclusively with liquid iron. This effect will appear only during the immersion of the first cylinder in liquid steel, during an experimental day. For this purpose, a 1.905 cm (3/4") diameter cylinder was never immersed as first. If a 2.54 cm diameter cylinder is immersed then the zirconium percentage which will intermix only with liquid iron increases to 99.6%. A rough estimation can give a value about the effect of the reaction with oxygen on the generated exothermic heat. The heat of formation of  $\text{ZrO}_2$  is given by Elliott<sup>118</sup> equal to - 1080 kJ/mol. The (maximum) heat liberated from this

reaction will then be equal to  $0.02 (-1080) = -21.6$  kJ. The heat generated due to the exothermic dissolution of a 2.54 cm in diameter zirconium cylinder is  $99.6\% 5.48 (-82.634) = -451.0$  kJ, because approximately 500 g or 5.48 mol of zirconium will ultimately dissolve in a test like that. One now has  $(21.6/451.0) 100\% = 4.8\%$  or in other words, at least the 95% of the recorded exothermic events during the free dissolution period are attributed to the mixing of the dissolving zirconium cylinder with the liquid iron.

#### 6.6 THE DISSOLUTION OF THE Fe-Zr (~80 wt% Zr) FERROALLOY IN LIQUID STEEL

A few lumps of the 80% grade ferrozirconium were immersed in steel baths, in order to study the dissolution characteristics of this ferroalloy. The ferroalloy samples used in these tests were identical to those used by the steel industry. Their length varied from 9 cm to 13 cm and their width from 4 cm to 7 cm. These specimens were supplied by Shieldalloy Corporation, Newfield, New Jersey, U.S.A.. The chemical composition of these samples was 79.70% Zr (almost 80%), 0.1% C, 0.009% S, and the balance was iron.

Experiments were carried out in quiescent baths (i.e., power off), as well as in inductively stirred steel melts (i.e., power on). Figure 6.13 illustrates a typical experimental result for the dissolution of an 80% grade ferrozirconium lump in an inductively stirred steel bath at

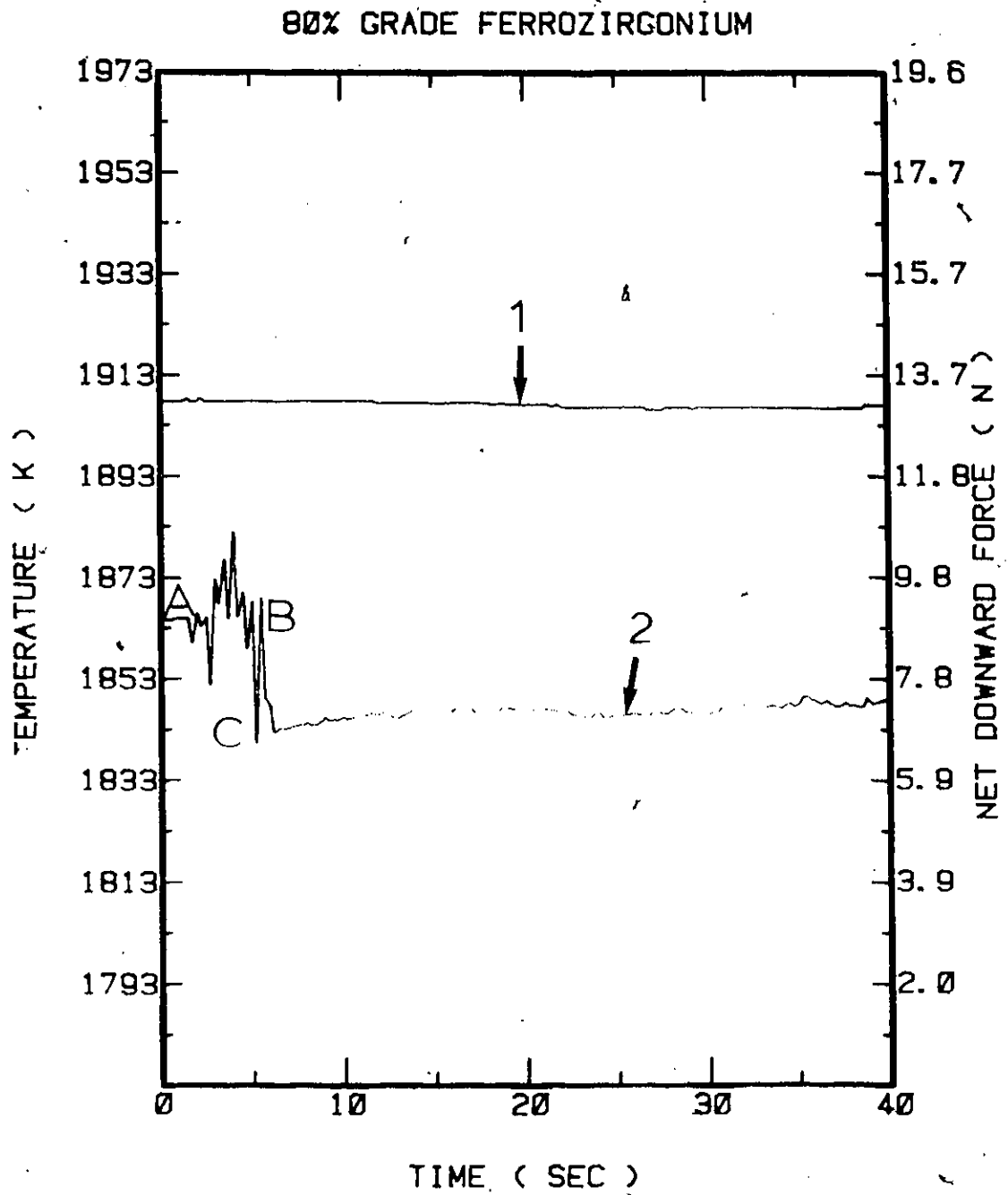


Figure 6.13 Results from a typical dissolution experiment of a (80% grade) ferrozirconium lump in liquid steel at  $1635^{\circ}\text{C}$  (1908 K).  
 1) Measured steel bath temperature;  
 2) Registered net downward force.

1635°C (1908 K). Curve 1 shows the temperature of the liquid steel, and Curve 2 depicts the net downward force by time as recorded by the DAPC facility. The DAPC facility started collecting the data a few seconds prior to immersion. Point A (Curve 2) corresponds to the moment when the sample was held motionless above the bath. After that, the sample was lowered towards the surface of the melt, and as of that, vibrations were recorded. The immersion period corresponds to the segment BC; point C corresponds to the moment (6th second) when the lump was immersed into the liquid steel. The model predicted the end of the steel shell period at the 11th second. As it has been pointed out by Argyropoulos<sup>62</sup>, the mathematical formulation that is applied to the analysis of dissolution results for pure metals in liquid steel, can also be used for the analysis of dissolution results for ferroalloys. In other words, equation (6.2) can be used in this case as well, but now, the parameters will refer to the ferroalloy. Measuring the weight of each lump in the air and in the water, its density was determined. An average value for the density of these specimens was found to be 6738 kg/m<sup>3</sup> with a sample standard-error of estimate equal to 95 kg/m<sup>3</sup>. As the density of this material is less than the density of the liquid steel (i.e., almost equal to 6944 kg/m<sup>3</sup> at 1600°C or 1873 K), one should expect that the rate of change of the net downward force should be positive, as in the case of pure zirconium. The same trend, although not so

much pronounced, is followed by Curve 2 of Figure 6.13, at the free dissolution period. As the density of the liquid steel and that of the lumps are very close, as far as their values are concerned, the accuracy of the method decreases. Therefore, apart from the experimental results obtained by the method, the initial and final weights of the lumps were strongly taken under consideration during the analysis of the data.

The mass flux  $m''$ , or in other words, the mass of the dissolving ferroalloy per unit area per unit time, can be used to adequately describe the rate phenomena. Assuming the dissolving lump to be a sphere of the same volume, the rate of change of the radius by time can then be deduced as the ratio of the mass flux divided by the density of the ferroalloy. Experimental results for the mass flux, and estimated values for the rate of change of the ferroalloy radius, considered as a sphere, are presented in Table 6.1. From this Table, one can easily notice that the induction stirring increases the solution rate of this ferroalloy in liquid steel. It must be pointed out that the liquidus temperature of this ferroalloy (i.e., Fe-80% Zr), according to the Fe-Zr phase diagram (Figure 3.4), is around  $1050^{\circ}\text{C}$  or 1323 K. Therefore, it seems that this ferroalloy exhibits melting instead of dissolution in liquid steel. In Figure 6.14, predictions for the total melting times of 80% grade ferro-zirconium spheres of various diameters, are presented.

Table 6.1

Experimentally measured rates  
of the 80% grade ferrozirconium

Quiescent Steel Bath1610°C (1883 K)

Mass Flux (m") (kg/m <sup>2</sup> /sec)	Dissolution Speed (-dr/dt) (cm/sec)
0.56 (+ 0.08)	8.31 10 <sup>-3</sup>

Inductively Stirred Steel Baths

Mass Flux (m") (kg/m <sup>2</sup> /sec)	Dissolution Speed (-dr/dt) (cm/sec)
<u>1620°C (1893 K)</u>	
1.37 (+ 0.20)	2.10 10 <sup>-2</sup>
<u>1635°C (1908 K)</u>	
1.53 (+ 0.23)	2.27 10 <sup>-2</sup>

### 80% GRADE FERROZIRCONIUM

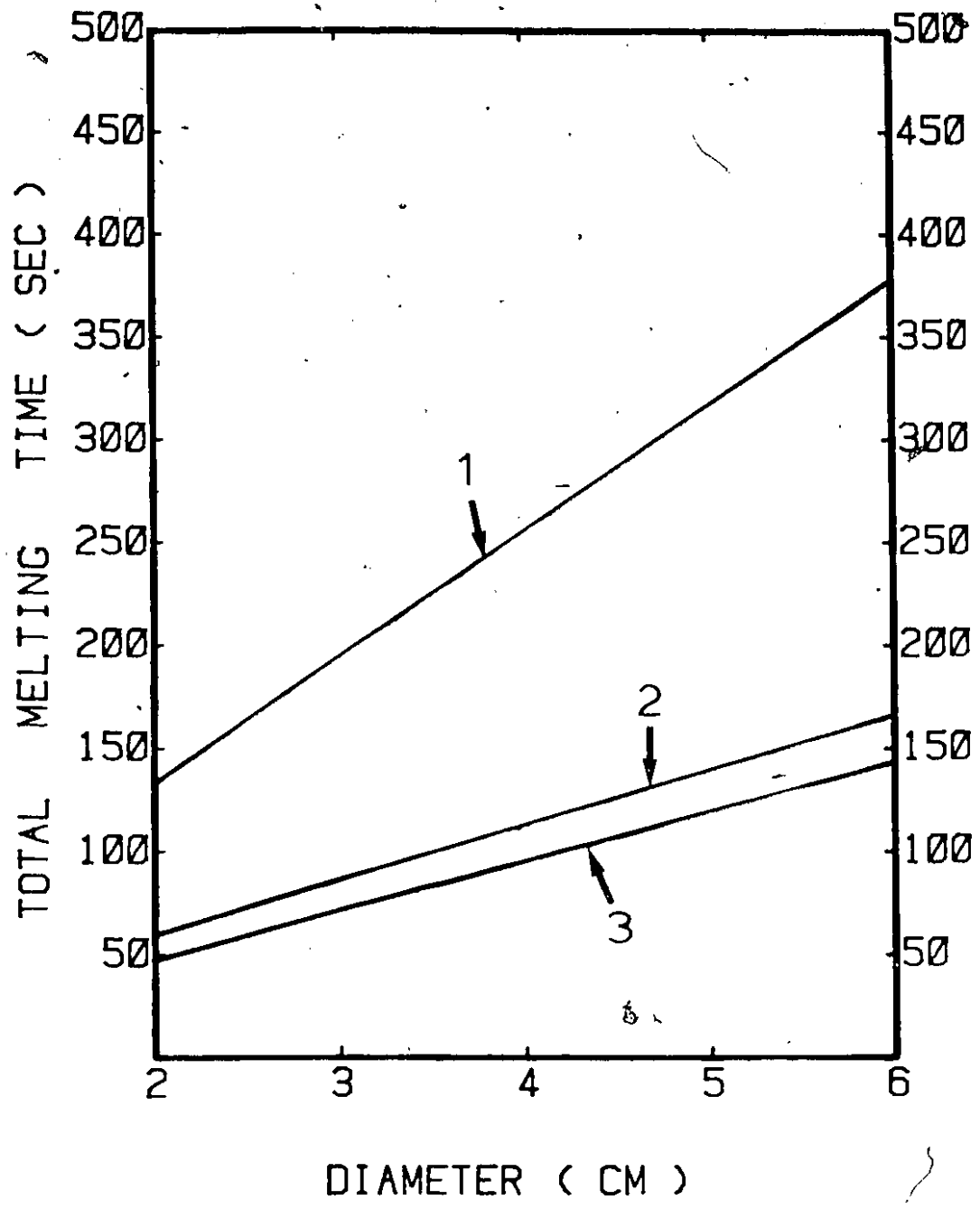


Figure 6.14 Predicted total melting times versus lump diameter (considered as a sphere) for various conditions:  
Static conditions (power off):  
1) Liquid steel at 1610°C (1883 K).  
Dynamic conditions (power on):  
2) Liquid steel at 1620°C (1893 K);  
3) Liquid steel at 1635°C (1908 K).

Curve 1 shows the total melting time (steel shell period plus melting period), for ferrozirconium spheres of various diameters immersed in quiescent steel baths at  $1610^{\circ}\text{C}$  (1883 K). Curve 2 and 3 present similar predictions for inductively stirred melts at  $1620^{\circ}\text{C}$  (1893 K) and  $1635^{\circ}\text{C}$  (1908 K), respectively. Again, one can notice that shorter melting times are expected, if spheres from this ferroalloy are immersed in inductively stirred steel melts.

#### 6.7 DISCUSSION

Estimated heat and molar fluxes in the steel shell/zirconium reaction zone are presented in Table 6.2. As seen in Section 6.4.1, the predicted locations of the steel shell/liquid steel interface and that of the inner steel shell boundary agree rather well with the experimental data. This indicates that the heat fluxes estimated at the outer and inner steel shell surfaces are both independently correct. The starting time for the reaction at the steel shell - zirconium interface depends mainly upon two factors: the cylinder diameter and the steel bath superheat.

The semi-empirical method of estimating heat fluxes generated during the steel shell period involves a 15% uncertainty. This is due to two factors: the first derives from the convective heat transfer correlations used at the outer surface of the steel, while the second arises from the fact that steel-shell melt back and exposure of zirconium

Table 6.2

Estimated Heat And Mass Fluxes During the Steel Shell and Free Dissolution Periods

	CGS Units	SI Units	
PERIOD	Heat flux at the interface	$10.75 \pm 2.15 \text{ cal/cm}^2/\text{sec}$	$0.45 \pm 0.09 \text{ MW/m}^2$
	Molar flux of iron	$1.47 \cdot 10^{-3} \pm 2.9 \cdot 10^{-4} \text{ mol/cm}^2/\text{sec}$	$14.7 \pm 2.9 \text{ mol/m}^2/\text{sec}$
SHELL	Molar flux of zirconium	$1.41 \cdot 10^{-3} \pm 2.8 \cdot 10^{-4} \text{ mol/cm}^2/\text{sec}$	$14.1 \pm 2.8 \text{ mol/m}^2/\text{sec}$
STEEL	Mass transfer coefficient of iron	$0.016 \pm 0.003 \text{ cm/sec}$	$16 \cdot 10^{-5} \pm 3 \cdot 10^{-5} \text{ m/sec}$
	Mass transfer coefficient of zirconium	$0.058 \pm 0.012 \text{ cm/sec}$	$58 \cdot 10^{-5} \pm 12 \cdot 10^{-5} \text{ m/sec}$
Free Dissolution Period	Heat flux during free dissolution (average value)	$8.65 \pm 2.45 \text{ cal/cm}^2/\text{sec}$	$0.36 \pm 0.10 \text{ MW/m}^2$

in liquid steel may be somewhat stochastic in nature. Thus, any slight imperfections in a hot, rapidly thinning shell will lead to premature exposure of zirconium in liquid steel.

As it has already been mentioned, the free dissolution period starts, once the steel shell period ends. At the dissolving interface the continuity of mass dictates that the net moles of zirconium lost from the dissolving cylinder per unit time, must be equal to the net moles of zirconium diffusing into the liquid steel per unit time. Mathematically, this can be expressed with equation (5.40) if niobium is substituted by zirconium. With a similar reasoning as the one described in Section 5.7, the following equation is derived:

$$-\frac{dr}{dt} = \frac{K_{Zr} C_{Zr}^{*L}}{\rho_{Zr}/M_{Zr}} \quad (6.7)$$

where  $dr/dt$  = the rate of change of the dissolving zirconium cylinder radius by time;

$\rho_{Zr}$  = the density of zirconium;

$M_{Zr}$  = the molecular weight of zirconium;

$C_{Zr}^{*L}$  = the liquidus concentration of zirconium at the temperature of steel bath;

$K_{Zr}$  = experimental mass transfer coefficient.

Based on this expression, an experimental mass transfer coefficient can be estimated. Mass transfer coefficients experimentally measured and, predicted from equation (5.46) during the initial stages of the free dissolution of zirconium

Table 6.3

Mass Transfer Coefficients of Zirconium  
in the Beginning of the Free Dissolution

Temperature	Experimental Mass Transfer Coefficient (cm/sec)	Predicted Mass Transfer Coefficient from eqn. 5.46 (cm/sec)
1600°C (1873 K)	$(7.2 \pm 1.0) 10^{-3}$	$5.6 10^{-3}$
1620°C (1893 K)	$(8.9 \pm 1.5) 10^{-3}$	$5.8 10^{-3}$
1640°C (1913 K)	$(10.6 \pm 1.8) 10^{-3}$	$6.0 10^{-3}$

are presented in Table 6.3. It is obvious that the experimentally measured mass transfer coefficients are larger than the predicted ones from equation (5.46) and, it seems that there is a strong influence of bath temperature on measured mass transfer coefficients. This trend was observed in every experiment.

An average  $dr/dt$  and an average steel bath temperature during the free dissolution period was estimated for the 21 different runs. The Tables 6.4 and 6.5 summarize these data for tests carried out under static conditions (power off) and dynamic conditions (power on), respectively. Using equation (6.7), an average mass transfer coefficient was also computed. In order to deduce an Arrhenius-type relationship between the mass transfer coefficient and the absolute temperature of the melt, these data were plotted as shown in Figure 6.15. The data represented by circles correspond to tests carried out under static conditions while, the ones represented by triangles correspond to experiments performed under dynamic conditions. It seems that there is not any appreciable effect of the fluid flow characteristics on the free dissolution of zirconium in liquid steel, at least for the experimental conditions under which the two sets of tests were carried out. Linear regression analysis was separately performed for the two sets of data (i.e., the mass transfer coefficients from tests with power off and on), and the resulting correlations of  $\log K$  vs.  $(1/T)$  gave mass transfer coefficients which

Table 6.4

Experimentally Measured  $(-dr/dt)$  and Mean Mass Transfer Coefficients during Zirconium Free Dissolution Under Static Conditions.

Run No.	Temperature		$(-dr/dt) 10^2$	$K_{Zr}^{OFF} 10^2$
	(°C)	(K)	(cm/sec)	(cm/sec)
1	1614	1887	8.79	9.41
2	1629	1902	9.00	9.64
3	1637	1905	9.25	9.91
4	1640	1913	11.58	12.41
5	1642	1915	12.05	12.91
6	1645	1918	11.60	12.43
7	1643	1916	11.30	12.10
8	1622	1895	8.22	8.80
9	1595	1868	6.81	7.30
10	1602	1875	6.77	7.26
11	1603	1876	6.61	7.09
12	1608	1881	8.45	9.05

Table 6.5

Experimentally Measured  $(-dr/dt)$  and Mean Mass Transfer Coefficients during Zirconium Free Dissolution Under Dynamic Conditions

Run No.	Temperature		$(-dr/dt) \cdot 10^2$ (cm/sec)	$K_{Zr}^{ON} \cdot 10^2$ (cm/sec)
	(°C)	(K)		
13	1618	1891	8.37	8.97
14	1621	1894	8.65	9.27
15	1638	1911	12.08	12.94
16	1645	1918	10.79	11.56
17	1657	1930	12.19	13.07
18	1605	1878	7.40	7.94
19	1600	1873	6.99	7.49
20	1613	1886	7.41	7.94
21	1635	1908	11.40	12.22

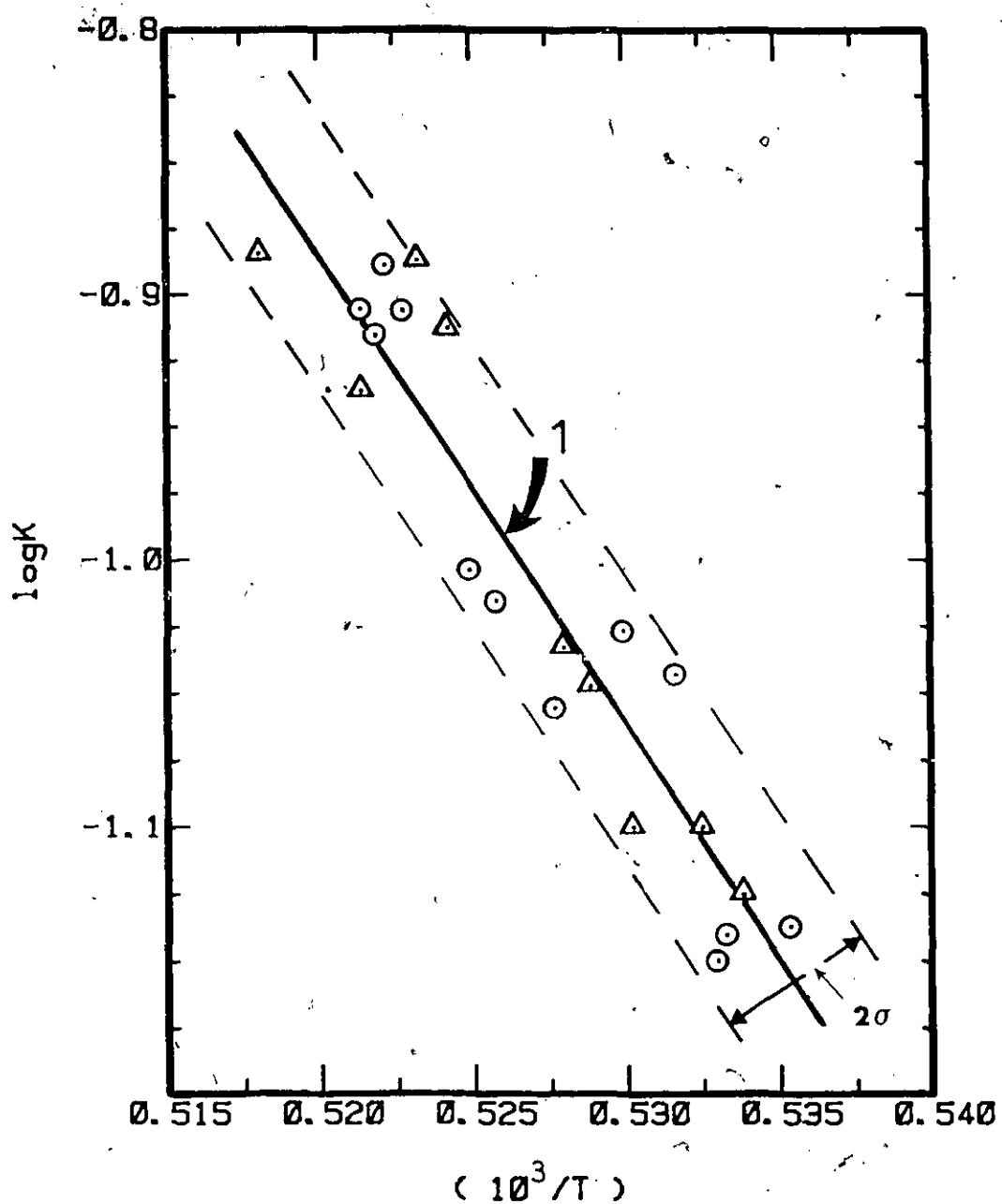


Figure 6.15 Arrhenius-type plot of the experimental mass transfer coefficients.

Mass transfer coefficients deduced from tests which were performed under:  
 (O) Static conditions (power off);  
 ( $\Delta$ ) Dynamic conditions (power on).

differed by 1.5% (maximum) for the temperature range 1580°C (1853 K) to 1660°C (1933 K). So, it was decided to correlate all the data together and the straight line 1 (Figure 6.15) illustrates this result in graphical form. In mathematical form the following equation was derived:

$$\log K_{Zr} = A - \frac{B}{T} \quad (6.8)$$

where  $A = 8.351 \pm 0.729$

$$B = 17757.8 \pm 1382.5$$

with a correlation coefficient 0.947, 19 degrees of freedom and a standard error of estimate 0.031. The apparent activation energy was found to be 81.2 ( $\pm$  6.3) kcal/mol or, 340 (+ 26.4) kJ/mol. Large values of the apparent activation energy have been reported in previous studies i.e., 65.1 kcal/mol (273 kJ/mol) for the dissolution of molybdenum<sup>41</sup> in liquid iron, 70.5 kcal/mol (296.3 kJ/mol) and 71.5 kcal/mol (300.6 kJ/mol) for the dissolution<sup>59</sup> of titanium and vanadium in liquid steel, respectively. Although these values are relatively large, liquid phase mass-transfer has been considered the rate controlling step. However, for the dissolution of zirconium in liquid steel this may not be the case as no effect from the induction stirring was identified. Even though this may be true and general for the case of zirconium, it is mandatory to restrict the generality of this conclusion to the experimental conditions under which these tests were carried out. It is necessary to extend this study in bigger vessels (i.e., ladles),

capable of containing larger quantities of liquid steel and in which, the stirring intensity will be more pronounced than the one generated by induction stirring in the steel baths, used for the present work. Consequently, without any further experimental results available, no conclusion can be drawn on the rate-controlling mechanism.

There are some more phenomena related to the tests themselves which should be discussed. Visual examination of the bath surface close to the dissolving zirconium cylinder showed it becoming much hotter and turbulent, with the upwelling plume of liquid becoming faster during the later stages of free dissolution. It has been shown in previous figures (i.e., Figures 6.10, 6.11) that the predicted temperature near the dissolving front exceeds the bath temperature and approaches the melting point of zirconium ( $1852^{\circ}\text{C}$  or  $2125\text{ K}$ ), during the final stages of the free dissolution period. In this way the mass transfer coefficients become more sensitive to temperature changes, and therefore, the mechanism of accelerated dissolution (eqn. 6.3) comes into effect. It must be a combination of effects that gives rise to this dissolution behaviour: The exothermic dissolution increases the temperature of the dissolving front, which in turn has as a result to accelerate the dissolution by increasing the mass transfer coefficient.

Linear regression analysis was performed to the results presented in Tables 6.4 and 6.5. The following relation was deduced:

$$-\left[\frac{dr}{dt}\right]_{\text{avg}} = a T + b \quad (6.9)$$

where  $a = 10.45 \cdot 10^{-4}$

$b = -1.89$

$T =$  temperature in Kelvin.

The correlation coefficient was found to be 0.941, with 19 degrees of freedom, and a standard error of estimate 0.007. With the application of the model in order to estimate the steel shell period for a particular diameter cylinder, and the statistically deduced equation (6.9), the total dissolution times required for the dissolution of zirconium cylinders at various diameters can be determined. Figure 6.16 shows these predictions for zirconium cylinders of various diameters immersed in steel baths at 1590°C or 1863 K (Curve 1), 1615°C or 1888 K (Curve 2), and 1640°C or 1913 K (Curve 3), under static conditions. Instead of using equation (6.9) to estimate the free dissolution period, another way to achieve this could be by direct integration of equation (6.3) which would give:

$$t_{fd} = \frac{r_0^2}{2C_1} \quad (6.10)$$

where  $t_{fd} =$  free dissolution period;

$r_0 =$  the initial radius of a zirconium cylinder;

$C_1 =$  a constant.

However, experimentally deduced values of the constant  $C_1$  revealed that  $C_1$  is approximately equal to  $r_0(a T + b)/2$ , and therefore, almost the same results would be obtained.

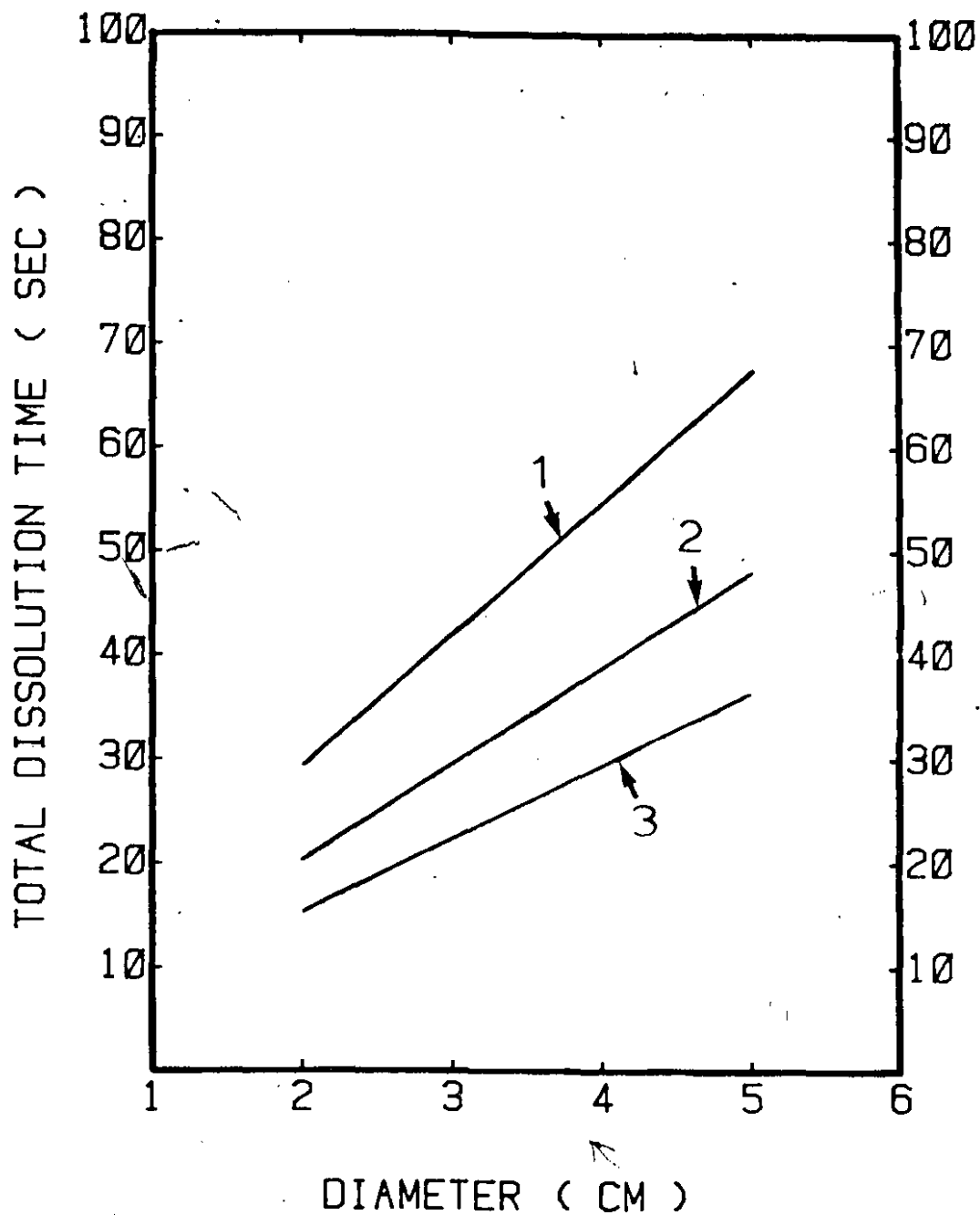


Figure 6.16 Predicted total dissolution times versus diameter under various temperatures:  
1) Liquid steel at  $1590^{\circ}\text{C}$  (1863 K);  
2) Liquid steel at  $1615^{\circ}\text{C}$  (1888 K);  
3) Liquid steel at  $1640^{\circ}\text{C}$  (1913 K).

In any case, it should be kept in mind that the predictions presented in Figure 6.16 are semi-empirical in nature.

Another very important aspect which should be pointed out is the exothermicity itself. Suppose for a moment that zirconium does not exhibit any exothermic dissolution in liquid steel. One might wonder to know the superheat of a hypothetical steel bath in which a zirconium cylinder melts, but with a melting speed similar to the dissolution speed determined experimentally in the actual tests. Of course, the temperature of this hypothetical steel bath should be above the melting point of zirconium (1852°C or 2125 K). At those high temperatures, the steel shell period is so small that can be neglected. The average (overall) heat flux ( $q''$ ) which is supplied to the melting zirconium cylinder is then:

$$q'' = \frac{m \Delta H}{A \Delta t} \quad (6.11)$$

where  $m$  = the melting mass of the zirconium cylinder;

$A$  = the average area of the cylinder;

$\Delta t$  = the total time required to melt the mass  $m$ ;

$\Delta H$  = the total amount of heat required to raise the temperature of a unit mass of zirconium from the room temperature to the melting point, plus the latent heat of fusion; using the F\*A\*C\*T system<sup>91</sup>, this value was found to be 887 kJ/kg (212 cal/g). The following relationship was found to relate the average area ( $A$ ) and the initial area ( $A_0$ ) of a zirconium cylinder:

$$A = f A_0 \quad (6.12)$$

where  $f$  is a correction factor having a value 0.7 within 2% uncertainty. Assuming that the melting occurs at the radial direction only, equation (6.11) can be written as:

$$q'' = \frac{\rho'}{2f} u_d \Delta H \quad (6.13)$$

where  $\rho$  = the zirconium density;

$$u_d = - \frac{dr}{dt}_{\text{avg}} = \text{the average dissolution speed} \\ (\text{eqn. 6.9}).$$

For simplicity, equation (6.13) can be re-written as:

$$q'' = 4.11 u_d \quad (6.14)$$

where the units of  $q''$  and  $u_d$  are MW/m<sup>2</sup> and cm/sec, respectively.

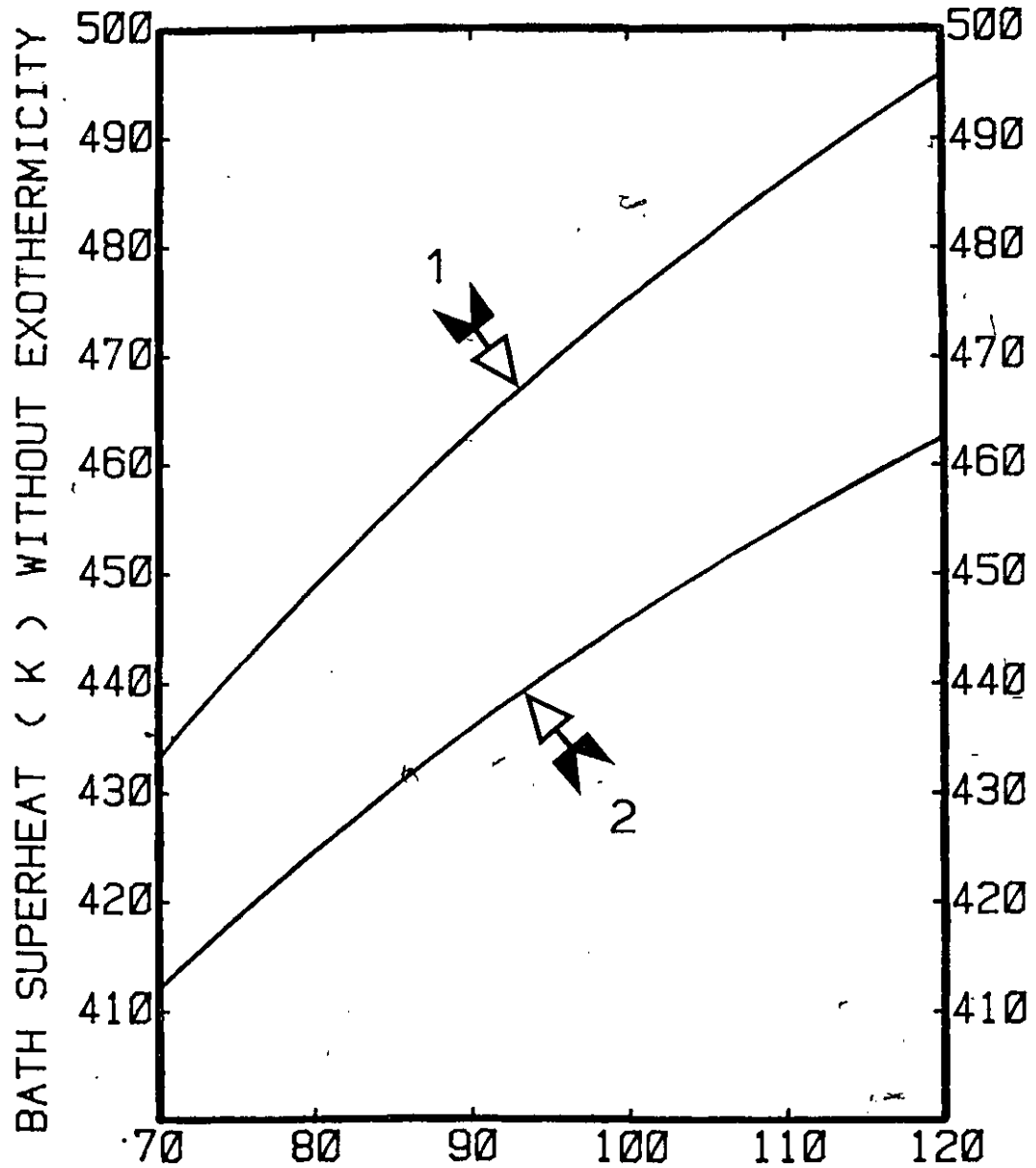
This equation reveals that there is a direct (i.e., proportional) relation between the required heat flux and the solution speed. The heat flux ( $q''$ ) is related with the heat transfer coefficient ( $h$ ) according to eqn. (6.15):

$$q'' = h (T_B - T_{\text{mp,Zr}}) = h \Delta T_{\text{Zr}} \quad (6.15)$$

where  $T_B$  = the temperature of the hypothetical steel bath;

$T_{\text{mp,Zr}}$  = the zirconium melting point.

For the determination of the heat transfer coefficient ( $h$ ), the correlation (5.19) was extrapolated from the common steel-practice temperatures (i.e., around 1600°C or 1873 K) up to the hypothetical steel bath temperatures. After some mathematical manipulations of equations (6.15) and (5.19), the resulting formulas were:



BATH SUPERHEAT ( K ) WITH EXOTHERMICITY

Figure 6.17- Predictions for the effect of exothermicity on the steel bath superheat.  
1) Without any induction stirring;  
2) With induction stirring.

$$\Delta T_{Zr} = 1.69 \cdot 10^{-3} (q'')^{3/4} \quad \text{when } c = 0.17$$

(i.e., power off) (6.16)

and

$$\Delta T_{Zr} = 1.35 \cdot 10^{-3} (q'')^{3/4} \quad \text{when } c = 0.23$$

with  $q''$  in MW/m<sup>2</sup>. (i.e., power on) (6.17)

Figure 6.17 has been drawn according to estimations based on equations (6.14), (6.16), and (6.17). Curves 1 and 2 depict the effect of exothermicity on the steel bath superheat under static and dynamic conditions, respectively. Of course, at those high steel bath temperatures, the induction stirring may not have the same significance as at lower temperatures, but one can obtain at least a qualitative picture. It is interesting to note, that the exothermicity substantially decreases the bath superheats required to dissolve zirconium in liquid steel. In the absence of any exothermic event, melting could be considered the only mechanism that could give rise to solution rates similar to the ones deduced experimentally.

## CHAPTER 7

### 7. THE DISSOLUTION OF NIOBIUM ALLOYS IN LIQUID STEEL

#### 7.1 INTRODUCTION

In this chapter, the dissolution of the high purity ferroniobium alloy in liquid steel will be examined. The effect of the dissolved oxygen on the dissolution speed of standard ferroniobium in liquid steel will be discussed. Finally, the dissolution of a Nb-Ni alloy in liquid steel, will be studied as well.

#### 7.2 EXPERIMENTAL WORK

The steel baths were of the same material and quantity as mentioned in Section 4.2.1. The experimental procedure, as far as the adjustment of the steel bath chemistry, the immersion of the bath thermocouple, the weight sensor, and the microprocessor based DAPC facility are concerned, was similar to the one described in the Sections 4.2.2 through 4.2.5. Instead of the immersion of cylindrical specimens, lumps of ferroalloys identical to those used by the steel industry were immersed. The length of these lumps varied from 9 cm to 13 cm and the width from 4 cm to 7 cm. Table 7.1 gives the chemical compositions of the ferroalloys used; they were supplied by Shieldalloy Corporation, Newfield, N.J., U.S.A..

Table 7.1

## Chemical Compositions of Ferroalloys Tested

Ferroniobium Standard Grade	Ferroniobium High Purity Grade
Nb = 66.00%	Nb = 64.00%
C = 0.17%	C = 0.06%
Si = 2.43%	S = 0.007%
Al = 3.33%	Al = 0.75%
Fe = Balance	Si = 0.02%
	N = 0.008%
	Fe = Balance
Nb-Ni Alloy	
Nb = 64.5%	
C = 0.02%	
S = 0.002%	
Si = 0.12%	
Al = 0.76%	
O = 0.02%	
N = 0.01%	
Sn = 0.01% (max)	
Pb = 0.001%	
P = 0.011%	
Fe = 0.126%	
Ni = Balance	

### 7.3 RESULTS AND DISCUSSION

Figure 7.1 shows a typical experimental result for the dissolution of a high-purity ferroniobium lump in liquid steel, under static conditions (i.e., power off). Curve 1 depicts the bath temperature while Curve 2 illustrates the net downward force, as a function of time. The DAPC facility started collecting the data a few seconds prior to immersion. At point A the lump was above the melt; the segment BC denotes the immersion period. The steel shell period (segment CD) was completed at the 19th second, after which the free dissolution period followed. The mass flux ( $m''$ ), or in other words, the dissolving mass of this lump per unit surface per unit time was estimated (based on these experimental results) to be equal to  $0.069 \text{ g/cm}^2/\text{sec}$  ( $0.69 \text{ kg/m}^2/\text{sec}$ ). Another experimental result is shown in Figure 7.2. This test was carried out under dynamic conditions that is, the power to the induction furnace was kept on during the experiment. The mass flux  $m''$  was found to be  $0.112 (\pm 0.009) \text{ g/cm}^2/\text{sec}$  ( $1.12 \pm 0.09 \text{ kg/m}^2/\text{sec}$ ). Although the average bath temperature of the second test was higher than the first, an effect was actually found from the fluid flow conditions in the vicinity of the dissolving ferroalloy on its dissolution speed. So, larger dissolution rates were determined for the experiments which were performed under dynamic conditions. Previous work on this subject<sup>62</sup> has shown that the dissolution characteristics can be enhanced

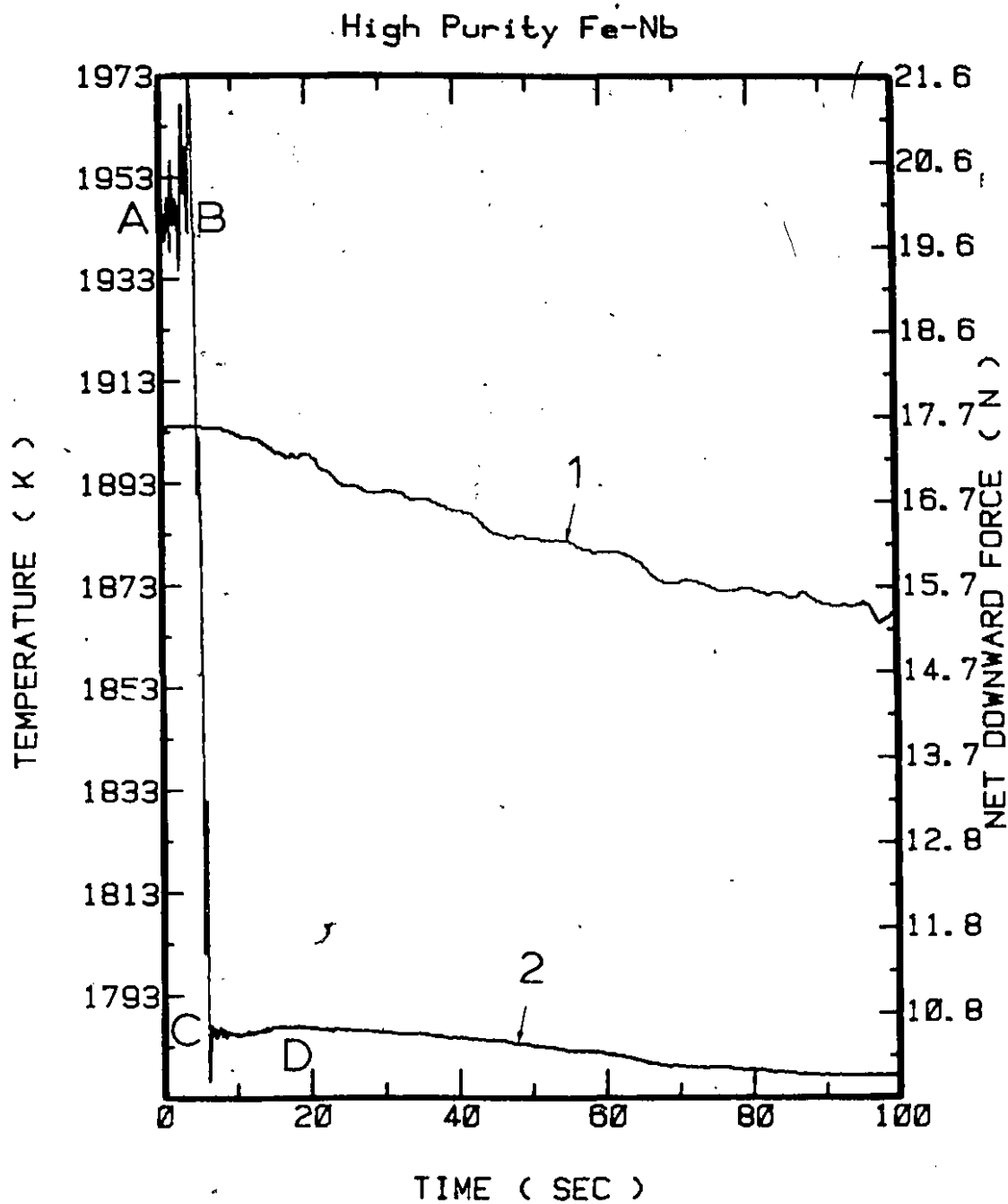


Figure 7.1 Results from a typical dissolution experiment of a high-purity ferroniobium lump in liquid steel under static conditions.  
 1) Measured steel bath temperature;  
 2) Registered net downward force.

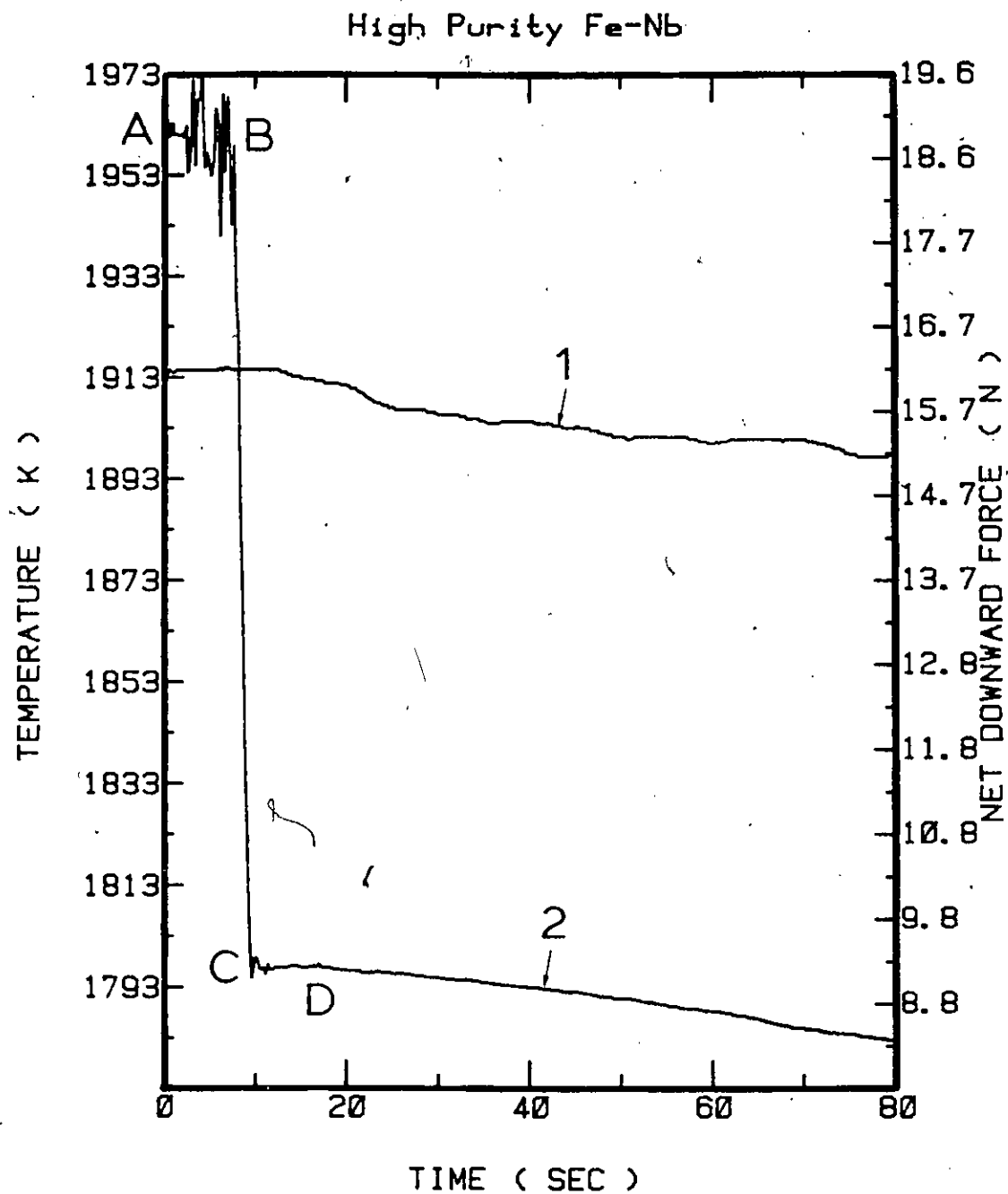


Figure 7.2 Results from a typical dissolution experiment of a high-purity ferroniobium lump in liquid steel under dynamic conditions.  
 1) Measured steel bath temperature;  
 2) Registered net downward force.

## High Purity Fe-Nb

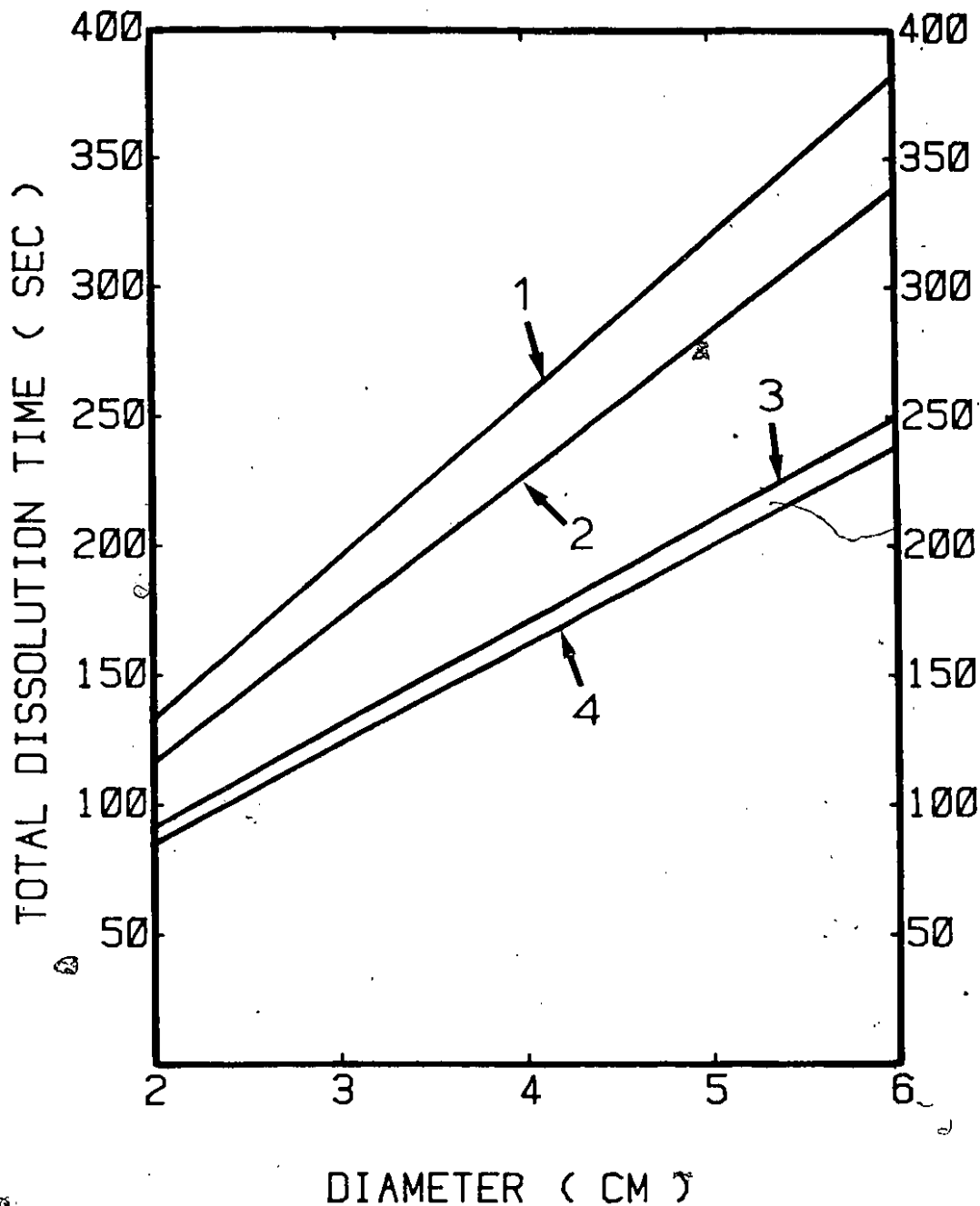


Figure 7.3 Predictions for the total dissolution times of high-purity ferroniobium lumps, considered as spheres, as a function of lump diameter and experimental conditions:

- Static conditions (power off):
- 1) Liquid steel at  $1610^{\circ}\text{C}$  (1883 K);
  - 2) Liquid steel at  $1630^{\circ}\text{C}$  (1903 K);
- Dynamic conditions (power on):
- 3) Liquid steel at  $1620^{\circ}\text{C}$  (1893 K);
  - 4) Liquid steel at  $1630^{\circ}\text{C}$  (1903 K).

up to 60% under the influence of induction stirring. Similar results have been observed in this study, as well. Figure 7.3 depicts predictions for the total dissolution times of high purity ferroniobium lumps considering them as spheres of various diameters. Curves 1 and 2 give predictions for the total dissolution times of lumps under static conditions, while Curves 3 and 4 give predictions for the total dissolution times under dynamic conditions. The bath temperatures are supposed to be: 1610°C or 1883 K (Curve 1), 1630°C or 1903 K (Curves 2 and 4), and 1620°C or 1893 K (Curve 3). The high-purity grade ferroniobium has been found<sup>62</sup> to dissolve faster than the standard grade ferroniobium, which is extensively used in the steel industry, under the same experimental conditions. Nevertheless, induction or argon stirring of the liquid steel in the ladle is important for shorter dissolution times and homogenization of the melt.

#### 7.4 THE EFFECT OF OXYGEN ON THE RECOVERY AND DISSOLUTION OF THE Fe-Nb ALLOYS IN LIQUID STEEL

Modern steelmaking practice requires ferroalloys with repeatable and consistently high recoveries. The use of ladle furnaces or ladle metallurgy stations for refining and alloying, currently increases in modern steelmaking practice. Emphasis on recovery of alloying and speed of solution will be required for these ladle furnaces in order to optimize their use. An important factor which influences the

recovery of alloys is the active oxygen in molten steel. Various steelmaking operations have experienced different recoveries on ferroalloys. However, what is even worse, is that the recoveries are quite often erratic. This is usually true in steelmaking practices where different microalloying ferroalloys are used under semi-killed steel bath conditions.

The prime objective of this study, was to understand the fundamental factors that control the recovery of solid ferroalloy additives (with emphasis on standard ferroniobium), and quantify these factors in simple mathematical (statistical) formulas.

Recovery depends upon the physicochemical properties of the ferroalloy, such as solution speed and density, as well as on the dissolved oxygen in liquid steel. It has been proposed<sup>70</sup> that a mathematical expression must exist:

$$R = f ( u, \rho, [O] ) \quad (7.1)$$

where R = recovery;

u = solution speed;

$\rho$  = density;

[O] = dissolved oxygen in liquid steel.

Dissolved oxygen content is all of the non-combined oxygen dissolved in liquid steel. Active oxygen content is that part of the dissolved oxygen, which is not associated with other elements in the steel. For the results presented in this section, the dissolved oxygen will be considered as equal to the active oxygen content. For the low residual

concentrations of dissolved niobium in liquid steel (as in this case), the dissolved and the active oxygen contents are equal within a 5% uncertainty.

Conditions of ladle metallurgy stations were simulated in the induction furnace described in Section 4.2. The steel bath was prepared by melting down 65 kg of ARMCO IRON. The bath temperature was brought up to 1600°C (1873 K), and thereafter maintained to within  $\pm 10$  K by adjusting the input power to the induction furnace. Only for this measurement, Leeds and Northrup Dip-Tip thermocouples were used. The power to the induction furnace was kept on during the experiments. The standard grade ferroniobium lumps had an average length and width of 11 cm and 5 cm, respectively; their chemical composition is given in Table 7.1. Figure 7.4 presents a schematic cross-section of the experimental apparatus. The solution speed characteristics of the ferroalloys were measured with a weight sensor (Section 4.2.4). The active oxygen and the bath temperature were measured with the CELOX oxygen-probe system made by Electro-Nite Co. The analog outputs of the weight sensor and the oxygen probe system were fed into the  $\mu$ MAC-5000. An intelligent measurement facility (INMEFA) capable of collecting and storing the analog data, was built and programmed for this research work. The interested reader should refer to reference 83 for more details about this data acquisition and process-control facility. A BAIRD-ATOMIC

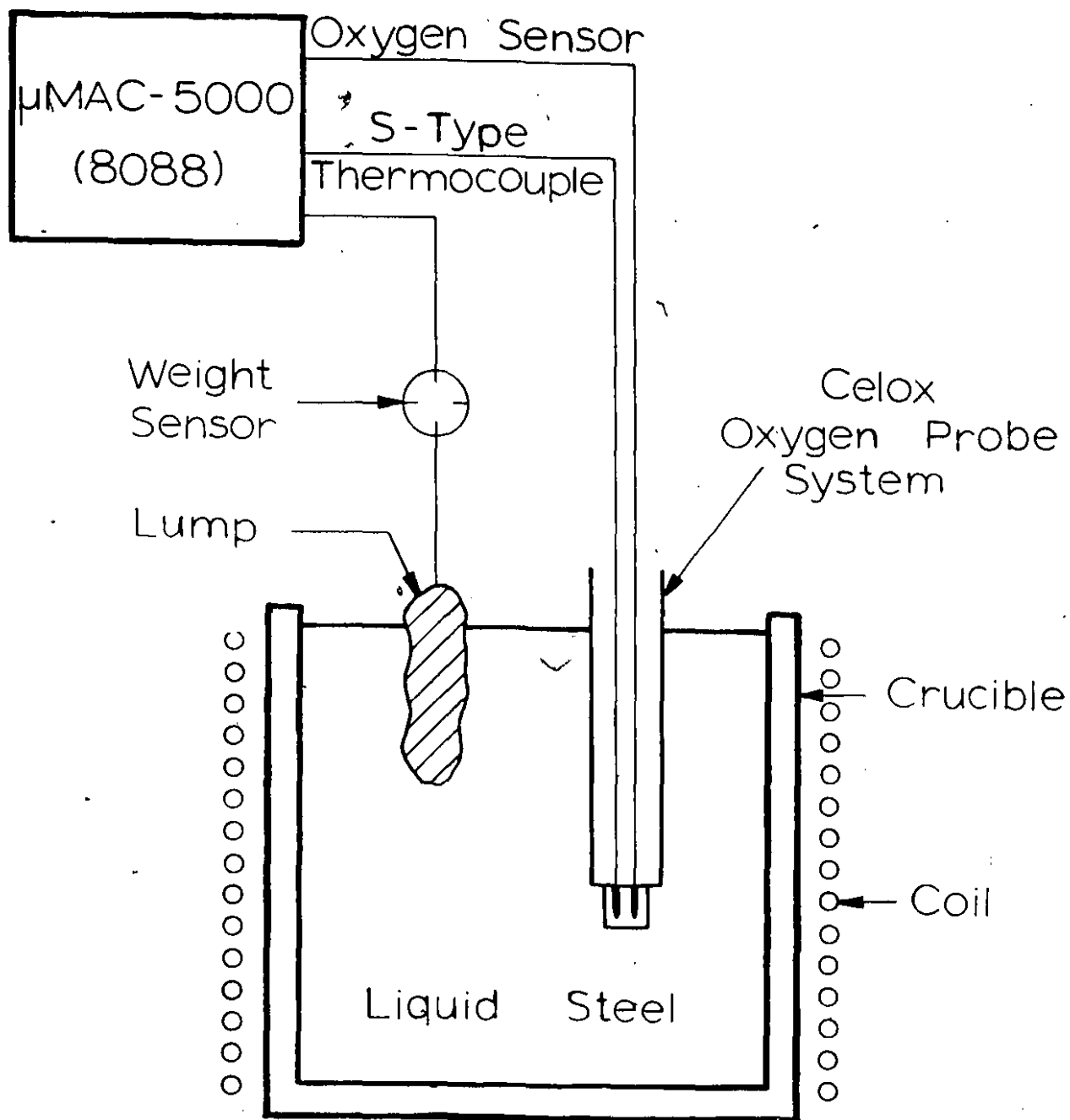


Figure 7.4 Schematic cross-section of the induction furnace with ferroalloy lump, weight sensor, CELOX oxygen-probe system, and the intelligent satellite microperipheral  $\mu\text{MAC-5000}$ .

Spectrometer (SPECTROVAC 1000 Model DV-2) was used for the chemical analysis of samples, which were aspirated from the steel bath. In general terms, the following procedure was followed: When the ARMC0 IRON had melted and the temperature had first reached 1600°C (1873 K), the measured active oxygen was found to be 1200 ± 50 ppm. Prior to every solution rate measurement, the active oxygen and the temperature of steel bath were recorded. After measuring the solution speed, an aspirated sample was taken from the steel bath for chemical analysis. The following formula was used for the calculation of recoveries:

$$R_{\text{Nb}} = \frac{m_{\text{Nb}}}{m_{\text{FeNb}}} 100\% \quad (7.2)$$

where  $R_{\text{Nb}}$  = niobium recovery;

$m_{\text{Nb}}$  = mass of the ferroalloy that was found in the liquid steel after chemical analysis;

$m_{\text{FeNb}}$  = mass of the ferroalloy which was found to be transferred into the liquid steel by the weight sensor.

Figure 7.5 presents typical dissolution of standard ferroniobium into liquid steel. These results were obtained immediately after the measurements illustrated in Figure 7.6. Curve 1 (Figure 7.6) shows that the temperature of the melt was around 1873 K, and Curve 2 of the same figure illustrates that the active oxygen content was almost 1100 ppm. The slope of the segment DE (Figure 7.5) is very small, and this is an indication of a very low dissolution speed of standard

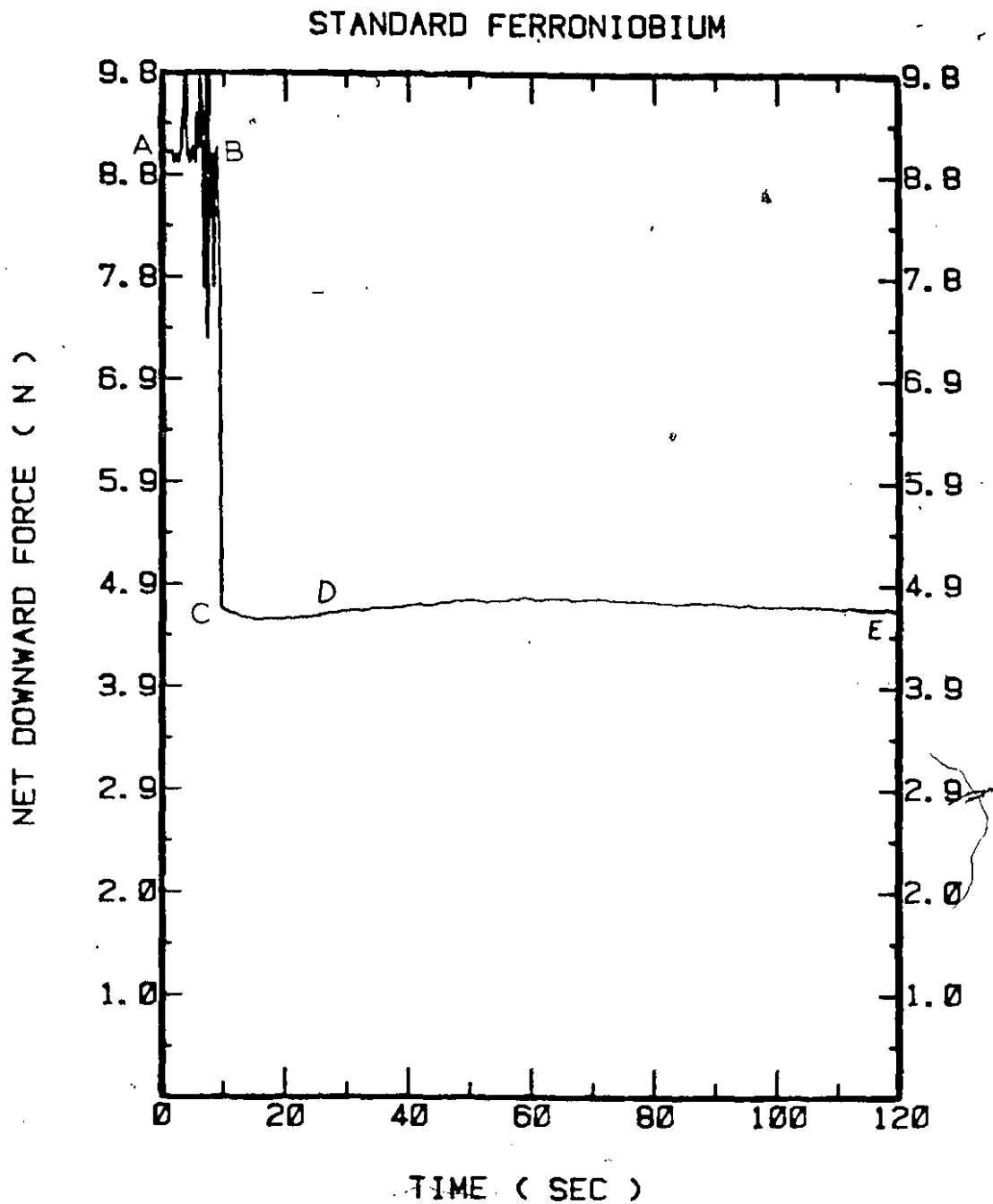


Figure 7.5 Typical experimental result obtained from measuring dissolution of standard ferro-niobium in liquid steel. The active oxygen of liquid steel for this case is shown in Figure 7.6.

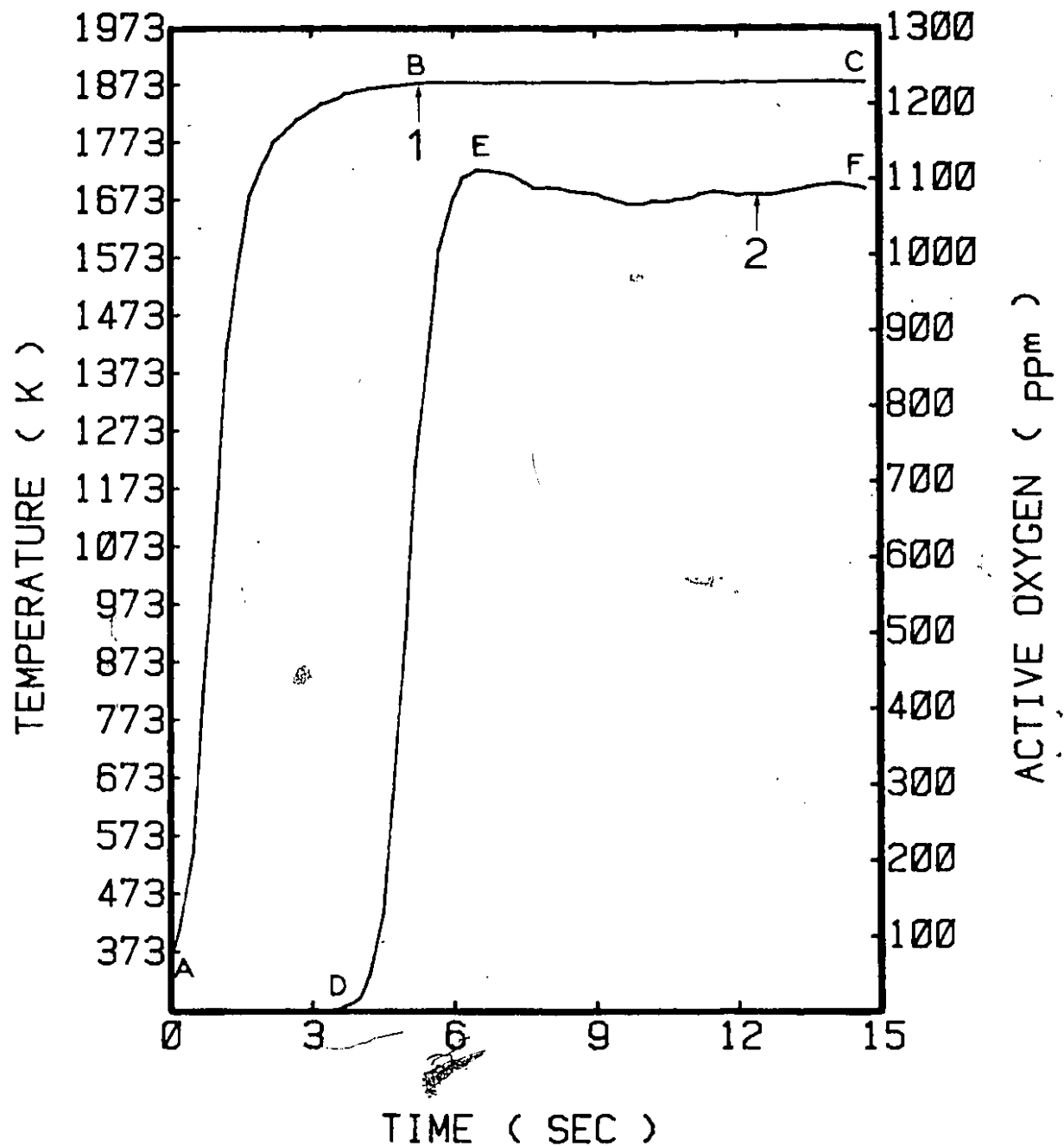


Figure 7.6 Typical experiment results obtained by the CELOX oxygen-probe system. Just prior to measuring the dissolution rate of the standard ferroniobium lump (Fig. 7.5), curve 1 shows the measured temperature, and curve 2 depicts the recorded active oxygen in liquid steel in ppm.

ferroniobium in a steel bath with 1100 ppm active oxygen content.

Figure 7.7 shows experimental results for standard ferroniobium, where the measured recovery is plotted against the measured active oxygen of the steel bath. Linear regression analysis of these results was performed, in order to deduce a relationship between the recovery of niobium and the active oxygen in the steel bath. The equation for Curve 1 in Figure 7.7 is:

$$R_{\text{Nb}} = 70.5 - 0.045 (O) \quad (7.3)$$

with a correlation coefficient of 0.973 at 7 degrees of freedom and a standard error of estimate 4.47. These results show quite clearly that as the active oxygen increases the expected recoveries decrease. This is because, under these conditions the ferroalloys act as deoxidizers. In the case of fully killed steel (i.e., very small active oxygen), the present correlation agrees well with the niobium efficiency given by Silver<sup>149</sup>: 75% ( $\pm 11\%$ ).

Figure 7.8 shows the effect of active oxygen on the dissolution speed of standard ferroniobium lumps. It seems that there is a significant effect on the dissolution speed resulting from the active oxygen. Linear regression analysis of these results was performed for a relationship between the solution rate and the active oxygen in the steel bath. The equation for Curve 1 in Figure 7.8 is:

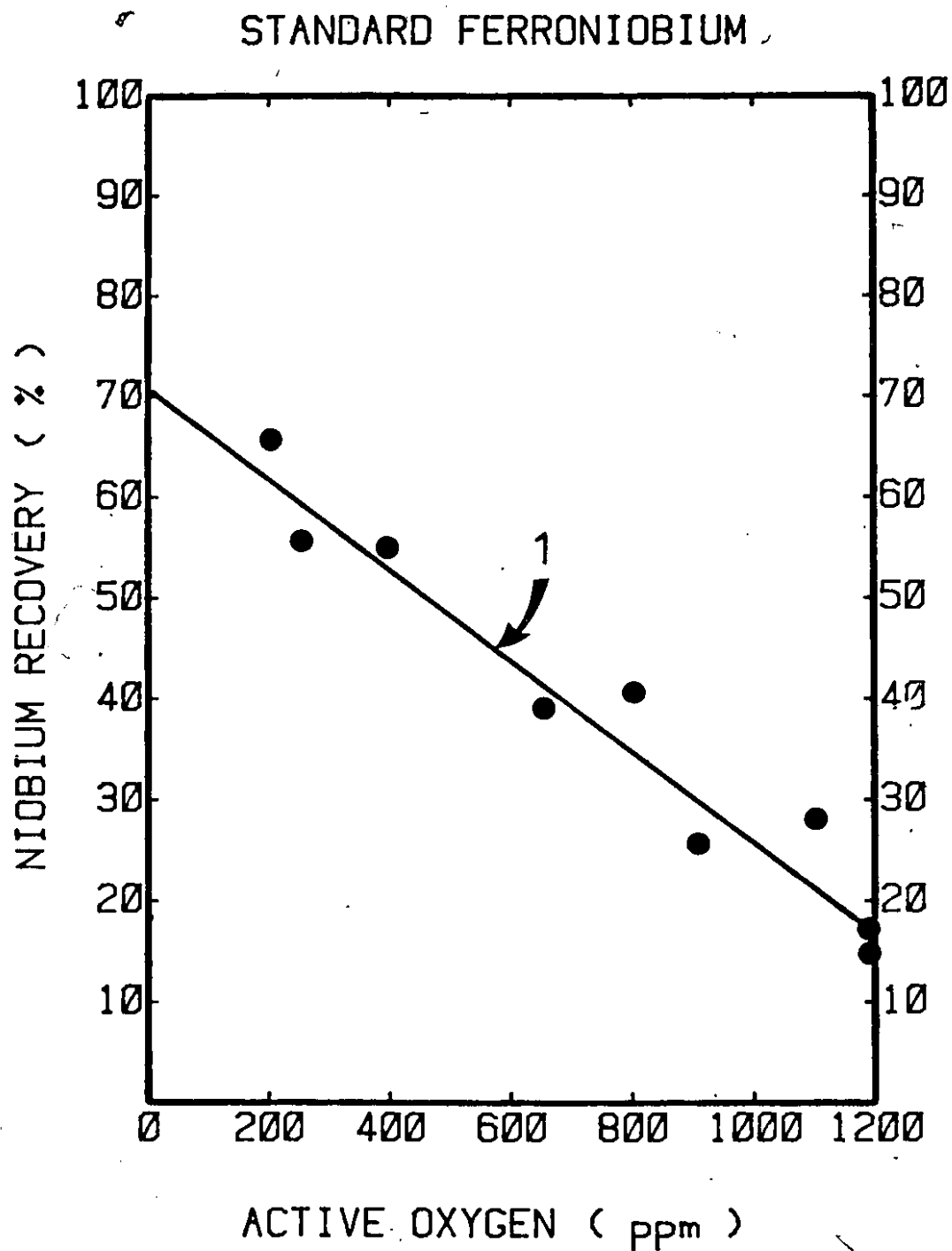


Figure 7.7 Niobium recovery from standard ferroniobium lumps as a function of active oxygen in liquid steel. Curve 1 shows the regression line.

### STANDARD FERRONIObIUM

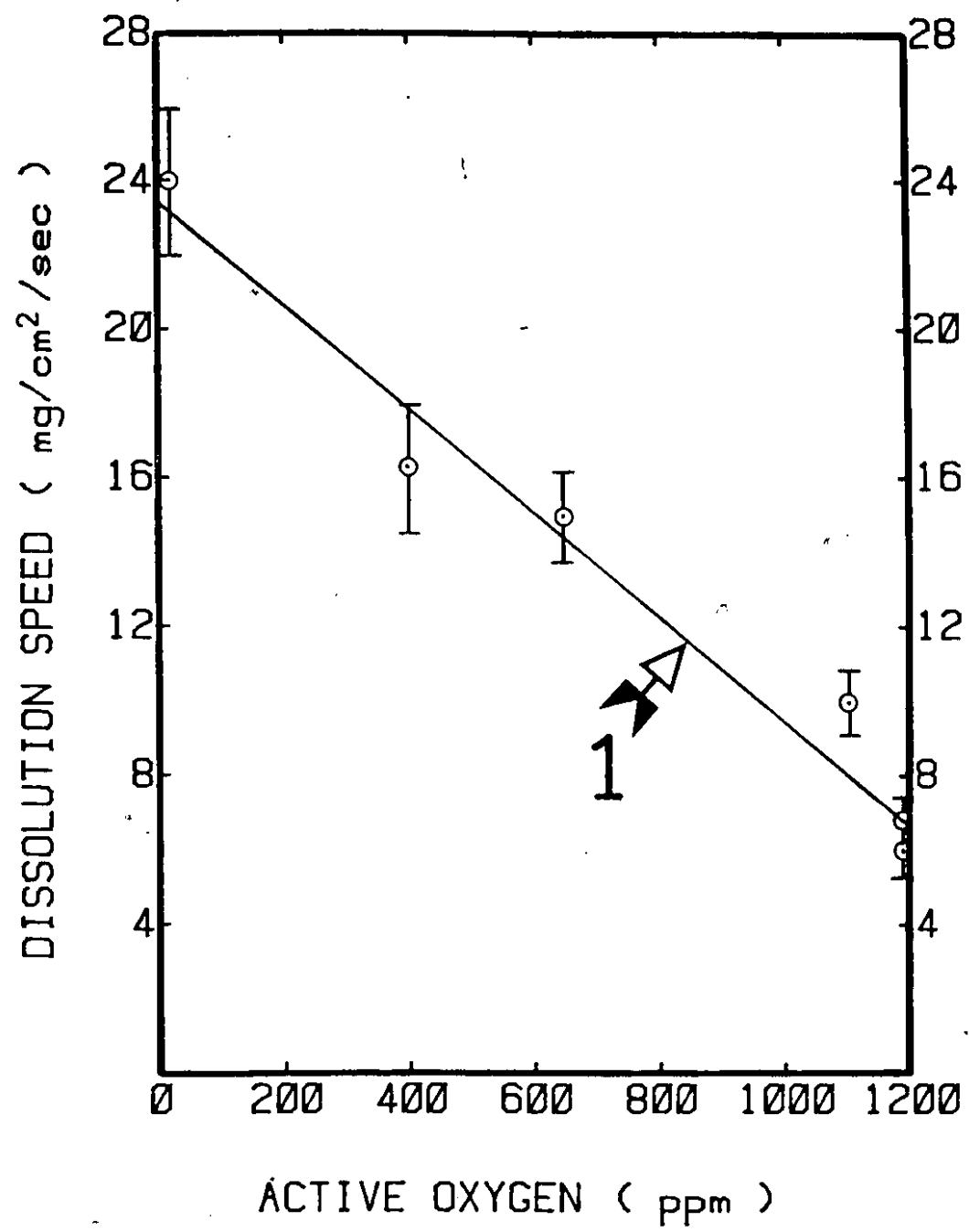


Figure 7.8 Dissolution speed of standard grade ferro-niobium lumps as a function of active oxygen in liquid steel.

$$u = 23.4 - 0.014 [O] \quad (7.4)$$

where  $u$  = dissolution speed (in  $\text{mg}/\text{cm}^2/\text{sec}$ ) with a correlation coefficient of 0.984 at 4 degrees of freedom and a standard error of estimate 1.34. Although the active oxygen content does not seem to influence the dissolution speed of ferroalloys with melting range below the steel bath temperature, it exhibits a negative effect on the solution rate of ferroalloys with melting points above the temperature of the liquid steel; the 80% grade ferrovanadium is another example (see reference 83). This can be explained by the fact that these (high melting point) ferroalloys follow a dissolution (not melting) mechanism, and consequently, their assimilation into liquid steel is very slow. Since the standard ferroniobium has very slow dissolution kinetics, it has a greater chance of forming solid refractory oxides whenever it is used in a steel bath with a high active oxygen content. This in turn, might reduce their effective dissolution speed. Similar results have been observed for the dissolution characteristics of the 80% grade ferrovanadium in liquid steel<sup>83</sup>.

#### 7.5 THE DISSOLUTION OF Nb-Ni ALLOYS IN LIQUID STEEL

The Nb-Ni alloys are not so extensively used in the steel industry. Depending on specific customer demands however, these alloys can sometimes be employed. Furthermore, ~~the~~ simultaneous introduction of two important alloying

elements (niobium and nickel) into liquid steel, with the use of just one alloy addition, may also have positive economic benefits. Finally, as it will be discussed in this section, the fast solution rates that this alloy exhibits in liquid steel, make it an attractive alternative with respect to customary ferroniobium and/or ferronickel alloys.

The solution rates of lumps from this alloy in liquid steel were experimentally measured. The chemical composition of the Nb-Ni alloy used, is given in Table 7.1. The densities of these lumps were found to be in the range  $8740 \pm 174 \text{ kg/m}^3$ .

Figure 7.9 illustrates a typical experimental result from the dissolution of a lump of this alloy in liquid steel. This test was performed under static conditions in a steel bath with an average temperature of  $1625^\circ\text{C}$  (1898 K). Curve 1 depicts the bath temperature as recorded by the DAPC facility during the test. Curve 2 shows the monitored net downward force. Similarly, the segment BC signifies the immersion period, while the segment CD represents the steel shell period. The part DE of Curve 2, is the free dissolution period of the lump in the molten steel. It seems that this alloy exhibits a relatively fast solution rate, and therefore, no significant changes to the net downward force are recorded during the period represented by the segment EF. Table 7.2 gives the measured solution rates (or equivalently, the mass fluxes) of this alloy in quiescent steel baths at various temperatures. Table 7.2 also presents an average rate of

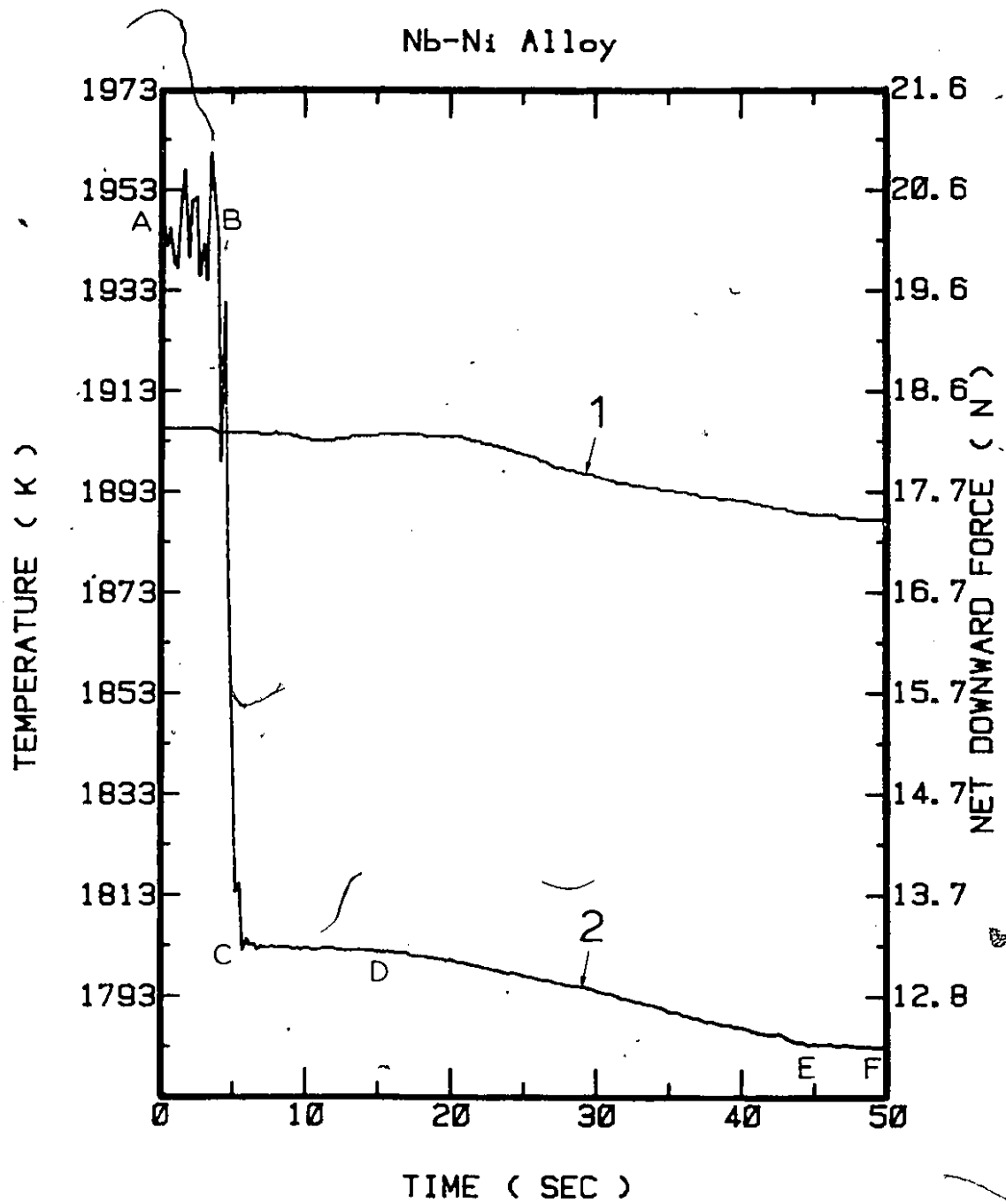


Figure 7.9 A typical experimental result from the melting of a niobium-nickel lump in liquid steel.  
 1) Measured steel bath temperature;  
 2) Registered net downward force.

Table 7.2

Solution Rates of Nb-Ni Lumps  
in Liquid Steel Under Static Conditions

Temperature	Mass (g/cm <sup>2</sup> /sec)	Flux (kg/m <sup>2</sup> /sec)	(-dr/dt) 10 <sup>3</sup> (cm/sec)
1605°C (1878 K)	0.103 (± 0.008)	1.03 (+ 0.08)	11.78
1610°C (1883 K)	0.110 (+ 0.009)	1.10 (+ 0.09)	12.59
1625°C (1898 K)	0.147 (+ 0.012)	1.47 (+ 0.12)	16.82
1634°C (1907 K)	0.220 (± 0.018)	2.20 (± 0.18)	25.17

change of radius of hypothetical spheres of this alloy, which exhibit the given solution rates at the corresponding average bath temperatures. One can generally notice, that this alloy dissolves relatively fast in liquid steel, even under static conditions. An inspection of the Nb-Ni phase diagram<sup>120</sup> shows that the liquidus temperature of the 65 wt% Nb - 35 wt% Ni alloy is about 1310°C or 1583 K. Deeley<sup>1</sup> gives 1583 K and 1613 K for the solidus and liquidus temperatures of this ferroalloy, respectively. It seems that the solution mechanism of this alloy in liquid steel is melting, and not dissolution. Figure 7.10 shows predictions for the total melting times of Nb-Ni spheres of various diameters in liquid steel under static conditions.

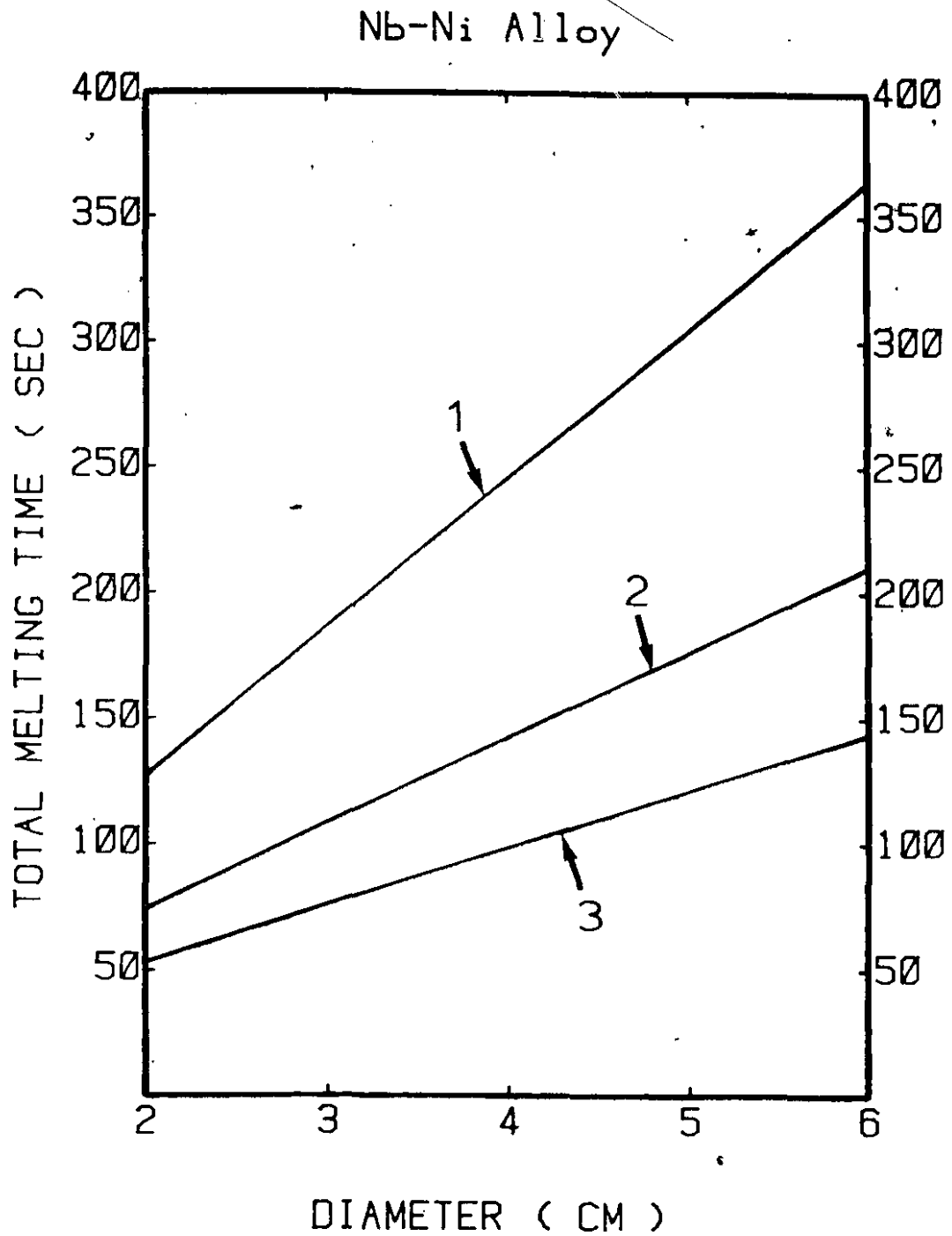


Figure 7.10 Predictions for total melting times of spherical niobium-nickel lumps in liquid steel under static conditions:  
1) Liquid steel at 1600°C (1873 K);  
2) Liquid steel at 1615°C (1888 K);  
3) Liquid steel at 1630°C (1903 K).

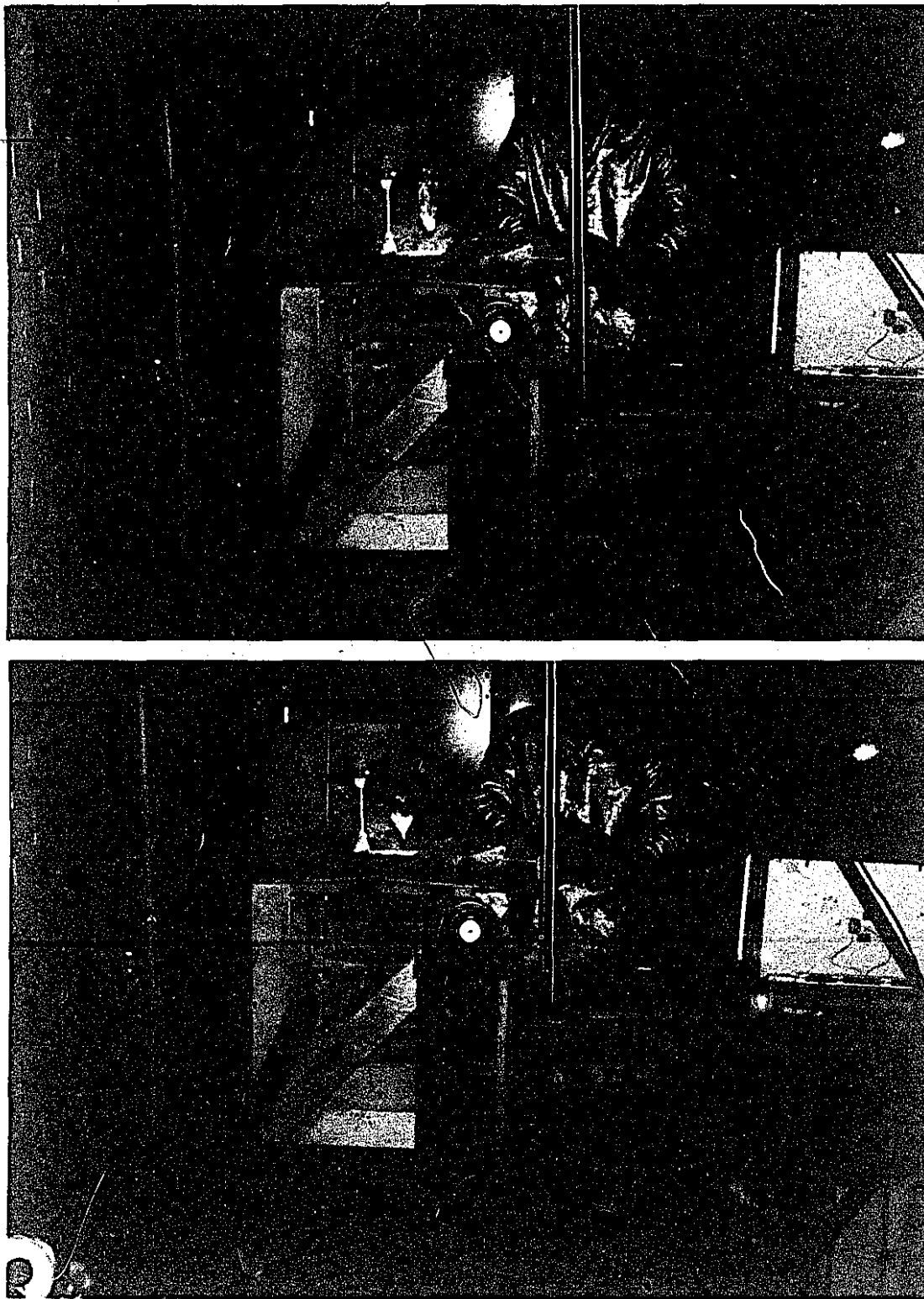


Figure 7.11 A typical sequence of events occurring during a typical melting test of a niobium-nickel alloy in liquid steel.

CHAPTER 88. CONCLUSIONS

The purpose of this work was to investigate the phenomena which take place during the dissolution of niobium and zirconium in liquid steel. Some conclusions are summarized below:

1) For the dissolution of niobium and zirconium cylinders in liquid steel two distinct periods were identified. The 'steel shell period' and the 'free dissolution period'.

2) Depending on the steel bath superheat and the fluid flow patterns in the vicinity of a niobium cylinder, which is kept motionless in liquid steel, a reaction may or may not take place at the steel shell/niobium interface. The conditions under which this reaction does occur have been investigated, and the reaction products have been identified. As this reaction generally takes place at the final stages of the steel shell period, the produced exothermic heat has a negligible effect on the duration of the steel shell period.

3) Niobium dissolves relatively slowly in liquid steel and its dissolution rate is greatly enhanced when the melt is inductively (or otherwise) stirred.

4) In the early stages of the steel shell period, and when the temperature at the steel shell/zirconium interface is around  $947^{\circ}\text{C}$  (1220 K), the dissolution reaction starts. A liquid film of eutectic composition then forms and an exothermic reaction is initiated. The heat generated from

this reaction makes the steel shell period shorter. The heat involved in this reaction has been quantified and its net effect (in the form of heat flux) has been determined.

5) The dissolution rates of zirconium cylinders have been measured during the free dissolution period. Due to the vigorous exothermic dissolution of zirconium in liquid steel, the temperature at its dissolving front exceeds the bath temperature causing the dissolution to accelerate. In the final stages of the free dissolution period, the temperature of the zirconium cylinder increases so much, that it reaches the zirconium melting point.

6) For the experimental conditions under which these tests were carried out, the dissolution rate of zirconium was not influenced by the induction stirring of the melt. Without any more experimental evidence (i.e., experiments carried out in bigger vessels), this conclusion should be restricted for those conditions under which this study was undertaken.

7) An existing mathematical model has been extended, in order to describe the coupled heat and mass transfer events which take place during the dissolution of both metals in liquid steel. The model provided a good quantitative representation of the processes studied.

8) The dissolution of some ferroniobium and ferro-zirconium alloys in liquid steel was investigated. The effect of oxygen on the niobium recovery and the dissolution of standard ferroniobium lumps, was also examined. A mass

transfer mechanism seems to control the dissolution rates of most ferroalloys studied. In the case of the 80% grade ferrozirconium and the 65% Nb-Ni alloys, melting seems to be the mass transfer mechanism which determines their assimilation in liquid steel. D

CHAPTER 99. FUTURE WORK

As it has been mentioned in the Chapters 6 and 8, the dissolution rates of pure zirconium cylinders in liquid steel seems to be independent of the fluid flow characteristics of the steel bath. This conclusion is restricted only to the experimental conditions under which these tests have been carried out. Similar tests should be performed in ladle metallurgy stations for example, where larger quantities of steel can be treated and more powerful stirring systems can be applied. In this way the dissolution rates of zirconium could be measured under the maximum possible degree of turbulence.

Another area where further work is called for is in the determination of the various factors which reduce the dissolution rates of Class II ferroalloys (i.e., ferroalloys with melting range above the steel-bath temperature) in liquid steel with high level of active oxygen content.

Finally, the heats of mixing of liquid iron-zirconium alloys should be measured experimentally.

CHAPTER 1010. CLAIM TO ORIGINALITY

According to the author's opinion, the following aspects are contributions to original knowledge:

1) The steel shell period of niobium cylinders in liquid steel has been investigated for the first time. Conditions under which a reaction takes place at the steel shell-niobium interface have been examined. The reaction products have been identified.

2) The free dissolution period of niobium cylinders in liquid steel has been studied. The dissolution rates, at various bath temperatures and fluid flow conditions (static or dynamic), have been measured in a detailed manner for the first time.

3) A thermodynamic study for the heats of mixing of Fe-Zr liquid alloys has been performed, and mathematical equations have been proposed.

4) The steel shell period of zirconium cylinders in liquid steel has been examined for the first time. The reaction which occurs at the steel shell-zirconium interface has been investigated, and the reaction products have been identified.

5) The exothermic, self-accelerating dissolution of zirconium cylinders in liquid steel has been experimentally measured for the first time. For the experimental conditions under which the tests were carried out, the induction stirring did not seem to influence the dissolution rates.

6) A mathematical model has been proposed, which gives predictions for the coupled heat and-mass transfer phenomena which participate during the free dissolution period of niobium and zirconium in liquid steel.

7) The effect of oxygen on the dissolution and recovery of the standard ferroniobium has been investigated for the first time.

7

ACKNOWLEDGEMENTS

The author would like to express his sincere appreciation, gratitude, and respect to Professor S. A. Argyropoulos for his guidance and assistance during the course of this work.

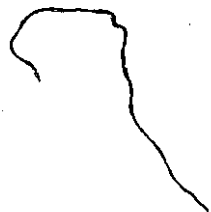
I am grateful to Professor R. Baliga from the Department of Mechanical Engineering, for the constructive discussions we had on the mathematical modelling of the heat transfer events during the free dissolution period.

I would like to express my appreciation to Professor D. Berk from the Department of Chemical Engineering, for his reading part of the manuscript of this thesis, and for his ideas and recommendations on the free dissolution of zirconium in liquid steel.

I am thankful to:

- the technician, B. Grondin, for his careful drilling of the specimen holes for the introduction of the thermocouples;
- the technician, R. Paquette, for his assistance in the execution of the experiments;
- Mrs. Quangbi Chen for the careful preparation of the samples used for microprobe analysis;
- Mr. Donato De Santis, a colleague and friend, for his proof-reading the text of this thesis;
- Dr. Brian L. Jones from NIOBIUM PRODUCTS CO. LTD., for his kindness in providing one niobium cylinder (3.81 cm in diameter) for free;
- the people of the Electro-Nite Company for providing Celox oxygen probe systems.

Finally, the author would like to express his sincere appreciation to the Natural Sciences and Engineering Research Council of Canada and the Faculty of Graduate Studies and Research of McGill University for providing support for this work.



APPENDIX I

TYPICAL RESULTS FROM THE

Nb IMMERSION TESTS



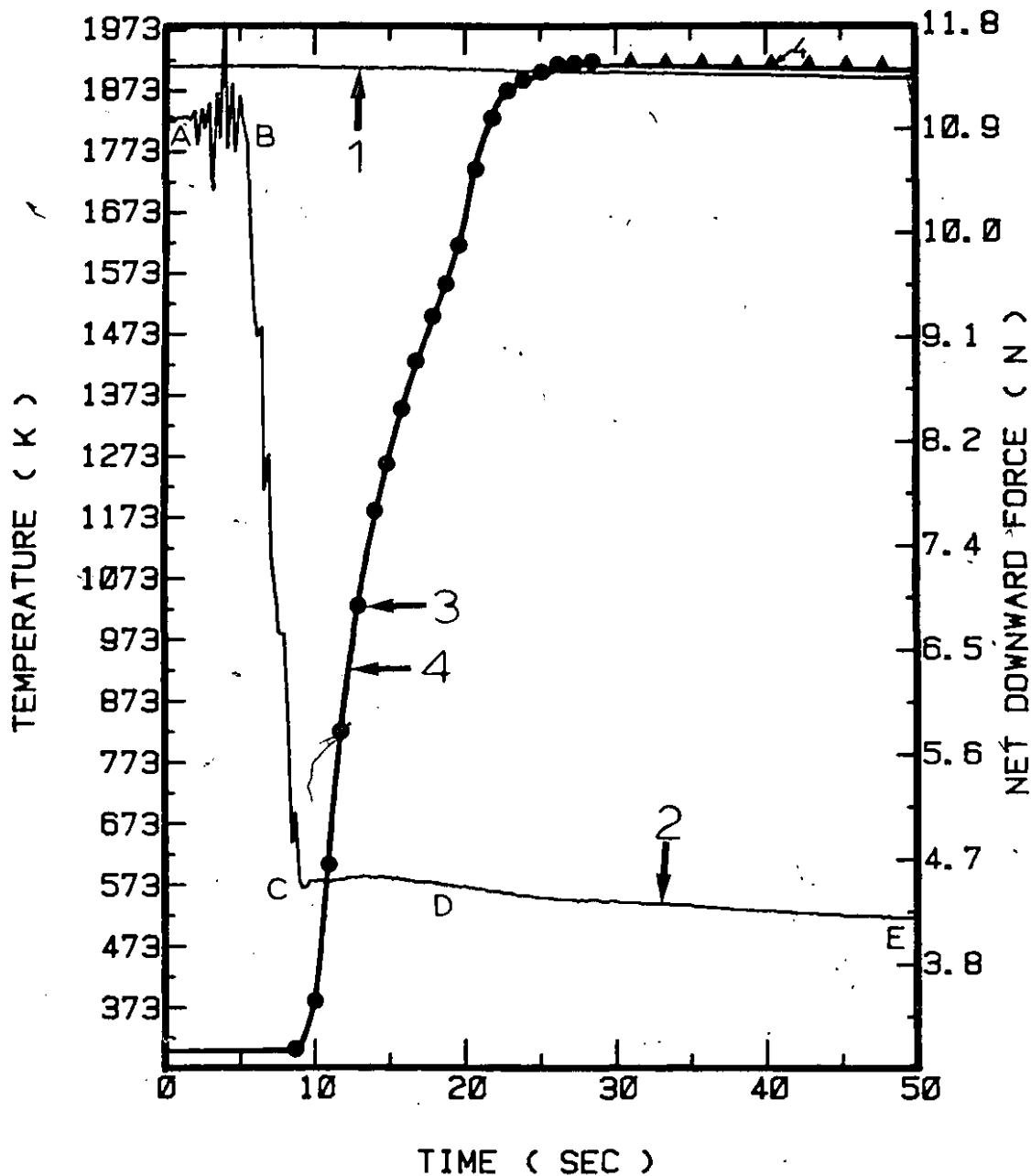


Figure I-1 Results from a typical niobium dissolution experiment (Run no. 7, Table 5.2) in liquid steel. The cylinder diameter was 2.54 cm and its length was 18 cm.

- 1) Measured steel bath temperature;
- 2) Registered net downward force;
- 3) Measured and predicted (4) centerline temperature.

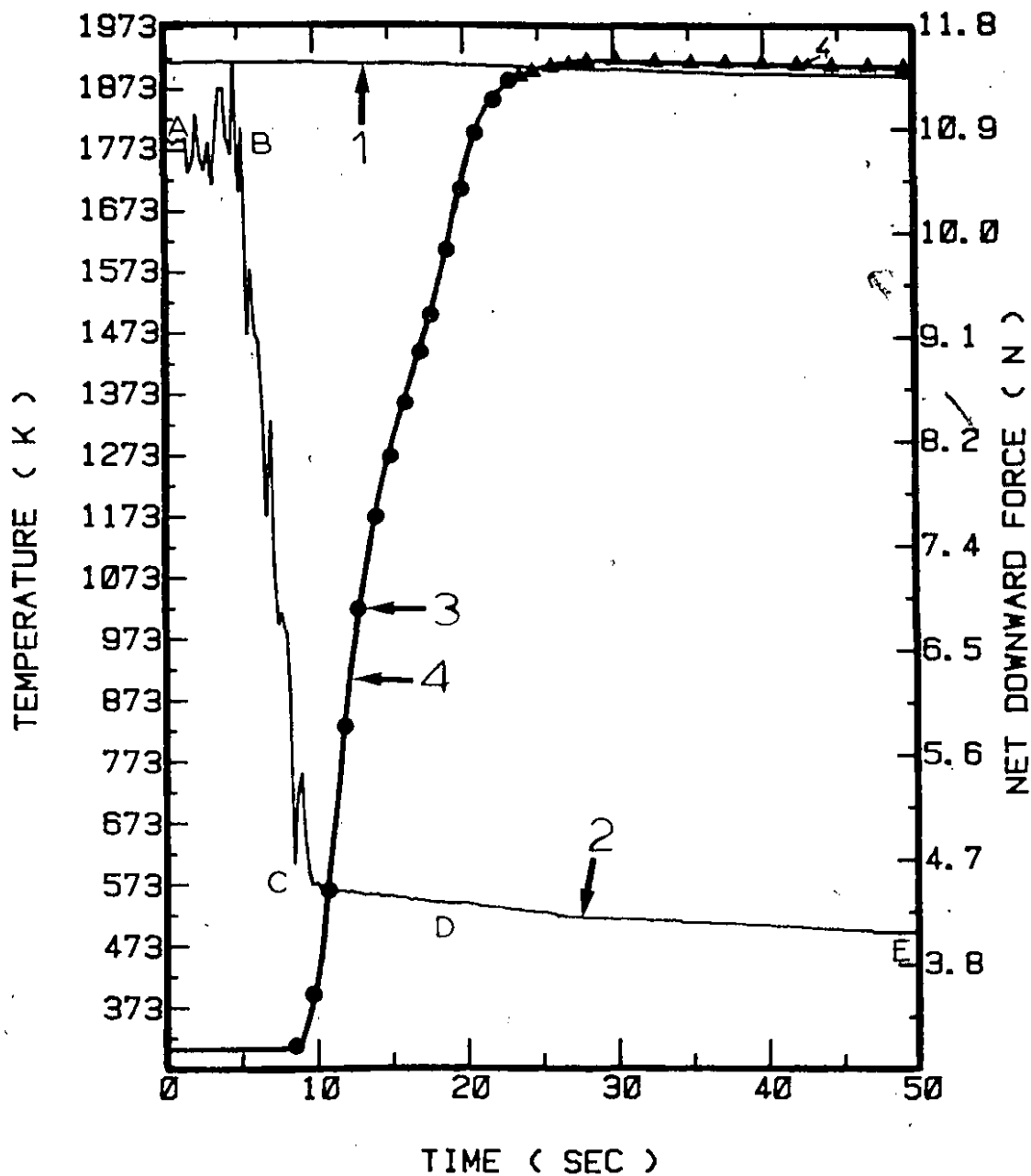


Figure I-2 Results from a typical niobium dissolution experiment (Run no. 6, Table 5.2) in liquid steel. The cylinder diameter was 2.54 cm and its length was 18 cm.

- 1) Measured steel bath temperature;
- 2) Registered net downward force;
- 3) Measured and predicted (4) centerline temperature.

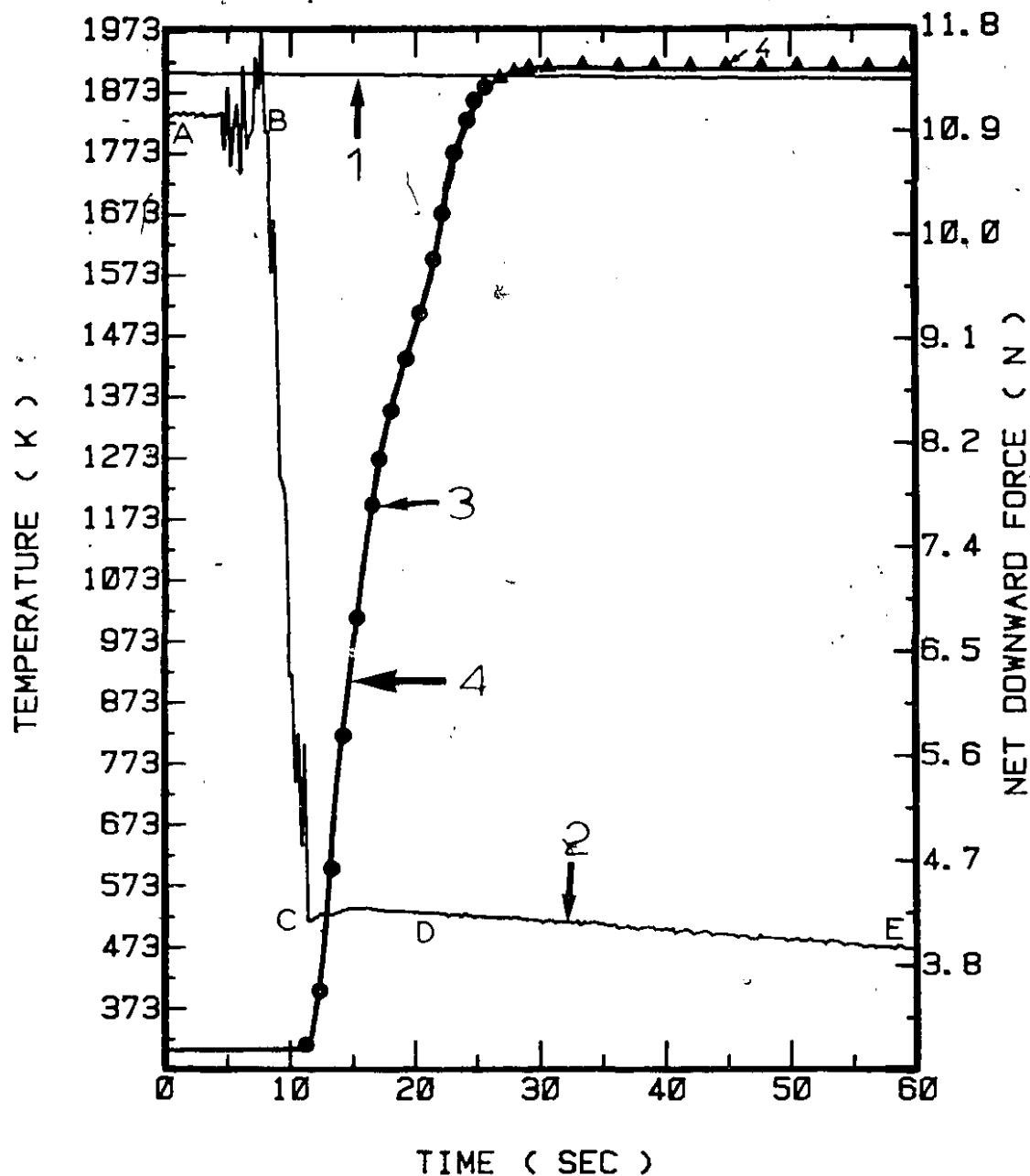


Figure I-3 Results from a typical niobium dissolution experiment (Run no. 2, Table 5.2) in liquid steel. The cylinder diameter was 2.54 cm and its length was 18 cm.

- 1) Measured steel both temperature;
- 2) Registered net downward force;
- 3) Measured and predicted (4) centerline temperature.

SR

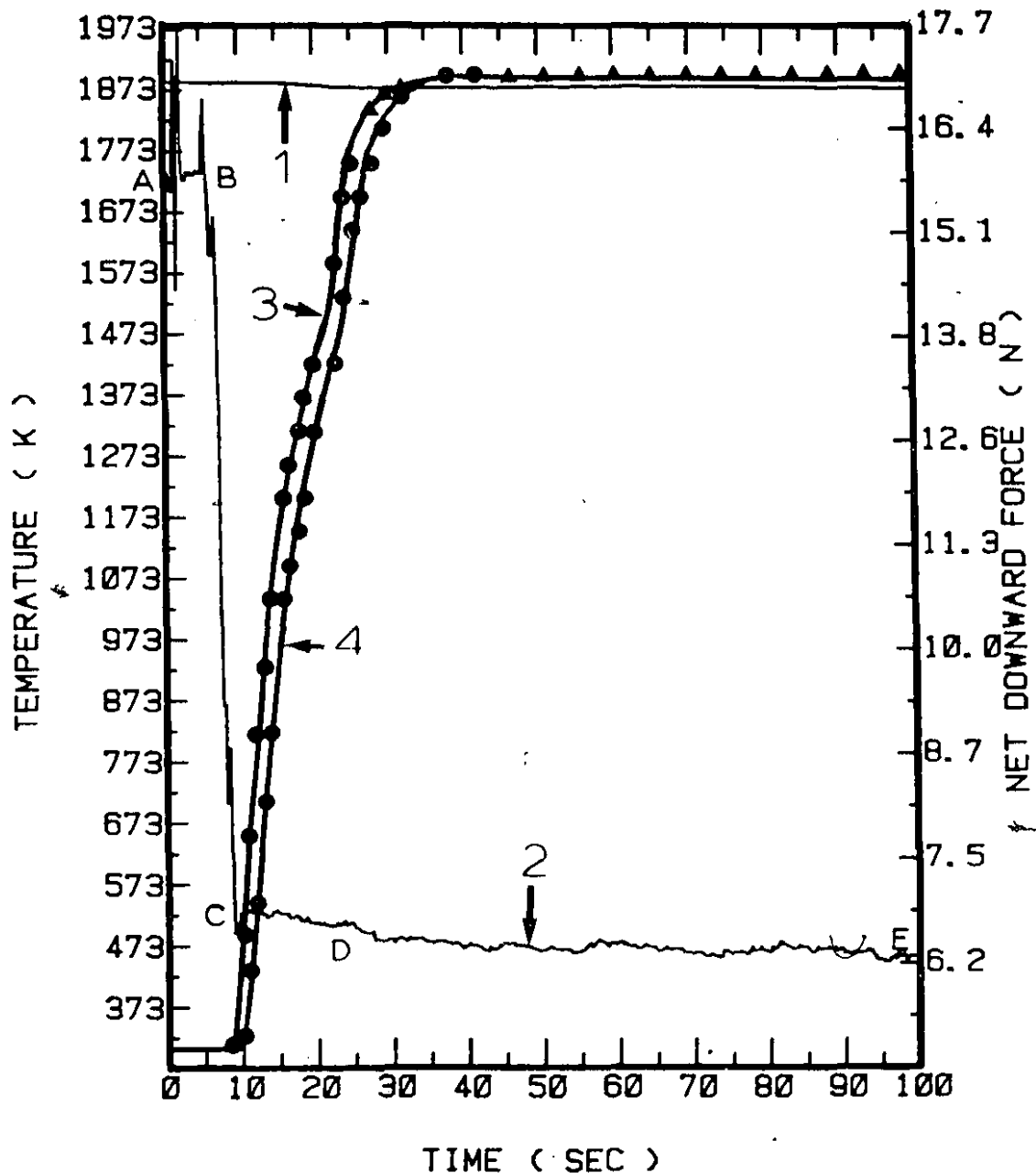


Figure I-4 Results from a typical niobium dissolution experiment (Run no. 14, Table 5.2) in liquid steel. The cylinder diameter was 3.81 cm and its length was 12.4 cm.

- 1) Measured steel bath temperature;
- 2) Registered net downward force;
- 3) Measured and predicted temperature 1.4 cm apart from the cylinder axis;
- 4) Measured and predicted centerline temperature.

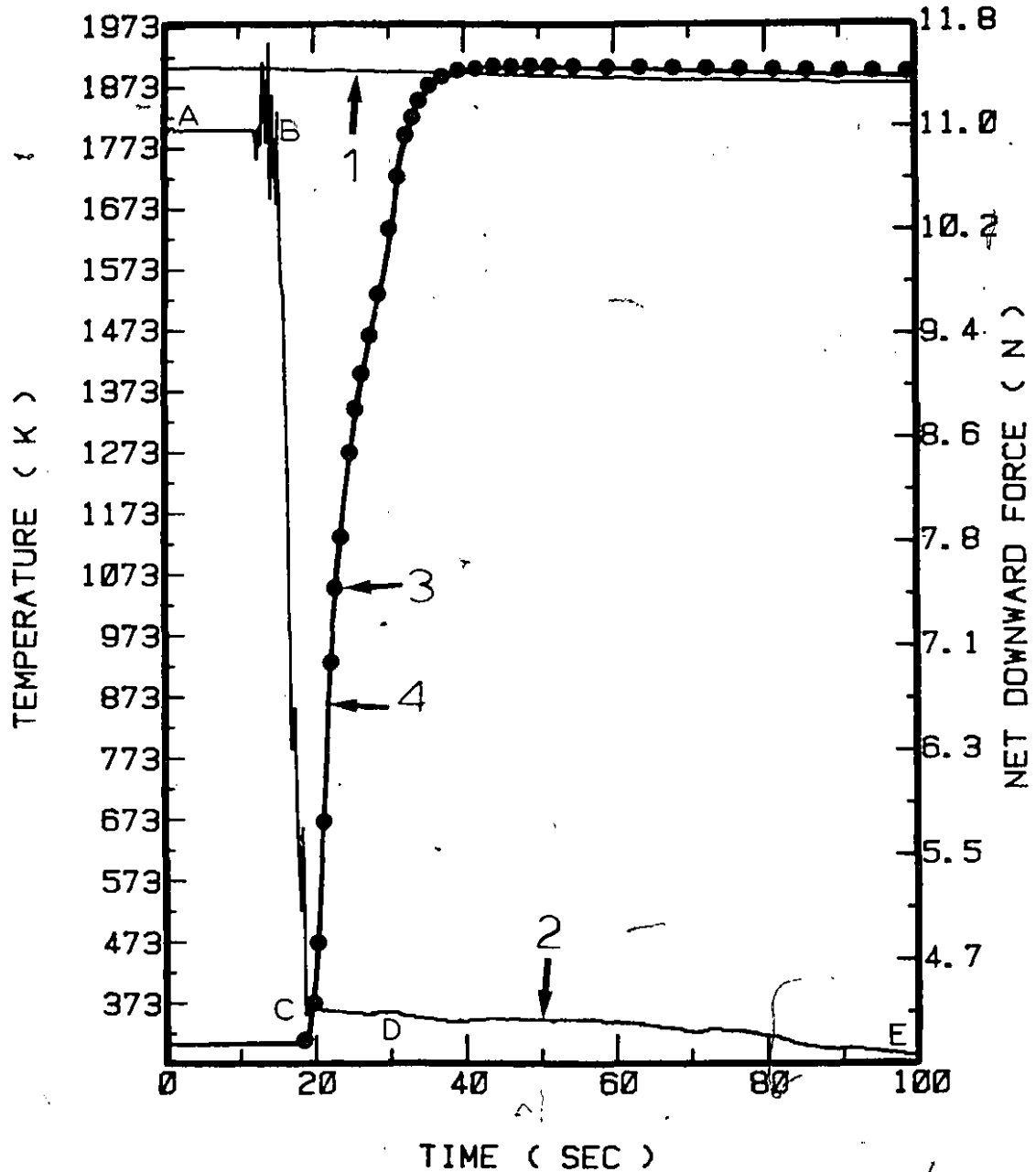


Figure I-5 Results from a typical niobium dissolution experiment (Run no. 1, Table 5.2) in liquid steel. The cylinder diameter was 2.54 cm and its length was 18 cm.

- 1) Measured steel bath temperature;
- 2) Registered net downward force;
- 3) Measured and predicted (4) centerline temperature.

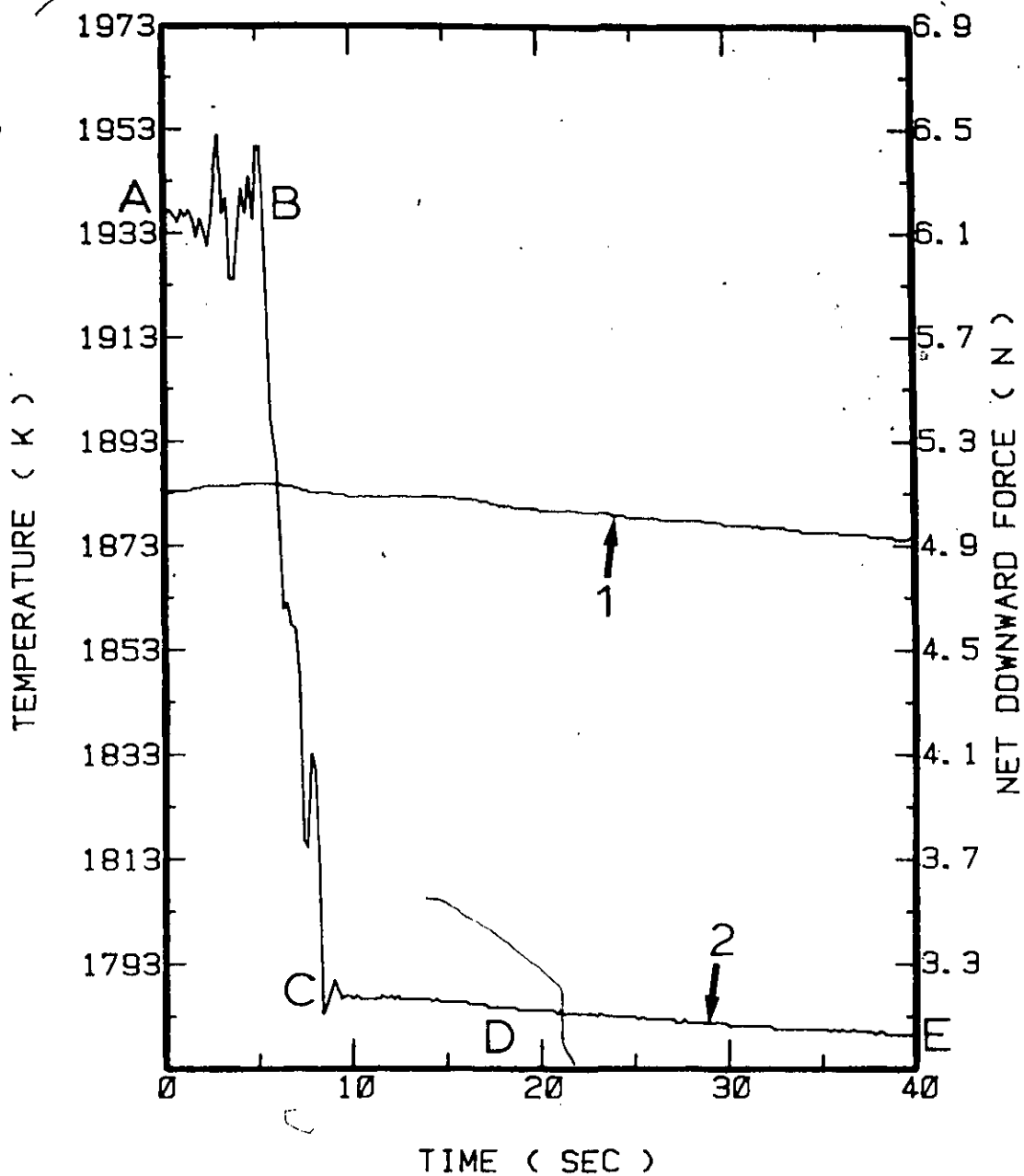


Figure I-6 Results from a typical niobium dissolution experiment (Run no. 8, Table 5.2) in liquid steel. The cylinder diameter was 1.905 cm and its length was 18 cm.  
 1) Measured steel bath temperature;  
 2) Registered net downward force.

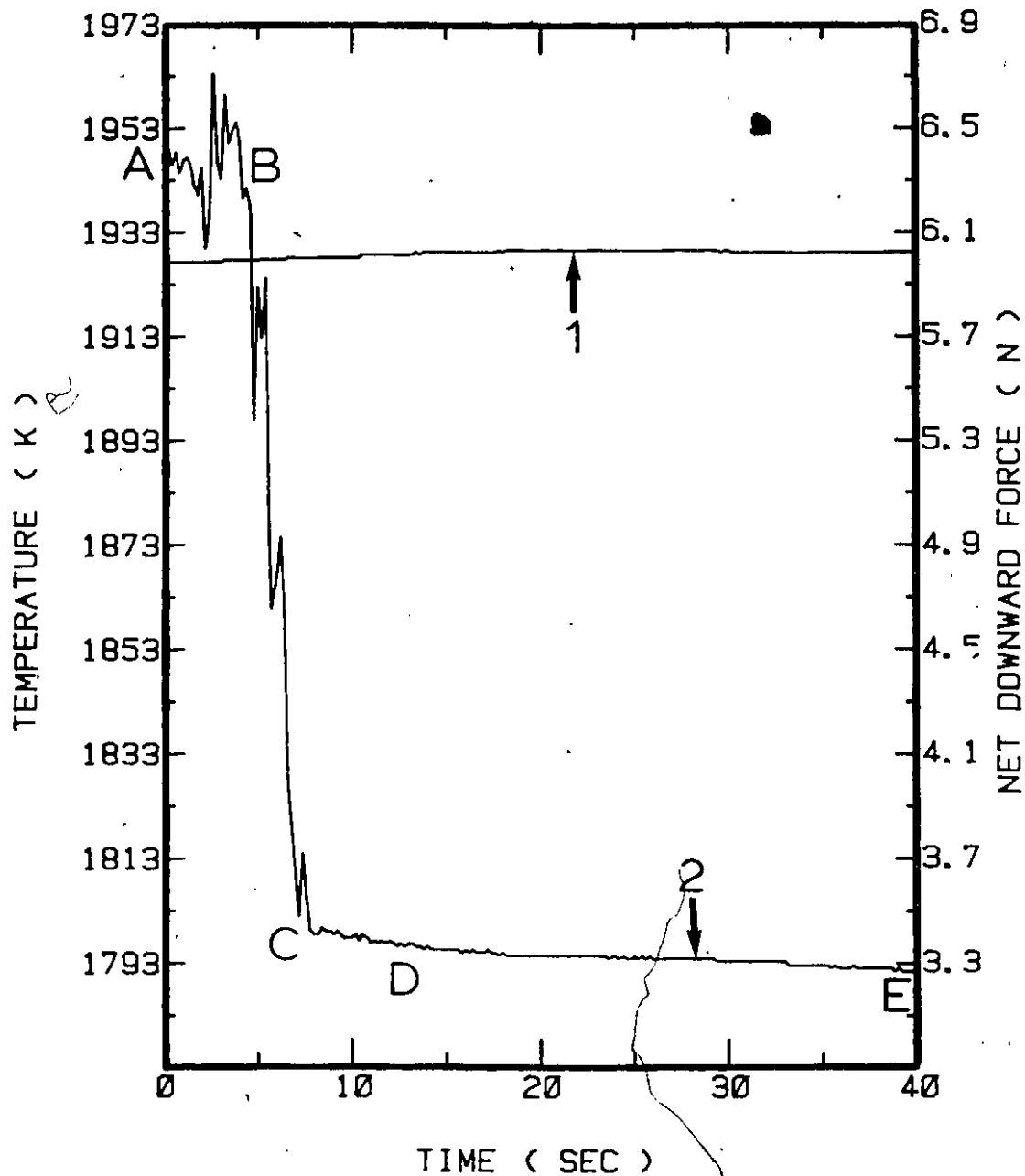


Figure I-7 Results from a typical niobium dissolution experiment (Run no. 11, Table 5.2) in liquid steel. The cylinder diameter was 1.905 cm and its length was 18 cm.  
 1) Measured steel bath temperature;  
 2) Registered net downward force.

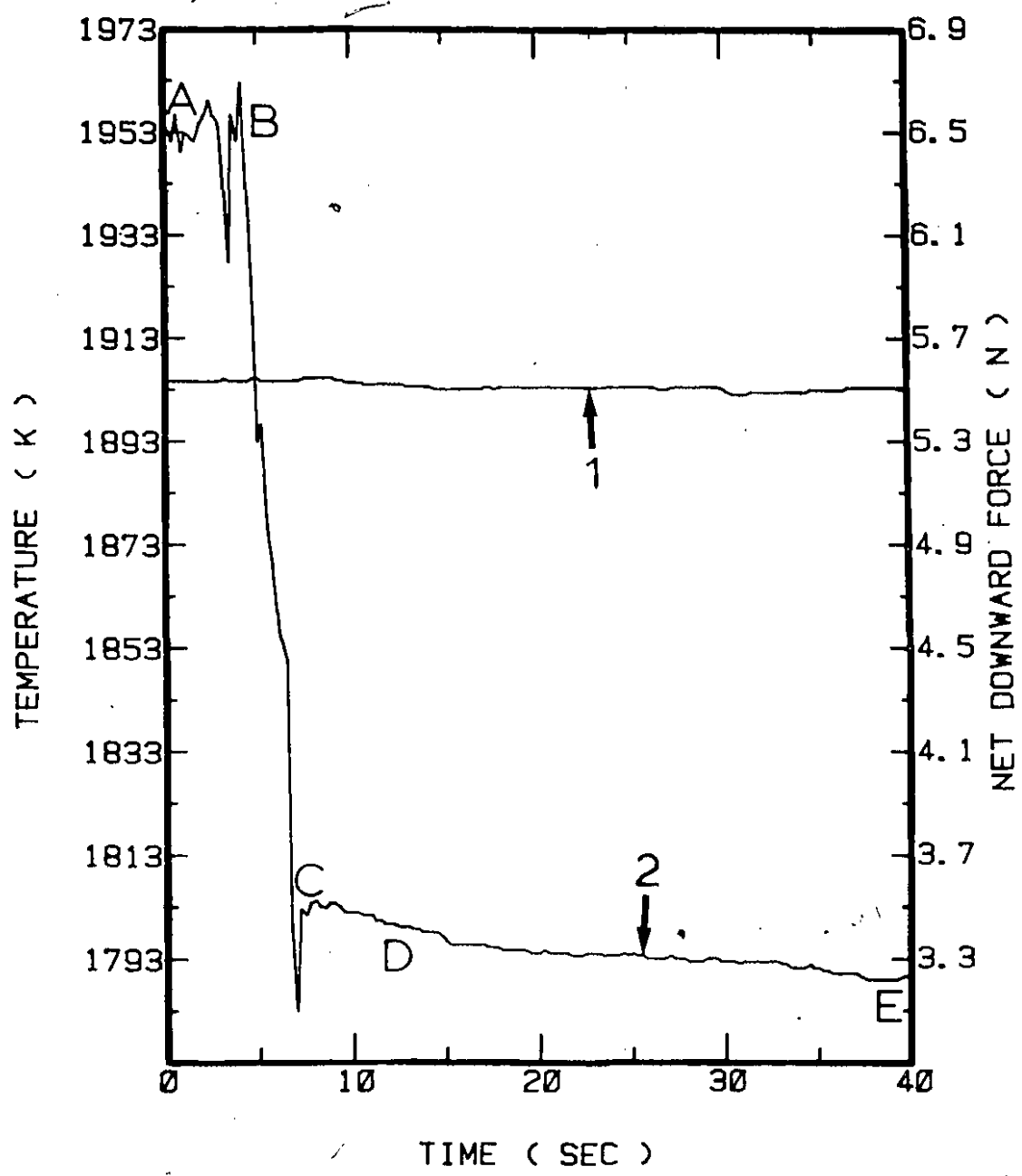


Figure I-8 Results from a typical niobium dissolution experiment (Run no. 18, Table 5.2) in liquid steel. The cylinder diameter was 1.905 cm and its length was 18 cm.  
1) Measured steel bath temperature;  
2) Registered net downward force.

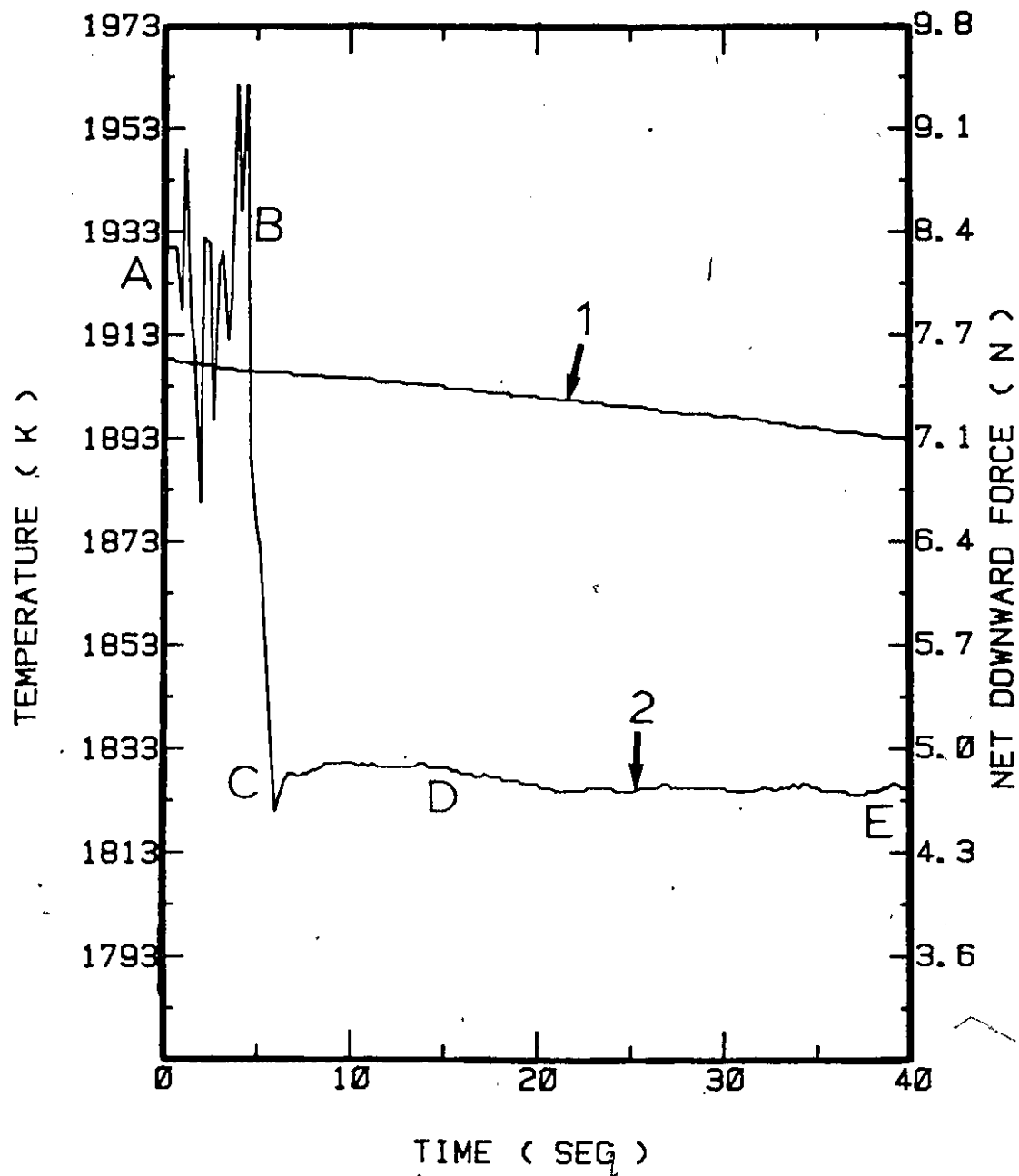


Figure I-9 Results from a typical niobium dissolution experiment (Run no. 13, Table 5.2) in liquid steel. The cylinder diameter was 1.905 cm and its length was 18 cm.  
 1) Measured steel bath temperature;  
 2) Registered net downward force.

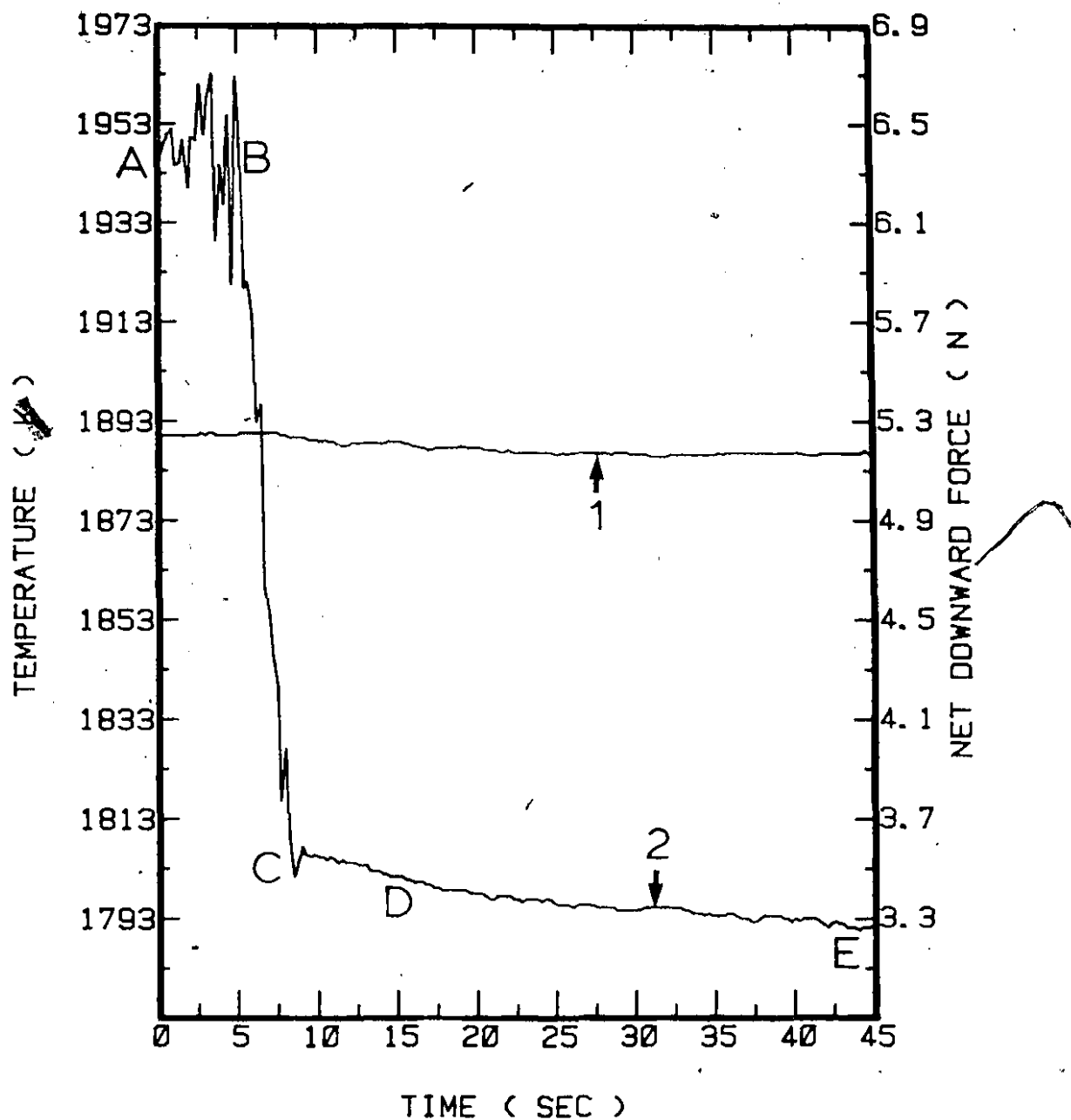


Figure I-10 Results from a typical niobium dissolution experiment (Run no. 15, Table 5.2) in liquid steel. The cylinder diameter was 1.905 cm and its length was 18 cm.  
 1) Measured steel bath temperature;  
 2) Registered net downward force.

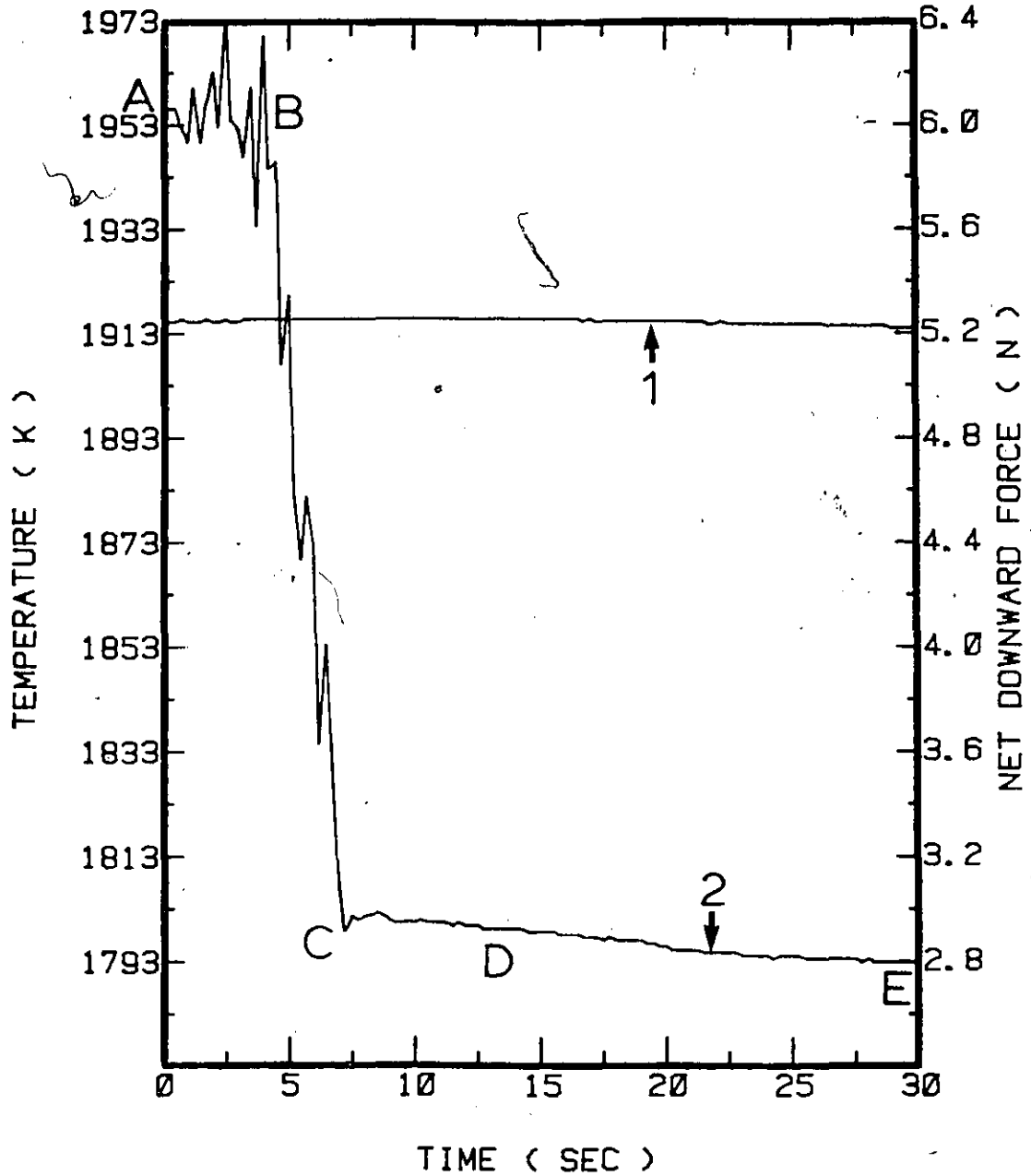


Figure I-11 Results from a typical niobium dissolution experiment (Run no. 9, Table 5.2) in liquid steel. The cylinder diameter was 1.905 cm and its length was 18 cm.  
 1) Measured steel bath temperature;  
 2) Registered net downward force.

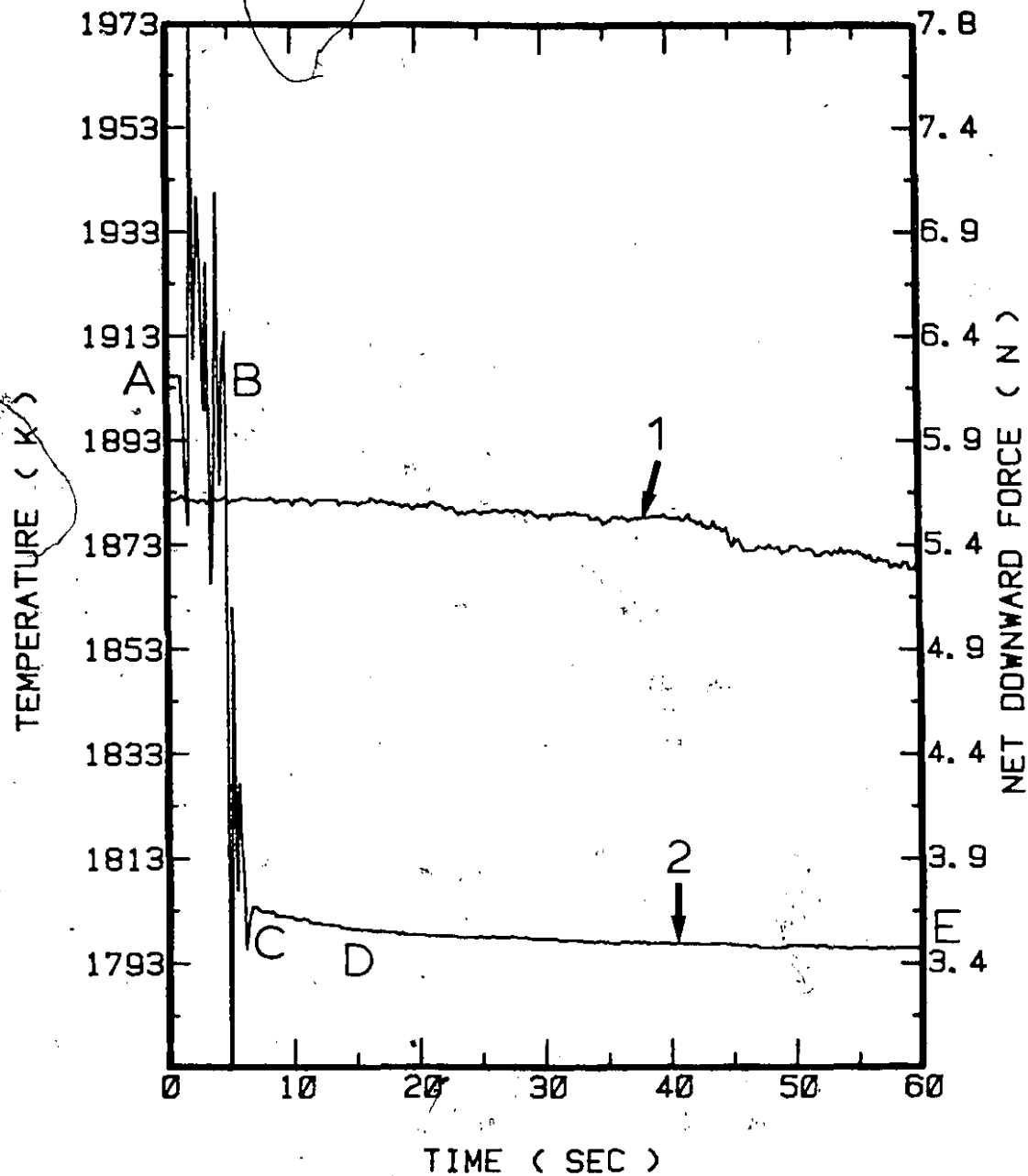


Figure I-12 Results from a typical niobium dissolution experiment (Run no. 16, Table 5.2) in liquid steel. The cylinder diameter was 1.905 cm and its length was 18 cm.  
 1) Measured steel bath temperature;  
 2) Registered net downward force.

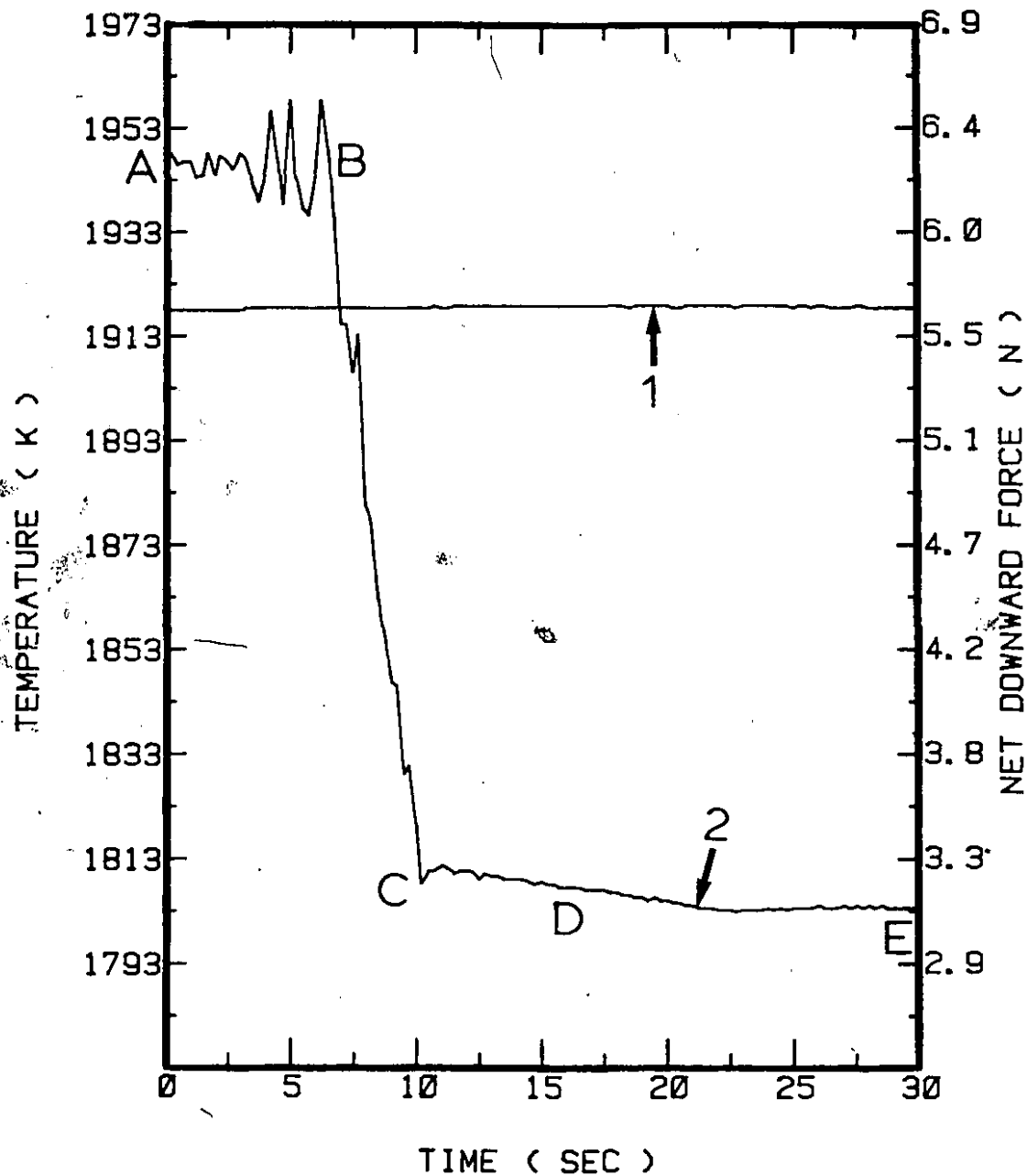


Figure I-13 Results from a typical niobium dissolution experiment (Run no. 10, Table 5.2) in liquid steel. The cylinder diameter was 1.905 cm and its length was 18 cm.  
 1) Measured steel bath temperature;  
 2) Registered net downward force.

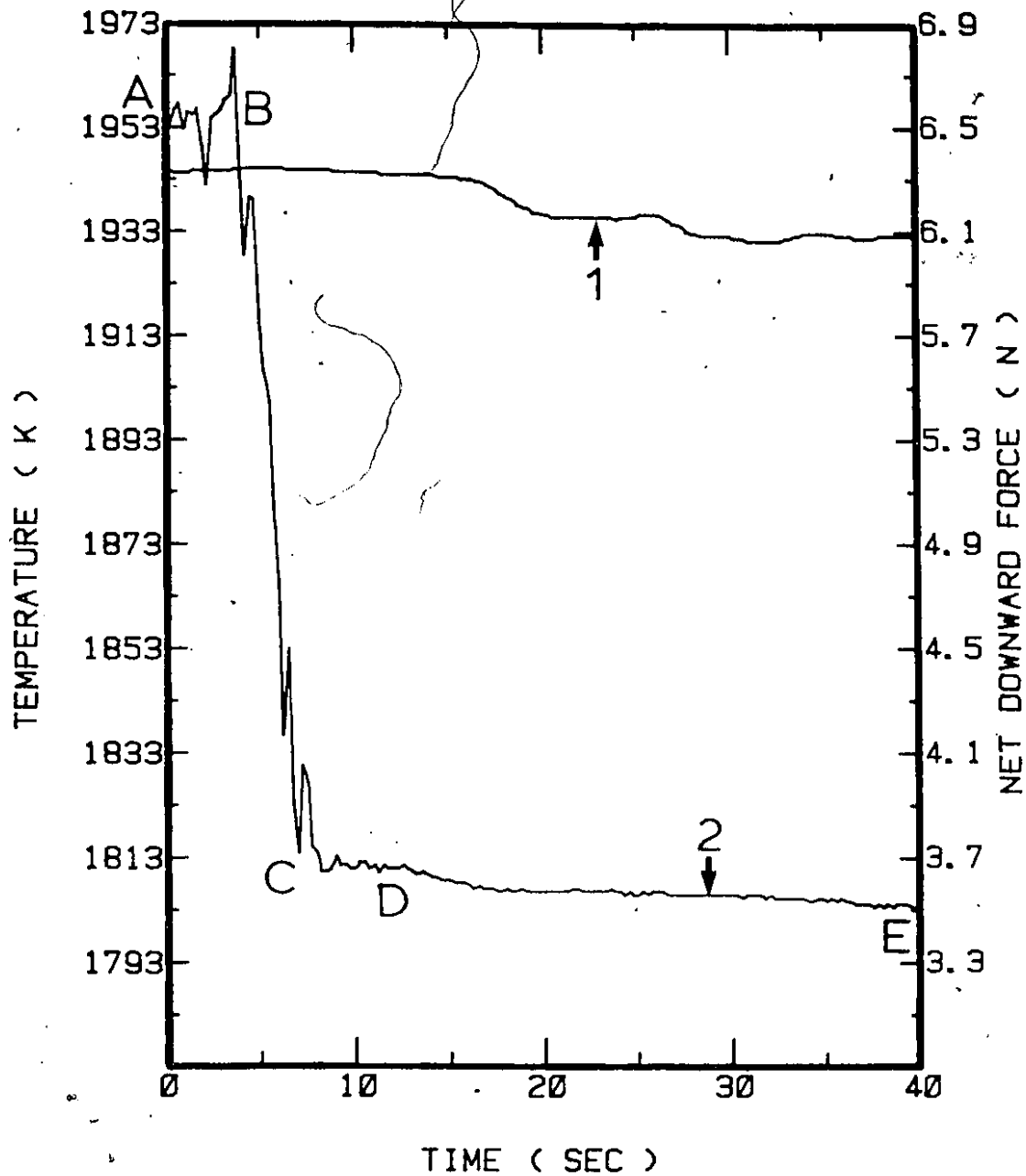


Figure I-14 Results from a typical niobium dissolution experiment (Run no. 12, Table 5.2) in liquid steel. The cylinder diameter was 1.905 cm and its length was 18 cm.  
 1) Measured steel bath temperature;  
 2) Registered net downward force.

APPENDIX II

TYPICAL RESULTS FROM THE

Zr IMMERSION TESTS

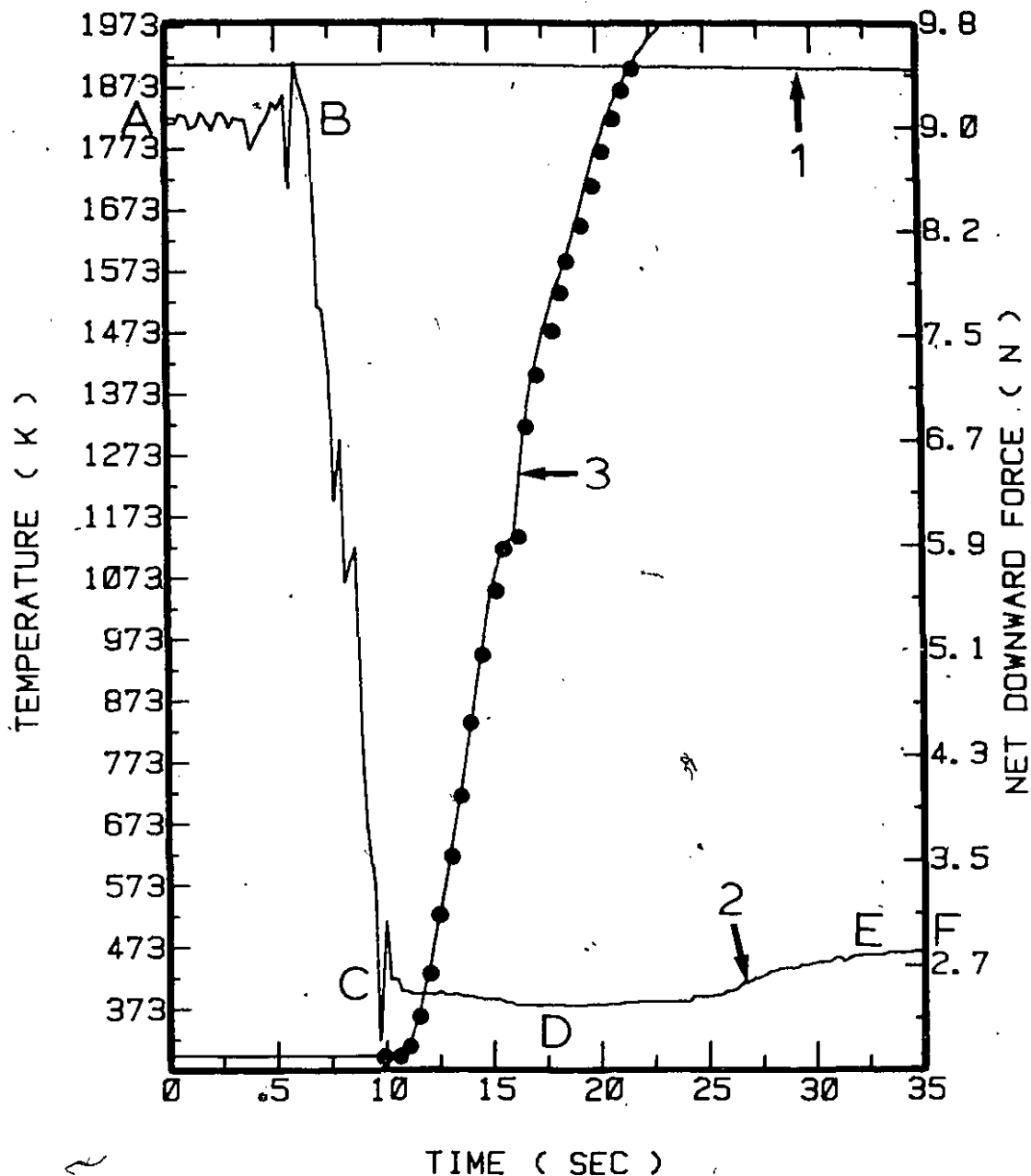


Figure II-1 Results from a typical zirconium dissolution experiment (Run no. 2, Table 6.4) in liquid steel. The cylinder diameter was 2.54 cm and its length was 18 cm.

- 1) Measured steel both temperature;
- 2) Registered net downward force;
- 3) Measured and predicted centerline temperature.

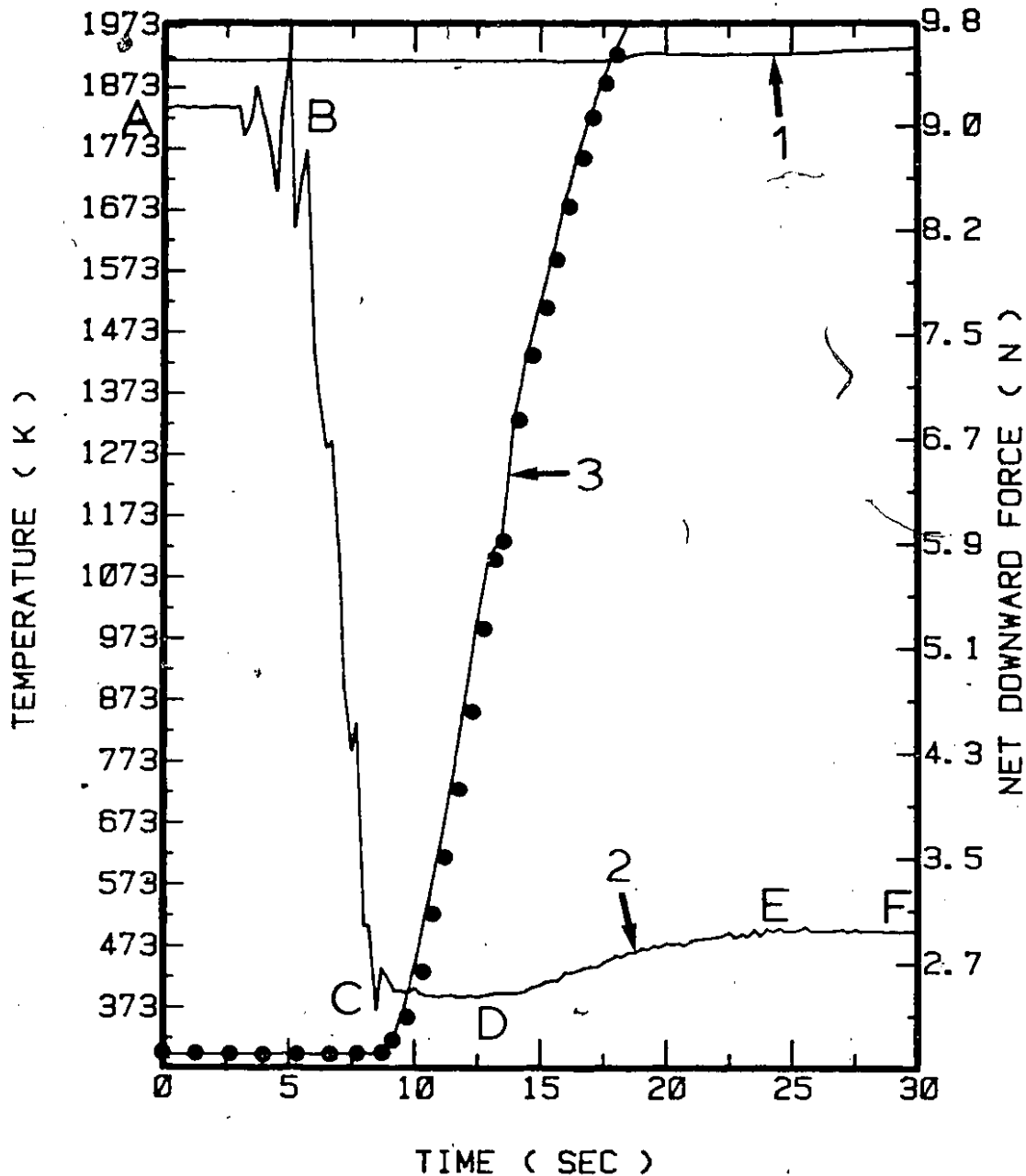


Figure II-2 Results from a typical zirconium dissolution experiment (Run no. 6, Table 6.4) in liquid steel. The cylinder diameter was 2.54 cm and its length was 18 cm.

- 1) Measured steel bath temperature;
- 2) Registered net downward force;
- 3) Measured and predicted centerline temperature.

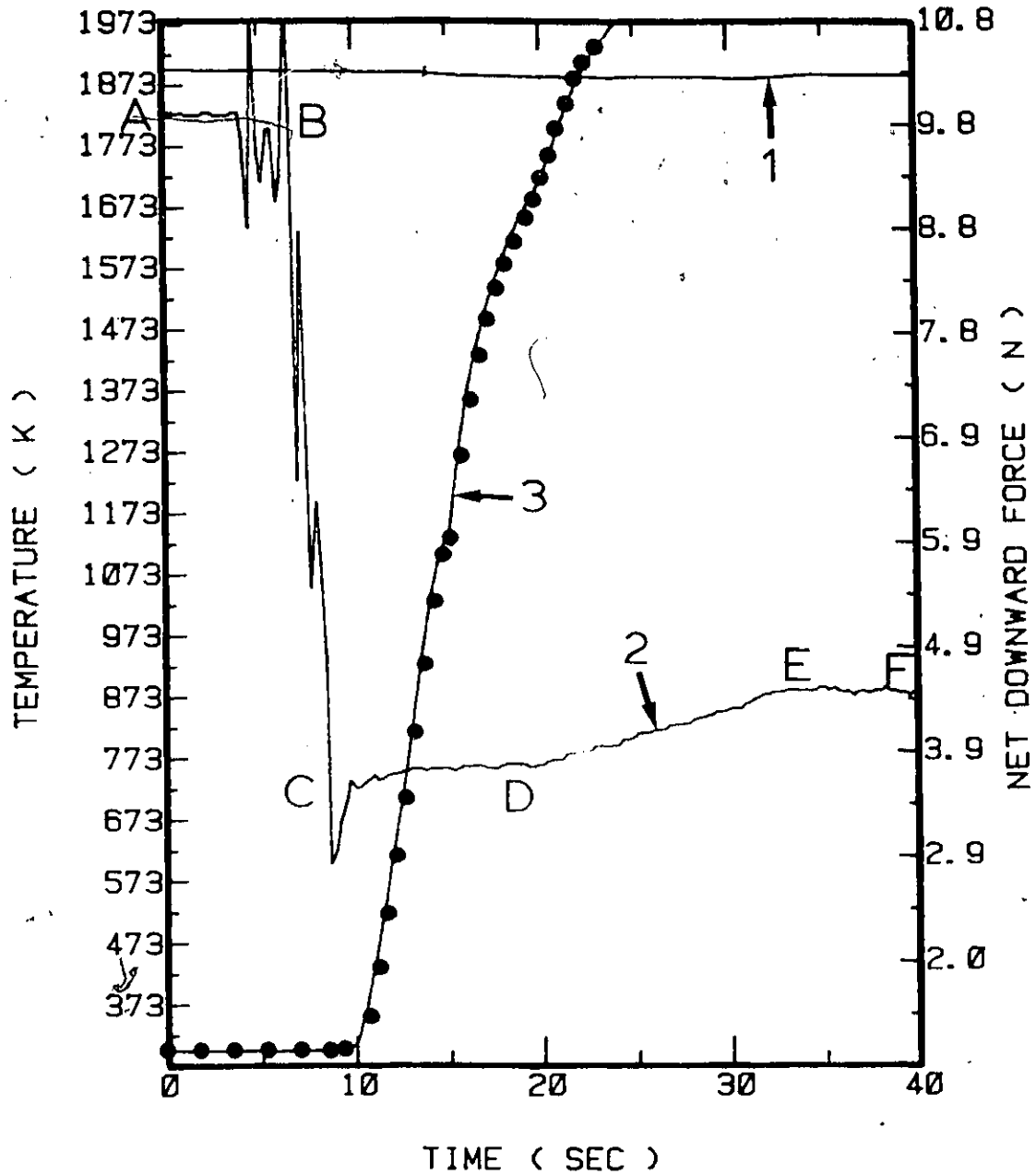


Figure II-3 Results from a typical zirconium dissolution experiment (Run no. 12, Table 6.4) in liquid steel. The cylinder diameter was 2.54 cm and its length was 18 cm.

- 1) Measured steel bath temperature;
- 2) Registered net downward force;
- 3) Measured and predicted centerline temperature.

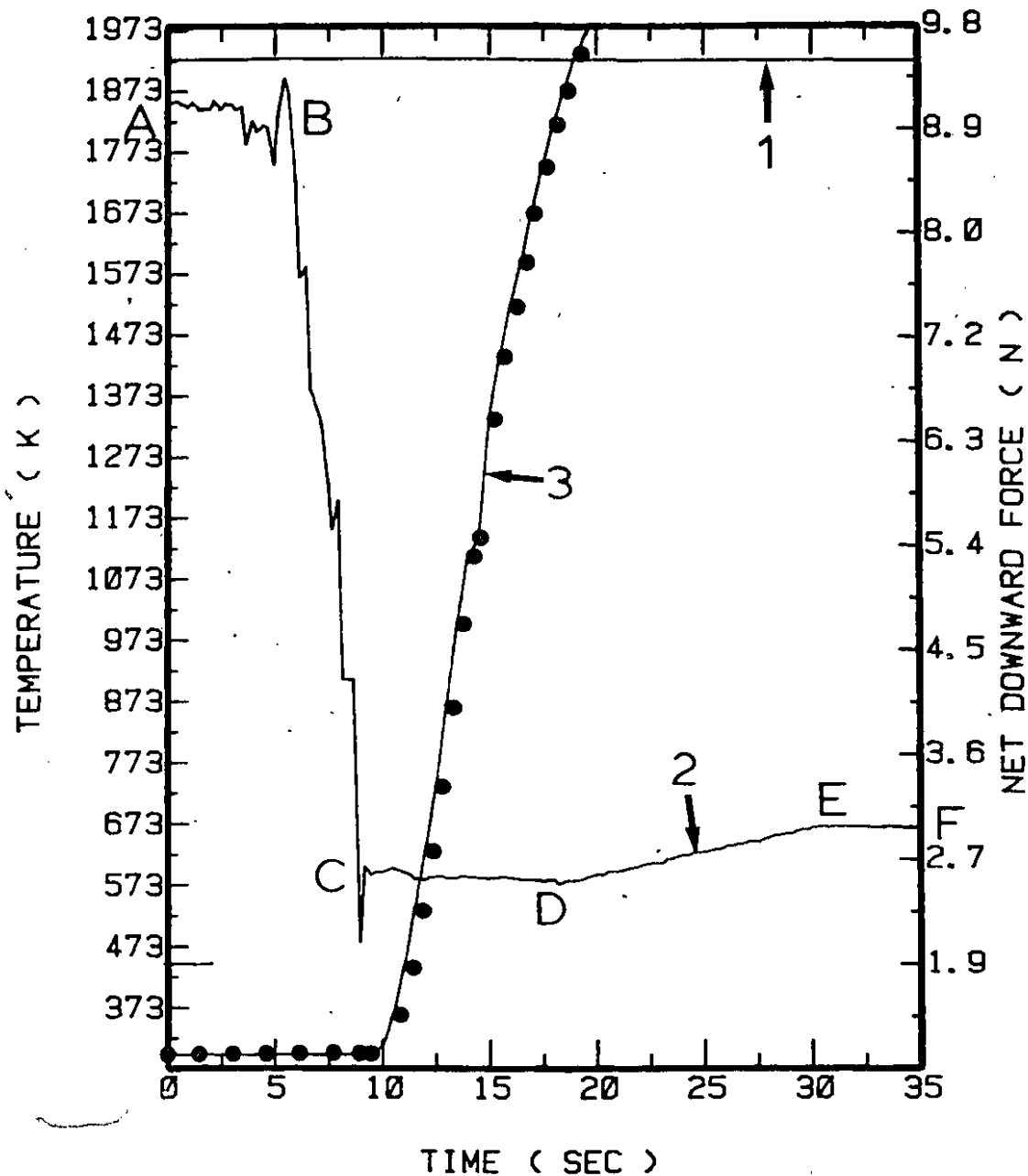


Figure II-4 Results from a typical zirconium dissolution experiment (Run no. 7, Table 6.4) in liquid steel. The cylinder diameter was 2.54 cm and its length was 18 cm.

- 1) Measured steel bath temperature;
- 2) Registered net downward force;
- 3) Measured and predicted centerline temperature.

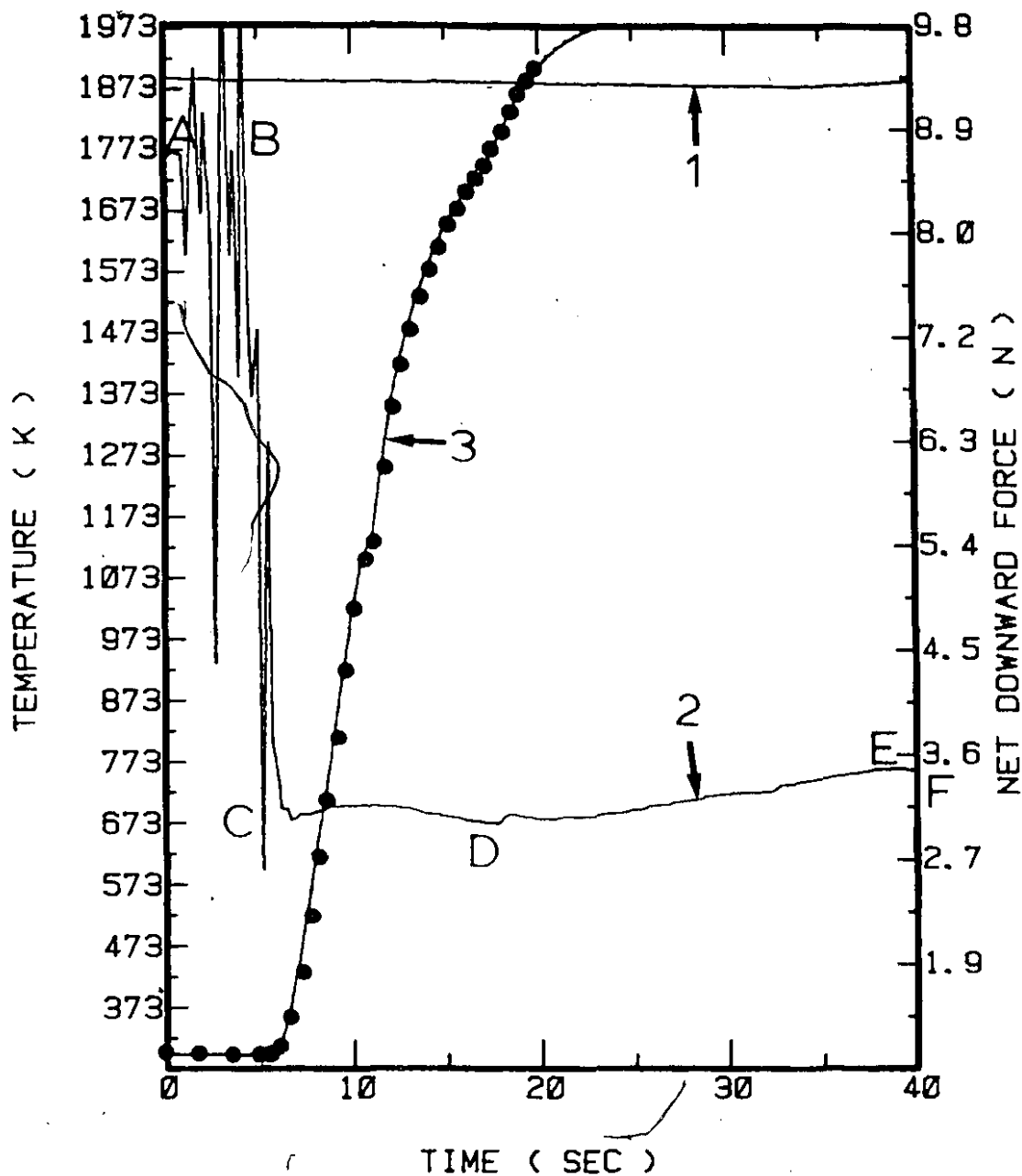


Figure II-5 Results from a typical zirconium dissolution experiment (Run no. 11, Table 6.4) in liquid steel. The cylinder diameter was 2.54 cm and its length was 18 cm.

- 1) Measured steel bath temperature;
- 2) Registered net downward force;
- 3) Measured and predicted centerline temperature.

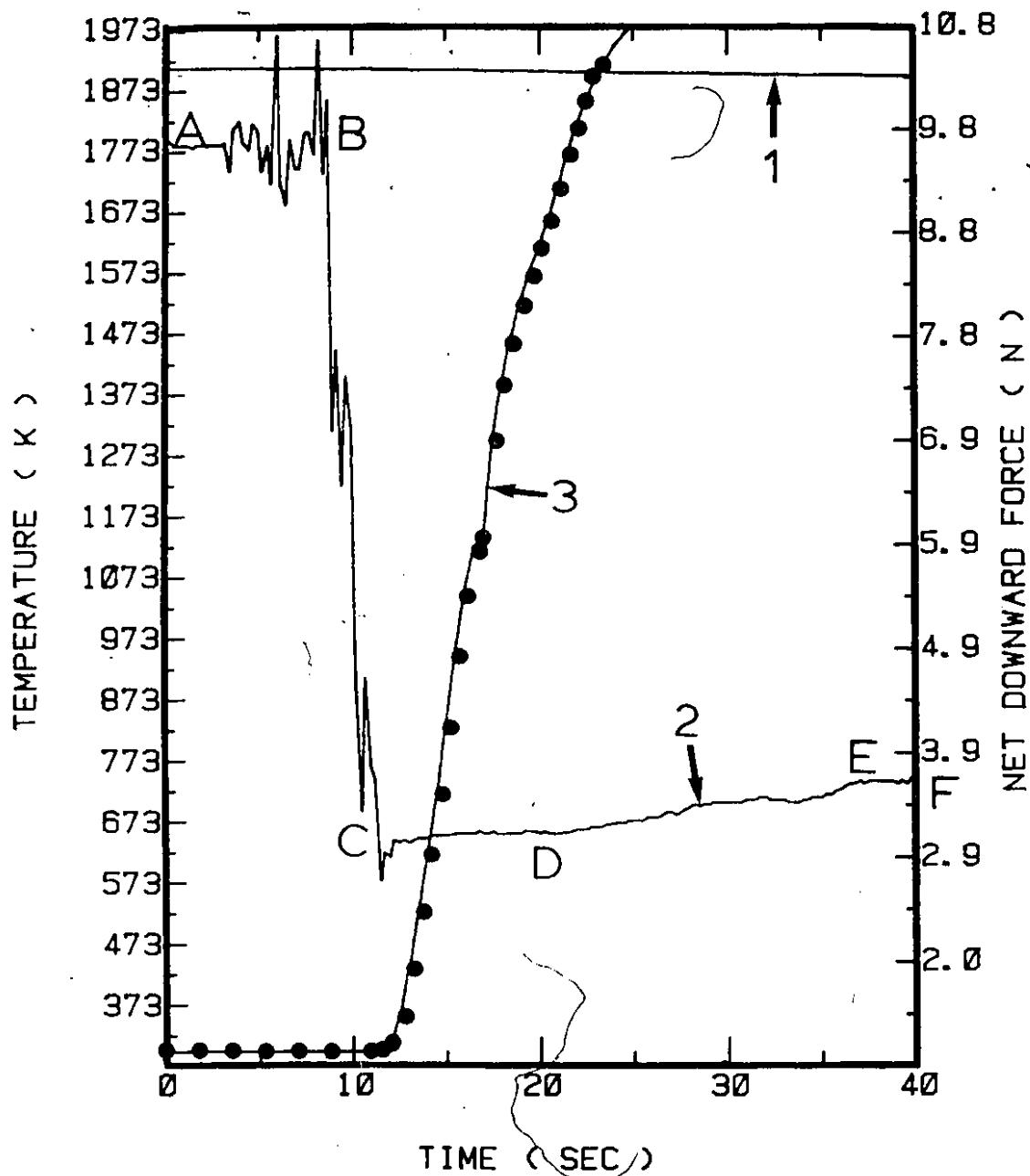


Figure II-6 Results from a typical zirconium dissolution experiment (Run no. 8, Table 6.4) in liquid steel. The cylinder diameter was 2.54 cm and its length was 18 cm.

- 1) Measured steel bath temperature;
- 2) Registered net downward force;
- 3) Measured and predicted centerline temperature.

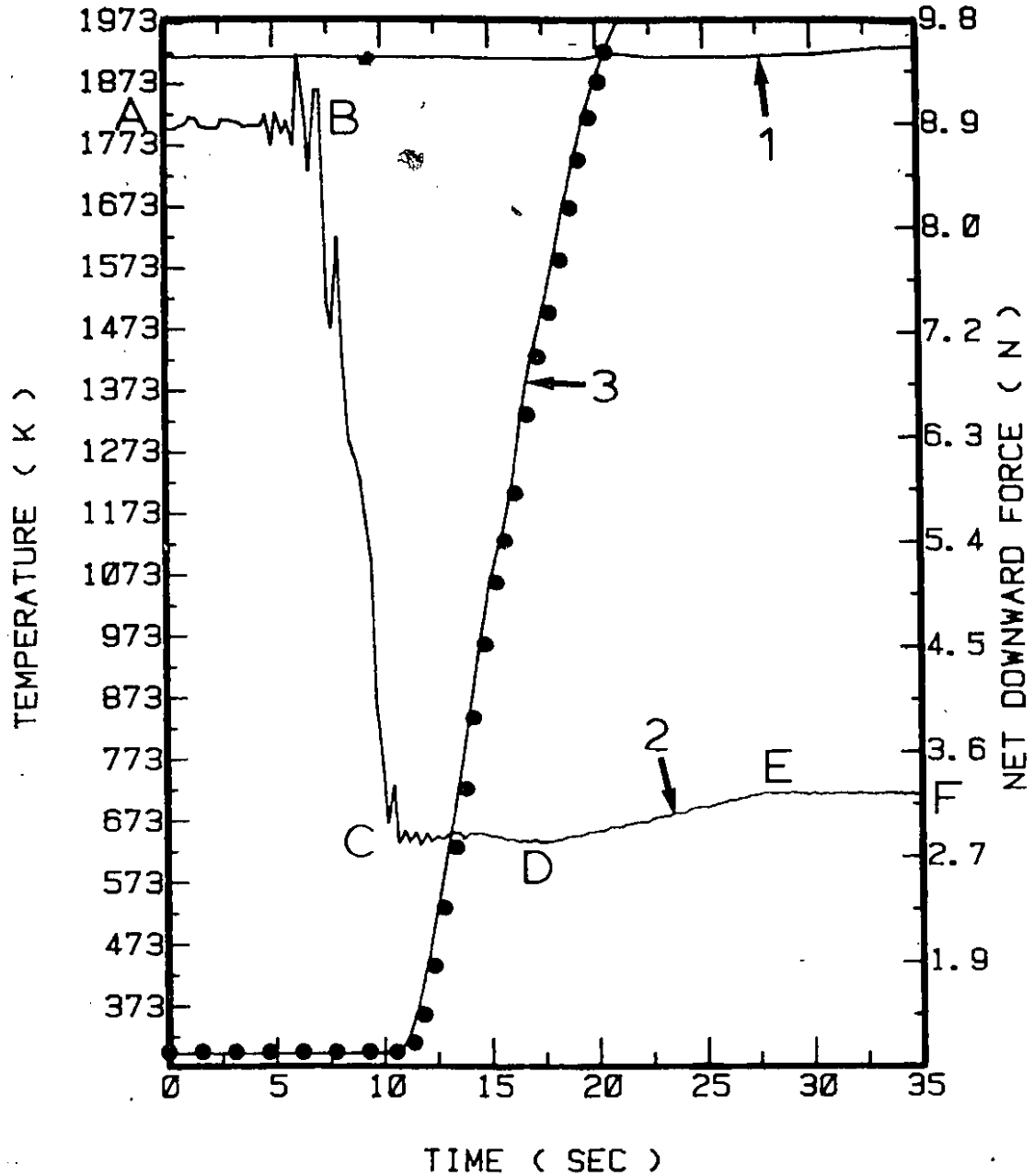


Figure II-7 Results from a typical zirconium dissolution experiment (Run no. 4, Table 6.4) in liquid steel. The cylinder diameter was 2.54 cm and its length was 18 cm.

- 1) Measured steel bath temperature;
- 2) Registered net downward force;
- 3) Measured and predicted centerline temperature.

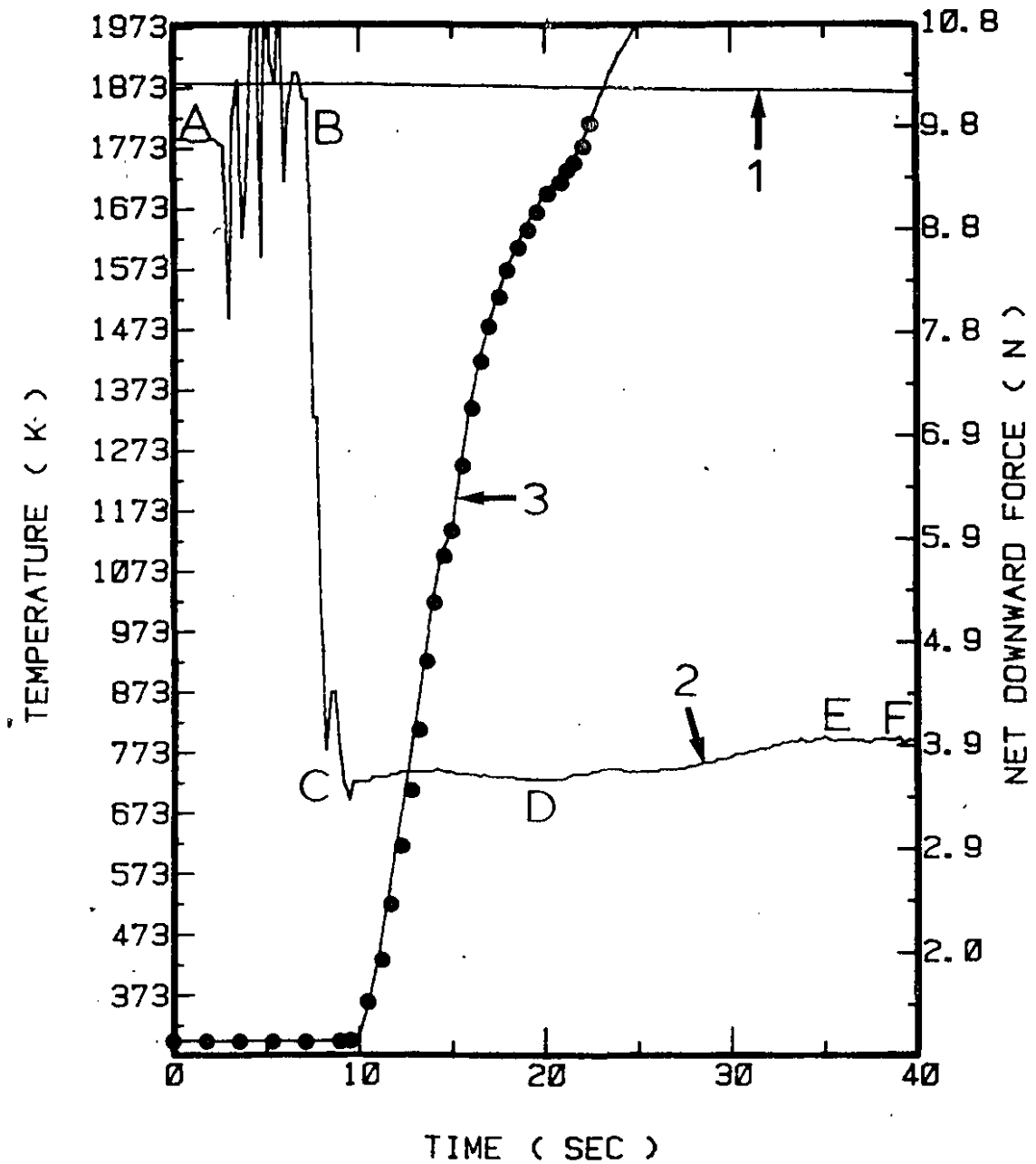


Figure II-8 Results from a typical zirconium dissolution experiment (Run no. 9, Table 6.4) in liquid steel. The cylinder diameter was 2.54 cm and its length was 18 cm.

- 1) Measured steel bath temperature;
- 2) Registered net downward force;
- 3) Measured and predicted centerline temperature.

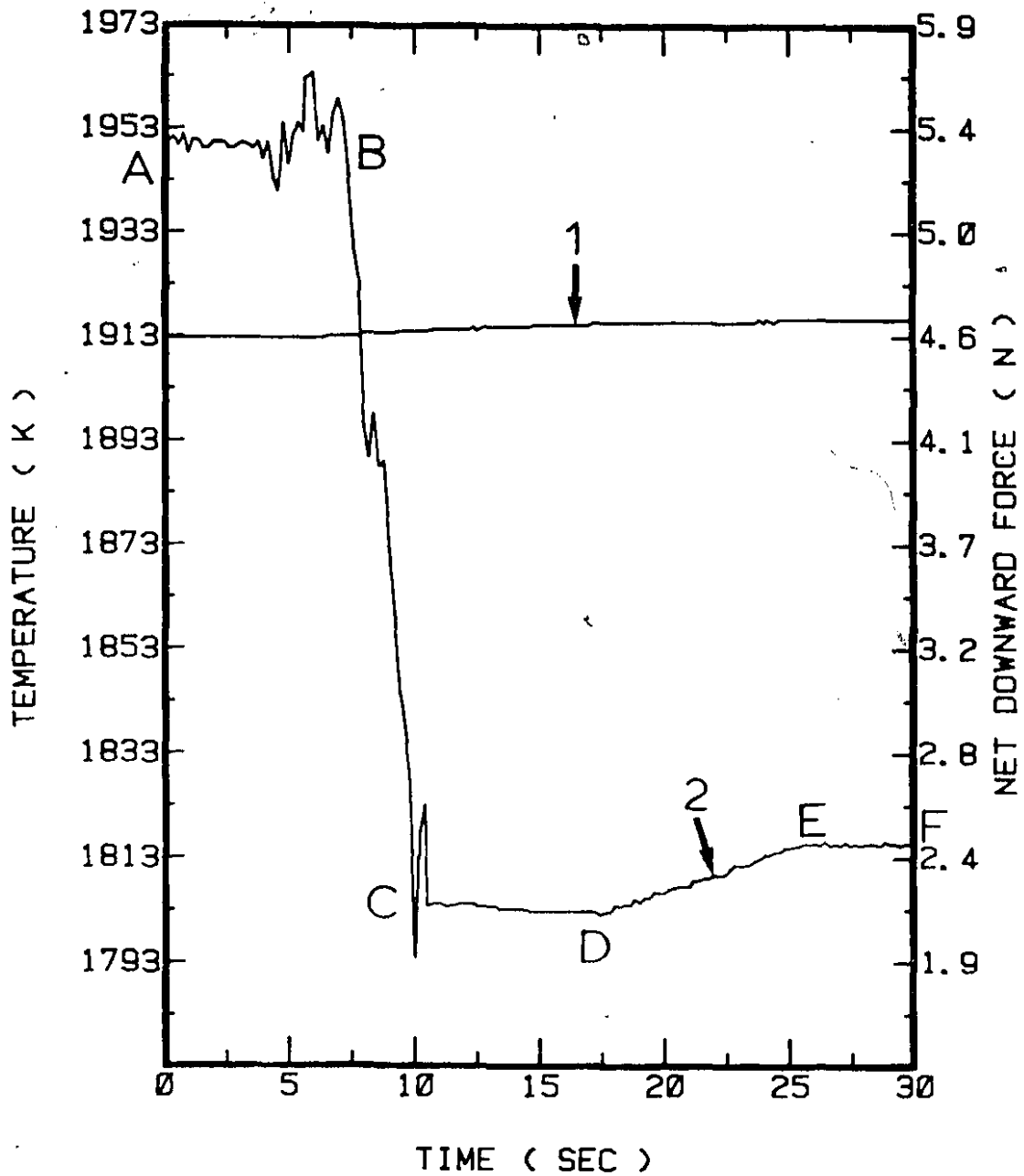


Figure II-9 Results from a typical zirconium dissolution experiment (Run no. 5, Table 6.4) in liquid steel. The cylinder diameter was 1.905 cm and its length was 18 cm.  
 1) Measured steel bath temperature;  
 2) Registered net downward force.

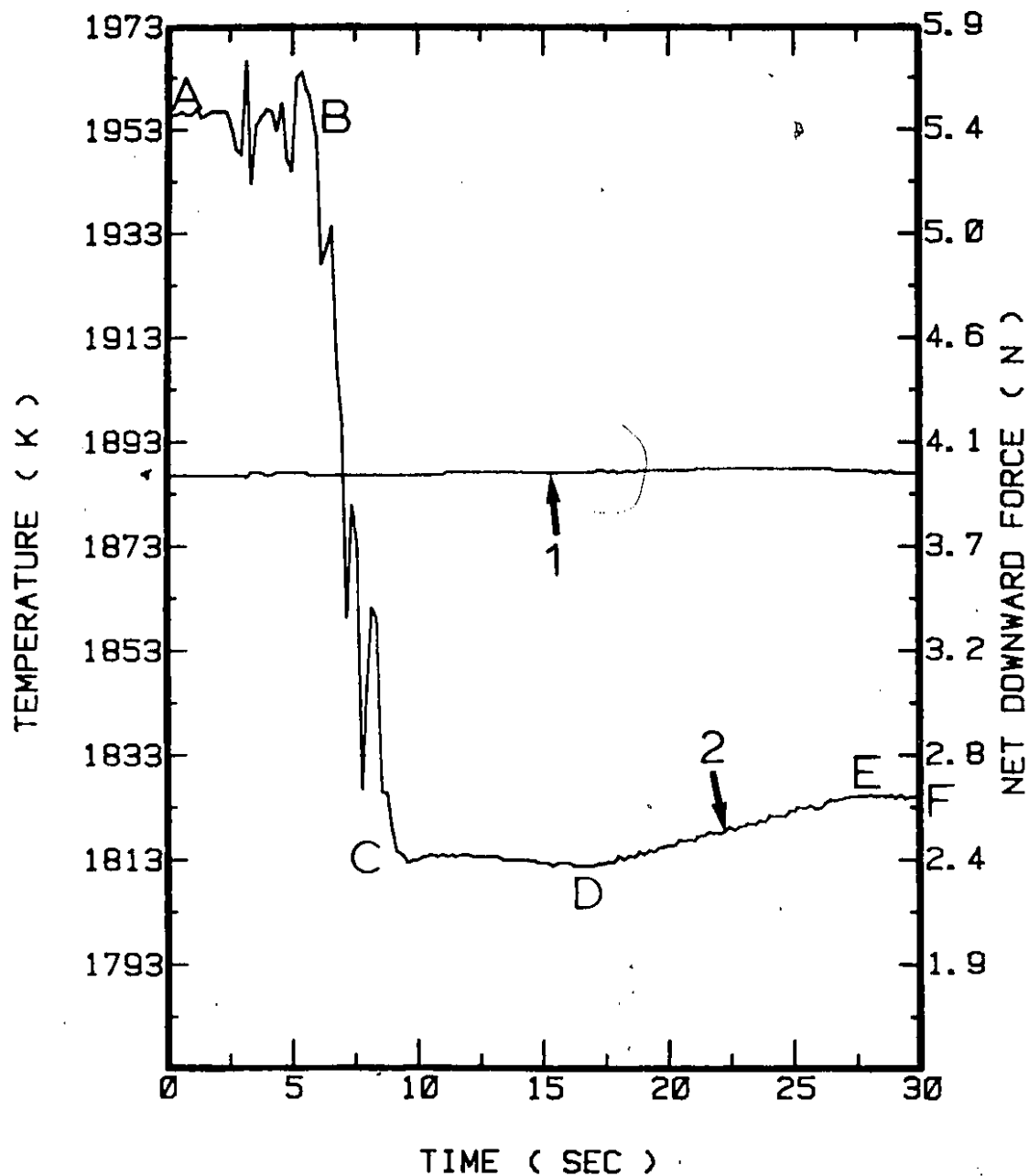


Figure II-10 Results from a typical zirconium dissolution experiment (Run no. 1, Table 6.4) in liquid steel. The cylinder diameter was 1.905 cm and its length was 18 cm.  
 1) Measured steel bath temperature;  
 2) Registered net downward force.

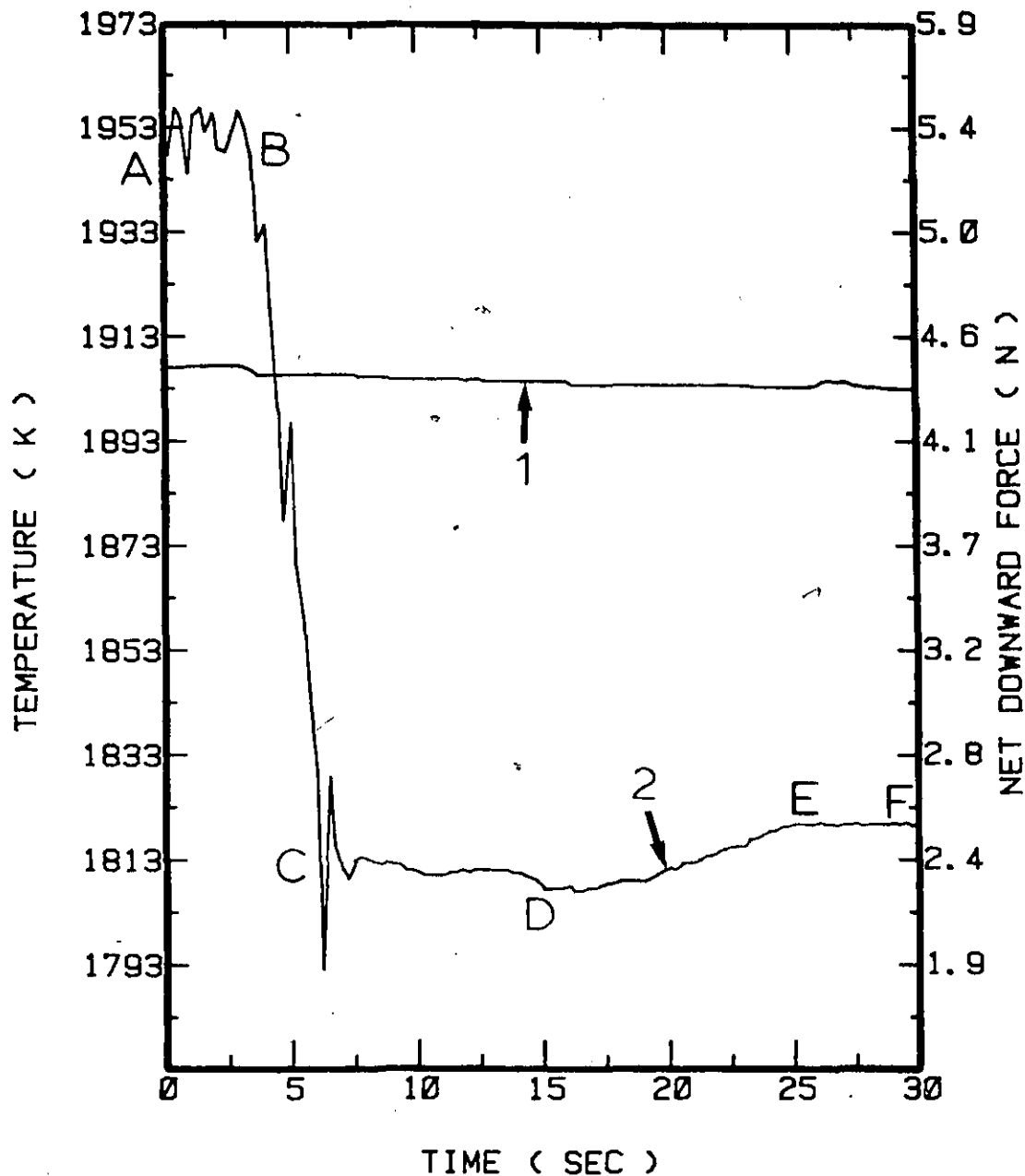


Figure II-11 Results from a typical zirconium dissolution experiment (Run no. 3, Table 6.4) in liquid steel. The cylinder diameter was 1.905 cm and its length was 18 cm.  
 1) Measured steel bath temperature;  
 2) Registered net downward force.

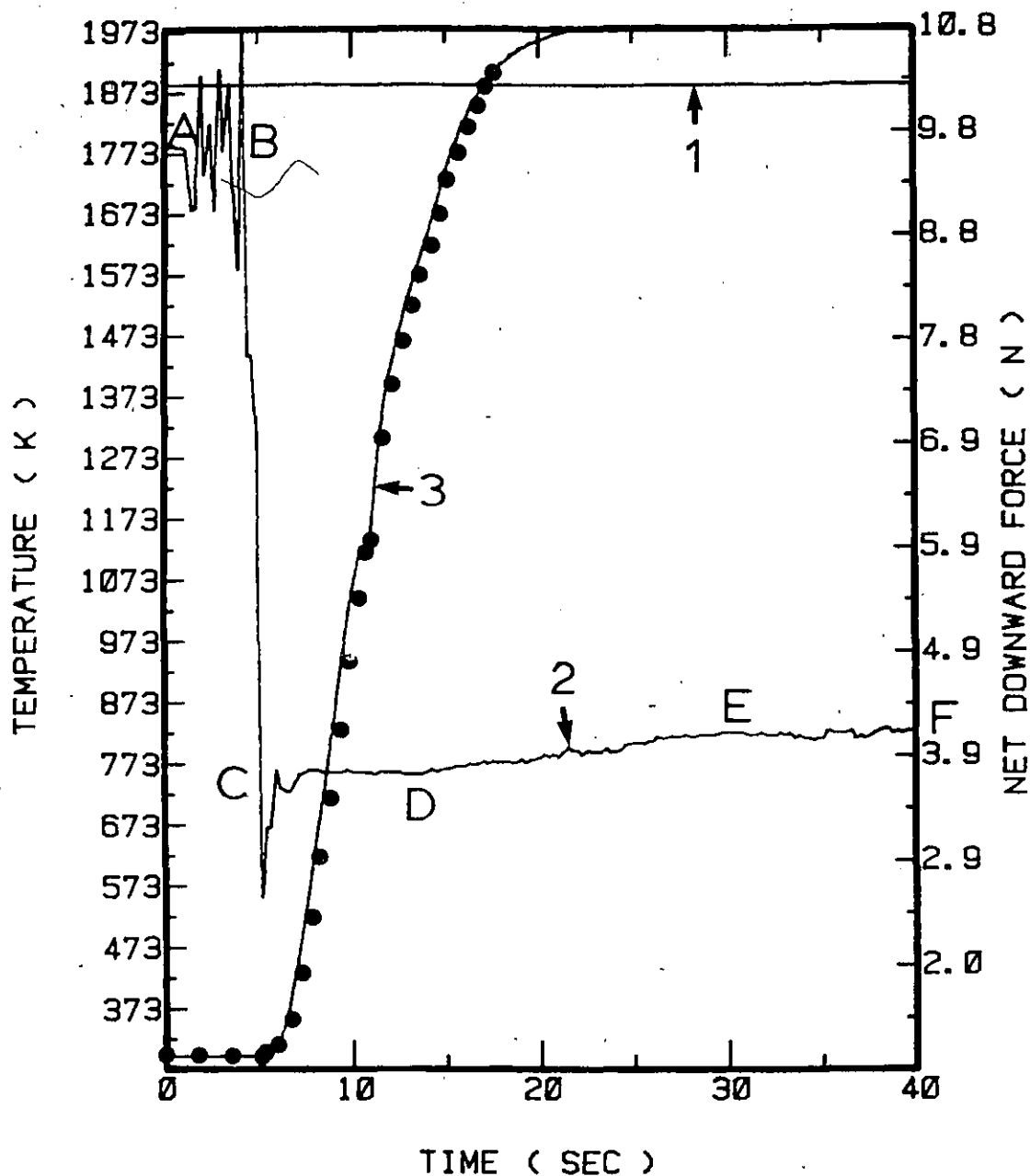


Figure II-12 Results from a typical zirconium dissolution experiment (Run no. 18, Table 6.5) in liquid steel. The cylinder diameter was 2.54 cm and its length was 18 cm.

- 1) Measured steel bath temperature;
- 2) Registered net downward force;
- 3) Measured and predicted centerline temperature.

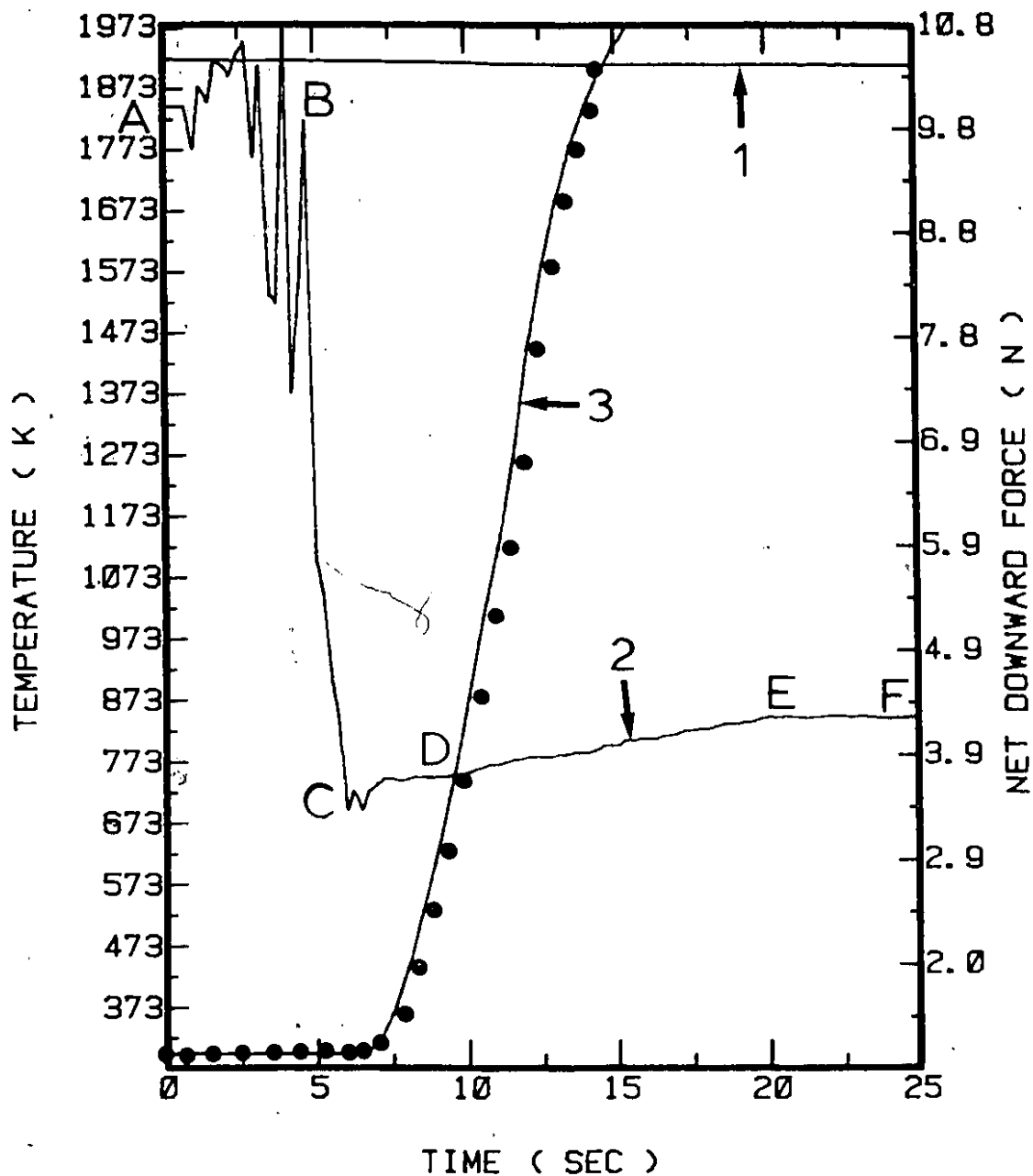


Figure II-13 Results from a typical zirconium dissolution experiment (Run no. 21, Table 6.5) in liquid steel. The cylinder diameter was 2.54 cm and its length was 18 cm.

- 1) Measured steel bath temperature;
- 2) Registered net downward force;
- 3) Measured and predicted centerline temperature.

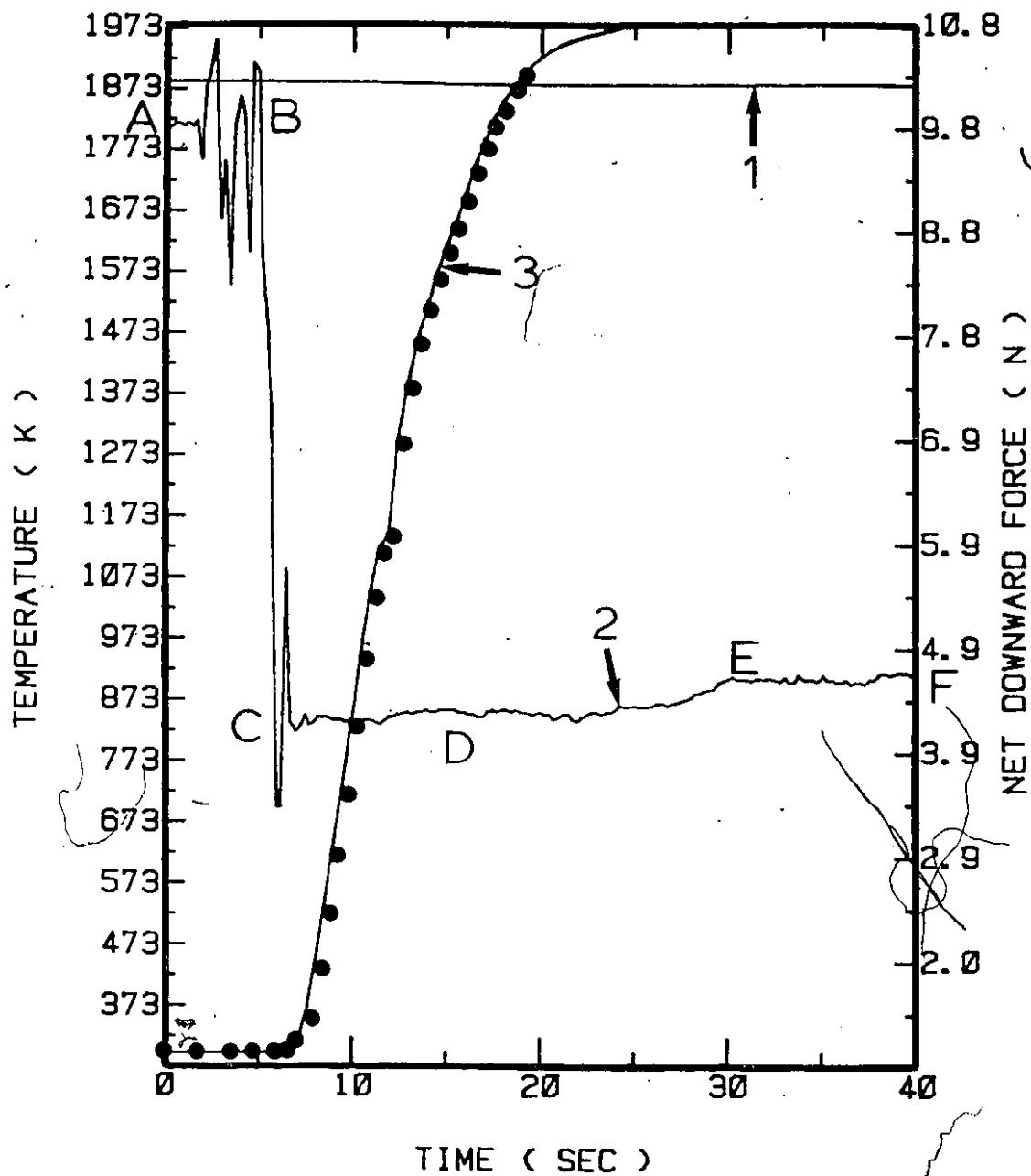


Figure II-14 Results from a typical zirconium dissolution experiment (Run no. 19, Table 6.5) in liquid steel. The cylinder diameter was 2.54 cm and its length was 18 cm.

- 1) Measured steel bath temperature;
- 2) Registered net downward force;
- 3) Measured and predicted centerline temperature.

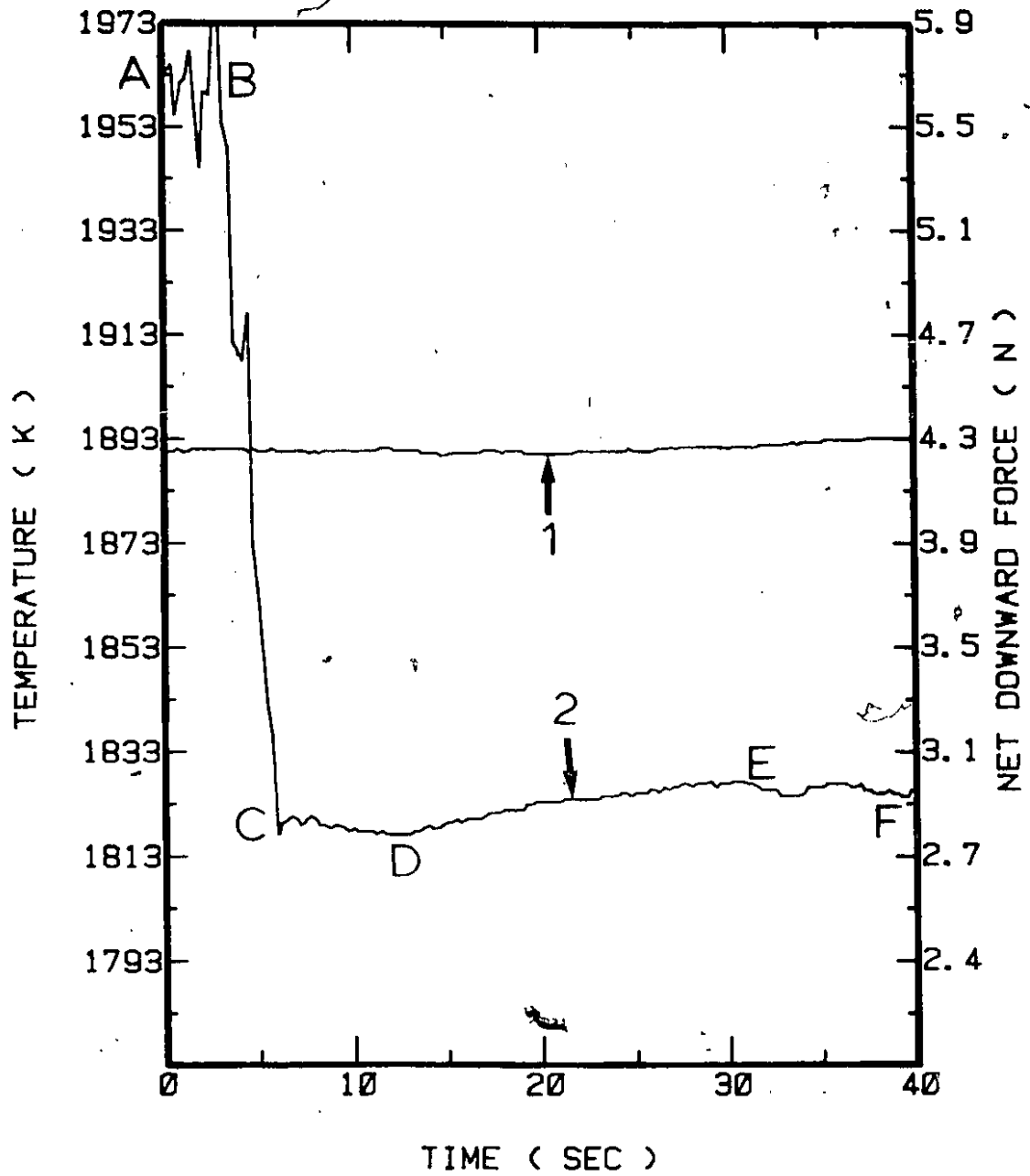


Figure II-15 Results from a typical zirconium dissolution experiment (Run no. 13, Table 6.5) in liquid steel. The cylinder diameter was 1.905 cm and its length was 18 cm.  
1) Measured steel bath temperature;  
2) Registered net downward force.

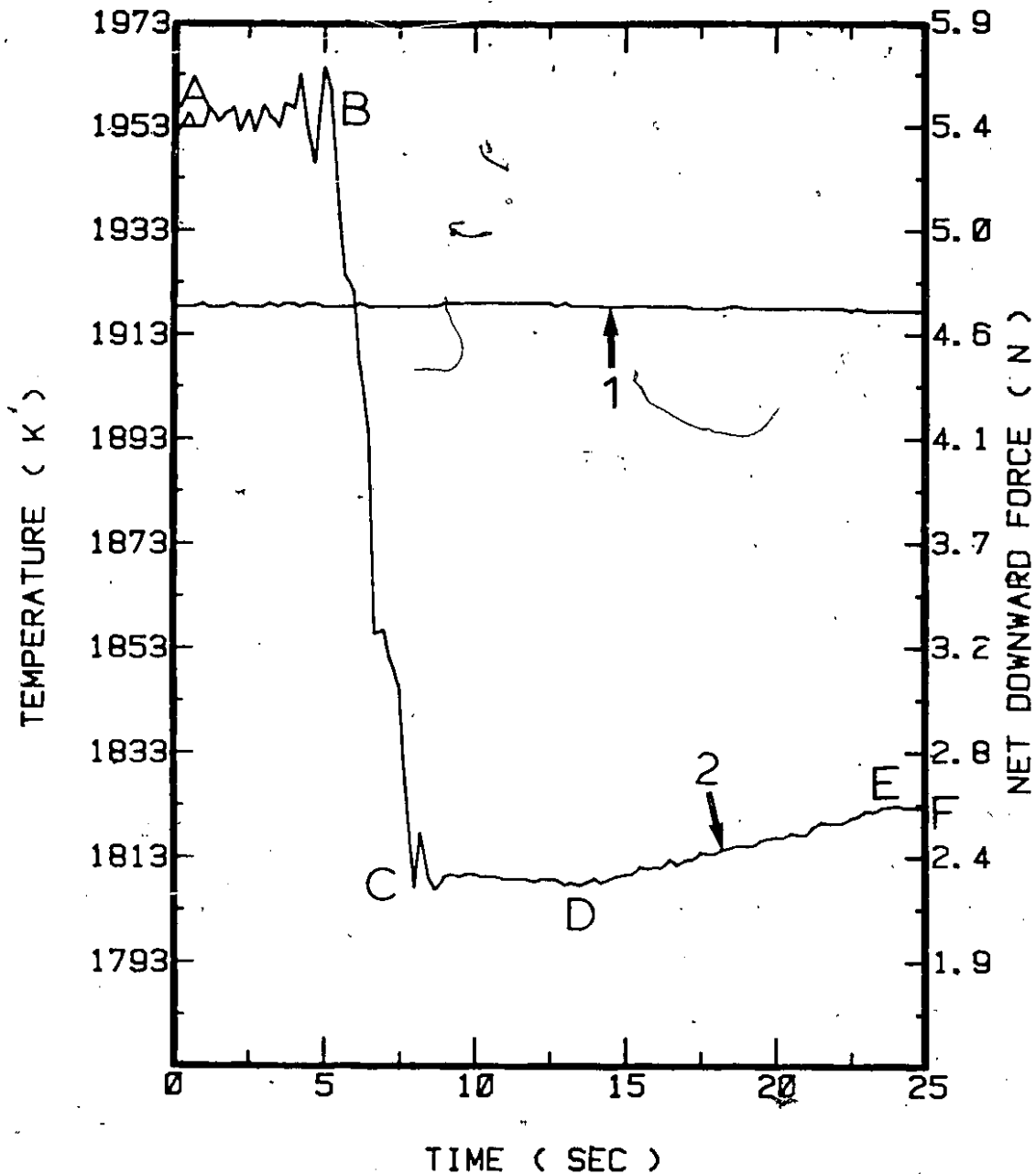


Figure II-16 Results from a typical zirconium dissolution experiment (Run no. 16, Table 6.5) in liquid steel. The cylinder diameter was 1.905 cm and its length was 18 cm.  
 1) Measured steel bath temperature;  
 2) Registered net downward force.

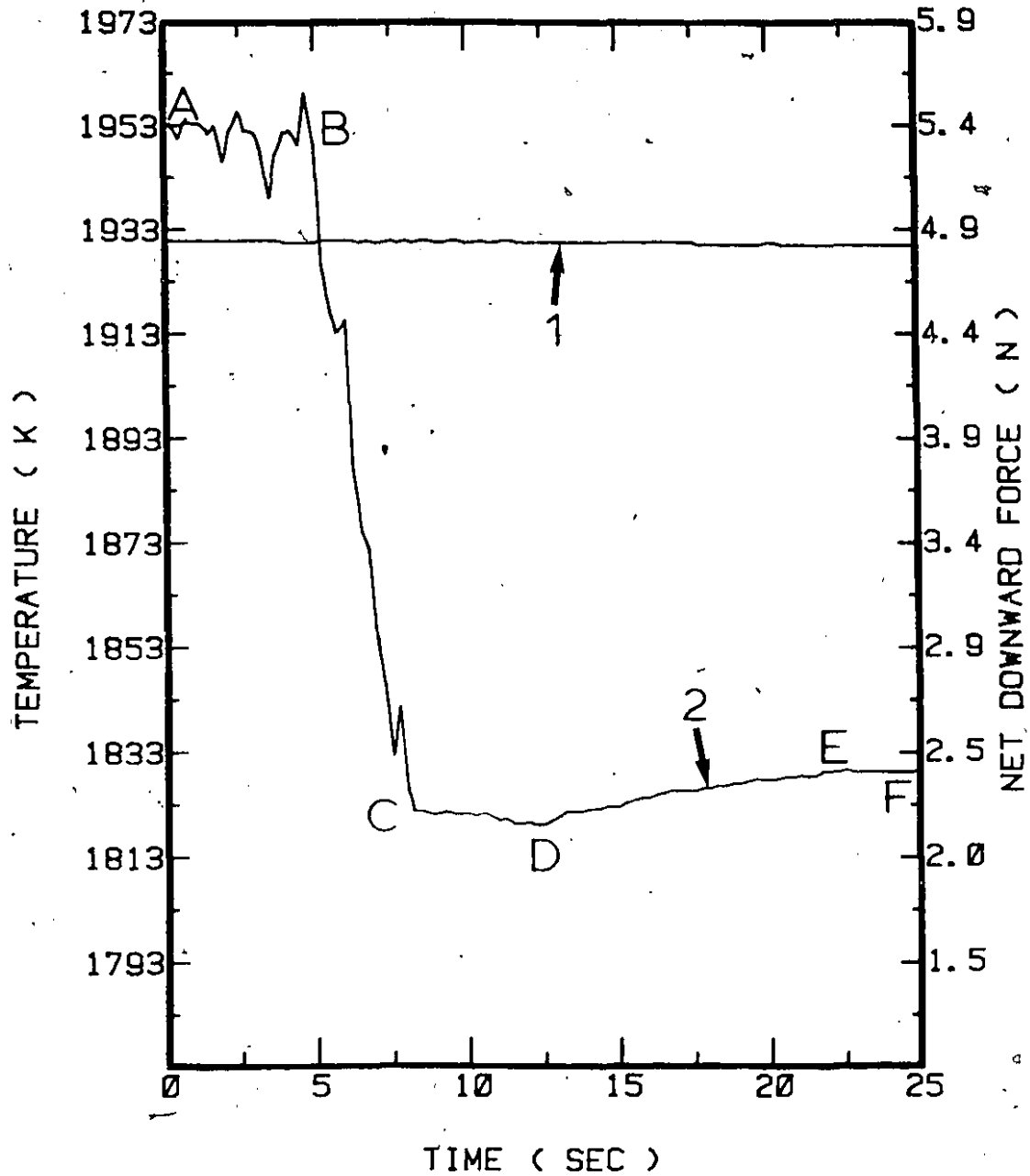


Figure II-17 Results from a typical zirconium dissolution experiment (Run no. 17, Table 6.5) in liquid steel. The cylinder diameter was 1.905 cm and its length was 18 cm.  
 1) Measured steel bath temperature;  
 2) Registered net downward force.

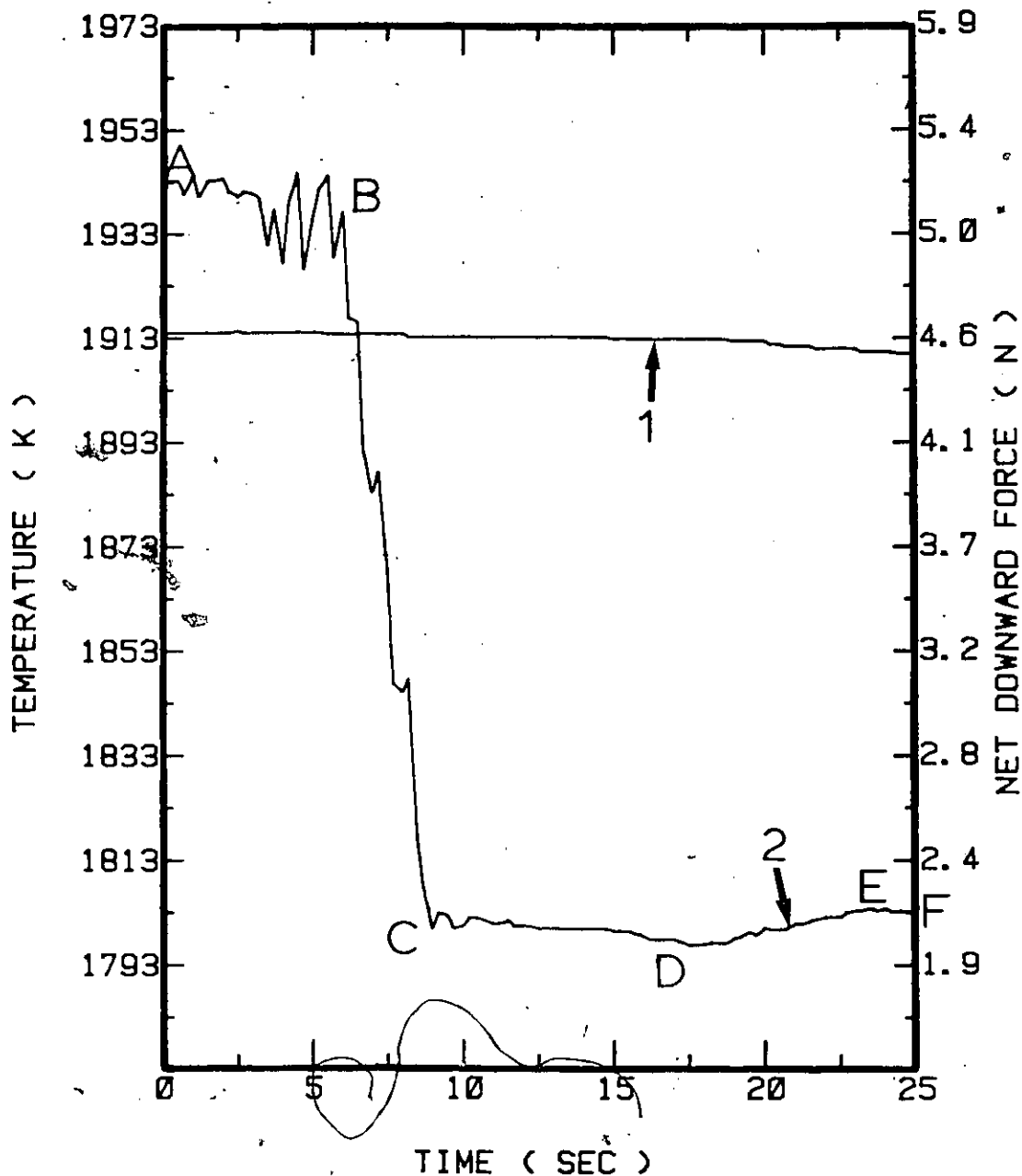


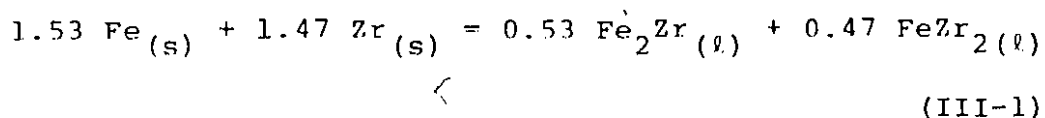
Figure II-18 Results from a typical zirconium dissolution experiment (Run no. 15, Table 6.5) in liquid steel. The cylinder diameter was 1.905 cm and its length was 18 cm.

- 1) Measured steel bath temperature;
- 2) Registered net downward force.

APPENDIX III

ESTIMATION OF EXOTHERMIC HEATS OF MIXING  
AND Zr MASS TRANSFER COEFFICIENTS  
DURING STEEL SHELL PERIOD

At the steel shell-zirconium interface, solid steel at a temperature below its melting point is dissolving and mixing with solid zirconium. It was found experimentally (Section 6.2) that the relative amounts of Fe and Zr in the reaction zone were 39 wt% Fe and 61 wt% Zr, with main reaction products the intermetallic compounds  $\text{Fe}_2\text{Zr}$  and  $\text{FeZr}_2$ . Consequently, the exothermic dissolution reaction can be represented by:



where

$$\frac{1}{1.53} N_{\text{Fe}}'' = \frac{1}{1.47} N_{\text{Zr}}'' \quad (\text{III-2})$$

and  $N_{\text{Fe}}''$ ,  $N_{\text{Zr}}''$  are the molar fluxes of Fe and Zr towards the reaction zone from opposite directions. This intermixing results in an enthalpy change  $\Delta H_R$ . The study of this enthalpy change was performed using the F\*A\*C\*T system<sup>91</sup>. The data were taken from Reference 89 and were selected for pure ordered compounds<sup>121</sup>, as far as the two intermetallic compounds were concerned. Predictions from the model revealed

that the steel-shell temperature in the vicinity of the reaction zone was around 1450°C (1723 K), for most of the time during the steel shell period. At this temperature the following result was found:

$$\Delta H_R = -7.61 \text{ kcal/mol of zirconium}$$

or

$$\Delta H_R = -31.84 \text{ kJ/mol of zirconium} \quad (\text{III-3})$$

It should be noted that  $\Delta H_R$  becomes more negative as the temperature increases, obtaining a value 35% larger (in absolute value) than the one given by equation (III-3) at 1600°C (1873 K).

The semi-empirically determined heat flux fitting the dissolution data was found to be in the range of 8.6 to 12.9 cal/cm<sup>2</sup>/sec (or 0.36 to 0.54 MW/m<sup>2</sup>). So, the molar flux is given by:

$$N_{Zr}'' = \frac{q_s''}{\Delta H_R} \quad (\text{III-4})$$

which ranged from 1.130 10<sup>-3</sup> to 1.695 10<sup>-3</sup> mol Zr/cm<sup>2</sup>/sec.

The mass transfer coefficient can be defined as:

$$K_{Zr} = \frac{\text{molar flux of Zr}}{\text{net concentration driving force}}$$

or

$$K_{Zr} = \frac{N_{Zr}''}{(C_{Zr} - C_{Fe/Zr})} \quad (\text{III-5})$$

where the 'driving force' ( $C_{Zr} - C_{Fe/Zr}$ ) can be calculated as follows:

$$C_{Zr} = \text{mole of Zr in (Pure Zr)/cm}^3 = 0.07115$$

and

$$C_{\text{Fe/Zr}} = \text{mole of Zr in (mixture 61 wt\% Zr)/cm}^3 = 0.04662$$

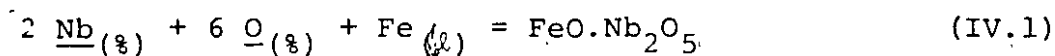
Consequently, for the system studied, the mass transfer coefficient of zirconium varied from 0.046 to 0.069 cm/sec. In a similar way the mass transfer coefficient of iron was calculated and found to range from 0.013 to 0.019 cm/sec.

The thickness of the reaction zone could therefore be deduced based on a knowledge of the heat released and the stoichiometry of the reaction.

APPENDIX IV

DEOXIDATION WITH NIOBIUM

Niobium forms the spinel,  $\text{FeO}:\text{Nb}_2\text{O}_5$ , at low residual concentrations<sup>108</sup>:



The equilibrium constant for the above chemical reaction is<sup>108</sup>:

$$\log K = \frac{88300}{T} - 36.76 \quad (\text{IV.2})$$

At 1600°C (T = 1873 K), the equation (IV.2) gives:

$$\log K = 10.384 \quad (\text{IV.3})$$

Assuming that there is not any change in the composition of the oxide phase (i.e., the spinel  $\text{FeO} \cdot \text{Nb}_2\text{O}_5$  is a stoichiometric compound and solid) then its activity can be taken equal to 1. One then has:

$$\log K = -2 (\log [\% \text{Nb}] + \log f_{\text{Nb}}) - 6 (\log [\% \text{O}] + \log f_{\text{O}}) \quad (\text{IV.4})$$

where  $[\% \text{Nb}]$ ,  $[\% \text{O}]$ : concentration in wt% of Nb

and Oxygen respectively;

$f_{\text{Nb}}$ ,  $f_{\text{O}}$ : Henrian activity coefficients of niobium and oxygen.

The activity coefficient of niobium ( $f_{\text{Nb}}$ ) is given by the formula:

$$\log f_{\text{Nb}} = e_{\text{Nb}}^{\text{Nb}} [\% \text{Nb}] + e_{\text{Nb}}^{\text{O}} [\% \text{O}] \quad (\text{IV.5})$$

Similarly, the activity coefficient of oxygen ( $f_O$ ) is:

$$\log f_O = e_O^O [\%O] + e_{O}^{Nb} [\%Nb] \quad (\text{IV.6})$$

The parameters  $e_j^i$  are the first-order interaction coefficients between the elements  $i, j$ . In the case where  $i$  and  $j$  are the same (i.e., they refer to the same element), then the parameter  $e_i^i$  is the self-interaction coefficient for the element  $i$ . Values of the interaction coefficients are given by Elliott<sup>109</sup> and for this case:

$$e_{Nb}^{Nb} = -0.067, e_O^O = -0.2, e_{Nb}^O = -0.83, e_O^{Nb} = -0.14 \quad (\text{IV.7})$$

Plots of  $[\%O]$  in solution (and in equilibrium with the oxide) as a function of the  $[\%M]$  where  $M$  is the metal used for deoxidation, generally show a minimum, that is, an optimum quantity of deoxidizer<sup>110</sup>; above a certain concentration of  $M$  the level of oxygen rises ('overkill'). The same happens for the case of niobium and the minimum value of  $[\%O]$  is found at the following level of  $[\%Nb]$ :

$$[\%Nb]_{\min} = - \frac{0.434 x}{y e_O^{Nb} + x e_{Nb}^O} = 0.89 \quad (\text{IV.8})$$

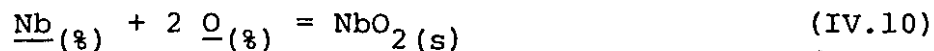
where  $x = 2, y = 6$  (from the stoichiometry of the reaction).

Using the equations (IV.3), (IV.4), (IV.5), (IV.6) and (IV.7) one can solve for the minimum wt% of oxygen in the melt when  $[\%Nb] = 0.89$  :

$$[\%O]_{\min} = 0.028 \quad (\text{IV.9})$$

So, at low residual concentrations of niobium in the melt if the oxygen level is below 280 ppm, no deoxidation can take

place by niobium. The oxide  $\text{NbO}_2$  is the product at higher concentrations<sup>108</sup>:



The equilibrium constant is:

$$\log K = \frac{32780}{T} - 13.917 \quad (\text{IV.11})$$

At  $T = 1873 \text{ K}$  :

$$\log K = 3.584 \quad (\text{IV.12})$$

Assuming the activity coefficient of the solid oxide ( $\text{NbO}_2$ ) to be unity and following the same procedure as previously, the wt% Nb at the minimum value of wt% O is:

$$[\% \text{ Nb}]_{\min} = \frac{(-0.434) 1}{2 (-0.14) + 1 (-0.067)} = 1.25 \quad (\text{IV.13})$$

The minimum [% O] is found to be:

$$[\% \text{ O}]_{\min} = 0.025 \quad (\text{IV.14})$$

Therefore, at higher concentrations of niobium in liquid steel if the dissolved oxygen is less than 250 ppm deoxidation by niobium is impossible. As the tests were carried out at oxygen levels of less than 10 ppm, no reaction could occur between the dissolving niobium and the oxygen in the melt.

REFERENCES

1. P.D. Deeley, K.J.A. Kundig, H.R. Spendelow, 'Ferroalloys and Alloying Additives Handbook', Shieldalloy Corporation-Metallurg Alloy Corporation, 1981.
2. R.I.L. Guthrie, 'Addition Kinetics in Steelmaking', Electric Furnace Proceedings, AIME, 1977, pp. 30-41.
3. S.A. Argyropoulos, R.I.L. Guthrie, 'The Exothermic Dissolution of 50 wt% Ferro-Silicon in Molten Steel', Canadian Metallurgical Quarterly, No. 18, 267-281, 1979.
4. S.A. Argyropoulos, R.I.L. Guthrie, 'The Influence of High Exothermic Heats of Dissolution to Molten Steel', 1979 Inter. Seminar Heat and Mass Transfer in Metallurgical Systems, Sept. 3-7, Dubrovnik, Yugoslavia, 1979.
5. S.A. Argyropoulos, 'The Effect of Microexothermicity and Macroexothermicity on the Dissolution of Ferroalloys in Liquid Steel', Proceedings of the 42nd Electric Furnace Conference, Toronto, Ontario, December 1984.
6. V.O. Dahlke, O. Knacke, 'Die Auflösung von Kohlenstoff in Flüssigen Eisen', Arch. Eisenhüttenw., No. 26, 373, 1955.
7. R. Krzeszewski, 'Kinetics of Dissolving Stable Carbon in Liquid Iron', Prace Int. Odlewnictwa, No. 13, 1, 1963.
8. M. Kosaka and S. Minowa, 'Mass Transfer from Graphite Cylinder into Liquid Fe-C Alloy', Tetsu-to-Hagane, No. 53, 1467, 1967.

9. R.G. Olsson, V. Koump. T.F. Perzak, 'Rate of Dissolution of Carbon in Molten Iron-Carbon Alloys', Trans. AIME, No. 236, 426, 1966.
10. V.D. Shantarin, V.V. Utochkin, V.S. Kubryavtsev, 'Diffusion of Carbon in Manganese-Based Melts', Izv. VUZ Chernaya Met., No. 6, 5, 1968.
11. V.P. Karshin, V.A. Grigoryan 'Kinetics of the Dissolution of Graphite in Iron-Carbon Melts', Izv. VUZ Chernaya Met., No. 11, 16, 1970.
12. V.M. Surovsky, N.K. Nekrasov, 'Kinetics of Solution of Carbon in Iron', Izv. VUZ Chernaya Met., No. 1, 164, 1971; Steel in the USSR, No. 1, 75, 1971.
13. P.M. Shurygin, V.I. Kryuk, 'The Kinetics of Dissolving Carbon in Iron-Carbon Solutions', Izv. VUZ Chernaya Met., Vol. 6, No. 12, 14, 1963.
14. V.P. Cherevko, B.M. Boichenko, V.M. Dusha, B.M. Korokin, 'Kinetics of Dissolution of Carbon Materials in Iron-Carbon Melts', Metallurgiya Koksokhimiya. Resp. Mezhred. Nauch.-tekhn. sb 1977, No. 52, 36-39.
15. A.K. Biletskii, V.S. Shumikhin, 'Dissolution of Solid Spherical Particles in a Liquid', Protessy Plavki. Liteinykh Splavov, 65-70, 1979.
16. A. Mihajlovic, B. Marincek, 'Dissolution Kinetics of Technical Graphites in Iron Melts', Arch. Eisenhuettenw., Vol. 44, No. 7, 507-512, 1973.

17. V.M. Surovskii, N.K. Nekrasov, 'Kinetics of the Dissolution of Carbon in a High-Carbon Melt', Sb. Tr., Mosk. Vech. Metall. Inst. 1972, No. 12, 13-16 (in Russian).
18. P.M. Shurygin, V.D. Shantrín, 'Diffusion in the Fe-C System', Fiz. Met. Metallovdénie, No. 17, 471, 1964.
19. P.M. Shurygin, V.D. Shantrín, 'Solubility of Metals in Fe-C Solutions', Izv. VUZ. Chernaya Met., Vol. 6, No. 10, 5, 1963.
20. J.W. Robison, A.B. Draper, 'Dissolution of Silicon Carbide in Liquid Gray Irons', Paper No. A 78-21, 107th AIME Annual Meeting, Denver, February, 1978.
21. R.D. Pehlke, P.D. Goodell, R.W. Dunlap, 'Kinetics of Steel Dissolution in Molten Pig Iron', Trans. AIME, No. 233, 1420, 1965.
22. R.G. Olsson, V. Koump. T.F. Perzak, 'Rate of Dissolution of Carbon-Steel in Molten Iron-Carbon Alloys', Trans. AIME, No. 233, 1654, 1965.
23. K. Niwa, M. Shimei, R. Shina, 'A Kinetic Study on the Reaction of the Alumina Crucible with Carbon Dissolved in Molten Iron', Nippon Kinzok Gakkai-Si, No. 30, 329, 1966.
24. M. Kosaka, S. Minowa, 'Dissolution of Steel Cylinder into Liquid Fe-C Alloy', Tetsu-to-Hagane, No. 52, 1429, 1966.

25. M. Kosaka, S. Minowa, 'Mass Transfer from Solid Metal Cylinder into Liquid Metal', Tetsu-to-Hagane, No. 52, 1429, 1966.
26. A.V. Klibus, B.M. Lepinskikh, A.A. Gorshkov, 'Kinetics of the Dissolution of a Copper-Magnesium Alloy in Molten Cast Iron', Dop. Akad. Ukrain. R.S.R., Vol. 6A, 536, 1967.
27. M. Kosaka, S. Minowa, 'Dissolution of Steel Cylinder into Liquid Fe-C Alloy', Tetsu-to-Hagane, No. 53, 983, 1967.
28. A.V. Kaibichev, B.M. Lepinskikh, E.E. Shvetsov, B.I. Sergin, 'Kinetics of Dissolution of Cerium in Cast Iron', Russian Castings Production, No. 3, 108, 1968.
29. A.A. Vostryakov, B.M. Lepinskikh, 'Kinetics of Dissolution of Iron in Oxide Melts', Izv. Akad. Nauk SSSR Met., No. 4, 33, 1968; Russ. Met., No. 4, 23, 1968.
30. B.M. Lepinskikh, A.V. Kaibichev, V.A. Pankratov, 'Kinetics of Dissolution of Magnesium Alloys in Iron-Carbon Melts', Trudy Inst. Met. Sverdorsk, No. 20, 160, 1969.
31. A. Simkovich, K. Li, C.L. McCabe, 'Dissolution of Alumina in Carbon-Saturated Liquid Iron', Trans. AIME, No. 245, 897, 1969.
32. H. Nomura, K. Mori, 'The Rate of Dissolution of Iron into Liquid Fe-C Alloy', Tetsu-to-Hagane, No. 55, 1134, 1969.

33. G.N.K. Iyengar, R.D. Pehlke, 'Dissolution of Boron Nitride in Liquid Iron', Met. Trans., No. 1, 2235, 1970.
34. H. Ooi, Y. Oguchi, H. Nakato, 'Rate of Desulfurization of Carbon-Saturated Iron Melts by a Rotating Cylinder of Calcium Carbide', Tetsu-to-Hagane, No. 56, 991, 1970.
35. J. Szekely, Y.K. Chuang, J.W. Hlinka, 'The Melting and Dissolution of Low-Carbon Steels in Iron-Carbon Melts', Met. Trans., No. 3, 2825, 1972.
36. R.I.L. Guthrie, P. Stubbs, 'Kinetics of Scrap Melting in Baths of Molten Pig Iron', Canadian Metallurgical Quarterly, Vol. 12, No. 4, 465-473, 1973.
37. Yeong-Ukim, R.D. Pehlke, 'Mass Transfer during Dissolution of a Solid into Liquid in the Iron-Carbon System', Met. Trans. AIME, Vol. 5, 2527-2532, 1974.
38. R.B. Gundlach, R.D. Pehlke, 'Rate of Molybdenum Solution in Carbon-Saturated Liquid Iron', Met. Trans. AIME, No. 3, 2337-2342, 1972.
39. A.A. Vostryakov, B.M. Lepinskikh, L.N. Shibanova, 'Kinetics of Dissolution of Iron in its Sulphide Melts', Deposited Dec. 1975, VINITI 2013-75, 15 pp.
40. R. Ohno, 'Rates of Dissolution of Rotating Iron Cylinders in Liquid Copper and Copper-Iron Alloys', (Res. Inst. Iron, Steel Other Met., Tohoku Univ., Sendai, Japan), Met. Trans., Vol. 4, No. 4, 909-915, 1973 (Eng.).

41. V.D. Shantarín, P.M. Shurygin, V.V. Utochkin, 'Kinetics of the Dissolution of Niobium in Iron-Carbon Melts', Izvest. Akad. Nauk SSSR, Metally, No. 3, 31-33, 1966.
42. L.I. Krupman, V.I. Yavoiskii, 'Kinetics of Ferroalloy Dissolution in a Steel-Teeming Ladle', Izv. Vysshikh Uchebn. Zavedenii, Chern. Met., Vol. 7, No. 9, 35-42, 1964.
43. V.D. Shantarín, P.M. Shurygin, 'Kinetics of Alloying Cast-Iron and Steel with Pure Metals and Ferroalloys', Liteinoe Proizv., No. 7, 19-21, 1964; Russian Castings Production, No. 7, 309-311, 1964.
44. K. Mori, T. Sakuraya, 'Rate of Dissolution of Solid Iron in a Carbon-saturated Liquid Iron Alloy with Evolution of CO', Trans. Iron Steel Inst. Jpn., Dec. 1982, 22, (12), 984-990, (in English).
45. T. Sakuraya, K. Mori, 'Dissolution of Solid Iron in Fe-C Melts with Evolution of CO', Tetsu-to-Hagane (J. Iron Steel Inst. Jpn.), Jan. 1983, 60-66, 32-41, (in Japanese).
46. V.S. Shumikhin, A.K. Biletsky, G.I. Batalin, V. Anishin, 'Study on Thermodynamic and Kinetic Parameters of Dissolution of Solid Materials in Ferrocarbonic Melts', Arch. Eisenhüttenwes., 52, (4), Apr. 1981, pp. 143-146, (in English).
47. M. Benda, 'Kinetics and Mechanism of Dissolving Ferro-Alloys in Molten Steel', Neue Hutte, 29, (4), April 1984, 130-133, (in German).

48. K-P. Minuth, 'Dissolution of Chromium Alloys in Liquid Steel', Ph.D. thesis, Dep. of Metallurgy, Aachen Institute of Technology, February 1984, (in German).
49. Y. Shigeno, M.T. Tokuda, M. Ohtani, 'Influence of Sulfur and Phosphorus on the Dissolution Rate of Graphite Into Fe-C Melt', J. Jpn. Inst. Met., July 1982, 46, (7), 713-720, (in Japanese).
50. K. Suzuki, N. Kayama, 'Influence of Sulfur on the Behaviour of Graphite Dissolution in Molten Cast Iron', Imono (J. Jpn. Foundrymen's Soc.), July 1980, 52, (in Japanese).
51. A. Sato, R. Nakagawa, S. Yoshimatsu, A. Fukuzawa, T. Ozaki, 'Effect of Molten Slag on the Dissolution Rate of Reduced Iron Pellets in Iron Melts', Tetsu-to-Hagane (J. Iron Steel Inst. Jpn.), Oct. 1979, 65, (12), (in Japanese).
52. K. Bungardt, K. Wiebking, H. Brandis, H. Schmalzried, 'The Dissolution of Molybdenum and Tungsten in Iron Melts as a Contribution to the Process of Dissolution of Solid in Liquid Materials. I. - Dissolution of Solid Metallic Bodies in Metal Melts Unaffected by Convection; II. - Dissolution of Solid Metallic Bodies in Metal Melts Influenced by Convection', DEW. Techn. Ber., Vol. 9, No. 3, Sept. 1969, 407-438; discussion 431-437 (in German).

53. I.P. Kazachkov, I.B. Parimonchik, 'Kinetics of Fusion of Ferro-Alloys', *Steel in USSR*, 123-124, February 1973.
54. P.G. Terziyan, 'The Kinetics of the Solution of Ferro-alloys in Molten Steel', *Stal*, No. 2, 126-127, 1973.
55. G.S. Ershov, V.M. Bychev, 'Kinetics of the Dissolution of Titanium Nitride and Diffusion of Oxygen in Molten Iron', *Izvest. Akad. Nauk SSSR, Metally*. No. 1, 62-63, 1975 (in Russian).
56. I.P. Kazachov, I.B. Parimonchik, 'Factors Determining the Rate of Dissolution of Alloys in Molten Steel', *Metall. Koksokhim.*, No. 49, 56-60, 1976 (in Russian).
57. S.A. Argyropoulos, 'The Kinetics of Ferro-Alloy Solution in Liquid Steel', Master's Thesis, Dep. of Mining and Metallurgical Eng., McGill University, Montreal, Canada, 1977.
58. L. Courtsoyannis, H. Henein, R.I.L. Guthrie, 'Some Kinetic and Hydrodynamic Aspects of Making Aluminum and Ferro-alloy Additions to Steel Baths', *Physical Chemistry of Production or Use of Alloy Additives*, Proceedings of Sessions from the 103rd AIME Annual Meeting, Edited by John Farrel, 45-67, 1974.
59. F.A. Mucciardi, 'A Study of Light Alloy Addition Techniques in Steelmaking', Ph.D. Thesis, Dept. of Mining and Metallurgical Eng., McGill University, Montreal, October, 1980.

60. S.A. Argyropoulos, 'Dissolution of High Melting Point Additions in Liquid Steel', Ph.D. thesis, Dep. of Mining and Metallurgical Eng., McGill University, August, 1981.
61. S.A. Argyropoulos, R.I.L. Guthrie, 'The Dissolution of Titanium in Liquid Steel', Metallurgical Transactions-B, Vol. 15B, 47-58, March, 1984.
62. S.A. Argyropoulos, R.I.L. Guthrie, 'Titanium Additions in Steelmaking', 5th International Conference on Titanium, (Industrial Applications), Munich, September, 1984.
63. S.A. Argyropoulos, 'Dissolution Characteristics of Ferralloys in Liquid Steel', Electric Furnace Conference Proceedings, Vol. 41, Iron & Steel Society of AIME, December, 1983.
64. A.P. Budakov, Yu.P. Filimonov, 'Dissolution of Molybdenum in Liquid Steel', Izv. V.U.Z. Chernaya Metall., 1985, (5), 70-72, (in Russian).
65. C.E. Seaton, A.A. Rodriguez, M. González, M. Manrique, 'The Rate of Dissolution of Pre-Reduced Iron in Molten Steel', Trans. Iron Steel Inst. Jpn., Jan. 1983, 23, (1), 14-20, (in English).
66. S-O. Ericsson, P-O. Mellberg, 'Influence of Sulphur on the Rate of Carbon Dissolution in Liquid Iron', Scand. J. Metall., 1981, 10, (1), 15-18, (in English).

67. Q. Han, T. Han, J. Wang, 'Determination of Diffusion Coefficient of Carbon in Liquid Iron', *Acta Metall. Sin.*, Dec. 1980, 16, (4), 435-441, (in Chinese).
68. W. Helber, 'Dissolution of Chromium Metal and Ferro-Chrome in Molten Iron', Ph.D. thesis, Dep. of Metallurgy, Aachen Institute of Technology, July 1969, (in German).
69. A.E. Semin, A.B. Usachev, A. Ya. Stomakhin, 'The Influence of Ferrochromium Carbon Content on Its Solution Rate in Liquid Steel', *Izv. V.U.Z. Chernaya Metall.*, 1981, (7), 41-43, (in Russian).
70. S.B. Essel'bakh, Ya.l. Gelb'shtein, A.O. Gorst, N.G. Mayorova, 'Dissolution and Assimilation of Iron Inoculants in Pouring Ladles', *Liteinoe Proizvod.*, July 1980, (7), 7-9, (in Russian).
71. S.A. Argyropoulos, P.D. Deeley, 'Exothermic Alloy for Addition of Alloying Ingredients to Steel', United States Patent, Patent Number 4, 472, 196, Sept. 18, 1984.
72. G.S. Ershov, A.A. Kasatkin, I.V. Gavrilin, 'Diffusion of Various Alloying Elements in Liquid Fe in the Temperature Range 1550-1700°C', *Izv. Akad. Nauk SSSR, Met.*, No. 2, 76-79, 1978; 'Diffusion and Defect Data', 195-196, 1978.
73. Y. Ono and T. Shigematsu, 'Diffusion Coefficients of Vanadium, Cobalt and Molybdenum in Molten Iron', *Journal Japan Inst. Metallurgy*, Vol. 41, No. 1, 62-68, 1977.

74. D.Y. Povolotskii, V.E. Roshchin, A.N. Keis, 'Diffusion of Deoxidants in Molten Iron', Steel in the USSR, Vol. 2, No. 4, 289-291.
75. C.J. Smithells, 'Metals Reference Book', Fifth edition, Butterworths, 1976.
76. R. Hultgren, P.D. Desai, D.T. Hawkins, M. Gleiser, K.K. Kelley, D.D. Wagman, 'Selected Values of the Thermodynamic Properties of the Elements', American Society for Metals, 1973.
77. R. Hultgren, P.D. Desai, D.T. Hawkins, M. Gleiser, K.K. Kelley, 'Selected Values of the Thermodynamic Properties of Binary Alloys', American Society for Metals, 1973.
78. J.F. Elliott, M. Gleiser, V. Ramakrishna, 'Thermochemistry for Steelmaking', Addison-Wesley Publishing Company Inc., 1963.
79. L.D. Lucas, in 'Physicochemical Measurements in Metals Research', (R.A. Rapp, ed.), p. 219, Wiley Int., New York, 1970.
80. K.W. Lange, 'Zur Temperaturleitfähigkeit des Eisens', Arch. Eisenhüttenw., No. 41, 559, 1970.
81. E.T. Turkdogan, 'Physical Chemistry of High-Temperature Technology', Academic Press, 1980.
82. S. Wagner, G. St. Pierre, 'Thermodynamics of the liquid Binary Iron-Titanium by Mass Spectrometry', Metal. Trans., No. 5, 887, April, 1974.

83. P.G. Sismanis, S.A. Argyropoulos, 'The Effect of Oxygen on the Recovery and Dissolution of Ferroalloys', Proceedings of the 69th Steelmaking Conference, Washington, D.C., April 1986.
84. Metals Handbook, Volume 1, Ninth Edition, American Society for Metals.
85. S.A. Argyropoulos, R.S. Valiveti, B.M. Closset, 'A Facility for Local and Remote Data Acquisition and Process Control in Metallurgy', Journal of Metals, Vol. 35, No. 10, Oct. 1983, pp. 30-35.
86. O. Kubaschewski, 'Iron-Binary Phase Diagrams', Springer-Verlag, Berlin, 1982.
87. G.B. Barbi, 'High Temperature Electrochemical Determination of the Thermodynamic Stability of the Iron-Rich, Iron-Niobium Intermetallic Phase', Z. Naturforsch., Vol. 24a, 1580-5, 1969, (in English).
88. V.N. Drobyshev, T.N. Rezhukhina, 'X-Ray Investigation of the Nb-Fe System and the Determination of the Thermodynamic Properties of the Compound NbFe<sub>2</sub>', Russian Metallurgy, (2), 85-9, 1966.
89. A.K. Niessen, F.R. de Boer, R. Boom, P.F. de Châtel, W.C.M. Mattens, A.R. Miedema, 'Model Predictions for the Enthalpy of Formation of Transition Metal Alloys II', CALPHAD, Vol. 7, No. 1, pp. 51-70, 1983.
90. Y. Iguchi, S. Nobori, K. Saito, T. Fuwa, 'A Calorimetric Study of Heats of Mixing of Liquid Iron Alloys',

- Fe-Cr, Fe-Mo, Fe-W, Fe-V, Fe-Nb, Fe-Ta, TETSU-TO-HAGANE, 68, No. 6, pp. 89-96, 1982, (in Japanese).
91. C.W. Bale, A.D. Pelton, W.T. Thompson, F\*A\*C\*T System, Montreal, Quebec, Canada, 1982, THERMFACT LTD/LTEE.
  92. T.O. Malakhova, Z.M. Alekseyeva, 'The Zr-Fe Phase Diagram in the Range 20-40 at.% Fe and the Crystalline Structure of the Intermetallic Compound  $Zr_3Fe$ ', Journal of the Less Common Metals, 81, 1981, 293-300.
  93. F. Aubertin, U. Gonser, S.J. Campbell, H.-G. Wagner, 'An Appraisal of the Phases of the Zirconium-Iron System', Z. Metallkunde, Vol. 76, 1985, (4), pp. 237-244.
  94. Z. Altounian, C.A. Volkert, J.O. Strom-Olsen, 'Crystallization Characteristics of Fe-Zr Metallic Glasses from  $Fe_{43}Zr_{57}$  to  $Fe_{20}Zr_{80}$ ', J. Appl. Phys., 57, (6), 1985, pp. 1777-1782.
  95. A. Schneider, H. Klotz, J. Stendel, G. Strauss, Pure Applied Chem., 1961, (2), 13.
  96. J.C. Gachon, J. Hertz, 'Enthalpies of Formation of Binary Phases in the Systems FeTi, FeZr, CoTi, CoZr, NiTi, and NiZr, by Direct Reaction Calorimetry', CALPHAD, Vol. 7, No. 1, pp. 1-12, 1983.
  97. V.G. Dyubanov, A. Ya. Stomakhin, A.F. Filippov, 'Investigation of Enthalpies of Formation of Dilute Solutions Based on Iron, Cobalt and Nickel', Izvestiya VUZ, Chernaya metallurgiya, 1975, No. 3, pp. 5-7, (in Russian).

98. Y. Iguchi, Faculty of Engineering, Tohoku University, Japan, (private communication), August 1983.
99. O.I. Ostrovskiy, A. Ya. Stomakhin, V.A. Grigoryan, 'Thermodynamic Properties of Melts based on Iron or Nickel', Izvestiya AN SSSR, Russian Metallurgy, 1977, pp. 71-75, (in English).
100. H.K. Hardy, 'A Sub-Regular Solution Model and its Application to some Binary Alloy Systems', Acta Metallurgica, Vol. 1, 1953, pp. 202-209.
101. C.H.P. Lupis, J.F. Elliott, 'Prediction of Enthalpy and Entropy Interaction Coefficients by the Central Atoms Theory', Acta Metallurgica, Vol. 15, 1967, pp. 265-276.
102. C.H.P. Lupis, 'Chemical Thermodynamics of Materials', North-Holland, New York, 1983.
103. F.P. Incropera, D.P. DeWitt, 'Fundamentals of Heat Transfer', John Wiley & Sons, Inc., New York, 1981.
104. P.G. Sismanis, S.A. Argyropoulos, 'Measuring Convection in Steel Metal Baths', Proceeding of the 5th Process Technology Conference Detroit, Michigan, 1985, pp. 167-177.
105. P.G. Sismanis, 'An Experimental Technique to Measure Convection in Liquid Metals', Master of Eng. Thesis, Department of Mining and Metallurgical Eng., McGill University, Montreal, Canada, March, 1985.
106. S.W. Churchill, M. Bernstein, 'A Correlating Equation for Forced Convection From Gases and Liquids to a

- Circular Cylinder in Crossflow', *Journal of Heat Transfer, Transactions of the ASME*, Vol. 99, May 1977, pp. 300-306.
107. D.B. Evans, R.D. Pehlke, 'Equilibria of Nitrogen with the Refractory Metals Titanium, Zirconium, Columbium, Vanadium, and Tantalum in Liquid Iron', *Transactions of the Metallurgical Society of AIME*, Vol. 233, August, 1965, pp. 1620-1624.
  108. C. Bodsworth, H.B. Bell, 'Physical Chemistry of Iron and Steel Manufacture', 2nd edition, Longman (Publisher), London, England, 1972, pp. 413-416.
  109. J.F. Elliott, 'Physical Chemistry of Liquid Steel', *Electric Furnace Steelmaking*, published by the Iron and Steel Society, 1985, Chapter 21, pp. 291-319.
  110. C.H.P. Lupis, 'Chemical Thermodynamics of Materials', Elsevier Science Publishing Co., Inc., 1983, pp. 257-259.
  111. R.H. Perry, C.H. Chilton, "Chemical Engineers' Handbook", 5th ed., McGraw-Hill, New York, NY, 1973, Chapter 10.
  112. R.B. Bird, W.E. Stewart, E.N. Lightfoot, 'Transport Phenomena', John Wiley & Sons, 1960, Chapter 21.
  113. J.R. Welty, R.E. Wilson, C.E. Wicks, 'Fundamentals of Momentum, Heat, and Mass Transfer', John Wiley & Sons, 2nd edition, New York, 1976, pp. 583-584 and pp. 634-641.
  114. M. Kosaka, S. Minowa, 'Mass Transfer from Solid Metal Cylinder into Liquid Metal', *Tetsu-to-Hagane*, 52, (12), 1966, pp. 1748-1762.

115. E. Ravoo, J.W. Rotte, F.W. Sevenstern, 'Theoretical and Electrochemical Investigation of Free Convection Mass Transfer at Vertical Cylinders', Chemical Engineering Science, 1970, Vol. 25, pp. 1637-1652.
116. T. Ishida, 'Rate of Dissolution of Solid Nickel in Liquid Tin under Static Conditions', Met. Transactions, Vol. 17B, June, 1986, pp. 281-289.
117. F.A. Mucciardi, 'Heat Flow to Cylinders Submerged in Liquid Metal Baths', Master's Thesis, Dept. of Mining and Metallurgical Eng., McGill University, Montreal, January 1977.
118. J.F. Elliott, 'Physical Chemistry of High Temperature Reactions', Electric Furnace Steelmaking, published by the Iron & Steel Society - AIME, Chapter 20, 1985.
119. J. Silver, 'Alloys and Metals for the Production of High-Strength Low-Alloy Steels', Ferroalloys and Other Additives to Liquid Iron and Steel, ASTM Special Technical Publication 739, J.R. Lampman and A.T. Peters (editors), pp. 170-179, 1981.
120. E.A. Brandes (editor), 'Smithells Metals Reference Book', 6th edition, Butterworths, 1983, p. 11-369.
121. O. Kubaschewski, C.B. Alcock, 'Metallurgical Thermochemistry', Pergamon Press, 5th Edition, p. 183 and p. 187.